

I. Dynamics of Block Copolymer Nanostructures

II. Polymerizability of Cyclic Olefins and Ring-Closing Metathesis

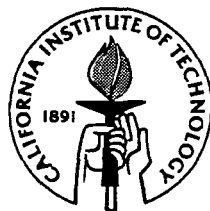
Dissertation by
Zhong-Ren Chen

In Partial Fulfillment of the Requirements
for the Degree of
Doctor of Philosophy

California Institute of Technology
Division of Chemistry and Chemical Engineering
Pasadena, California

1998

(Submitted December 9, 1997)



Copyright © 1997

Zhong-Ren Chen

All Rights Reserved

Dedicated to My Parents

Mother (1925-1997)

Father (1924-1997)

for their love and support till their last moments

Acknowledgment

At first, I would like to thank my research advisor Julie Kornfield and co-advisor Bob Grubbs, for their encouragement, support, and guidance. I feel so lucky that I have such wonderful advisors. Bob's hands-off style gave me the opportunity to explore when I started the first project on molecular modeling. Julie has been a constant source of enthusiasm, inspiration, and optimism. I would also like to thank my thesis committee members Professor Zhen-Gang Wang and Dr. Chan U. Ko of Avery Dennison, and my candidacy committee member Professor Masao Doi for their time and effort.

1997 is the year that I will never forget. I lost both of my parents. They provided me with endless love and support till their last moments. I remember, when I was three years old, in a chilly snowing evening, my mother, my sisters and I were waiting for father. We were hungry, cold, worried, and scared. He was walking back home from tens of miles away, since bus was too expensive. They worked so hard, risked their lives, and sacrificed their health to raise their children. I remember, they were so happy when I got enrolled in a good college, although they even could not write down their own name. They were too poor to attend school. I owe thanks to my sisters and brothers for their love, support, and understanding. They spent days and nights for many years taking care of our parents, so I could focus on my study.

I am so lucky since Caltech provides such a pleasant, supportive, and intellectual working atmosphere. Jerome Claverie (I spell his last name as Clever) introduced me into molecular modeling and olefin metathesis. I enjoyed collaboration with such a wonderful scientist in cyclics project. Scott Miller taught me a lot of ring-closing metathesis.

I am very grateful for the assistance of Vinay Gupta, Ramanan Krishnamoorti, and Barbara Wang. They introduced me into the state-of-the-art-of rheo-optical methods and block copolymers. I enjoyed support and friendship from Kathy Bubash (our former group secretary) and Anne Hormann (our current secretary). I would also thank Suresha Gupta for assistance in using computers. I thanks Pat and Jean (Biology division), and Carol (Materials Science) for initiating TEM work.

Special thanks are due to Ani Issaian, a wonderful microscopist. My thesis would not have so many beautiful TEM pictures without her collaboration. I owe many thanks to Dr. Steve Smith of Procter & Gamble and his graduate student Arman Ashraf for the synthesis of all the block copolymers, and Dr. Mike Satkowski, also of Procter and Gamble, and his graduate student Jeff Grothaus for performing the small-angle x-ray scattering experiments. Thanks are also due to Robert (Yeng-Long) Chen, a talented undergraduate at Caltech. Without his SURF work, many experiments may never have been performed.

I cherish the joy, moral support, and friendship with talented people at Caltech, especially in Kornfield group and Grubbs group. A random list includes Ani, Guru, Weijun, Jagdish, Sunil, Bhavana, Deniz, Ravi, Giyoong, Vinay, Susan, Barbara, Ramanan, Steve, Chung, and Kannan of Kornfield group; Jerome, Zhe, Pu, Amy, Bobby, Scott, Geoff, Bill, many Mikes, and many Toms of Grubbs group. I will miss birthday celebrations with Cecelia, Roger, Shervin, Jennifer, Simon, Leon, Kate, Mehrdad, and Wayez.

I am so fortunate living with undergraduate and graduate friends in Braun house. We enjoyed friendship, nice dinners, and dancing in Santa Monica, Monterey Park, Hollywood, and of course, in Braun house. Lin (Harvard), Emily (Cornell), Maria, Ben, Kenny (Oracle), Kevin, and Mat, I wish you the best in your work, school and life.

Thesis Abstract

Self-assembly of block copolymers provide versatile means to create nanostructures with potential applications in nanotechnologies. The form and size of these structures are controlled by the type and the length of each block, and the number of blocks. Active processing using symmetry-breaking fields such as flow can extend self-assembled order into the macroscopic dimensions, thus gain desired directional properties, such as transport, optical, and electrical properties.

Towards the integrated synthesis and processing of functional block copolymer nanostructures, dynamics and thermodynamics of block copolymer nanostructures must be understood. The dynamics of flow-induced alignment of block copolymers will provide the basis to predict the direction, rate, and degree of alignment, while defect dynamics and thermodynamics will give insight into the possibilities of formation of desired nanostructures. In chapter 1, I will overview key issues of flow-induced alignment based on literature and new results from the first two chapters of the thesis. A three-dimensional mapping summarizes the flow behavior of diblock copolymers in terms of molecular characteristics and processing conditions. Various mechanisms that had been proposed since two decades ago are reviewed and re-evaluated.

In chapter 2, I will present detailed results revealed by a powerful experimental method, which combines in-situ rheo-optical measurements and ex-situ structural characterization by electron microscopy and x-ray scattering. A PS-PI (10K-10K) diblock is used as a model system. Three different trajectories of alignment are investigated: perpendicular alignment and two qualitatively different routes to parallel alignment. At the highest frequencies, symmetry arguments explain the transient development of a bimodal texture en route to alignment of layers parallel to the planes of shear. At lower frequencies, larger scale relaxations introduce rearrangements out of the deformation plane that permit formation of lamellae perpendicular to the shear plane. These explain the change in character of the pathway to parallel alignment and the emergence of perpendicular alignment with decreasing frequency. For each trajectory in general, the initial 'fast' process enhances not only the projection of the orientation distribution that corresponds to the final state, but also

increases other projections of the distribution; the late-stage 'slow' process eliminates these other projections and perfects a single alignment.

ABC triblock copolymer can form a fascinating array of nanostructures. Phase behavior, dynamics of oscillatory-shear alignment, and other issues raised by ABC triblock copolymers, such as dynamics of lamellar perforation in three-nanophase-separated states will be discussed in chapter 3. Both thermotropical and shear-induced phase transitions are observed. Dramatic changes of morphology and alignment behavior are induced simply by switching the permutation of the blocks, molecular size, shear condition, and temperature. In three-nanophase-separated lamellar materials, a new type of defect is found: correlated perforation. As these defects annihilate upon annealing, long range correlations produce striking patterns, including those that resemble a ship's wake. The creation and evolution of these defect structures present challenge and opportunities in developing novel nanostructures.

Olefin metathesis by transition metal complex has been a powerful method in polymer and organic synthesis. In chapter 4, I will present a model to predict the ring-chain equilibria in ring-opening-closing reaction. Statistical mechanics and molecular mechanics provide the basic tools in problem formulation and parameter determination. Polymerizability of cyclic olefins are predicted by this model, and agree well with ring-opening metathesis polymerization experiments. We have extended this model to assist ring-closing metathesis of eight-member rings, which can be a useful starting material for drug synthesis.

Content

Dedication		iii
Acknowledgment		iv
Thesis Abstract		vi
Content		viii
Part I	Dynamics of Block Copolymer Nanostructures	
Chapter 1	Overview	1
	Abstract	1
	1. Basic Concepts of Flow-Induced Alignment	5
	2. Experimental Needs and Approaches	8
	A. Determination of Characteristic Frequencies	8
	B. Characterization of the Time Evolution of Microstructure	11
	C. Characterization of Well-Aligned States	15
	3. Trajectories, Kinetics, and Structural Evolution	16
	A. Trajectories of Alignment	16
	B. Kinetics of Alignment	18
	C. Structural Evolution	20
	4. Alignment Mechanisms	24
	5. Effect of Macromolecular Architecture: Bridges and Loops	32
	A. ABA Triblock Copolymers	33
	B. ABC Triblock Copolymers	34
	6. Implications and Future Work	36
	Schematics of ABC Triblock Copolymer Morphologies	39
	References	40
	Caption of Figures	48
	Figures	52
Chapter 2	PS-PI Diblock: Dynamics of Alignment and Structural Evolution	76
	Abstract	76
	1. Introduction	77
	2. Experimental Section	80
	3. Results	86
	A. Initial Unaligned State	86
	B. Shear-Induced Alignment at $\omega < \omega_c'$: the Path to Perpendicular Orientation	87
	C. Shear-Induced Alignment at $\omega_c' < \omega < 10\omega_c'$: One Route to Parallel Orientation	90
	D. Shear-Induced Alignment at $\omega_c' \ll \omega$: Another Route to Parallel Orientation	93
	4. Discussion	97
	A. Evolution of Microstructure	98
	B. Implications Regarding Alignment Mechanisms	100
	5. Conclusions	105
	References	108
	Caption of Figures	114
	Figures	118

Chapter 3	ABC Triblocks: Phase Behavior and Shear Orientation	143
	Abstract	143
	1. Introduction	145
	2. Experimental Section	146
	3. Phase Behaviors	149
	4. Effect of Shear Flow: Shear Orientation and Shear-Induced Phase Transitions	154
	A. ABA-Type Two-Phase Lamellae	155
	B. AB Diblock Lamellae: Symmetric and Asymmetric	157
	C. Three-Phase Lamellae: Shear Orientation and Defect Dynamics	160
	D. Hexagonal Cylinders: Alignment and Phase Transitions	162
	5. Conclusions	165
	Appendix: Tables for Shift Factors	167
	References	168
	Caption of Figures	172
	Figures	177
Part II	Polymerizability of Cyclic Olefins and Ring-Closing Metathesis	
Chapter 4	Polymerizability of Cyclic Olefins and Ring-Closing Metathesis	239
	Abstract	239
	1. Introduction	240
	2. Theory and Methods	243
	2.1 Calculation of the Entropic Term	244
	2.2 Calculation of the Enthalpic Term	244
	2.3 Ring-Chain Equilibrium Calculation	247
	2.4 Computational Methods	248
	3. Results and Discussion	249
	3.1 Effect of Ring Strain on Equilibrium Constants	249
	3.2 Equilibrium Cyclics Distribution for Cycloolefins	250
	3.3 Effect of Reaction Conditions on Ring-Chain Equilibrium	252
	3.4 Definition of Critical Concentration	253
	3.5 General Approach to Predict Polymerizability	254
	4. Conclusion	255
	References	257
	Caption of Figures	261
	Figures	263
	Appendix: Ring-Closing Metathesis	277
Appendix	Small-Angle X-Ray Scattering Patterns	284
	TEM Micrographs	287

Chapter 1 Overview

Abstract

Toward the integrated synthesis and processing of functional block copolymer nanostructures, the physics of flow-induced alignment of block copolymers must be understood to predict the direction, rate, and degree of alignment. In this review we focus on key issues regarding flow-induced alignment of lamellae. A three-dimensional mapping summarizes previous results on the selection of alignment directions (parallel or perpendicular) and their pathways in terms of three dimensionless parameters: frequency, temperature, and strain amplitude. Trajectories, kinetics, and structural evolution are explored in a fourth dimension (time). The challenge of developing adequate experimental methods to monitor transient structure is discussed. A comprehensive experimental approach, which combines in-situ rheo-optical measurements and ex-situ structural characterization by electron microscopy and x-ray scattering, is presented as a new tool to track changes of microstructure and orientation during flow-induced alignment. Various mechanisms that have been proposed over the past two decades are reviewed and re-evaluated based on recent experimental results. Outstanding questions and new issues raised by ABC triblock copolymer nanostructures are discussed.

Nanostructural engineering represents a new avenue to improve the performance of materials such as metals,¹ polymers,²⁻⁴ ceramics,⁵ and those beyond traditional classification.⁶⁻⁸ Advances in understanding the chemistry and physics of materials provide the tools for synthesis and structural manipulation.¹⁻¹⁰ Without altering the chemical composition, introduction of desired microstructure can enhance or even create outstanding properties from a traditional material. Self-assembly, among other approaches, provides a versatile means to create desired nanostructures in bulk materials or at interfaces, with potential applications in biomaterials,^{6,10,11} optics,¹² and microelectronics.¹³ This review deals with a particular class of self-assembled materials, block copolymers, that offer control of the form and size of their local nanostructure by design of the macromolecular architecture.^{3,9,10,14-20} These polymers are also amenable to producing materials in which the local structure can be aligned over macroscopic dimensions and the number of defects in the local structure can be drastically reduced through processing.²¹ The dynamics of macroscopic alignment are critical in tailoring materials' structure and properties and is the focus of the present review.

Block copolymers (BCPs) represent an important class of microstructurally engineered materials in large part because their morphology and dynamics can be systematically controlled by choosing the blocks' compositions and relative lengths.¹⁴⁻³⁰ For example, diblock copolymers consisting of two flexible but chemically different segments can form cubic arrays of spheres, hexagonal arrays of cylinders, bicontinuous cubic phases or lamellae, depending on the relative lengths of the blocks.²⁰ Self-assembly of block copolymers can be combined with the orientational ordering tendencies of liquid crystalline polymers (LCP) by synthesizing polymers in which at least one block is a LCP.^{27,30,31} For rod-coil diblock copolymers, interesting zigzag and arrowhead morphologies have been observed.²⁷ Greater diversity in the form of the nanostructure can be achieved by connecting three distinct blocks to form ABC triblock copolymers, which assemble such sophisticated structures as helical strands surrounding cylinders in a continuous matrix.¹⁴⁻¹⁶ Confinement within the self-assembled nanostructure of a block copolymer can be used to affect further structure

development within it, such as the subsequent crystallization of one of the blocks.²⁸ Similarly, the form of the BCP nanostructure can be used as a template for the synthesis of a solid by polymerization of an epoxy²⁹ or by controlled nucleation and growth of inorganic particles.³²

Self-assembly of BCPs typically leads to local order. This local order can be extended to the macroscale by processing using applied fields to achieve directional properties, such as transport, optical, and electrical properties. Recently, in a diblock copolymer consisting of polystyrene and a side-chain ferroelectric liquid crystalline polymer, bistable ferroelectric switching was detected in an aligned lamellar material, though there is no ferroelectric response without orientation.³⁰ Symmetry-breaking fields, such as flow and electric fields have been used to induce alignment.^{2,21-26,33-65} Flow provides an efficient and versatile means to achieve global alignment, as demonstrated by materials subjected to extrusion,²⁴ oscillatory and steady shear,^{25,26,39-63} extensional flow,⁶⁴ and roll-casting.⁶⁵ Further, the alignment direction of lamellae may switch by 90° with a small change in processing conditions.³⁹ This ‘flipping’ phenomenon may ultimately provide responsive, switchable material properties.

The physical basis of the effects of molecular architecture and processing conditions must be understood for the integrated synthesis and processing of functional materials based on aligned block copolymer nanostructures. For example, which type of flow is the the most effective in inducing global order? Which parameters control the direction, rate, and perfection of alignment for a specific type of block copolymer? How do we design a block copolymer so that directional properties can be achieved by convenient processing conditions? To address these critical issues, investigations are underway to determine the effect of flow conditions and macromolecular characteristics on the direction,^{2,39-50,63} rate,^{49,51,63} and mechanisms^{2,25,26,35,39,47,55,63} that lead to macroscale order. Scattering, microscopy, and rheo-optical methods are used to characterize the form and orientation distribution of these nanostructures under shear. Unfortunately, any one of these methods alone can not provide all of the necessary structural information. Scattering does not provide adequate time resolution, microscopic methods such as TEM are not in-situ methods,

and rheo-optical methods are not capable of capturing detailed structural information. A combination of real-time rheo-optical methods with ex-situ structural characterization using both SAXS and TEM has provided new insight into the physics of alignment, establishing a framework for understanding much of the alignment behavior of lamellar BCPs.^{2,63}

This review focuses on recent progress in the physics of flow-induced alignment in lamellar block copolymers. Only oscillatory shear is discussed, since it permits systematic investigation of the coupled effects of the rate and amplitude of deformation in relation to the relaxation dynamics of the self-assembled nanostructure. The extensive body of experimental results on the dynamics of lamellar systems in particular permits a critical evaluation of the concepts that have been put forward to explain their alignment behavior. Comprehensive reviews are available for general aspects of the thermodynamics²⁰ and dynamics^{21,22} of block copolymer melts and solutions. The present article is divided into five sections: 1) basic concepts regarding the direction and types of lamellar alignment, conditions that induce each type of alignment, and their relationship to the intrinsic dynamical properties of BCPs; 2) experimental approaches to test these basic concepts; 3) distinct alignment trajectories, their kinetics and the evolution of structure during the alignment process; 4) mechanisms of flow-induced alignment; and 5) the effects of different polymer architectures on flow behavior. The fundamental physics of alignment discussed in the first four sections is based mainly on investigations of polystyrene-polyisoprene (PS-PI) diblock copolymers, since this model system is suitable to almost all types of experimental methods, including rheo-optical, x-ray and neutron scattering, and transmission electron microscopy, and has been studied most intensively. Among the effects of polymer architecture, particular attention is given to ABC triblock copolymers since they are able to form complex and interesting nanostructures. To close, we highlight the implications of current work and offer some suggestions for future studies.

1. Basic Concepts of Flow-Induced Alignment

Large amplitude oscillatory shear (LAOS) can produce either “parallel” or “perpendicular” alignment in a nearly symmetric poly(ethylene-propylene)-poly(ethylene) (PEP-PEE) (Figure 1) and PEP-PEE-type BCPs (such as PEP-PE).^{39,40,46} This “flipping” phenomenon is also observed in PS-PI and other PS-PI-type BCPs (styrene-diene BCPs and their hydrogenated counterparts).^{2,39–50,63} To explain the observed frequency-dependent alignment behavior, two characteristic frequencies have been proposed: the frequency above which the distortion of chain conformation dominates the materials’ viscoelasticity (ω'_c);^{46,47,49,67–70} and the frequency below which the relaxation of domains becomes significant (ω_d). Between ω'_c and ω_d the distortion of the nanostructure dominates the viscoelastic response of the material.

Four frequency regimes have been found and different types of alignment dominate in each regime. Perpendicular alignment may be induced by shearing at frequencies that couple with the dynamics of the nanostructure, i.e., frequencies too fast for domain-scale relaxation, but slow enough that chain conformation is relaxed $\omega_d < \omega < \omega'_c$ (Regime I). Two regimes exist at higher frequencies $\omega > \omega'_c$ that are associated with parallel alignment, but through two qualitatively different pathways. At frequencies slightly above ω'_c , parallel alignment occurs through a transient orientation distribution that consists of parallel and perpendicular orientations and the range of orientations between the two (Regime II: $\omega'_c < \omega < 10 \cdot \omega'_c$). Frequencies far above ω'_c can also induce parallel alignment, but through bimodal distributions rich in parallel and transverse orientations (Regime III: $\omega > 10 \cdot \omega'_c$). At low frequencies (Regime IV: $\omega < \omega_d$) the alignment direction tends to be parallel in some systems (e.g. PEP-PEE-type)^{39,40,46} and perpendicular in others^{2,41,42,44,47,49,50,63} (such as PS-PI-type, except following a specific thermal treatment: prolonged annealing close to the BCPs’ upper glass transition^{48,55,56}). Within each regime, strain amplitude affects the rate and degree of alignment; strain amplitude can even alter the direction of alignment, particularly if the frequency is in the vicinity of the boundary between Regimes I and II⁵⁰

and perhaps near the boundary between Regimes IV and I.⁵⁸ The complex interplay of temperature, frequency, and strain amplitude can be represented using a three-dimensional mapping (Figure 1). Rich information on the way alignment occurs is manifested in the additional dimension of time. Within a given frequency regime (Regime I, II, or III),⁶⁶ the time evolution of microstructures follows a particular type of trajectory.^{49,50} For each trajectory, the initial fast process is responsible for the selective creation of layers, while the later slow process is responsible for selective elimination of all orientations but one, and leads to the final unidirectional, single-crystal-like structure.⁶³

Theoretical explanations of the alignment regimes focus on the relative stability of distinct well-aligned states. The transverse alignment is most unstable, since the equilibrium spacing is disturbed by shearing. Fluctuations on a layered structure can couple to shear if the lamellae are in the parallel orientation, making this alignment less stable than perpendicular.^{33,34} However, the effect of fluctuations will be confined to frequencies fast enough that the fluctuations are not averaged out ($\omega > \omega_d$) and slow enough that distortion of the nanostructure is not overwhelmed by more local responses, such as conformational distortion of the polymer chains ($\omega < \omega'_c$). These concepts are in accord with the observation that perpendicular alignment is induced by deformation frequencies at which the dynamics are dominated by the layered nanostructure ($\omega_d < \omega < \omega'_c$, “lamellar regime”) (Figure 2) and at temperatures in proximity to the order-disorder transition temperature (ODT).³⁹ Parallel alignment is predicted to be more stable than perpendicular below a critical frequency controlled by the characteristic lifetime of fluctuations ($\omega < \omega_d$).³³ These arguments can describe the experimentally observed behavior of the PEP-PEE system.³⁹

In order to explain parallel alignment at higher frequencies ($\omega > \omega'_c$) for PS-PI and other similar systems, the concept of viscoelastic contrast has been introduced.⁴⁷ At frequencies faster than the conformational relaxation of the chains ($\omega > \omega'_c$), the deformation couples to more local dynamics, and differences between the types of layers in the ordered structure can be probed. If there is considerable difference in the mechanical properties of the two types of layers (such as with PS-PI), the modulus of the parallel state is lower than that of the

perpendicular state, and this may explain the selection of parallel alignment. Thus, three frequency regimes have been identified: $\omega < \omega_d$ where parallel alignment can be induced, $\omega_d < \omega < \omega'_c$ where perpendicular alignment can be induced, and $\omega'_c < \omega$ where parallel alignment can be induced in lamellar arrays in which the layers have dissimilar viscoelastic properties.

These concepts regarding the relative stability of monodomains have provided a valuable guide to experiment. They explain three frequency regimes based on the final alignment direction. But concepts that deal with differently oriented monodomains are not sufficient to clarify the mechanisms of alignment. This is illustrated by the existence of at least two qualitatively different routes to the same final state, e.g. parallel at $\omega > \omega'_c$.

To understand pathways to alignment, concepts regarding the mechanisms of orientation selection and defect dynamics have been put forward since the early 1970's. In the early work of Keller and Hadziioannou, the concepts of grain rotation, anisotropic viscoelasticity, selective melting and defect migration have been considered.^{24,25} The selective melting hypothesis has taken on a special role in explaining the development of perpendicular alignment under conditions close to the ODT.³⁹ It has also been suggested that two or more mechanisms may act in combination to produce alignment.^{25,26,41} However, in-situ information was not available to examine the validity and relative importance of these ideas. Further, these concepts need to be made more specific in order to assist theoretical advances. For example, what type of defects dominate? Does the answer depend on flow conditions (ω , T)? Does the relative importance of different types of defects change as the system moves through the alignment process?

To answer these questions, developing appropriate experimental methods to characterize the transient structure is crucial. In addition, methods to determine the characteristic frequencies ω'_c and ω_d are needed to test theories regarding the frequency regimes that lead to particular alignment. Therefore, before we review recent progress in understanding the nature and kinetics of alignment processes, we first discuss the experimental tools that exist and their current limitations.

2. Experimental Needs and Approaches

Our discussion of the experimental approaches used to test the basic concepts of flow-induced alignment begins with methods to determine ω'_c and ω_d using melt rheology and optical rheometry. As has been pointed out, ω'_c appears to define one of the key boundaries, between Regimes I and II; ω_d may be related to the relaxation of domains and may define the boundary between Regimes IV and I. The evolution of structure during shearing provides direct information on the mechanisms of alignment, so experimental approaches to characterize the time evolution of structures under shear will be addressed. We close this section by commenting briefly on the characterization of well-aligned states.

A. Determination of Characteristic Frequencies

Developing robust, reproducible, and precise experimental methods to determine ω'_c and ω_d is of practical importance to locate alignment behavior in the frequency spectrum for a given polymer. So far there is only one method for determining the parameter ω'_c that meets these criteria. The storage modulus ($G'(\omega)$) of the ordered, but unaligned state is compared to that of the disordered material, and ω'_c is determined as the frequency below which the ordered state has a substantially larger modulus than the disordered material (Figure 3a).^{47,67,72} At these low frequencies the unaligned, ordered material usually has $G'(\omega) \propto \omega^{0.5 \pm 0.1}$ and the disordered material is in its terminal region where $G'(\omega) \propto \omega^2$. The uncertainty in determining ω'_c is small, since it can be determined by the intercept of lines with very different slopes in a log-log plot of G' vs ω .^{47,67} This method can also be applied by comparing ordered but partially aligned states to the disordered state; similar values of ω'_c are obtained⁴⁷, but the uncertainty is somewhat larger, since alignment shifts the dynamic moduli of the ordered material toward those of the disordered phase. The method applies to diblocks of both PEP-PEE^{46,67} and PS-PI^{47,49,51,63} types, ABA triblocks,^{44,76} and even two-nanophase-separated ABC triblocks.⁸² There are some limitations related to this

method: it requires an accessible ODT for the BCP and is feasible only for a limited range of molecular size. As molecular weight increases, extrapolation is needed for some systems (Figure 3b).^{49,63} Since the order-disorder transition temperature T_{ODT} increases dramatically with the block copolymer length, chain relaxations become so fast in the disordered state that they can move out of the experimentally accessible frequency range.

To overcome these limitations, Kannan et al.⁴⁶ determined $\omega'_{c,so}$ (very close to ω'_c) using a rheo-optical method. For a block copolymer in which the intrinsic contribution dominates the birefringence, the stress-optical rule holds above a particular frequency $\omega'_{c,so}$. Above this frequency distortion of chain conformation dominates both the stress and birefringence. Thus, ω'_c was identified without heating the sample over T_{ODT} . However, this method is valid only for polymers that have much greater intrinsic birefringence than form birefringence, such as PEP-PEE. Further, the measurements should be made in the ordered but unaligned state, since shear-induced alignment shifts $\omega'_{c,so}$ to lower frequencies. Reliable preparation of this ordered but unaligned state requires an accessible ODT.

As to the other important frequency ω_d , Koppi et al.³⁹ evaluated it for PEP-PEE, using an unaligned sample and a perpendicularly aligned sample, by measuring the storage modulus in the shear plane (G'_{yz}). A small “bump” in the frequency dependence of G'_{yz} of the perpendicularly aligned sample was attributed to defect motions. Kannan et al. noticed that the value of $\omega''_{c,so}$ was very close to ω_d evaluated by Koppi et al.; thus, it may be possible to estimate ω_d by rheo-optical methods as well. Although these approaches provide a rough estimate of ω_d , determination of a meaningful value of ω_d requires that it be measured for a well-defined state. It is believed that ω_d is controlled by grain boundaries and defects,^{39,46,69} and is not an intrinsic property; its value would depend on the domain size,^{46,69} since increasing the domain size could reduce this cut-off frequency.⁶⁹ Thus, it is important that the condition for characterizing the domain structure be highly reproducible. This is readily achieved when all previous flow and thermal history has been erased, i.e. using an unaligned sample obtained by ordering in the absence of aligning field. Alternatively, one might consider a final, well-aligned structure as a potential reference state. However, in

terms of physical meaning, a measure of domain or defect dynamics only makes sense for polydomain samples. A truly “well-aligned” material (see next section), while reproducible, would not provide a meaningful value of ω_d .

Progress is needed to overcome the limitations of the existing methods to determine ω'_c and ω_d . Zhang et al.^{48,55,56} have suggested alternative methods to estimate ω_c and ω_d using the loss tangent ($\tan\delta = G''/G'$) and dynamic viscosity ($\eta' = G''/\omega$). They estimate ω_c and ω_d as the upper and lower points in the $\tan\delta$ vs. $\log\omega$ curve between which $\tan\delta$ has a loss peak (Figure 3c), or as the upper and lower limits in the log-log plot of η' vs. ω beyond which η' has a stronger dependence on frequency (Figure 3d). These methods seem not to work for polymers that are not entangled, such as a lamellar PS-PI with an accessible ODT. For example, consider the application of these methods to a PS-PI block copolymer that has a molecular weight close to those used in most of the literature (Figure 3bcd).^{2,41–44,47–51,54,56–58,63} This BCP lacks an entanglement plateau, and it is impossible to locate ω_c using the loss tangent, especially for the ordered but unaligned state, since it is almost a flat line rather than a curve (Figure 3c). Using $\eta'(\omega)$, it is equally difficult to determine ω_c (Figure 3d). For the two aligned states (parallel and perpendicular), the values of ω_c estimated using these suggested methods vary with the alignment direction (Figure 3d, $\omega_{c,parallel} > \omega_{c,perpendicular}$). A rough estimate of ω_d is made for a parallel aligned sample since it shows a hint of a loss peak; however there is inherently a large uncertainty since there are no criteria for selecting a particular frequency on the low frequency side of the loss peak (Figure 3c) and the inflection in η' is very slight. The values of ω'_c extracted from these two methods (Figure 3cd) are inconsistent with each other, and differ significantly from the value obtained with the well-defined method described above (Figure 3b). As mentioned before, ω_c is an intrinsic parameter, and does not depend on the state of samples. Indeed, almost the same value of ω'_c is obtained for unaligned, parallel aligned, and perpendicular aligned samples when using the storage modulus method.⁴⁷ Thus, the proposed methods to determine ω_c based on the loss tangent and dynamic viscosity are not as precise or robust as the storage modulus method.

Flow-induced alignment trajectories below and above ω'_c are well-defined (boundary between Regimes I and II in Figure 1, since ω'_c can be determined by the storage modulus method; however, it is very difficult to locate regimes based on ω_d (boundary between Regimes I and IV). Parallel alignment has been observed for PEP-PEE type diblocks at $\omega < 0.03 \cdot \omega'_c$ (presumed to be $\omega < \omega_d$), while perpendicular alignment can still be induced at very low frequency for PS-PI diblocks (as low as $0.0001 \cdot \omega'_c$).^{47,49,51} Perhaps this is due to a difference between the values of ω_d/ω'_c for the two systems, since their textures and domain sizes might not be the same. Parallel alignment has been reported in a lamellar PS-PI in the frequency range $0.01 \cdot \omega_c < \omega < 0.1 \cdot \omega_c$, if the samples were pressed and annealed prior to shearing.⁵⁶ However, parallel alignment can be induced by pressing and annealing even without subsequent shearing.^{52,61,64,73}

In summary, the determination of ω'_c is straightforward for samples with accessible ODT. Further improvements are needed for methods to determine ω'_c when the ODT is not accessible and to determine ω_d in general.

B. Characterization of the Time Evolution of Microstructure

A variety of experimental methods are used for characterizing the evolution of structure during flow alignment. The advantages and limitations of each method are discussed here in terms of suitability for in-situ studies, richness of the information that can be extracted, and possible artifacts. Electron microscopy, X-ray and neutron scattering, and rheo-optics will be the methods of interest. Finally, we comment on a combined approach that takes advantage of the usefulness of individual methods while minimizing their limitations.

Electron microscopy is uniquely suited to imaging the type and density of defects that define the domain structure in a block copolymer.^{26,41,42,45,53,54,63,73-75} The length scale of interest ranges from tens of nanometers, for the initial condition in an unaligned material obtained by moving through the ODT with no aligning field,^{41,63} up to micron scale as defects are almost completely eliminated from the material.^{54,63} By carefully following the sample

orientation during microsectioning and imaging, the orientations of the lamellae relative to the flow geometry can be obtained as well.^{41,42,63} Three limitations of TEM are: 1) the structure of the material may be altered by sectioning, staining, and imaging with high energy electron beams, 2) only a small area in the sample can be viewed at a time, so it is difficult to get a statistical view of the degree of alignment, and 3) it is not attractive for kinetic studies since electron microscopy is not an in-situ method. The first two limitations may be alleviated by using field emission gun scanning electron microscopy (FG-SEM).⁵³ In spite of its limitations, no other techniques could replace electron microscopy, since this is the only method that records the local structure in the material.

X-ray and neutron scattering applied along all three axes of the flow geometry^{2,40,55,63} provide detailed information on the dimensions of the nanostructure and the shape of its orientation distribution. The progression of structure at intermediate states of flow-induced alignment in PS-PI-type systems are captured by cooling through the BPC's upper glass transition temperature, then removing the sample for characterization.^{2,26,40-42,44,45,53-55,63,73-75} While the results provide a sampling of complex microstructural changes induced by shearing, they have some significant limitations. Like TEM, three-axis SAXS/SANS can not be performed in situ, so both methods have poor time resolution and suffer from uncertainties in the relaxation of structure after cessation of shearing, and any distortion of structure during unloading and subsequent sample preparation. Further, in most studies that have used ex-situ characterization methods, little information was available to guide the selection of sampling conditions.^{26,55} Typically the rheological signature of alignment was the only in-situ measurement; unfortunately, the rheological properties often vary weakly and even non-monotonically with substantial changes in alignment.⁴⁹ Thus, it has been difficult to interpret prior results in the context of an overall alignment trajectory, or to view the structural development along a particular path to alignment in the context of distinct families of alignment trajectories.

The challenges associated with ex-situ studies have motivated the development of in-situ methods that use SAXS,^{40,45} SANS,^{61,62} or polarimetry^{2,46,49-51,63} to monitor flow-induced

alignment. In-situ scattering methods are most frequently applied along a single axis;⁷⁶ using a Couette geometry it is possible to monitor scattering in both the $(\nabla\mathbf{v}, \nabla\times\mathbf{v})$ - and $(\mathbf{v}, \nabla\times\mathbf{v})$ -planes.^{62,60} The time resolution of both SAXS and SANS continues to improve, and scattering patterns acquired tens to hundreds of seconds apart have been reported.^{62,76} Flow-induced alignment can occur on a timescale of seconds, which requires in-situ probes that have much greater speed. In addition, limited access to synchrotron and neutron beam time motivates in-situ measurements that can be made using more readily available instrumentation.

Since there are many factors that affect alignment kinetics, large numbers of experiments are needed to map transient behavior as a function of multiple parameters. Therefore, kinetic studies require an efficient method to obtain quantitative measurement of progressive alignment, in-situ with high time resolution. Rheological characterization can provide the desired time resolution and can be measured in real time, but it is not sensitive to the structural changes.^{26,41,49,51,52,63,73} For example, the effective dynamic moduli can be measured simultaneously during shearing; but it is not yet possible to relate them with orientational order, since a given value can correspond to many microstructural states.⁴⁹ Conversely, a given alignment trajectory does not always have the same rheological signature. For example, it has been suggested that subtle changes in the loss tangent ($\tan \delta$ ranging from 0.85 to 1.2) can be used to track progress along the Regime III alignment trajectory.⁵⁵ However, the small dip and subsequent increase observed in that sample is not observed in other very similar PS-PIs along the Regime III trajectory (See chapter 2).

Introduction of in-situ rheo-optical measurements during flow provided the desired time resolution (as fast as 10 ms) to probe the microstructural evolution during shear. Birefringence, which is sensitive to the degree of alignment and is correlated to the orientational order of BCP morphologies that have anisotropic optical properties (e.g. lamellae and cylinders), represents a reasonable choice for real-time kinetic studies. The interpretation of the transient birefringence for systems in which the microphases have significantly different refractive indices (form birefringence \gg intrinsic

birefringence)^{49-51,63,77,78} and systems with microphases having nearly equal refractive indices (intrinsic birefringence \gg form birefringence)^{46,78} has been described. For systems that have sufficiently low birefringence, measurements can readily be made along two or potentially all three axes of the flow geometry (Figure 4). When the birefringence is large, the optical path must be kept small to avoid the retardation going over more than a few orders. In this case complete characterization of the refractive index tensor could be performed using multiple beams at oblique angles with respect to $\nabla\mathbf{v}$.^{79,80} While flow birefringence has the advantage of speed and the ease of sending a laser beam through multiple axes of a flow cell, compared to SAXS and SANS it has much lower information content. Instead of revealing the shape of the orientation distribution, birefringence is only sensitive to the second moment of this distribution. Information on possible flow-induced distortion of the nanostructure that is revealed in the wave-vector dependence of SAXS and SANS can not be obtained from birefringence measurements. Further, interpretation of the birefringence results requires attention to the possible depolarization of light due to the polydomain structure in unaligned⁸¹ and partially aligned⁷⁹ materials. Awareness of the relative magnitudes of the form and intrinsic contributions to the birefringence is required when interpreting flow birefringence when the deformation rate is high enough to perturb chain conformation.⁴⁶ Like scattering measurements, a birefringence measurement made along only one axis is insufficient to characterize orientation.^{2,49-51,63} Thus, when dealing with new materials, one needs to confirm the interpretation of the optical data using structural characterization by scattering and/or microscopy.^{2,51,63}

To achieve high time resolution and complete information on both the orientation distribution and domain structure that correspond to a given point along the path to alignment, it is natural to combine the individual methods that have these strengths. In this spirit, recent studies have used in-situ flow birefringence for its speed, ex-situ SAXS along velocity, velocity gradient, and vorticity axes for its ability to reveal the shape of the orientation distribution, and ex-situ TEM along all three directions (\mathbf{v} , $\nabla\mathbf{v}$, and $\nabla \times \mathbf{v}$) to view the texture. This new approach has provided insight into the microstructural character

of the “fast” and “slow” processes along the three types of alignment trajectories in Regimes I, II, and III.^{2,63} The success of this experimental approach motivates future studies that combine an in-situ probe (flow-birefringence, SAXS or SANS), with ex-situ scattering along three axes (SAXS or SANS) and electron microscopy along three axes (TEM or FE-SEM).

C. Characterization of Well-Aligned States

Developing reliable methods to characterize well-aligned nanostructures is crucial, since the degree of order and density of defects can strongly affect the performance of well-aligned functional materials. TEM and other microscopic techniques provide the ultimate methods for observing the microstructures in a block copolymer.^{26,41,42,44,45,53,54,73–75} The lamellar dimensions and their directional distributions can be measured by the intensity distributions in the $(\nabla\mathbf{v}, \mathbf{v})$, $(\nabla\mathbf{v}, \nabla\times\mathbf{v})$, and $(\mathbf{v}, \nabla\times\mathbf{v})$ -planes using small-angle x-ray or neutron scattering experiments.^{2,26,39–42,45,48,63} Observations of birefringence in the $(\nabla\mathbf{v}, \mathbf{v})$, $(\nabla\mathbf{v}, \nabla\times\mathbf{v})$, and $(\mathbf{v}, \nabla\times\mathbf{v})$ planes can also provide a quantitative measure of the degree and direction of alignment.⁷⁷ Rheometry is the least sensitive method for determining whether a single-crystal-like state has been reached; however, rheometry can give a rough idea of the alignment direction in some systems (Figure 5), if the correspondence between mechanical properties and microstructure has been previously established by scattering or microscopy. Therefore, electron microscopy is the only method capable of determining whether the alignment is “perfect” (i.e. not only aligned, but also nearly defect-free). Complementary methods, such as SAXS, SANS and birefringence are able to quantify progress toward an aligned state and to detect when the BCP is *not* well-aligned.

Here we use the term “well-aligned” only in reference to samples that have sharp peaks in their scattering patterns and uniform layers in TEM (Figure 11 point F).⁶³ Unfortunately the terms “aligned” state and “pure” state have been used in the literature in reference to transient states that are, in many cases, far from a well-aligned state.^{41,42,44,45,47,48,52,53,55–58} For example, the “pure transverse state”⁵⁵ reported previously, when viewed in context,

seems to be a weakly anisotropic transient state at the early stage of the parallel alignment trajectory at very high frequencies (between points I and A on a Regime III trajectory, Figure 6c).⁶³ Indeed, there are many structures with strong unimodal scattering that are transient states along the way to a well-aligned structure as indicated by in-situ birefringence and SAXS (e.g., points C of Figure 6).^{2,63} Verified by TEM micrographs, we have shown that a strongly perpendicular state corresponds to a saturated high value of 1,3-birefringence (Figure 4) close to a theoretical one for a monodomain state (indicated by the value marked F on the right hand side of the graph in Figure 6a).⁵⁰ Using SAXS and TEM we have also shown that a well-aligned parallel state is achieved when the 1,3-birefringence returns to zero.^{2,50,63} The birefringence has proven to be a much more sensitive indicator of a final well-aligned state than are the rheological properties.

3. Trajectories, Kinetics, and Structural Evolution

A. Trajectories of Alignment

Three-dimensional mapping (Figure 1) provides a basis for viewing the alignment behavior in terms of three parameters: temperature, frequency, and strain amplitude. Qualitative aspects of the pathway leading to each alignment can also be represented on such a plot (e.g. the change in character of the trajectory to the parallel state between regions II and III). However, this representation can not capture the rich information on how alignment occurs that is manifested in the additional dimension of time. The evolution of structure during shearing provides direct information on the mechanisms of alignment, which gives insight into the origin of the frequency and temperature regimes associated with distinct orientation tendencies.

The pathways to distinct aligned states consist of a cascade of processes. At fixed frequency, temperature and strain amplitude, the character of the processes changes significantly with time. Qualitatively, this change in alignment dynamics as alignment

proceeds can be rationalized as a consequence of the coarsening of the domain structure and the change in orientation distribution of the lamellae. Within a given frequency regime, flow alignment follows a characteristic path; we refer to this as a “family of trajectories” along the time dimension. Three different families of trajectories have been identified:⁶⁶ one family of trajectories of perpendicular alignment in Regime I, and two different families of trajectories towards parallel alignment in regimes II and III.^{2,49,50,63}

Comprehensive studies have been made to identify flow alignment trajectories in different frequency regimes by rheo-optical methods.^{49–51} Typically, within Regime I, the 1,3-birefringence increases steadily and finally reaches a saturated positive value during shearing (Figure 6a). There are two different signatures of parallel alignment: one with transient positive 1,3-birefringence (Regime II, Figure 6b), another with transient negative 1,3-birefringence (Regime III, Figure 6c). These distinct optical signatures indicate different transient microstructures for these three alignment trajectories. In the boundary between Regimes I and II (at $\omega \simeq \omega'_c$), the direction of alignment depends on strain amplitude: below a particular strain amplitude γ_c , perpendicular alignment is induced along a trajectory similar to that shown in Figure 6a; above γ_c , the final orientation is parallel through a trajectory similar to that shown in Figure 6b; at γ_c , a novel trajectory has been identified recently.⁸² During the alignment process at this specific condition ($\omega = \omega_c$ and $\gamma_o = \gamma_c$), the 1,3-birefringence increases rapidly to a transient peak value and drops gradually, in a manner similar to that seen for the “fast process” and first portion of the “slow process” of trajectory II (from point I to point M in Figure 7). Then the 1,3-birefringence increases steadily to a saturated value (much greater than the transient peak value) in a manner similar to trajectory I, and leading to perpendicular alignment (from point M to F in Figure 7).

A positive 1,3-birefringence en route to parallel alignment could be interpreted as indicating the existence of transient parallel and perpendicular orientations;⁴⁹ ex-situ SAXS confirms this interpretation and shows that the orientation distribution contains all orientations between parallel and perpendicular, but not transverse.⁶³ A transient negative 1,3-birefringence indicates that more transverse layers exist than perpendicular ones.⁴⁹ This

negative birefringence has been shown to correspond to the coexistence of transverse layers and parallel layers as transient states on the way towards parallel alignment, manifested in four-spot patterns revealed by ex-situ SAXS^{2,55,63} (Figure 6c). In fact, the evolution of the four-spot pattern with shearing time and strain amplitude⁵⁵ corresponds nicely to the birefringence's dependence on these parameters⁵⁰ (Figure 8). Since it is not straightforward to rescale the time or strain amplitude to account for the differences between the two BCPs studied by Gupta et al.^{49,50} and Zhang et al.,⁵⁵ exact matching of the two sets of results is difficult. The correspondence indicated in Figure 8 is a qualitative one; in contrast, a direct correspondence is established by an integrated approach that combines rheo-optical measurements with ex-situ structural characterization (Figure 6abc).^{2,63}

The remainder of this section describes the kinetics and microstructure evolution of each of the three families of trajectories in Regimes I, II and III. These facts lay the groundwork for an up-to-date examination of current concepts regarding alignment mechanisms in Section 4.

B. Kinetics of Alignment

The kinetics of alignment are of practical importance, since they provide the basis for estimating the processing time needed to harvest a well-aligned state, or a particular transient state, such as a bimodal parallel-transverse structure. The kinetics are also of fundamental importance, since they give clues regarding the mechanisms of alignment. Many factors, including shearing conditions (temperature, shear frequency, and strain amplitude), and material properties (e.g. order-disorder transition temperature T_{ODT} , glass transition temperatures of each microphase, degree of entanglement, and characteristic frequency ω'_c) affect the alignment kinetics. Some of the most important thermodynamic and dynamic conditions can be parameterized using dimensionless groups, such as the strength of segregation ($\sim T/T_{ODT}$), the chain mobility ($(T/T_g)_A$, $(T/T_g)_B$, $(M/M_e)_A$, $(M/M_e)_B$), and the viscoelastic contrast between the layers ($T_{g,A}/T_{g,B}$). Shearing frequencies can be

made dimensionless using a relevant characteristic relaxation timescale of the chains, or nanostructure, or domains. The choice of ω/ω'_c as a dimensionless frequency appears to be particularly significant since $\omega/\omega'_c \approx 1$ coincides with the boundary between Regimes I and II.

Shear conditions other than frequency (such as strain amplitude^{51,58}) affect the alignment trajectory; the region in (ω, T, γ_o) , space associated with a given type of trajectory is referred to as an “alignment regime”. Within a particular alignment regime, changes in alignment conditions such as ω , T , and γ_o do not alter the direction of alignment. But these parameters affect the rate and sometimes ultimate degree of alignment.⁵⁰ Usually the rate of alignment increases with frequency, temperature, and especially strain amplitude.^{50,63,82}

Rheo-optical methods have been successfully used to characterize the kinetics of alignment of PEP-PEE⁴⁶ and PS-PI (Figure 9).^{49,51,63} For PS-PI within Regime I, in the early stage of alignment (point I to B in Figure 6a), 1,3-birefringence increases more rapidly than in the later stage of alignment (point B to F in Figure 6a). This could indicate that, during the course of shearing, there is a transition in the character of alignment, as though one process overtakes another in importance. To test this idea, the experiment is repeated with different strain amplitudes. Higher strain amplitude results in much faster overall alignment. In the initial “fast process” from point I to B in Figure 6a, the kinetics speed up more strongly with strain than those of the later “slow process” from point B to F. The effect of strain on the timescale of the development of alignment is highly nonlinear: the time scale decreases as γ_o^{-3} at the initial “fast process” (Figure 9b).^{49,63} It is difficult to scale the late stage of alignment though, since the effects of strain amplitude are much weaker in the subsequent “slow process”.

Within Regime II, the 1,3-birefringence increases very quickly early in the alignment process (point I to B in Figure 6b) and then decreases slowly (point B to F in Figure 6b). As expected, the overall alignment process speeds up with increasing strain amplitudes. The strain effect is stronger during the early stage of the process (“fast process”): the time needed to reach the transient peak value of Δn_{13} decreases as γ_o^{-5} (Figure 10a).

During the subsequent “slow process”, the transient decay of 1,3-birefringence from the peak superimposes if time is rescaled by γ_o^{-3} (Figure 10b).⁵¹ These changes in scaling signal a difference in mechanisms of alignment between the initial fast process and the later slow process. Within Regime III, a change in character of the alignment mechanism is again indicated by the different strain dependence of the initial fast process and subsequent slow process.^{50,63} Unfortunately, it is impossible to tell what these different mechanisms are from birefringence measurements alone. Information on structure evolution during the “fast process” and “slow process” in each alignment regime (I, II, and III) can uncover the nature of each process, as described in the next section.

C. Structural Evolution

Detailed information on structural evolution is a prerequisite to understanding the mechanisms of the alignment processes regarding 1) the distinct families of trajectories and 2) the nature of initial “fast processes” and subsequent “slow processes”. Here we briefly discuss previous work regarding the microstructure and defects in the initial unaligned and final well-aligned states. Structure development during the alignment process is discussed in the context of the strengths and limitations of various experimental methods. Then structural evolution is described along three families of trajectories (I, II, and III).

Microstructures of BCPs in the initial unaligned state are very different from those in the final well-aligned state. Prior to applying shear flow, quenched⁶³ or solvent casted⁴¹ samples appear to have a poorly organized, polydomain structure. Almost 70% of the material can exhibit a “pebbly” texture in which the density of defects is so high that the lamellar morphology is obscured.^{41,2} The remaining material appears lamellar, but with a high concentration of various defects, including partially formed focal-conics.^{41,63} SAXS patterns from such materials show uniform rings in three orthogonal directions, and there are no preferential lamellar orientations. In a well-aligned sample, lamellae are well defined and highly oriented. Few types of defects exist and the defect density is much lower than in

the unaligned state.^{41,54,63}

Regarding the structure evolution during shear processing from the initial unaligned state to the final well-aligned state, Zhang and Wiesner⁵⁵ have reported a particularly interesting progression of X-ray scattering patterns with shearing time. The results revealed the transient appearance and disappearance of a bimodal orientation distribution with coexisting parallel and transverse orientations, suggesting a dynamic context for interpreting four-spot patterns observed by Hashimoto et al.⁴⁵ (in-situ), and Winey et al. (ex-situ).⁵² It also suggested the shape of the orientation distribution that might correspond to transient 1,3-birefringence results that indicated the appearance and disappearance of a strong transverse component en route to parallel alignment in Regime III (Figure 8).⁴⁹ However, it was not possible to connect the structural changes evident in the SAXS results with the rapid initial process and slow late-stage process that had been identified in Regime III.^{49,50} Further, it was difficult to recognize that these SAXS results pertained to one type of trajectory to parallel alignment (Regime III), but not to others (regime II and IV). It was also difficult to recognize the similarity between behaviors of entangled, strongly segregated^{45,52,54,55} and non-entangled, weakly segregated^{49,63} systems. This is partly a consequence of the difficulty of performing a comprehensive ex-situ survey of the transient structure for many flow conditions in the three-dimensional space (T, ω, γ_0) for multiple samples. Without this broader perspective to guide the interpretation, it was possible to overly confine the relevance of the results in terms of materials (i.e., restricted to entangled, strongly segregated materials) and to over-generalize their relevance in terms of flow conditions (i.e., generalizing to all paths to parallel alignment). Such misunderstandings are hard to avoid unless ex-situ studies are linked to comprehensive in-situ results that guide the selection of sampling conditions.

Comprehensive rheo-optical measurements can provide an overall perspective on the range of alignment behaviors that occur as a function of the processing conditions. This perspective can allow one to select one particular set of conditions (ω, T) that is representative of a whole alignment regime. Extensive rheo-optical results on the effect

of strain amplitude can guide the selection of a particular value of γ_0 to use to prepare samples for ex-situ electron microscopy and scattering measurements: the choice of γ_0 should be large enough to give a trajectory that leads to a well-aligned state, but small enough that the kinetics are sufficiently slow that they can be interrupted at desired stages of the alignment process, even in the initial fast process. Finally, rheo-optical measurements guide the selection of the points in time when samples should be taken for ex-situ characterization: they can record the point along the trajectory at which the sample was taken, as well as monitoring the relaxation of structure upon cessation of shearing and during subsequent cooling (or heating) to ambient conditions. Thus, while an optical observable like birefringence may not itself provide detailed structural information, it can be a powerful tool to guide ex-situ structural characterization.

A comprehensive approach that combines real-time birefringence measurements and ex-situ SAXS and TEM revealed the structural evolution during flow-induced alignment of a model diblock copolymer (PS-PI) in different alignment regimes (I,II,III).^{2,63} In the initial unaligned state, the sample consists predominantly (roughly 70%) of poorly organized regions rather than well-defined layers. Layered domains exist with a variety of defect structures, including partially formed focal conics (Fig. 11). Scattering results show that the initial structure is essentially isotropic (I in Fig. 6abc). During oscillatory shearing, the initial fast process in Regime III ($\omega'_c \ll \omega$) is seen in TEM to be responsible for the formation of well-defined layers from poorly organized material, but the population of layers that is created is not isotropic, as shown by SAXS (Figure 6c). A bimodal distribution is produced by the “fast process” in the very high frequency regime (Fig. 6c). In the transition to the slow process, the 1,3-birefringence indicates that the transverse population is at its maximum, representing the strongest bimodal character (parallel-transverse) that the system ever passes through on its way to parallel alignment. These transverse domains coexist with poorly organized regions and with approximately parallel regions containing ‘chevron’ bands (B in Fig. 11), reminiscent of the images of transverse islands in a matrix of parallel material reported by Hudson for a lamellar diblock.⁵⁴ The coarsening of the chevron

pattern dominates the slow process, during which the transverse domains are also eliminated. Finally, a well-aligned state is achieved, as shown by sharp scattering patterns (F in Fig. 6c) and uniformly aligned lamellae (F in Fig. 11).

The same level of detailed information on structural evolution during flow-induced alignment has also been achieved for the families of trajectories in Regimes I and II.^{2,63} These two types of trajectories begin in a way that is similar to each other in some respects, increasing the parallel and perpendicular projections and all orientations in between (Figure 6ab from I to A to B). However, in the later stages the two trajectories are qualitatively different. The slow process in Regime I continues to increase the perpendicular projection, but progressively eliminates the other orientations (Figure 6a from B to C to F). In Regime II, the later “slow process” reduces the perpendicular component of the orientation distribution as the parallel component becomes more and more dominant (Figure 6b from B to C to F).

By spanning the range of length and time scales involved, cascades of structural changes were visualized: formation of layers from poorly organized regions; the creation, growth, coarsening, and deformation of domains; the generation and elimination of defects, and the perfection of a well-aligned ‘single-crystal-like’ state. The body of results combining 1,3-birefringence, SAXS, and TEM allows disparate observations^{45,49–52,54,55} to be viewed in a unified way.^{2,63} Such a clear picture of the evolution of flow-induced alignment processes is impossible to obtain from the transient rheo-optical results^{49,51} or from structural studies that do not have a context for relating the sample points to their corresponding positions along a given alignment trajectory.^{45,52,54,55} Without TEM, SAXS alone is not able to uncover the existence of poorly organized regions, their transformation into layers, the types of defects that emerge and how the defect texture coarsens. On the other hand, without SAXS, TEM alone is not well suited to give a statistical distribution of layer orientations.

4. Alignment Mechanisms

Towards the goal of predicting the direction, rate, and degree of flow-induced alignment, many mechanisms have been put forward over the past two decades.^{25,26,33–36,39–55,73} Some concepts were proposed in an attempt to understand the selection of alignment directions, such as the orientation that has the “minimum moduli”;⁴⁷ some were dedicated to understanding the formation of aligned layers from isotropically distributed grains, such as “domain dissolution” (“melting”), “grain rotation”^{26,39,41,73} and “irreversible rocking”;⁴⁶ others were expected to explain both the direction and mechanism of alignment, such as “selective melting”³⁹ and “selective creation”^{2,63} of layers. Some authors explained particular alignment behaviors in terms of the material’s characteristics, such as “entanglement”,⁵⁵ “weak segregation”,³⁹ “strong segregation”,⁵⁵ or “viscoelastic contrast”.⁴⁷ A few proposed mechanisms have been confirmed by experimental observations such as “defect migration”, “selective creation”, and “selective elimination”; but many of them have not yet been validated. Arguments regarding the selection of alignment direction have been based primarily on the relative stability of different monodomains. Only a few ideas have come from information provided by in-situ measurements of dynamic responses of the material during flow-induced alignment.^{46,49–51,61,62,71}

In this section we use recent results from SAXS, SANS, rheological, rheo-optical and TEM studies to test the ideas that have been presented to explain the selection of alignment direction and the mechanisms of alignment in each regime. Most of the discussion deals with trajectories that begin with a well-defined, isotropic initial condition, prepared by disordering the material to erase all prior flow and thermal history and then taking it through the ODT to the desired temperature for processing. We begin with the lowest frequency regime (IV) and move to progressively higher frequencies (I, II and III). We conclude with brief comments on interesting effects associated with other initial conditions and what they may imply about alignment mechanisms.

In alignment Regime IV ($\omega < \omega_d$) parallel alignment is observed in PEP-PEE-type

BCPs.^{39,46} To explain the formation of parallel alignment at low shear frequency, the concept of defect motion (migration) was invoked. The fact that very low frequency shearing was required to induce parallel alignment suggested that it occurred by very slow relaxation processes, such as breaking and reforming the lamellae through the movement of dislocations or disclinations. Since the information from ex-situ SANS of the final state was not enough to support or negate these concepts, an in-situ rheo-optical study was carried out on the same system (PEP-PEE) under the same alignment conditions.⁴⁶ The transient stress-optic ratio and 1,2-birefringence during the parallel alignment process indicated that irreversible “rocking” of grains led progressively to parallel alignment. This result is in accord with the hypothesis that domain-scale responses lead to parallel alignment at low frequency. In this regime, the shear frequency is so low that the polymer chains and lamellae are fully relaxed; thus, shearing only deforms the domains and disturbs the defects between them.

As shear frequency increases, oscillatory shear may couple with the dynamics of the nanostructure (lamellae). In Regime I ($\omega_d < \omega < \omega'_c$) perpendicular alignment can be induced (in both PEP-PEE-type and PS-PI-type BCPs). In PEP-PEE this represents a flipping around ω_d . To explain this phenomena, it was suggested that fluctuations play a role in selective melting,³⁹ making the perpendicular orientation the least susceptible to shear-induced disorder. This concept provided a hypothesis regarding the the selection of one direction over another as a function of frequency and temperature: Perpendicular alignment would be selected at frequencies that couple to lamellar dynamics and at temperatures close to T_{ODT} .^{39,55}

The evidence that selective melting causes perpendicular alignment is indirect. The detailed structural evolution observed during the perpendicular alignment process^{2,63} provides an opportunity to re-evaluate this concept. If selective melting were playing an important role, it could be expected to dominate during the early stage of the alignment process when the amount of unfavorably oriented material is the greatest. One would expect an initial rapid growth of the perpendicular component, while other orientations would be depleted (or left unchanged). Instead, SAXS results show that the initial process does

not select perpendicular alignment over parallel—it enhances both of these, as well as all orientations between the two (Fig. 6). Further, electron micrographs show that the initial enrichment of this range of orientations occurs by a process that converts poorly organized regions into well-defined lamellae, suggesting a mildly “selective creation” of layers with a range of orientations instead of a strongly “selective melting” leading to a specific one. The selection of the perpendicular orientation occurs during the subsequent slow process as “selective elimination” occurs.^{2,63} It is unlikely that shear induced melting plays a role in the late stage of processes, since the most unstable orientations have been eliminated and the material has become relatively homogeneous, so that localized melting is decreasingly possible (and the energy involved in shearing is too low to cause bulk melting).

While the exact mechanisms are still not clear, the formation of well-defined layers during the fast process may involve defect dynamics such as the elimination of partially formed focal conic defects and, possibly, the rotation of the local phase-segregated structure within the poorly organized regions. The selectivity that is observed during the initial process in Regime I may be a consequence of the symmetry of oscillatory shear combined with the time scale of the deformation is longer than the single chain relaxation time. Shearing frequencies in Regime I are low enough to allow relaxations on the scale of the whole chain or even the nanostructure. These relaxations can produce out-of-plane reorganizations of structure that avoid higher energy distortions in the plane (such as the creation of transverse layers). By symmetry the only orientations that can be progressively reinforced by oscillatory shearing are those that are affected the same way by forward and reverse cycles, i.e., those with fore-aft symmetry. All of the other orientations that have fore-aft symmetry are enhanced. From the orientation distribution created by the initial fast process, the slow process winnows out all but the perpendicular alignment by “selective elimination”. This process takes place after layers and domains are clearly defined in the TEM images; thus, the selectivity of the slow process may involve dynamics at the scale of whole grains.

Moving up in frequency to the boundary between Regimes I and II, in the vicinity of ω'_c , the selection of alignment in PS-PI-type lamellae can be “flipped” from perpendicular to

parallel at fixed conditions of frequency and temperature simply by increasing the strain amplitude.⁵¹ Based on the concept that shear distorts fluctuations and causes selective melting, followed by ordering into perpendicular layers, higher strain amplitude should lead to stronger and more rapid perpendicular alignment, due to greater distortion of the fluctuations. Instead, increasing γ_o leads to parallel alignment. This suggests that the mechanisms for perpendicular and parallel alignment coexist, and that the strength of the parallel mechanism increases more rapidly with strain amplitude than that of the perpendicular mechanism. As the underlying processes that lead to each alignment become better defined, models of their kinetics may capture this difference in their strain-dependence. In turn, understanding the interplay of strain, frequency and temperature may explain the shape of the boundary surface in (ω, T, γ_o) -space that separates distinct alignment regimes.

As one moves fully from Regime I into Regime II by increasing frequency through ω'_c , the alignment tendency shifts to parallel for PS-PI-type lamellae,^{42,47–50,63,82} while no alignment has been reported in PEP-PEE-type polymers for $\omega > \omega'_c$. The most striking differences between the two systems are 1) that PS-PI-type materials have very different local friction in the distinct lamellae, while there is little “viscoelastic contrast” in PEP-PEE-type systems; and 2) the PS-PI-type polymers that are typically studied are not well entangled, while the PEP-PEE-type polymers are highly entangled. Based on the first difference, it has been suggested that the mechanism for parallel alignment at $\omega > \omega'_c$ may require “viscoelastic contrast”.⁴⁷ If so, this hypothesis may also explain the reason the alignment tendency changes at ω'_c . At lower frequencies the response is controlled by the layers as a whole; it is insensitive to more local dynamics since the chains are relaxed. Above ω'_c , chain conformation is distorted and more local relaxation dynamics play a role; thus, non-uniform monomeric friction could be involved, flipping the alignment direction to parallel. Alternative explanations of the flip in orientation at ω'_c include the hypothesis that the system adopts the orientation that minimizes the dynamic moduli at the frequency of the applied shear⁴⁷ and the concept that parallel alignment is favored at frequencies where the elastic character of the material dominates (relatively small $\tan \delta$).^{48,55,56} While these

ideas were inspired by the behavior of some specific PS-PI materials, they fail for other very similar PS-PI lamellae, as illustrated in Figures 12 and 3c, respectively.

The mechanisms that have been suggested to explain parallel alignment have not distinguished Regimes II and III, since most of them were put forward before the qualitatively different pathways to parallel orientation above ω'_c were identified. We discuss the ideas that presume the transverse orientation is eliminated most rapidly in the context of Regime II, in which this assumption holds. Later we will discuss concepts that relate to the mechanism of alignment through transient states rich in the transverse orientation.

As a possible mechanism for forming parallel layers, it has been suggested that unfavorably oriented domains might be destroyed, then formed into parallel oriented lamellae^{25,26,41,55}. A closely related idea is that small regions might be destroyed at any one time and converted progressively into parallel layers (partial dissolution of microdomains).^{26,41} The shearing energy applied to the initial unaligned state has been estimated to be sufficient to destroy small microdomains.⁴¹ Unfortunately, no method has been available to detect such destruction/reformation or domain dissolution (although recent fluorescence techniques⁹⁵ would open the way to in-situ rheo-optical probes of flow-induced disorder). Recent electron microscopy images of the evolution of microstructure with shearing in Regime II do show that poorly organized regions are progressively eliminated and well ordered layers increase, especially during the initial fast process.⁶³ This appearance is evocative of the destruction/reformation concept. However, the fast process does not lead to the selection of parallel alignment in particular; instead it enriches the whole range of orientations that are tangent to the flow direction (parallel, perpendicular and all orientations in between). The subsequent slow process in Regime II eliminates the perpendicular and intermediate orientations created during the initial fast process, but its mechanisms are not yet clear. A characteristic texture of sinuous defects oriented preferentially along the flow direction is established by the initial process. This larger-scale structure coarsens during the slow process. Thus, the mechanism of the slow process may involve larger scale relaxations, such as defect migration.

The path to parallel alignment at very high frequencies (Regime III, $\omega \gg \omega'_c$) involves an initial fast process that is quite unique: a bimodal distribution that consists of parallel and transverse lamellae is created. This transient is so different from the one in Regime II, that a distinct mechanism of parallel alignment must be responsible. Indeed, the concept of destruction/reformation in the literature would anticipate the most rapid destruction of the transverse component of the orientation distribution; some other mechanism must be at work to create the transverse/parallel texture. Based on the observation that this bimodal structure was evident in SAXS patterns for entangled PS-PI lamellar BCPs,^{45,52,55} it was suggested this orientation distribution resulted from an “entanglement effect” and elongation of chains along the flow direction.⁵⁵ However, the Regime III trajectory is observed for unentangled PS-PI’s, and at such small strain amplitudes (as small as $\gamma_o = 10\%$), that segmental orientation is hardly perturbed.^{63,49,51} Further, Regime III has not been reported in PEP-PEE-type polymers, which are well-entangled.

Two very general concepts may explain the creation of the bimodal parallel-transverse texture during the fast process in Regime III.² First, chain distortion may play a central role, since this texture has only been observed at shear frequencies so high the polymer chains are not able to relax ($\omega \gg \omega'_c$). Second, if these two considerations are taken together, only two orientations might be induced by very high frequency shearing: parallel and transverse. The other orientations with the right symmetry have a projection along the perpendicular orientation, so they can only form through larger scale relaxations that exchange material out of the shearing plane. The timescale of the deformation is too fast for these large-scale rearrangements to occur. This reasoning explain why transverse and parallel orientations could be enhanced, but does not explain why both are generated.

To explain the bimodal texture, a mechanism to generate both parallel and transverse layers during the fast process has been suggested. Two factors affecting the lamellar orientation due to shear are considered: the deformation of the layers and the distortion of chain conformation, as illustrated schematically in Figure 13. These effects can disturb the relative orientation of the chains with respect to the layers. Except for the special

cases of parallel or transverse lamellae (Figure 13a), this disturbance is more severe for one direction of shearing than the other (Figure 13b); each half-cycle of oscillatory shear can affect the system differently, leading to a net reorientation. For example, consider layers that are near parallel alignment, i.e., having layer normal in the $(\nabla\mathbf{v},\mathbf{v})$ -plane within $\pm 45^\circ$ of the velocity gradient direction. The half-cycle that would tend to rotate the layers away from parallel alignment also extends the chains more strongly away from the layer normal than the opposite half-cycle of shear (Figure 13b). The net effect of a full cycle will tend to rotate the layers toward parallel alignment (Figure 13c). For lamellae near transverse alignment, the asymmetry with respect to forward and reverse shear directions would progressively reinforce transverse alignment (Figure 13d). Thus, this mechanism can explain the enhancement of parallel and transverse components starting from an initially isotropic orientation distribution. Electron micrographs show that the growth of the bimodal orientation distribution occurs while poorly organized regions are converted to well defined layers. Indeed, a process that straightens out convolutions in the local structure would contribute to transforming poorly organized material into lamellae.

Simultaneous with the creation process that produced transverse and parallel domains, there should exist a mechanism that converts the unstable transverse domains to the more stable parallel orientation. This unspecified mechanism dominates the slow process, when most of the material exists in well-organized lamellae in either nearly transverse or nearly parallel orientations. One likely hypothesis is that the boundaries surrounding transverse domains tend to move progressively inward, leading to shrinkage and eventual disappearance of transverse regions. Electron micrographs also implicate defect migration in the refinement of the parallel alignment during the slow process. Tilt walls that are preferentially oriented normal to the flow direction separate regions that are somewhat tilted up and down relative to parallel alignment. Images of the microstructure suggest that these boundaries tend to migrate in the direction of the more severely misaligned region; when two walls meet, they merge into one. The result is a simultaneous coarsening of the chevron pattern of defects and a tightening of the orientation distribution of the near parallel lamellae.

Reflecting on the trajectories of Regimes IV, I, II and III, it appears that the changes in the character of both the fast and slow processes as one moves from very low frequencies ($\omega < \omega_d$), through moderately low frequencies ($\omega_d < \omega < \omega'_c$) and moderately high frequencies (above, but near ω'_c), to very high frequencies ($\omega \gg \omega'_c$) can be qualitatively understood in terms of the changes in the relaxation processes that can occur on the timescale of the deformation. Certain general mechanistic concepts may be relevant in all regimes. For example, defect migration appears to be important in the slow process in all regimes. However, the specific defects involved, their anisotropic arrangement and their specific motions differ from one regime to the next and with position along a given trajectory. These individual characteristics may account for the differences among their kinetics as functions of processing conditions, such as the distinct non-linear effects of strain on kinetics.

Up to this point, we have been discussing alignment behaviors that have been observed as the structure evolves from an isotropic, ordered initial condition. In some cases, the behavior appears to be insensitive to the precise initial condition. For example, the bimodal transverse-parallel texture has been observed in PS-PI-type diblocks that have ODT so high that it cannot be reached to erase the flow and thermal history associated with sample preparation.^{45,52} Consequently, the initial condition is almost invariably somewhat anisotropic; in addition, a particular annealing procedure has been applied to some samples, but not others.⁵⁵ In spite of these differences, the bimodal texture is produced by very high frequency shearing in the various systems. On the other hand, some very interesting changes in behavior as a function of initial condition have been discovered. Particularly in relation to the low frequency regime of parallel alignment (Regime IV), it has been reported that PS-PI type polymers exhibit parallel alignment at low frequencies, but only if they are pressed and annealed first.⁵⁶ This treatment is not a prerequisite for low frequency parallel alignment in PEP-PEE-type polymers. It is not yet known whether the dominant effect is due to the flow history (pressing tends to induce parallel alignment), the thermal history or a particular combination of the two. A closely-related phenomenon accessible only in PS-PI

samples that have been pre-treated to exhibit low-frequency parallel alignment is another variation of strain-induced flipping: at frequencies that lie in Regime I, it has been reported that small strains produce parallel alignment, while higher strains induce perpendicular.⁵⁸ It is not yet clear whether the parallel alignment that is generally present in pressed samples plays a role in this behavior as well. Clarification of the physical origins of these alignment behaviors will very likely lead to new insights into the alignment mechanisms of Regimes I and IV.

Highly aligned initial conditions have been used to examine the potential for switching materials back and forth between distinct aligned states and to examine the dynamics of specific defects. Switching experiments have shown that in PEP-PEE-type systems, parallel alignment induced in Regime IV can be flipped to perpendicular by imposing conditions that belong to Regime I; however, a perpendicular alignment cannot be flipped back to parallel by imposing conditions in Regime IV.^{39,46} On the other hand, in PS-PI-type lamellae, perpendicular alignment can be flipped to parallel by imposing conditions that lie in Regimes II or III; but the reverse transformation from parallel back to perpendicular cannot be produced.⁵⁰ Well-aligned parallel samples have been used to study the motion of edge-dislocations by imposing compression on the sample and monitoring the subsequent stress relaxation.⁵⁴ Nearly perfect parallel samples have been created using prolonged annealing after cessation of oscillatory shearing; the creation of tilt wall defects by oscillatory shear has been investigated.⁵³ Fundamental understanding of specific defect types and their motions appears to be of central importance to a range of alignment mechanisms and these studies serve as models for future work in this area.

5. Effect of Macromolecular Architecture: Bridges and Loops

Different macromolecular architectures affect chain conformation in microphase-separated block copolymers. Diblock copolymers, such as PEP-PEE and PS-PI types have only one possible topology, while ABA triblocks and ABC triblocks have more possibilities, such

as bridges and loops (Figure 14). A_2B type¹⁸ and star block copolymers¹⁷ may have interesting packing behavior due to asymmetric “crowding” along interfaces in the ordered state. Thus, the effect of macromolecular architecture represents an important dimension in understanding flow-induced alignment. In this section, we will discuss ABA type and ABC triblock copolymers. Flow-alignment of other types of macromolecular architectures remains to be explored.

A. ABA Triblock Copolymers

Although ABA triblock copolymers self-assemble into morphologies similar to diblocks,⁸³ their chain conformation is very different (Figure 14). Diblocks simply have their junctions tethered along the interface between A-rich and B-rich nanophases. On the other hand, ABA triblocks can adopt either a loop conformation with two ends in the same nanodomain or a bridge, with the two ends are in different nanodomains on either side of the B-rich layer. The percentage of bridge conformations has been measured experimentally by dielectric relaxation⁸⁴ and evaluated by theory.^{85–87}

It has been argued that the difference in flow alignment behavior of ABA and AB copolymers results from the presence of bridging chains. Riise et al. compared the alignment behavior of lamellar PS-PI and PS-PI-PS BCPs.⁴⁴ Since they used a molecular weight of PS-PI-PS almost exactly twice that of an extensively studied PS-PI, the PS-PI-PS sample can be envisioned as two of these PS-PI molecules tethered together at the isoprene ends. As described before, both parallel and perpendicular alignments were observed for the PS-PI diblock (Figure 1), but for the PS-PI-PS triblock, only perpendicular alignment was observed, even at frequencies above ω'_c . This was explained by the existence of bridges in the ABA triblock: in the parallel aligned diblock, the lamellae can easily slide past each other during shearing; while in the ABA triblock, sliding would be resisted by the bridges between adjacent layers. This was interpreted in terms of a decrease in viscoelastic contrast. Tepe et al. studied a PEP-PEE-PEP triblock⁷⁶ and found that shearing in the ordered state

produced only parallel lamellae, even for $\omega_d < \omega < \omega'_c$. This behavior is quite different from that of both the PEP-PEE diblocks³⁹ and the PS-PI-PS triblocks.⁴⁴ Tepe et al. argued that since bridging increases the stiffness of the PEE block, viscoelastic contrast could be increased; thus, parallel alignment is preferred. Unfortunately, there is no experimental evidence that bridging changes the viscoelastic contrast of BCPs.

B. ABC Triblock Copolymers

In terms of the effects of bridging chain conformations, ABC triblock lamellae represent the upper limit: when strongly segregated three-phase nanostructures are formed, all chains must adopt a bridge conformation (Figure 14). At least two types of interfaces exist in ABC triblocks, while there is only one type of interface in the AB and ABA block copolymers. Thus, ABC triblock copolymers can assemble fascinating arrays of nanostructures^{88–94} that are impossible to form using either AB or ABA block copolymers. Many interesting new flow alignment phenomena are expected in such rich systems and need to be explored. For example, for hierarchical structures such as helical strands surrounding cylinders in a continuous matrix, one could envision shearing the material in a first step that aligns the cylinders along the velocity direction, followed by small amplitude shear at an oblique angle to the axis of the cylinders to select only one handedness of the helices.

To investigate flow phenomena in ABC triblocks, a model system has been designed for future research.⁸² The three blocks in this model ABC system are styrene (S), isoprene (I), and a random copolymer of styrene and isoprene (R). This system has several advantages relative to the ABC triblocks that have received the most attention to-date (PS-PI-PVP, PS-PB-PMMA, and PS-PEB-PMMA). For example, the blocks can be grown in any order (SIR, SRI, or ISR),¹⁹ the relative magnitude of the interaction parameters can be tuned as a continuous variable by changing the styrene content in the random block, and the absolute magnitude of the interaction parameters can be tuned by partial hydrogenation of the isoprene units.

As a starting point, “symmetric” ABC triblocks were prepared. They have the same lengths for all three blocks, and the same content of styrene and isoprene in the random block. Four overall lengths (approximately 15K, 20K, 25K, and 35K per block, respectively) in all three permutations (RSI, SRI, RIS) are compared to each other. Here we summarize some preliminary results on the alignment behavior of lamellar nanostructures.⁸² Two-nanophase-separated lamellae (such as SRI-15, SRI-20, RSI-15, and SIR-20) and three-nanophase-separated lamellae (SIR-35, RSI-35, and SRI-35) are investigated. Most two-nanophase-separated lamellae (SRI-15, RSI-15) behave in a manner very similar to that of lamellar diblocks (Figure 15): they show three regimes of alignment (I, II, and III), fast and slow processes along each trajectory, and strain-dependent kinetics like PS-PI diblocks. SIR-20 behaves like the SIS triblock: only perpendicular alignment is achieved below and above ω'_c . Actually, TEM micrographs of SIR-20 suggest that the two end-blocks S and R are miscible (i.e., like ABA-type triblock lamellae). Micrographs of RSI-15 suggest that two adjacent blocks S and R are miscible (like asymmetric AB diblock lamellae), TEM images of SRI-15 and SRI-20 imply that the middle block R is partially miscible with both S and R blocks, resembling a weakly segregated symmetric diblock lamellae.

A new feature introduced to the lamellar system by ABC triblock copolymers is the occurrence of a new type of defect: three microphase lamellae with correlated perforations (Figure 16). The lamellae in SIR-35 consist of repeating stacks of [I-S-I-R]. The isoprene layers are observed to be continuous; however, the intermediate layers are composed of alternating sections of S and R. Where there is S on one side of the I layer, there is R on the other side. Thus, the defects represented by an S/R boundary within a given layer are correlated with R/S defects on the layers just across the adjacent I layers. As these defects annihilate each other upon annealing, the structure coarsens, and long range correlations produce striking patterns, including those that resemble a ship’s wake. Analogous defects are observed in RSI-35, but with S as the continuous layers. However, these defects are not observed in SRI-35, in which all layers are nearly defect-free. A possible explanation has been proposed for the formation of these defects at an order-order transition from two-

nanophase to three-nanophase segregation. If the two phase precursor has layers that are rich in the mid-block (B) segregated from layers in which the end blocks are mixed (A/C), then the transition to the three microphase structure will tend to occur by the lateral segregation of A from C, leading to the correlated perforations. If the two phase precursor has layers rich in the respective end blocks with the middle block mixed in one or both layers (i.e. (A/B)-(B/C) or A-(B/C) or (A/B)-C), three microphase layers can be formed with nice [A-B-C-B] three-phase four-layer structure without this type of defects. These early studies represent the first step towards developing new processing strategies for ABC triblock copolymers.⁸²

6. Implications and Future Work

As discussed in previous sections, significant advances have been made in understanding the physics of flow-induced alignment of block copolymers. A unified three-dimensional mapping has integrated virtually all results on lamellar diblock copolymer melts published so far, and this mapping has been successfully applied to two-nanophase-separated ABC triblock copolymer melts as well. In addition to these three dimensions (temperature, frequency, and strain amplitude), time has been explored as a fourth dimension.

Dimensionless frequencies describing a cascade of relaxations of polymer chains, nanophases, and microdomains are the major parameters determining the flow-alignment behavior of a given material. Characteristic frequencies ω'_c and ω_d appear to be the key players in this dimension. A robust, reproducible and precise method has been developed to measure ω'_c , but developing a method to determine ω_d remains a challenge.

Parameters related to other dimensions, such as dimensionless time, are less understood in terms of their effects on alignment behavior. Within a given regime, a single time scale is not sufficient, since the time scale for the early “fast process” varies differently with strain amplitude than that of the later “slow process”. Images of the microstructural changes in each process give insight into the reasons they behave differently. However, an explanation for the observed kinetics is still lacking. The role of many other thermodynamic and dynamic

factors, such as the strength of segregation, chain mobility, viscoelastic contrast, etc., are not yet clear. Certainly, the difference in alignment behavior of PEP-PEE-type and PS-PI-type diblock copolymers suggests that entanglement and/or viscoelastic contrast have interesting effects.

Further experimental work that addresses issues such as the effects of entanglement and viscoelastic contrast in determining flow alignment behavior would involve the careful selection of experimental methods and the design and preparation of ideal model systems. An integrated approach including in-situ and ex-situ characterization provides an appropriate experimental means. The model systems should be designed in such a way that the gap in the degree of entanglement and viscoelastic contrast between PEP-PEE-type and PS-PI-type BCPs is filled.

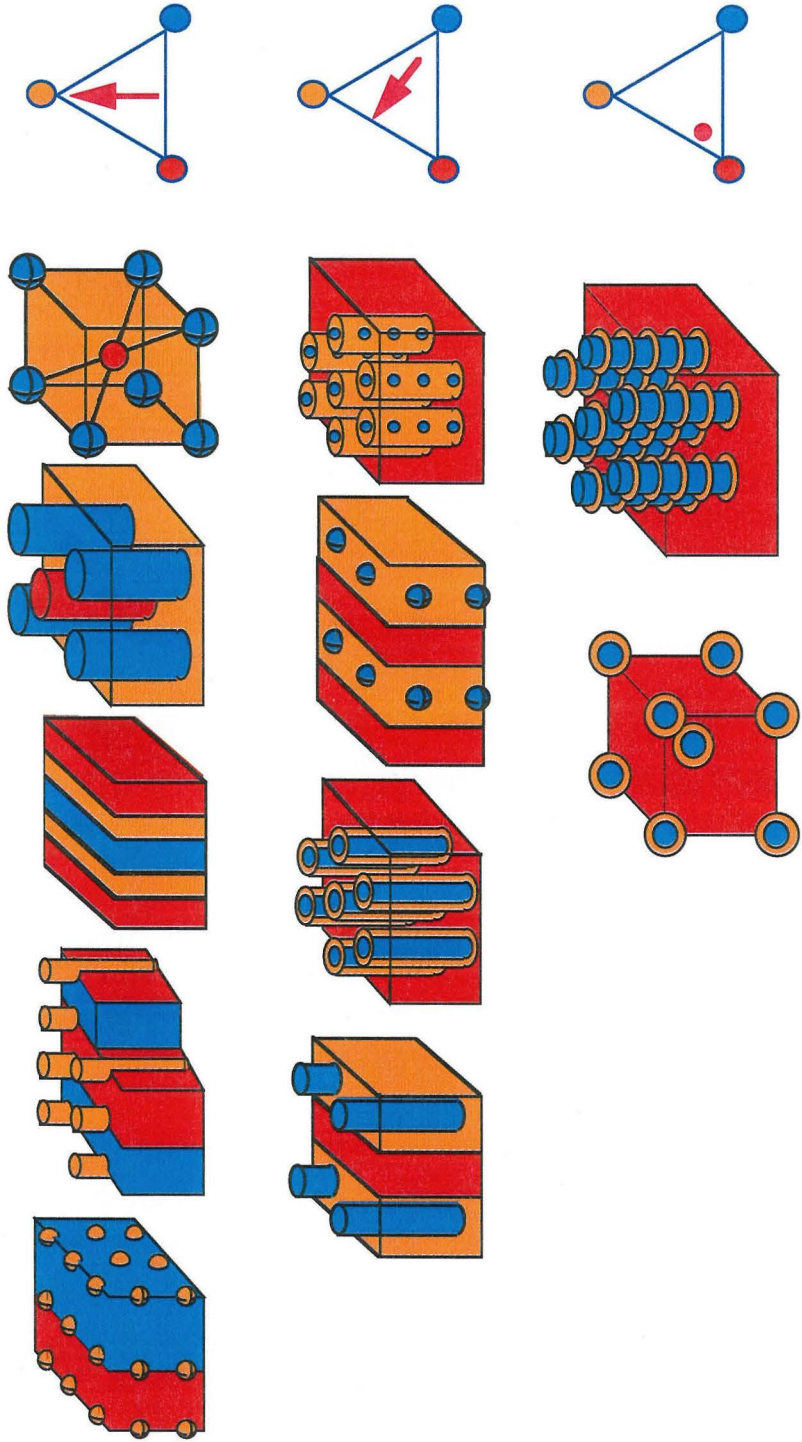
The mechanisms proposed over the past two decades have been re-evaluated recently.^{2,46,49,50,63} Selective melting appears not to be widely important,^{2,49,50,63} while selective creation is strongly indicated when the initial condition is an unaligned state obtained by quiescent ordering.^{2,63} Grain rotation is supported by the rheo-optical signature of parallel alignment in Regime IV.⁴⁶ Defect migration has been observed in many cases^{41,63} and the specific types of defects involved in different stages of alignment have been imaged for Regimes I, II, and III.⁶³ Many questions remain, such as the detailed mechanisms of flipping.

Experimental progress in understanding flow-induced alignment presents new opportunities in modeling and simulation, which in turn could yield valuable insights to guide the unified design of materials and processing conditions to exploit alignment phenomena. Observation of microstructural evolution at well defined stages in each alignment trajectory provides a new perspective on the way theoretical and simulation work could be approached. Instead of focusing on the final aligned states,^{34,35,37,39,42,44,47,48} recent advances^{2,46,49-51,63} suggest that we should treat flow-induced alignment as a dynamic process.³⁶ For each alignment trajectory, it may be possible to break the overall alignment process into parts that are tractable by analysis or simulation. For example, the conversion of poorly organized

material into lamellae might be treated as an individual part. This reorganization process would proceed differently at very high frequencies, where chain dynamics play a more important role than at low frequencies, where nanostructural dynamics dominate. Specific types of defect migration might be investigated theoretically as well. For example, the elimination of partial focal conic defects by oscillatory shear might be modelled to clarify the early fast process. The evolution of chevron patterns of defects under the influence of very high frequency ($\omega \gg \omega'_c$) oscillatory shear might be modeled, to gain insight into the slow process of the type (III) trajectories to parallel alignment. Theoretical understanding of these individual processes will bring us closer to the goal of describing the whole alignment process.

As more elaborate nanostructures can be formed by ABC triblock copolymers and other types of BCPs with complex architectures, flow-induced alignment of these hierarchically organized nanostructures will deserve increasing attention. Many new questions regarding flow-induced alignment behaviors will be raised. For example, when cylinders are present at the interfaces between the lamellae in ABC triblock copolymers, does it alter the alignment behavior of the lamellar superstructure? Are there parallel and perpendicular regimes for the layers? Do the cylinders orient along the flow direction? etc. Chiral nanostructures could be produced by applying shear flow of a helix-on-cylinder morphology to discriminate between right- and left-handed helices. In the case of BCPs that have one side-group liquid crystalline polymer (SGLCP) block, one may deal with both the alignment of BCP layers and the director orientation in the SGLCP nanophase. Understanding the flow-induced alignment behaviors of these novel nanostructures would pave the way to developing new functional self-assembled materials.

Morphologies of ABC Triblocks



REFERENCES

1. Olson, G.B. *Science* **1997**, *277*, 1237; Attard, G.S. et al. *Science* **1997**, *277*, 838.
2. Chen, Z.-R.; Kornfield, J. A.; Smith, S. D.; Grothaus, J. T.; Satkowski, M. M. *Science* **1997**, *277*, 1248.
3. Muthukukumar, M.; Ober, C.K.; Thomas, E.L. *Science* **1997**, *277*, 1225.
4. Decher, G. *Science* **1997**, *277*, 1232.
5. Kumar, K.N.P. et al. *Nature* **1997**, *358*, 48; Tolbert, S. H.; Firouzi, A.; Stucky, G. D.; Chmelka, B. F. *Science* **1997**, *278*, 264; Aksay, I. A. *Science* **1996**, *273*, 892.
6. Tirrell, D.A. *Nature* **1997**, *390*, 336; Yu, S.J.M. et al. *Nature* **1997**, *389*, 167.
7. Stupp, S.I.; Braun, P.V. *Science* **1997**, *277*, 1242.
8. Templin, M. et al. *Science* **1997**, *278*, 1795.
9. Wu, Z.; Grubbs, R.H. *Macromolecules* **1994**, *27*, 6700.
10. Deming, T.J. *Nature* **1997**, *390*, 386.
11. Aggeli, A. et al. *Nature* **1997**, *386*, 259; Coyne, K.J.; Qin, X.X.; Waite, J.H.; *Science* **1997**, *277*, 1830.
12. Mukamel, S.; Tretiak, S.; Wagersreiter, T.; Chernyak, V. *Science* **1997**, *277*, 781; Weissman, J. M.; Sunkara, H. B.; Tse, A. S. ; Asher, S. A. *Science* **1996**, *274*, 959;
13. Park, M.; Harrison, C.; Chaikin, P. M.; Register, R. A.; Adamson, D. H. *Science* **1997**, *276*, 1401; Chou, S. Y.; Krauss, P. R. ; Renstrom, P. J. *Science* **1997**, *272*, 85.
14. Auschra, C.; Stadler, R. *Macromolecules* **1993**, *26*, 2171; Krappe, U. ; Stadler, R.; Voigt-Martin, I. *Macromolecules* **1995**, *28*, 4558; *ibid* **1995**, *28*, 7583.
15. Mogi, Y. et al. *Macromolecules* **1994**, *27*, 6755;

16. Wei, Z.; Wang, Z.-G. *Macromolecules* **1995**, *28*, 7215.
17. Tselikas, Y. et al. *Macromolecules* **1995**, *29*, 2456.
18. Pochan, D.J. et al. *Macromolecules* **1996**, *29*, 5091.
19. Ashraf, A.; Smith, S.D. submitted
20. Bates, F.S.; Fredrickson, G.H. *Annu. Rev. Phys. Chem.* **1990**, *41*, 525.; Bates, F. S. *Science* **1991**, *251*, 898.
21. Bates, F.S.; Fredrickson, G.H. *Annual Rev. Mater. Sci.* **1996**, *26*, 501.
22. Colby, R.H. *Curr. Opin. Coll. Int. Sci.*, **1996**, *1*, 454.
23. Morkved, T.L.; Lu, M.; Urbas, A.M.; Ehrichs, E.E.; Jaeger, H.M. Mansky, P.; Russell, T.P. *Science* **1996**, *273*, 931.
24. Keller, A.; Pedemonte, E.; Willmouth, F.M. *Colloid Polym. Sci.* **1970**, *238*, 25.; Folkes, M.J.; Keller, A.; Scalisi, F.P. *Colloid Polym. Sci.* **1973**, *251*, 1.
25. Hadziioannou, G.; Mathis, A.; Skoulios, A. *Colloid Poly. Sci.* **1979**, *257*, 136; *ibid* **1979**, *257*, 15; Hadziioannou, G.; Mathis, A.; Skoulios, A. *Macromolecules* **1982**, *15*, 258.
26. Morrison, F. A.; Winter, H. H. *Macromolecules.* **1989**, *22*, 3533.; Morrison, F. A.; Winter, H.H.; Gronski, W.; Barnes, J. D. *Macromolecules.* **1990**, *23*, 4200.
27. Chen, J.T.; Thomas, E.L.; Ober, C.K.; Mao, G.P. *Science* **1996**, *273*, 343.
28. Quiram, J.D.; Register, R.A.; Marchand, G.R. submitted; Hamley, I.W.; Patrick, J.; Fairclough, A.; Ryan A.J.; Bates, F.S.; Towns-Andrews, E. *Polymer* **1996**, *37*, 4425; Kofinas, P; Cohen, R. E *Macromolecules* **1995**, *28*, 336; Shih, H.Y.; Kuo, W.F.; Pearce, E.M.; Kwe, T.K. *Polym. Adv. T.* **1995**, *6*, 417; Ryan, A.J.; Hamley, I.W.; Bras, W.; Bates, F.S. *Macromolecules* **1995**, *28*, 3860; Rangarajan, P.; Register, R.A.; Fetters,

- L.J.; Bras, W.; Naylor, S.; Ryan, A.J. *Macromolecules* **1995**, *28*, 4932; Nojima, S.; Kato, K.; Yamamoto, S.; Ashida, T. *Macromolecules* **1992**, *25*, 2237; Cohen, R. E.; Cheng, P.L.; Douzinas, K.; Kofinas, P; Berney, C.V. *Macromolecules* **1990**, *23*, 324; Khandpur, A.K.; Macosko, C.W.; Bates, F.S.; *J. Polym. Sci., B; Polym. Phys.* **1995**, *33*, 247; Sakurai, K.; MacKnight, W.J.; Lohse, D.J.; Schultz, D.N.; Sissano, J.A. *Macromolecules* **1993**, *26*, 3236; Pepe, T.; Schultz, M.F.; Zhao, J.; Tirrell, M.; Bates, F.S. *Macromolecules* **1995**, *28*, 3008; Schnablegger, H.; Rein, D.H.; Rempp, P.; Cohen, R.E. *J. Polym. Eng.* **1995**, *16*, 1; Robitaille, C.; Prud'homme, J. *Macromolecules* **1983**, *16*, 665; Seguela, R.; Prud'homme, J. *J. Polym.* **1989**, *30*, 1446.
29. Hilmyer, M.A.; Lipic, P.M.; Hajduk, D.A.; Almdal, K.; Bates, F.S. *J. Am. Chem. Soc.* **1997**, *119*, 2747.
30. Brehmer, M.; Mao, G.; Ober, C.K.; Zentel, R. *Macromolecular Symposia* **1997**, *117*, 175.
31. Zheng, W.Y.; Hammond, P.T. *Macromol. Rapid* **1997**, *17*, 11.
32. Antonietti, M.; Forster, S. in preparation
33. Bruinsma, R.; Rabin, Y. *Phys. Rev. A* **1992** *45*, 994.
34. Cates, M. E.; Milner, S. T. *Phys. Rev. Lett.* **1989**, *62*, 1856; Goualian, M.; Milner, S. T. *Phys. Rev. Lett.* **1995**, *74*, 1775.
35. Fredrickson, G. H. *J. Rheol.* **1994**, *38*, 1045.
36. Kodama, H.; Doi, M. *Macromolecules* **1996**, *29*, 2652.
37. Amundson, K.; Helfand, E.; Quan, X.; Hudson, S. D.; Smith, S. D. *Macromolecules* **1994**, *27*, 6559; Mansky, P.; Russell, T.P. *Science* **1996**, *273*, 931; Amundson, K.; Helfand, E.; Davis, D. D.; Quan, X.; Patel, S. S.; Smith, S. D. *Macromolecules* **1991**, *24*, 6546.; Amundson, K.; Helfand, E.; Quan, X.; Smith, S. D. *Macromolecules* **1993**,

- 26, 2698; Amundson, K.; Helfand, E. *Macromolecules*, **1993**, *26*, 1324.
38. Shiota, A.; Ober, C.K. *Macromolecules* **1997**, *30*, 4274
39. Koppi, K.; Tirrel, M.; Bates, F.S.; Almdal, K, Colby, R.H. *J. Phys. II* **1992**, *2*, 1941.
40. Koppi, K.; Tirrel, M.; Bates, F.S. *Phys. Rev. Lett.*, **1993**, *70*, 1449.
41. Winey, K. I.; Patel, S. S.; Larson, R. G.; Watanabe, H. *Macromolecules* **1993**, *26*, 2542.
42. Winey, K. I.; Patel, S. S.; Larson, R. G.; Watanabe, H. *Macromolecules* **1993**, *26*, 4373.
43. Larson, R. G.; Winey, K. I.; Patel, S. S.; Watanabe, H. *Rheol. Acta* **1993**, *32*, 245.
44. Riise, B.L.; Fredrickson, G.H.; Larson, R.G.; Pearson, D.S. *Macromolecules*, **1995**, *28*, 7653.
45. Okamoto, S.; Saijo, K.; Hashimoto, T. *Macromolecules*, **1994**, *27*, 5547.
46. Kannan, R. M.; Kornfield, J. A. *Macromolecules* **1994**, *27*, 1177.
47. Patel, S. S.; Larson, R. G.; Winey, K. I.; Watanabe, H. *Macromolecules* **1995**, *28*, 4313.
48. Zhang, Y.; Wiesner, U.; Spiess, H. W. *Macromolecules* **1995**, *28*, 778.
49. Gupta, V. K.; Krishnamoorti, R.; Kornfield, J. A.; Smith, S. D. *Macromolecules*, **1995**, *28*, 4464.
50. Gupta, V. K.; Krishnamoorti, R.; Kornfield, J. A.; Smith, S. D. *Macromolecules* **1996**, *29*, 1359.
51. Gupta, V. K.; Krishnamoorti, R.; Chen, Z.-R.; Kornfield, J. A.; Smith, S. D.; Satkowski, M. M.; Grothaus, J. T. *Macromolecules*, **1996**, *29*, 875.
52. Pinheiro, B.S.; Hajduk, D.A.; Gruner, S.M.; Winey, K.I. *Macromolecules*, **1996**, *29*, 1482.
53. Polis, D. L.; Winey, K. I. *Macromolecules*, **1996**, *29*, 8180.

54. S. D. Hudson, K. R. Amundson, H. G. Jeon, S. D. Smith, *Mat. Res. Soc. Bulletin* **1995** *20*, 42
55. Zhang, Y.M.; Wiesner, U. *J. Chem. Phys.*, **1995**, *103*, 4784.
56. Zhang, Y.; Wiesner, U.; Yang, Y.; Pakula, T.; Spiess, H.W. *Macromolecules*, **1996**, *29*, 5427.
57. Zhang, Y.; Wiesner, U. *J. Chem. Phys.*, **1997**, *106*, 2961.
58. Maring, D.; Wiesner, U. *Macromolecules*, **1997**, *30*, 660.
59. Morrison, F.A.; Mays, J.W.; Muthukumar, M.; Nakatani, A.I.; Han, C.C. *Macromolecules*, **1993**, *26*, 5271.
60. Nakatani, A.I.; Morrison, F.A.; Douglas, J.F.; Mays, J.W.; Jackson, C.L.; Muthukumar, M.; Han, C.C. *J. Chem. Phys.*, **1996**, *104*, 1589.
61. Balsara, N.; Hammouda, B.; Kesani, P. K.; Jonnalagadda, S. V.; Straty, G. C. *Macromolecules* **1994**, *27*, 2566; N. P. Balsara and B. Hammouda, *Phys. Rev. Lett* **1994**, *72*, 360; Balsara, N.P.; Dai, H. J. ; *J. Chem. Phys.* **1996** *105*, 2942 ;
62. Wang, H.; Kesani, P.K.; Balsara, N.P.; Hammouda, B. *Macromolecules* **1997**, *30*, 982.
63. Chen, Z.-R.; Issaian, A.; Kornfield, J.A.; Smith, S.D.; Grothaus, J.T.; Satkowski, M.M. *Macromolecules*, **1997**, *30*, 7096.
64. Lee, H. H.; Register, R. A.; Hajduk, D. A. ; Gruner, S. M. *Polymer Engineering and Science* **1996**, *36-10*, 1414.
65. Albalak, R.J.; Thomas, E.L. *J. Polym. Sci.: Polym. Phys.* **1993** *31*, 37 .
66. There is one family of trajectories in Regime IV that remains to be investigated in the future: the route to parallel alignment at very low frequencies, $\omega < \omega_d$. This regime has been studied by rheo-optical techniques in PEP-PEE-2, but this system is not amenable

to transmission electron microscopy. In PS-PI, this regime is not accessible without a prolonged annealing treatment.⁵⁶

67. Rosedale, J. H.; Bates, F. S. *Macromolecules* **1990**, *23*, 2329.
68. Sakurai, K.; MacKnight, W. J.; Lohse, D. J.; Schulz, D. N.; Sissano, J. A.; Wedler, W.; Winter, H. H. *Polymer* **1996**, *37*, 5159.
69. Kawasaki, K.; Onuki, A. *Physical Review A* **1990**, *42-6*, 3664.
70. Rubinstein, M.; Obukhov, S. P. *Macromolecules* **1993**, *26*, 1740.
71. Garetz, B.A.; Newstein, M.C.; Dai, H.J.; Jonnalagadda, S.V.; Balsara, N.P. *Macromolecules* **1993**, *26*, 3152; Balsara, N.P., Garetz, B.A.; Dai, H.J. *Macromolecules* **1992**, *25*, 6072; Balsara, N.P.; Perahia, D.; Safinya, C.R.; Tirrell, M.; Lodge, T.P. *Macromolecules* **1992**, *25*, 3896.
72. Chung, C.I.; Gale, J.C. *J. Polym. Sci. Polym. Phys. Ed.* **1976**, *14*, 1149; Chung, C.I.; Lin, M. I. *J. Polym. Sci. Polym. Phys. Ed.* **1978**, *16*, 545; Gouinlock E.V.; Porter, R.S. *Polym. Eng. Sci.* **1977**, *17*, 535;
73. Scott, D.B.; Waddon, A.J.; Lin, Y.-G.; Karasz, F.E.; Winter, H.H. *Macromolecules* **1992**, *25*, 4175.
74. Gido, S.P.; Thomas, E.L. *Macromolecules* **1997**, *30*, 3739; *ibid* **1994**, *27*, 849; *ibid* **1993**, *26*, 4506.
75. Laurer, J.H.; Hajduk; D.A. Fung; J.C.; Sedat, J.W.; Smith, S.D. *Macromolecules* **1997**, *30*, 3938.
76. Tepe, T.; Hajduk, D.A.; Hillmyer, M.A.; Wiemann, P.A.; Tirell, M.; Bates, F.S.; Almdal, K.; Mortensen, K. *J. Rheology* **1997**, *41*, 1147.
77. Allan, P., Arridge, R. G. C.; Ehtaiatkar, F.; Folkes, M. J. *J. Phys. D: App. Phys.*, **1991**, *24*, 1381.

78. Lodge, T. P.; Fredrickson, G. H. *Macromolecules* **1992**, *25*, 5643.
79. Hongladarom, K.; Burghardt, W.R.; Baek, S.G.; Cementwala, S.; Magda, J.J. *Macromolecules* **1993**, *26*, 772; Hongladarom, K.; Ugaz, V.M.; Cinader, D.K.; Burghardt, W.R.; Quintana, J.P. *Macromolecules* **1996**, *29*, 5346;
80. Kalogrianitis, S.G.; Van Egmond, J.W. *J. Rheo* **1997**, *41*, 343.
81. Balsara, N.P.; Perahia, D.; Safinya, C.R.; Tirrell, M.; Lodge, T.P. *Macromolecules* **1992**, *25*, 3896; Garetz, B.A.; Newstein, M.C.; Dai, H.J.; Jonnalagadda, S.V.; Balsara, N.P. *Macromolecules* **1993**, *26*, 3151; Balsara, N.P.; Garetz, B.A.; Dai, H.J. *Macromolecules* **1993**, *26*, 6072.
82. Chen, Z.-R. et al. in preparation.
83. Hashimoto, T.; Shibayama, M.; Kawai, H. *Macromolecules* **1980**, *13*, 1237; Mayes, A.M.; Olvera de la Cruz, M. *J. Chem. Phys.* **1991**, *95*, 4670.
84. Watanabe, H. *Macromolecules* **1995**, *28*, 5006.
85. Milner, S.T.; Witten, T.A.; *Macromolecules* **1992**, *25*, 5495; Zhulina, E.B.; Halperin, A. *Macromolecules* **1992**, *25*, 5730; Masten, M.W.; Schick, M. *Macromolecules* **1994**, *27*, 187; Matsushita, Y.; Nomura, M.; Noda, I.; Imai, M. *Physica B* **1995**, *213*, 697.
86. Werner, A.; Fredrickson, G. H. *J. Polym. Sci.: Polym. Phys. Ed.* **1997**, *35-5*, 849.
87. Wang, Z.-G.; Chang, C.; Unpublished results
88. Matsushita, Y.; Nomura, M.; Watanabe, J.; Mogi, Y.; Noda, I. *Macromolecules* **1995**, *28*, 6007; Matsushita, Y.; Tamura, M.; Noda, I. *Macromolecules* **1994**, *27*, 3680; Mogi, Y.; Mori, K.; Matsushita, Y.; Noda, I. *Macromolecules* **1992**, *25*, 5412; Mogi, Y.; Kotsuji, H.; Kaneko, Y.; Mori, K.; Matsushita, Y.; Noda, I. *Macromolecules* **1992**, *25*, 5408. Mogi, Y.; Mori, K.; Kotsuji, H.; Matsushita, Y.; Noda, I. *Macromolecules* **1993**, *26*, 5169.

89. Gido, S.P.; Schwark, D.W.; Thomas, E.L.; Goncalves, M.D. *Macromolecules* **1993**, *26*, 2636.
90. Dormidontova, E.E.; Khokhlov, A.R. *Macromolecules* **1997**, *30*, 1980.
91. Breiner, U.; Krape, U.; Abetz, V.; Stadler, R. *Journal of Macromolecular Chemistry and Physics* **1997**, *198-4*, 1051; Bechmann, J.; Auschra, C.; Stadler, R. *Macromol. Rapid Commun.* **1994**, *15*, 67; Balsamo, V.; Vongyldenfeldt, F.; Stadler, R. *Journal of Macromolecular Chemistry and Physics* **1996**, *197-10*, 3317; Breiner, U.; Krappe, U.; Stadler, R. *Macromol. Rapid Commun.* **1996**, *17-8*, 567.
92. Abetz, V.; Stadler, R.; Leibler, L. *Polymer Bulletin* **1996**, *37*, 135 Neumann, C.; Abetz, V.; Stadler, R. *Polymer Bulletin* **1996**, *36*, 43
93. Abetz, V.; Stadler, R. *Macro. Symp.* **1997**, *113*, 19. Stadler, R.; Auschra, C.; Beckmann, J.; Krappe, U.; Voigtmartin-I. *Macromolecules* **1995**, *28*, 3080.
94. Kane, L.; Spontak, R.J. *Macromolecules* **1994**, *27*, 1267.
95. Tcherkasskaya, O.; Spiro, J.G.; Ni, S.R.; Winnik, M.A. *J. Phys. Chem.* **1996**, *100*, 7114; Ni, S.R.; Zhang, P.; Wang, Y.C.; Winnik, M.A.. *Macromolecules* **1994**, *27*, 5742.

FIGURES

Fig. 1. Three-dimensional mapping of LAOS flow-induced alignment regimes in terms of temperature, frequency, and strain amplitude. The third dimension (strain amplitude) is shown inside the symbols using the scale indicated in the upper right corner: the strain amplitude used is indicated by the orientation of the mark within the symbol; a solid wedge indicates the range and strain amplitudes. Results on PS-PI are shown as circles,^{49,50,63,82} ellipses,^{41,47} and modulated ellipses^{48,56,58} (those with a thick line represent annealed samples). Rectangular arrowheads represent PEP-PEE results.^{39,46} Dimensionless frequencies are computed using ω'_c based on the storage modulus method (Figure 2a) wherever possible^{41,47,49,50,63,82}. The range of ω_d/ω'_c indicated is based on values given by Koppi et al.³⁹ and Wiesner et al.^{48,55,56}

Fig. 2. Dynamic regimes of block copolymers: distortion of chain conformation dominates the viscoelastic properties in the “polymeric regime” ($\omega > \omega_c$); distortion of the ordered structure, here lamellae, dominates in the “lamellar regime” ($\omega_d < \omega < \omega_c$). At much lower frequency there must exist a slow enough frequency that defects can move and domains can respond (ω_d). The value of ω_d and the dynamics that dominate at $\omega < \omega_d$ are poorly understood. In the polymeric regime, the heavy lines represent the dynamic moduli of both the disordered and ordered, but unaligned, states. In the lamellar regime the ordered, but unaligned, state has higher storage and loss moduli (bold lines) than the disordered state (narrow lines). Diblocks with very small χ_{AB} can be made long enough to be well entangled (top) while still having accessible ODT (e.g., PEP-PEE-type polymers). When χ_{AB} is larger, the length of the diblock must be kept short to have an accessible ODT; such diblocks are usually not entangled (bottom) (e.g., PS-PI-type polymers). These dynamic regions appear to correspond to distinct alignment regimes (see text).

Fig. 3. Various methods to determine ω'_c and ω_d from the melt rheology of block copolymers (see text for details). **a)** Determination of ω'_c from $G'(\omega)$ is illustrated for a PS-PI (12.5K-9.5K) diblock copolymer.⁴⁷ **b)** The same method to determine ω'_c requires extrapolation for a PS-PI (10K-10K).⁶³ **c)** The loss tangent method for estimating ω_c and ω_d for a PS-PI (10K-10K) diblock copolymer. **d)** The dynamic viscosity method to determine ω_c and ω_d for an unaligned PS-PI (10K-10K) diblock copolymer. Parts c) and d) use data at a single temperature to eliminate any uncertainty in time-temperature shifting. The value of ω'_c shown is the same as in part b).

Fig. 4. Notation for the birefringence measured by sending a polarized laser beam along three directions: a) 1,3-birefringence, b) 1,2-birefringence, and c) 2,3-birefringence.

Fig. 5. The storage and loss moduli of the unaligned and aligned states for a PS-PI (10K-10K) diblock copolymer:⁶³ **a)** unaligned and parallel aligned, **b)** unaligned and perpendicular aligned. Note that the parallel orientation has the lower modulus, even at frequencies in Regime I.

Fig. 6. Three families of alignment trajectories are observed for a PS-PI (10K-10K) diblock copolymer⁶³ that has been heated through the ODT to erase its thermal and flow history, then cooled to a particular temperature in the ordered state where flow-induced alignment is performed. **a)** Regime I route to perpendicular, **b)** Regime II route to parallel, and **c)** Regime III route to parallel (See Figure 1 for the range of temperatures, frequencies and strain amplitudes over which each type of alignment trajectory is observed).^{2,49,51,63} One optical trace and a series of five SAXS patterns for each regime are shown: Initial ordered but unaligned state (I); middle of the fast process (A); the transition from fast to slow processes (B); middle of the slow process (C); and the final well-aligned state (F).⁶³

Fig. 7. A novel trajectory in the boundary between Regimes I and II at a specific shearing condition: $\omega = \omega_c$ and $\gamma_o = \gamma_c$. The first half of the trajectory (from I to M) is similar to those in Regime II; the second half (from M to F) follows the path similar to those in Regime I. The dashed line (from M to F') represents the path followed to parallel alignment when γ_o is slightly greater than γ_c , all other conditions held fixed. (from I to M, and to F').

Fig. 8. Comparison of the real-time optical^{49,51} measurements with ex-situ SAXS results⁵⁵ reveals the similarity in alignment behavior of two different PS-PI samples. The SAXS patterns on the right side illustrate the effect of strain amplitude ($\gamma_o = 0.17, 0.33, 0.42$) for fixed shearing time (2 hours); and the bottom SAXS patterns represent the time evolution (40 min, 2 hours, 8.5 hours) of structure at a given strain amplitude ($\gamma_o = 0.30$). Analogous points are marked in the 1,3-birefringence traces using the symbols shown beside each SAXS pattern. The time evolution of SAXS patterns and their strain amplitude dependence resemble those manifested in the flow birefringence, even though SAXS results are for a polymer that is entangled with an inaccessible ODT while the birefringence results are for a PS-PI that is unentangled with accessible ODT.

Fig. 9. Rheo-optical monitoring of the perpendicular alignment process by oscillatory shearing at low frequency Regime I ($\omega < \omega'_c$): **a**) Effective storage modulus drops quickly at the beginning and remains almost constant afterward, and is not sensitive to the degree of alignment. **b**) Birefringence increases steadily during the process, and the effect of strain is shown as a third power law in the initial fast process. A PS-PI (10K-10K) diblock copolymer was used.⁶³

Fig. 10. Kinetics of parallel alignment during oscillatory shearing at high frequency Regime II ($\omega > \omega'_c$). The effect of strain amplitude is different in the initial **a**) fast process than in the subsequent **b**) slow process, indicating the change of alignment mechanisms during alignment.⁵¹

Fig. 11. Microstructural development during parallel alignment by oscillatory shearing via negative birefringence path (a bimodal transverse-parallel texture) at very high frequency Regime III ($\omega \gg \omega'_c$): **I**) initial ordered but unaligned state, **A**) in the middle of fast process, **B**) during the transition from fast to parallel process, **C**) in the middle of slow process, and **F**) well-aligned lamellae after prolonged shearing.⁶³

Fig. 12. Linear complex dynamic moduli of unaligned, parallel, and perpendicular aligned PS-PI diblock melts at 115°C. The absolute values of complex dynamic moduli are the lowest for parallel alignment in the whole range of frequency. ω'_c is about 2 rad/s at this temperature.⁶³

Fig. 13. The role of chain distortion in the development of the bimodal transverse-parallel texture en route to parallel alignment at very high frequencies ($\omega \gg \omega'_c$) (Regime III). The extensional component of shear affects chain conformation as shown schematically by the solid chains (deformed) compared with the dotted chains (undeformed). Convection of the layers produces a reorientation indicated by the solid lines (deformed) versus the dotted lines (undeformed). **a)** Parallel layers are affected the same way by forward and reverse cycles, so there is no tendency to reorient. **b)** Layers tilted away from the parallel orientation are affected differently by forward and reverse cycles. If their normal \mathbf{n} is tilted to the right, then the distortion of the chains is stronger in the forward than in the reverse direction; consequently, the net effect of a full cycle is to promote reorientation toward parallel alignment. **c)** Thus, layers with \mathbf{n} in the shaded sector on the right side of the $\nabla\mathbf{v}$ axis would tend to evolve toward parallel alignment ($\mathbf{n} // \nabla\mathbf{v}$). **d)** The same reasoning applies to orientations tilted in the opposite direction relative to parallel, so they would also tend to evolve toward parallel alignment (shaded region on the left side of the $\nabla\mathbf{v}$ axis). Similarly, orientations tilted away from transverse alignment would progressively rotate into transverse (shaded regions near the \mathbf{v} axis). Schematic diagrams regarding near-transverse layers have been shown elsewhere.²

Fig. 14. Chain conformations in AB diblock, ABA triblock, and ABC triblock copolymers. Only one type of interface (A-B) exists in both AB diblock and ABA triblock copolymers. ABA triblocks can form either bridges or loops. For ABC triblocks, only bridge conformations are allowed in three-nanophase-separated structures.

Fig. 15. Flow-alignment behaviors of two-nanophase-separated lamellar ABC triblocks. BLD2 is a blend of two samples (RSI-20:RSI-15=1:4).

Fig. 16. “Correlated perforations” in three-nanophase-separated lamellae of SIR-35. **a)** a high defect density is observed in samples quenched from the two-nanophase state. **b)** coarsening occurs during annealing in the three nanophase state.

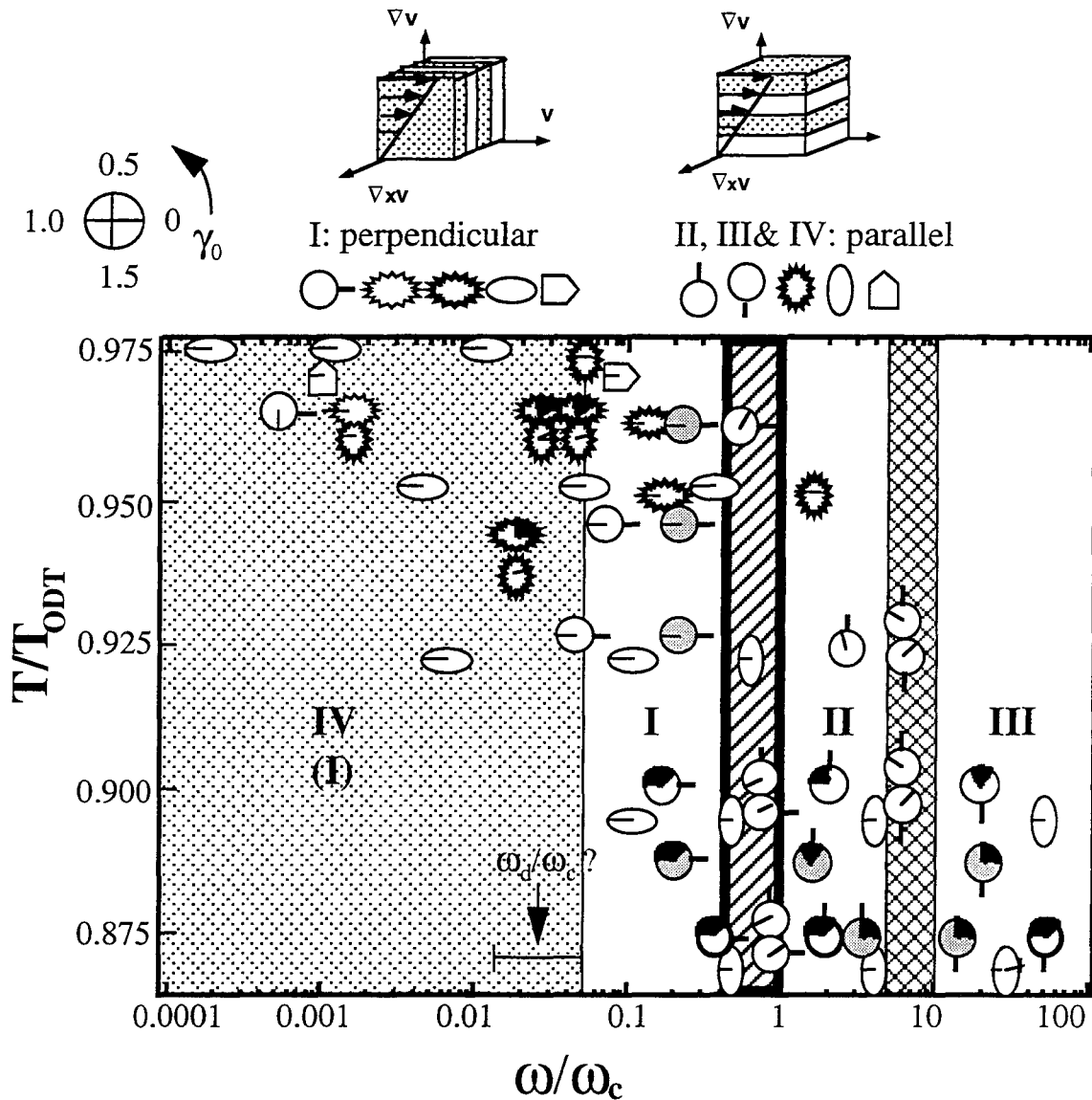


Fig.1

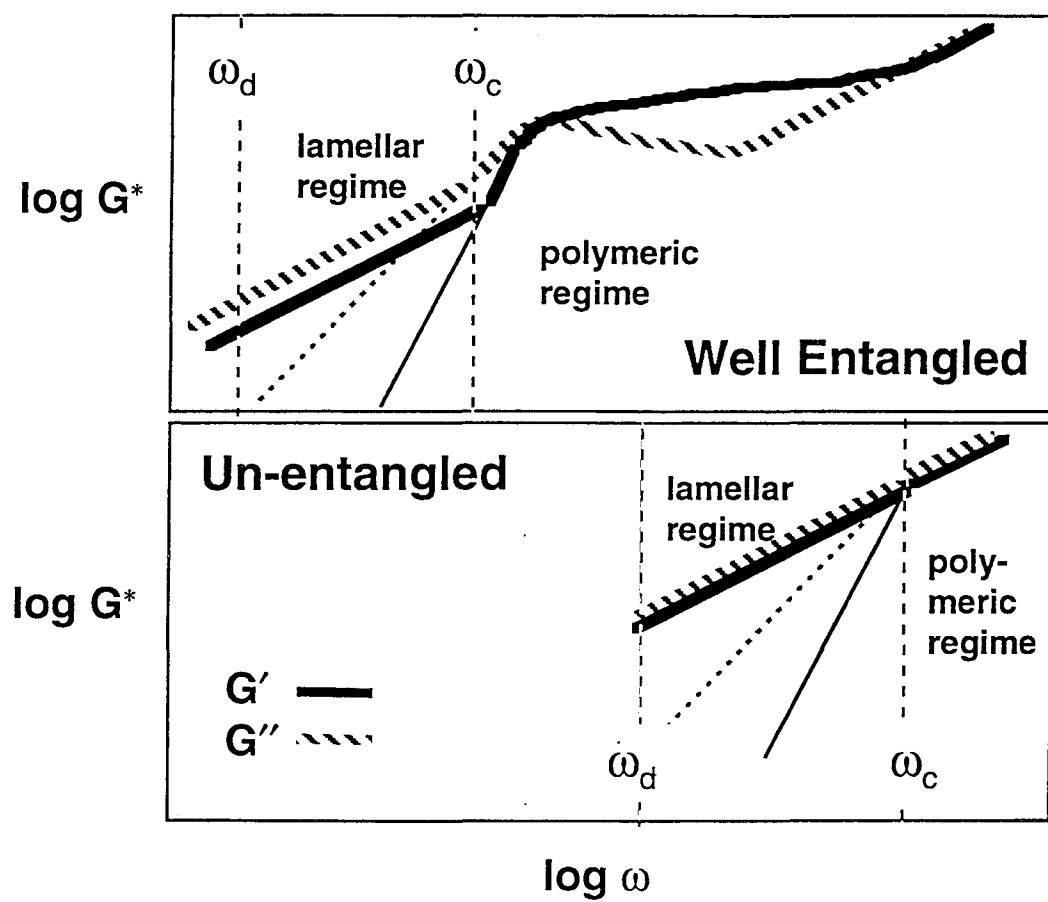


Fig.2

Fig.3a

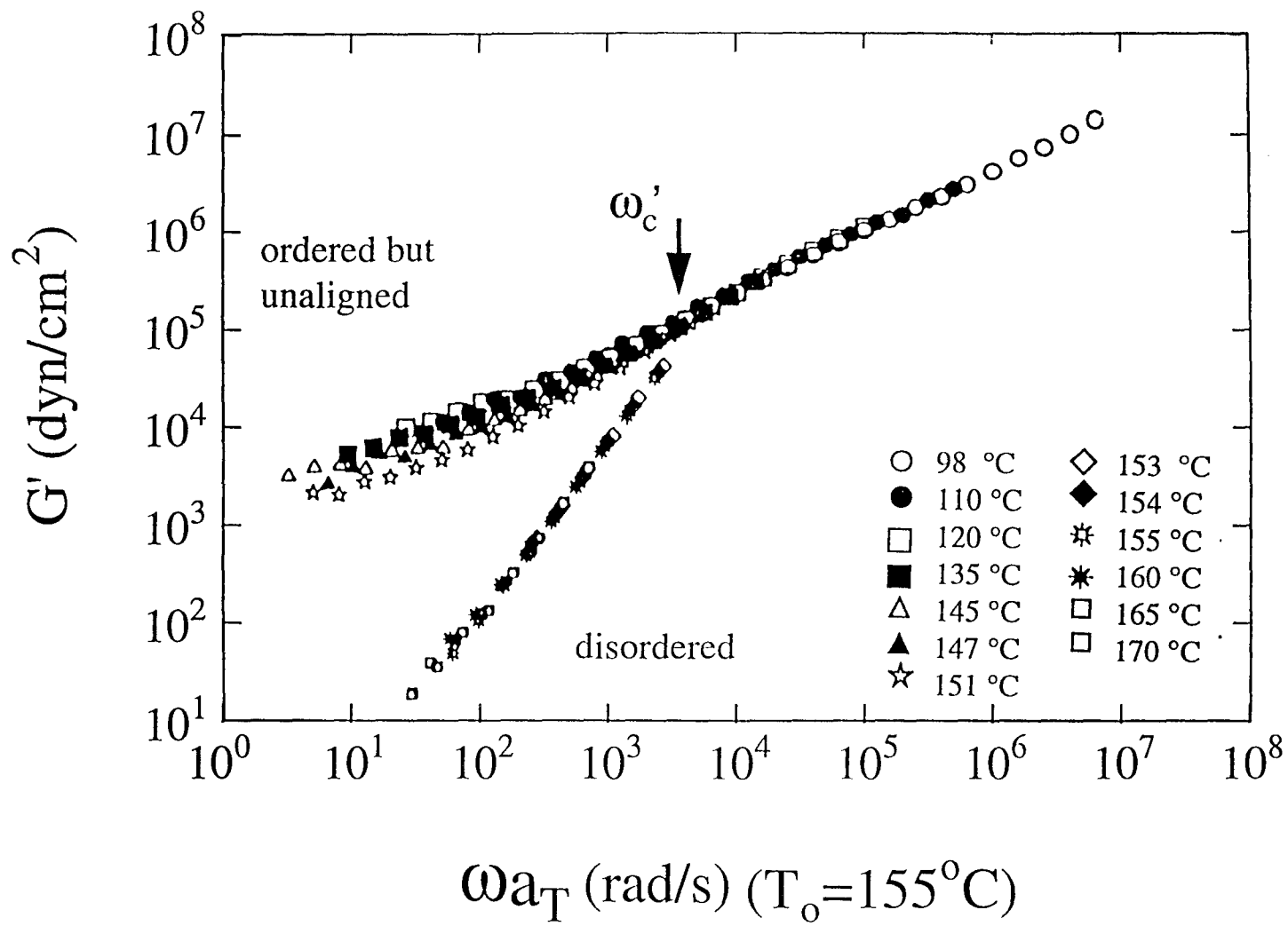


Fig.3b

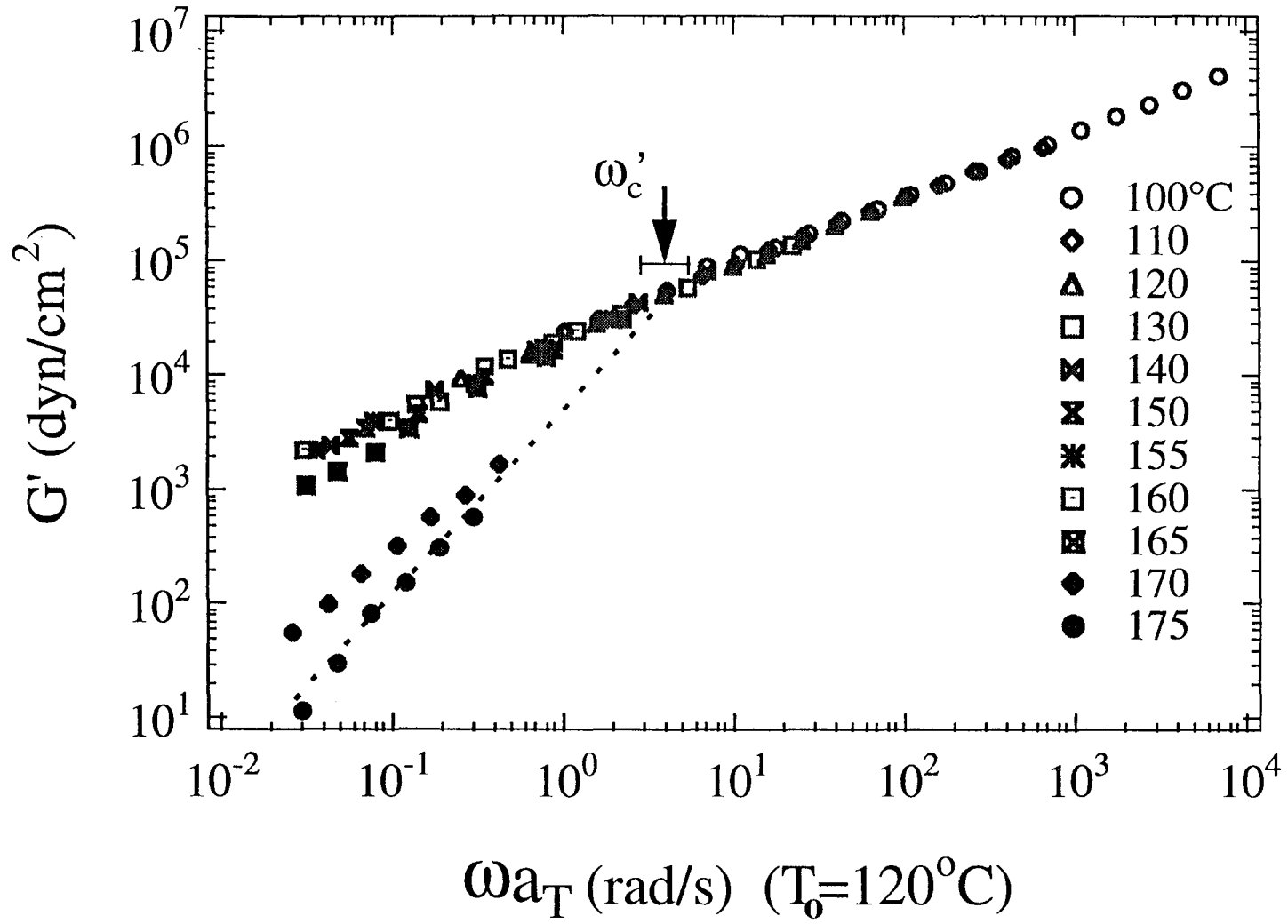


Fig. 3c

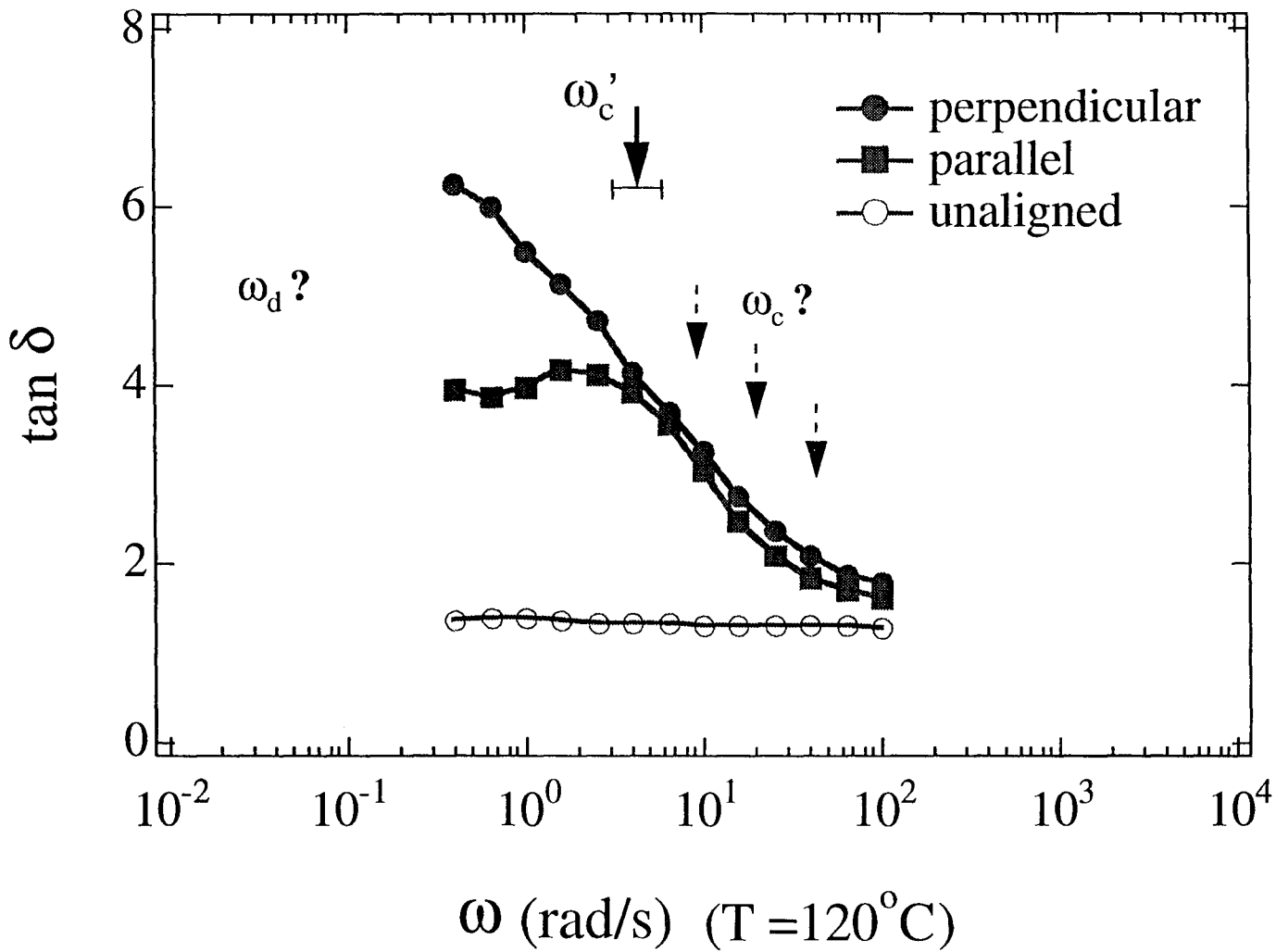
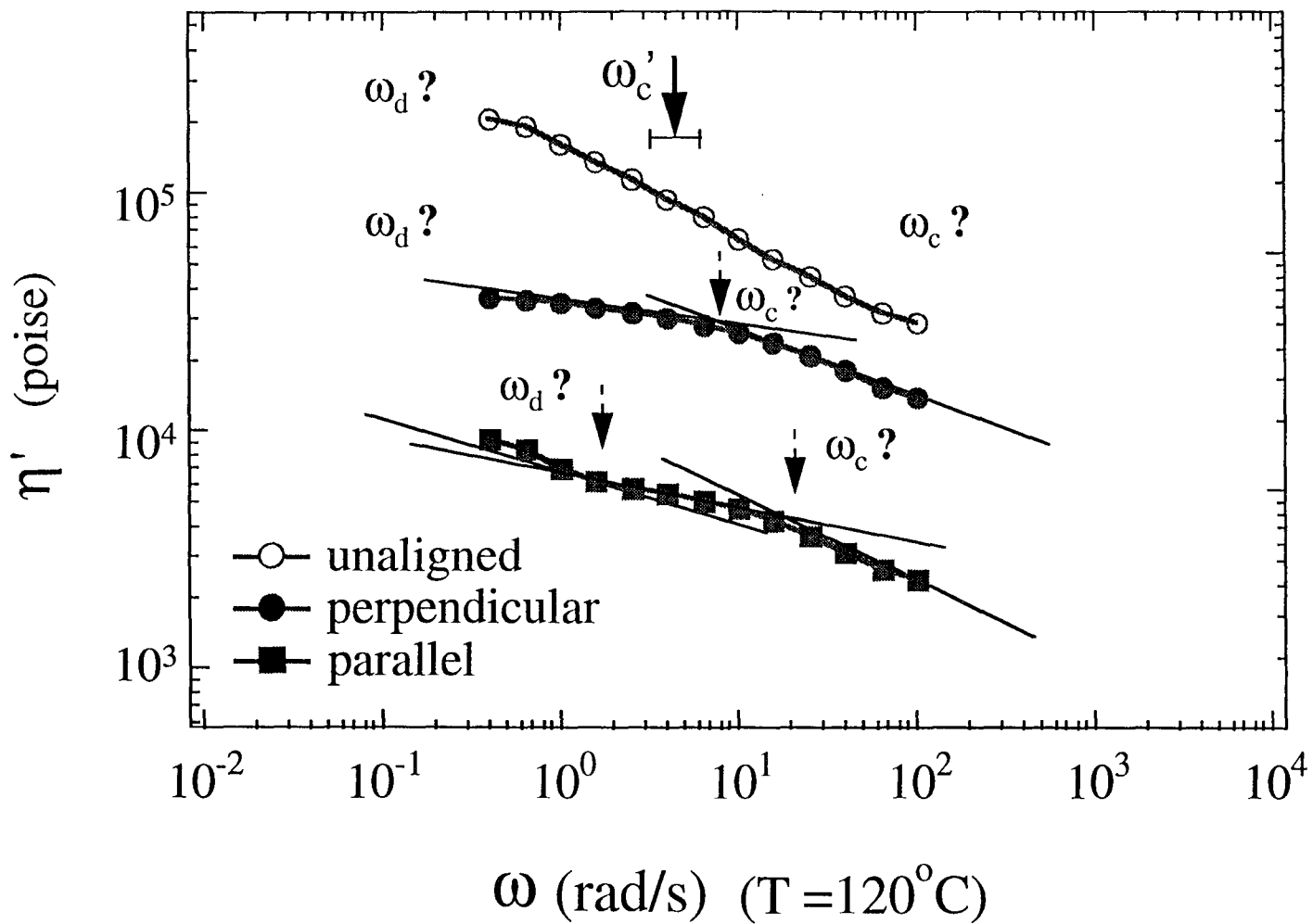


Fig.3d



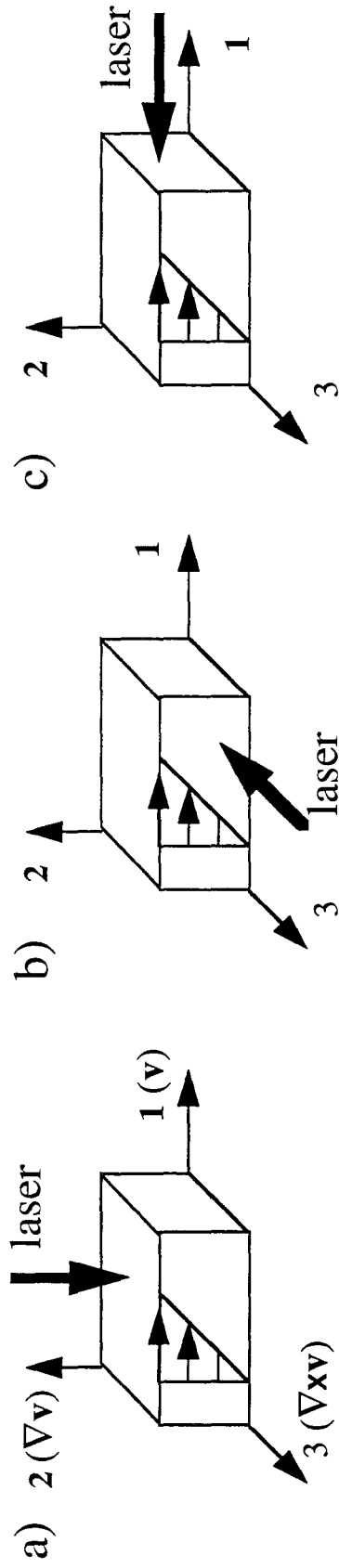


Fig.4

Fig.4

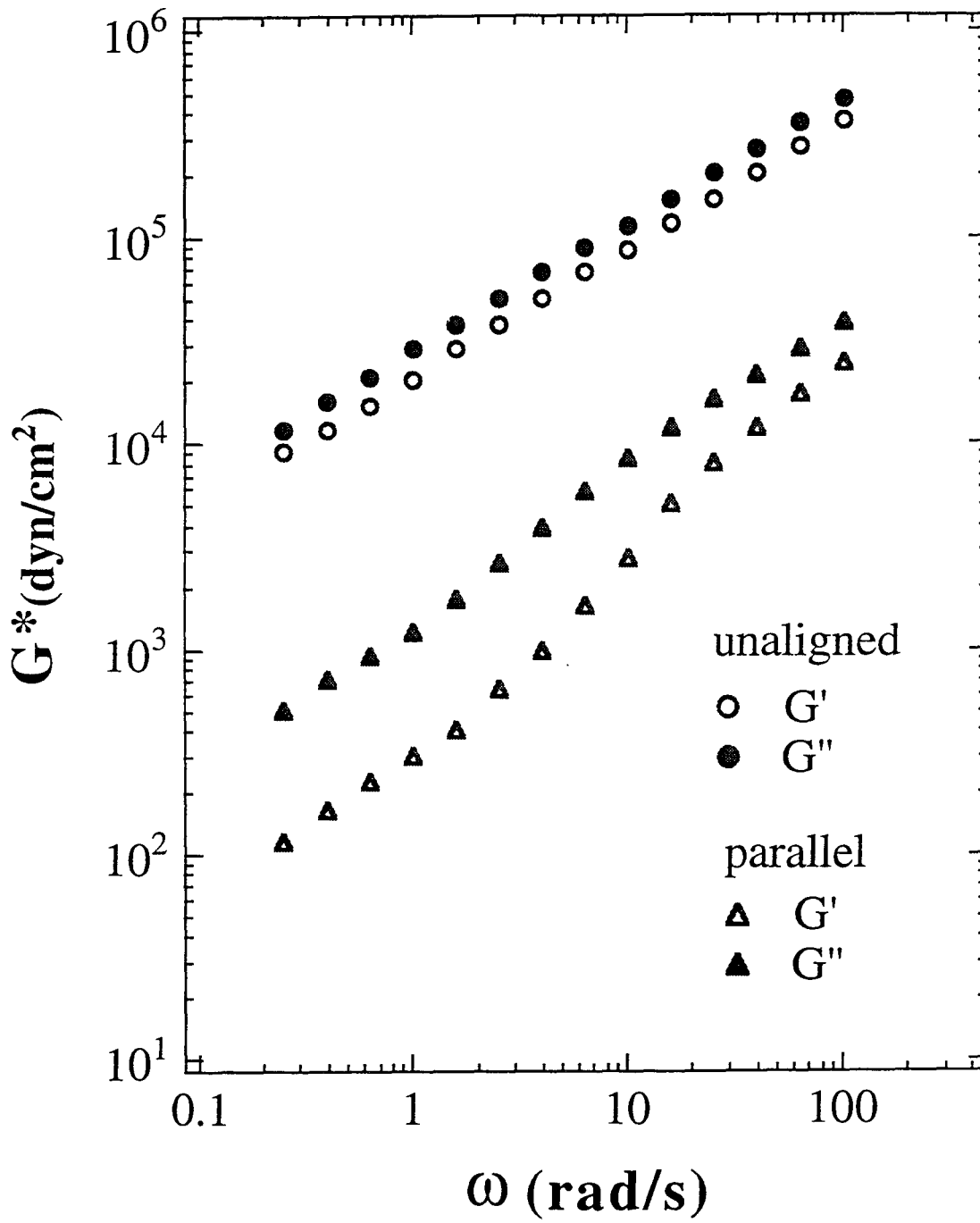


Fig.5a

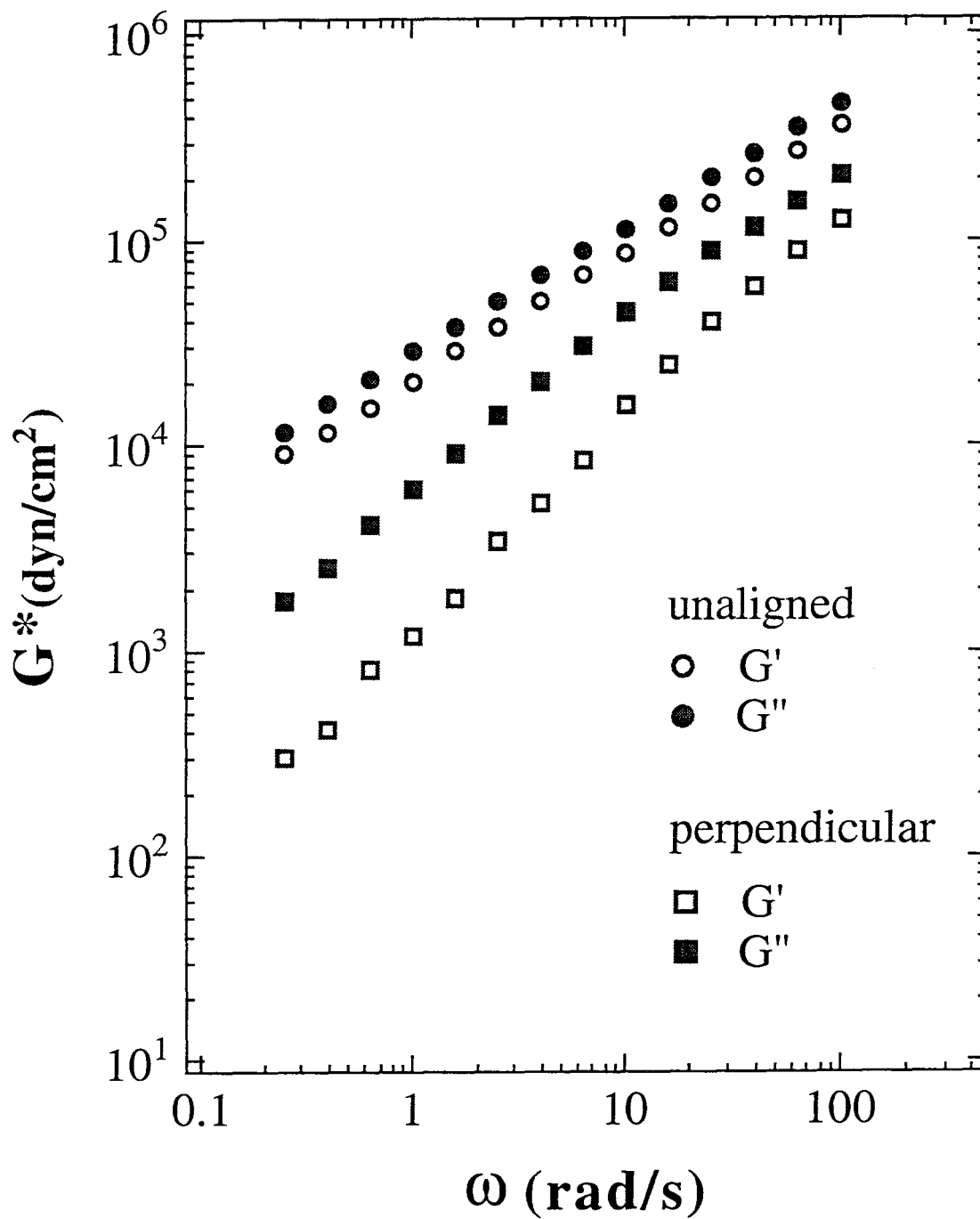


Fig.5b

Fig. 6a

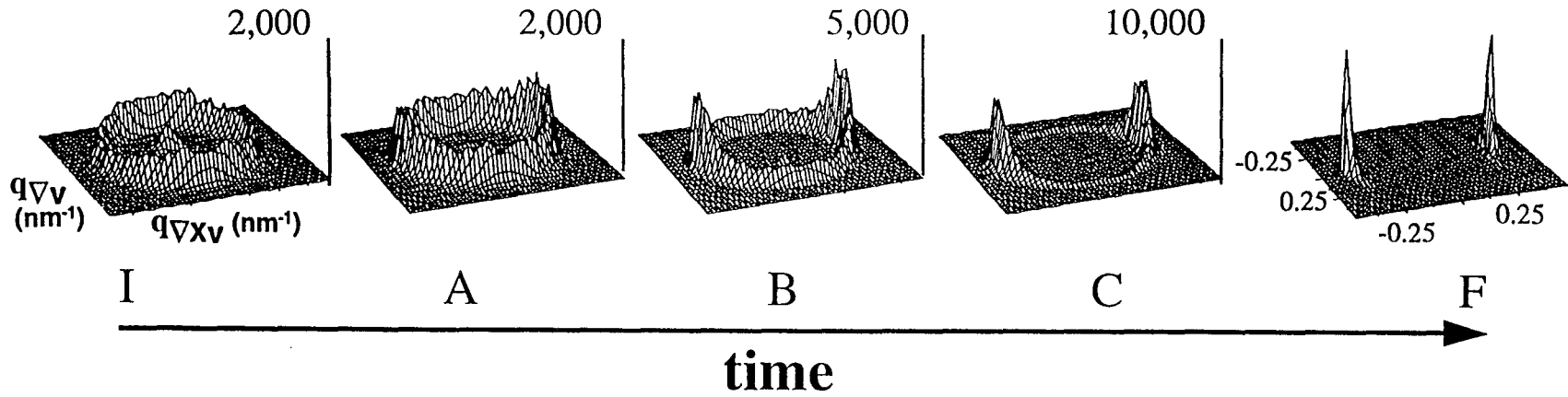
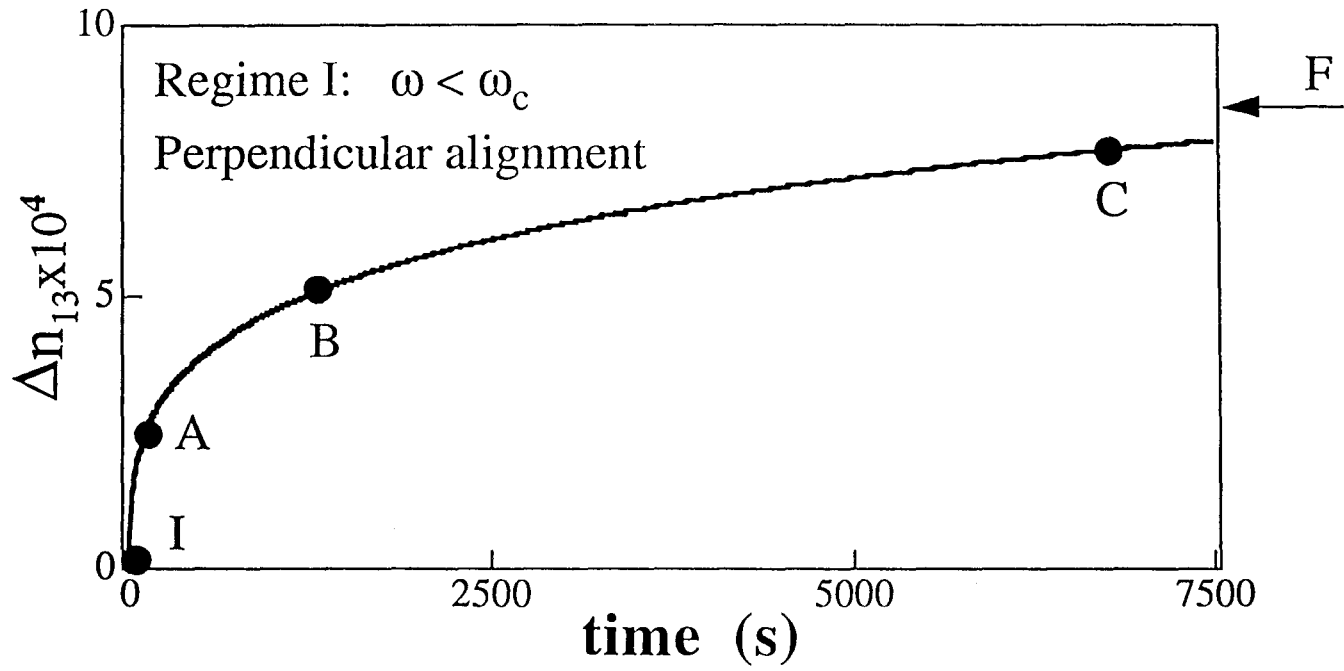


Fig.6b

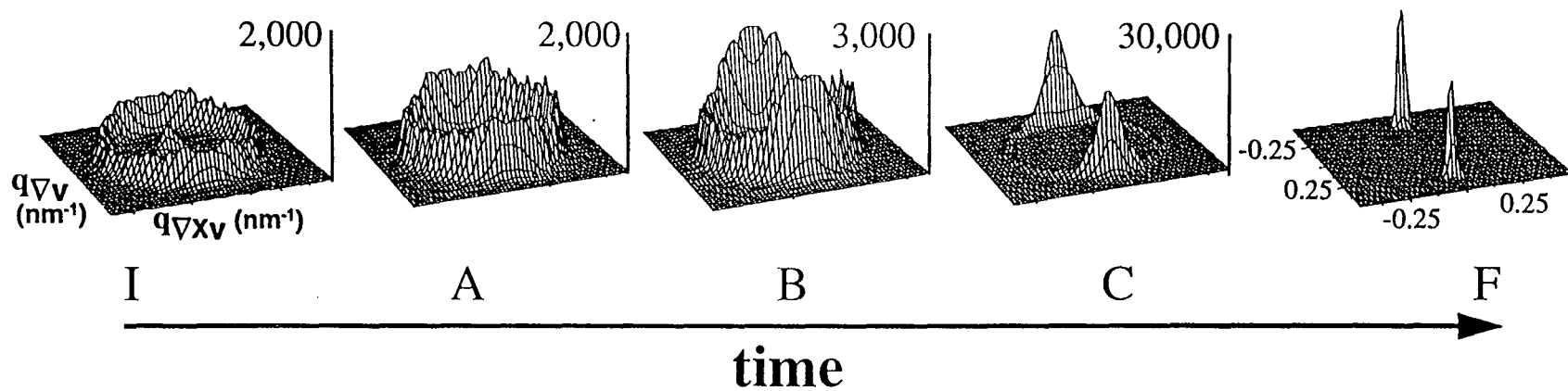
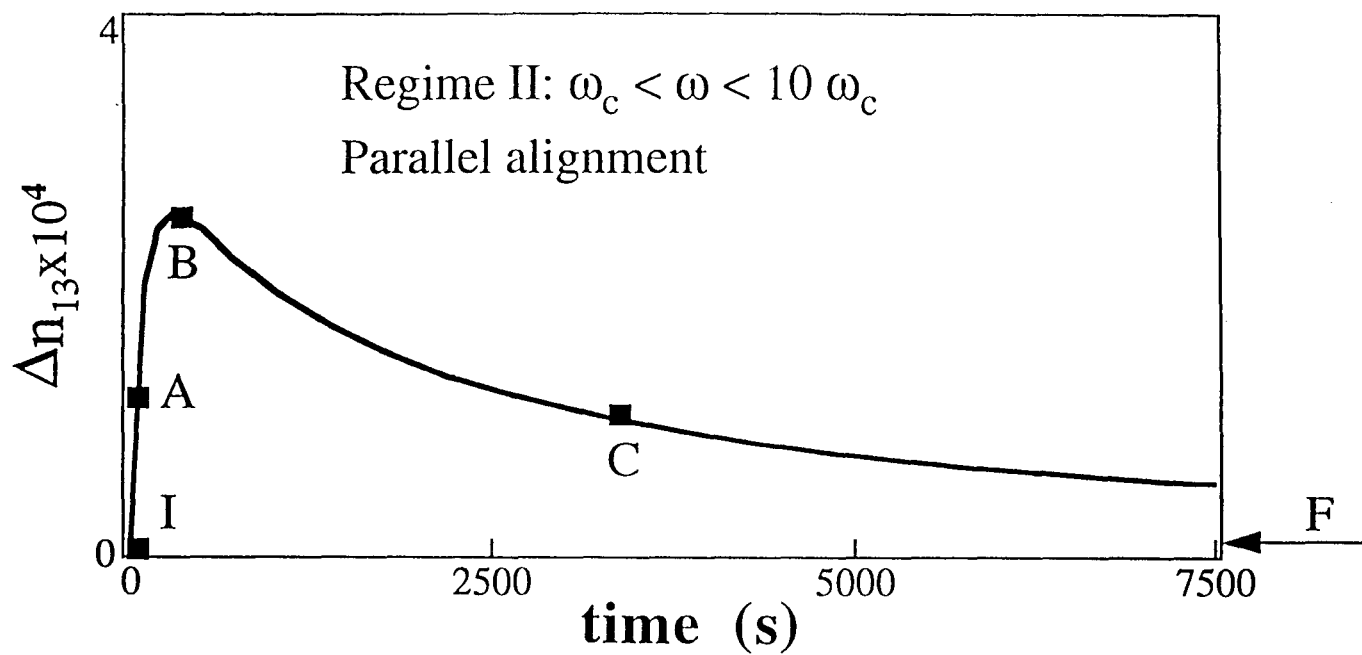
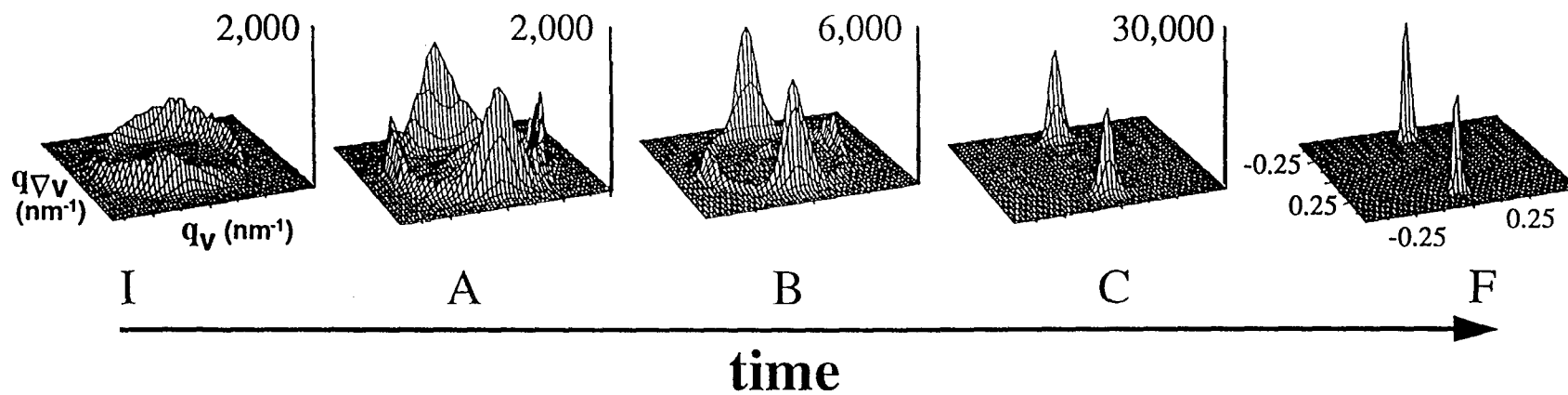
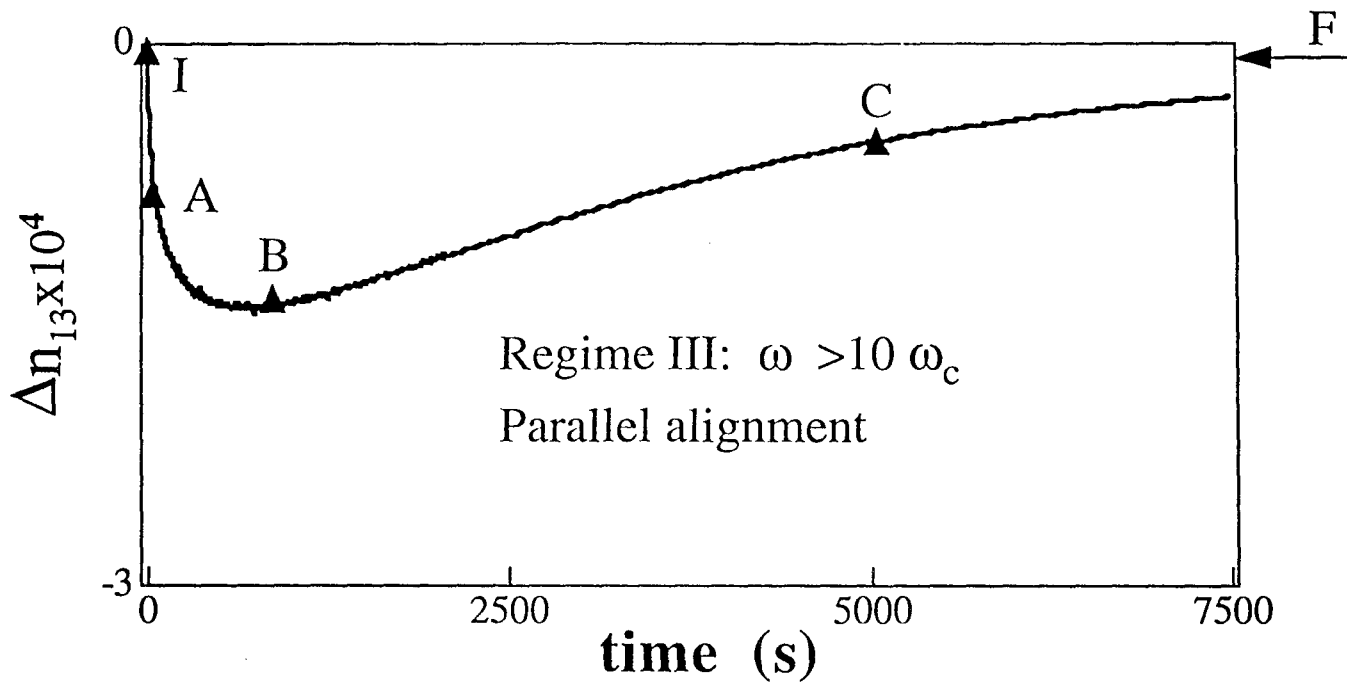


Fig. 6c



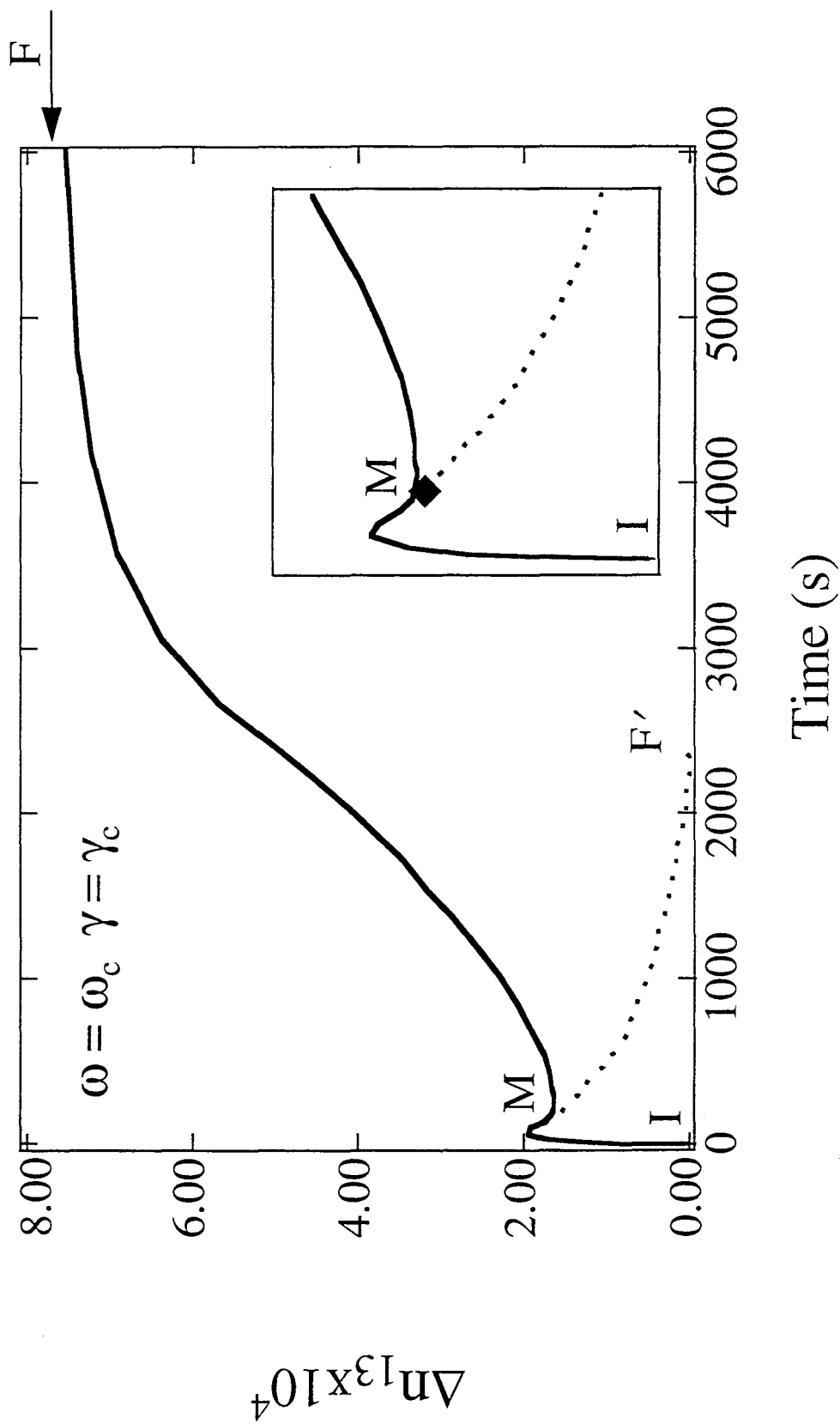


Fig.7

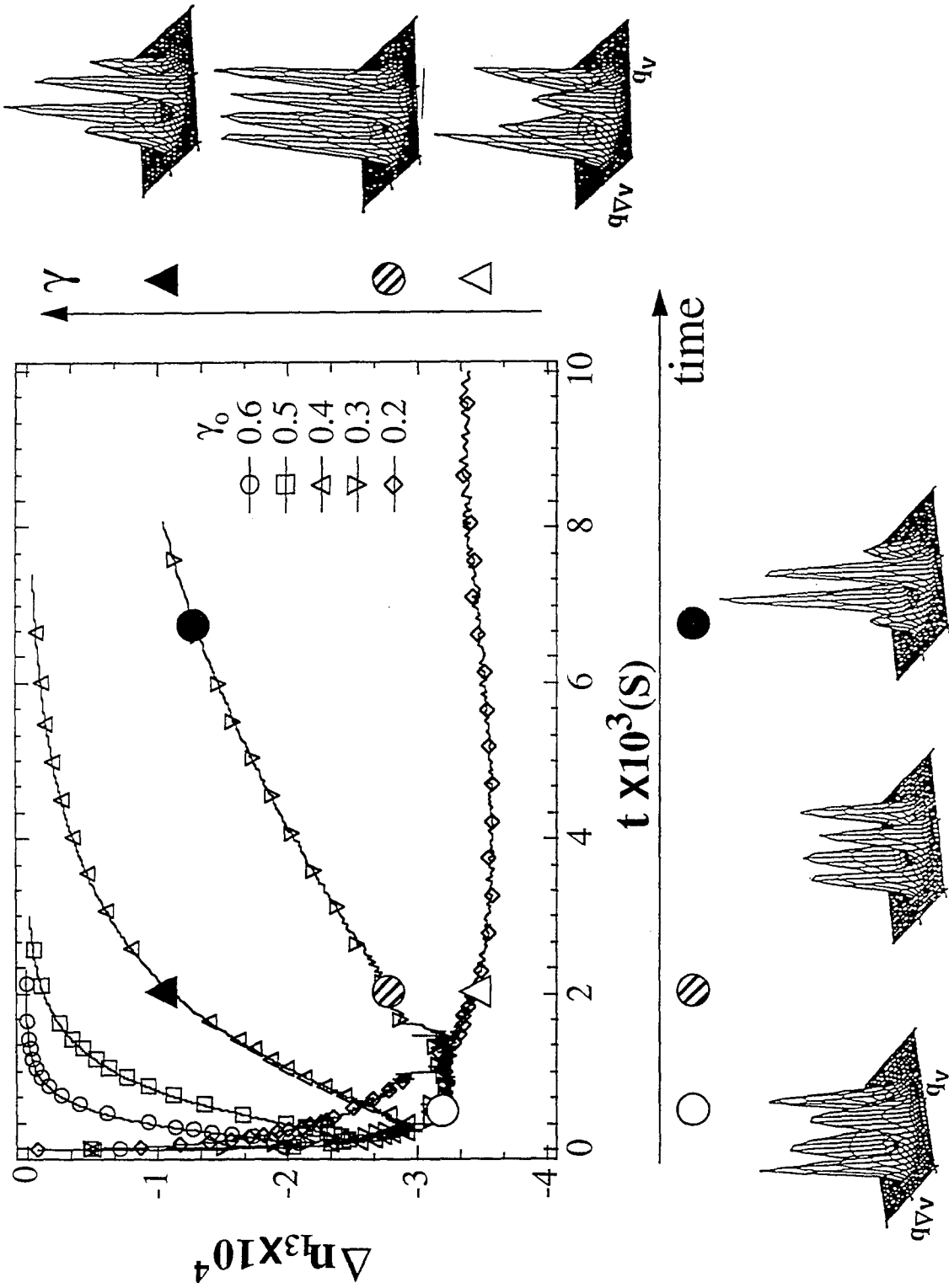


Fig.8

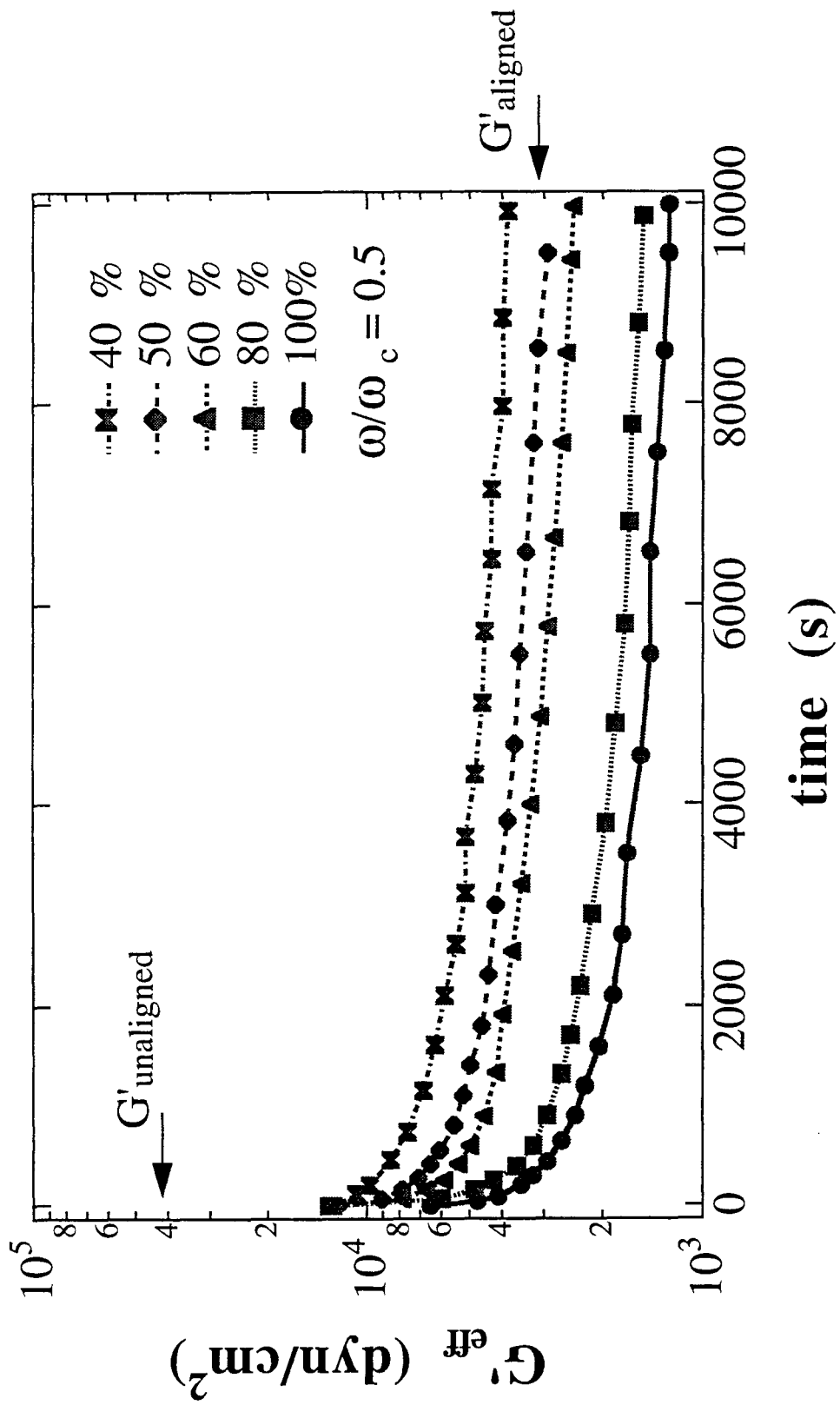


Fig.9a

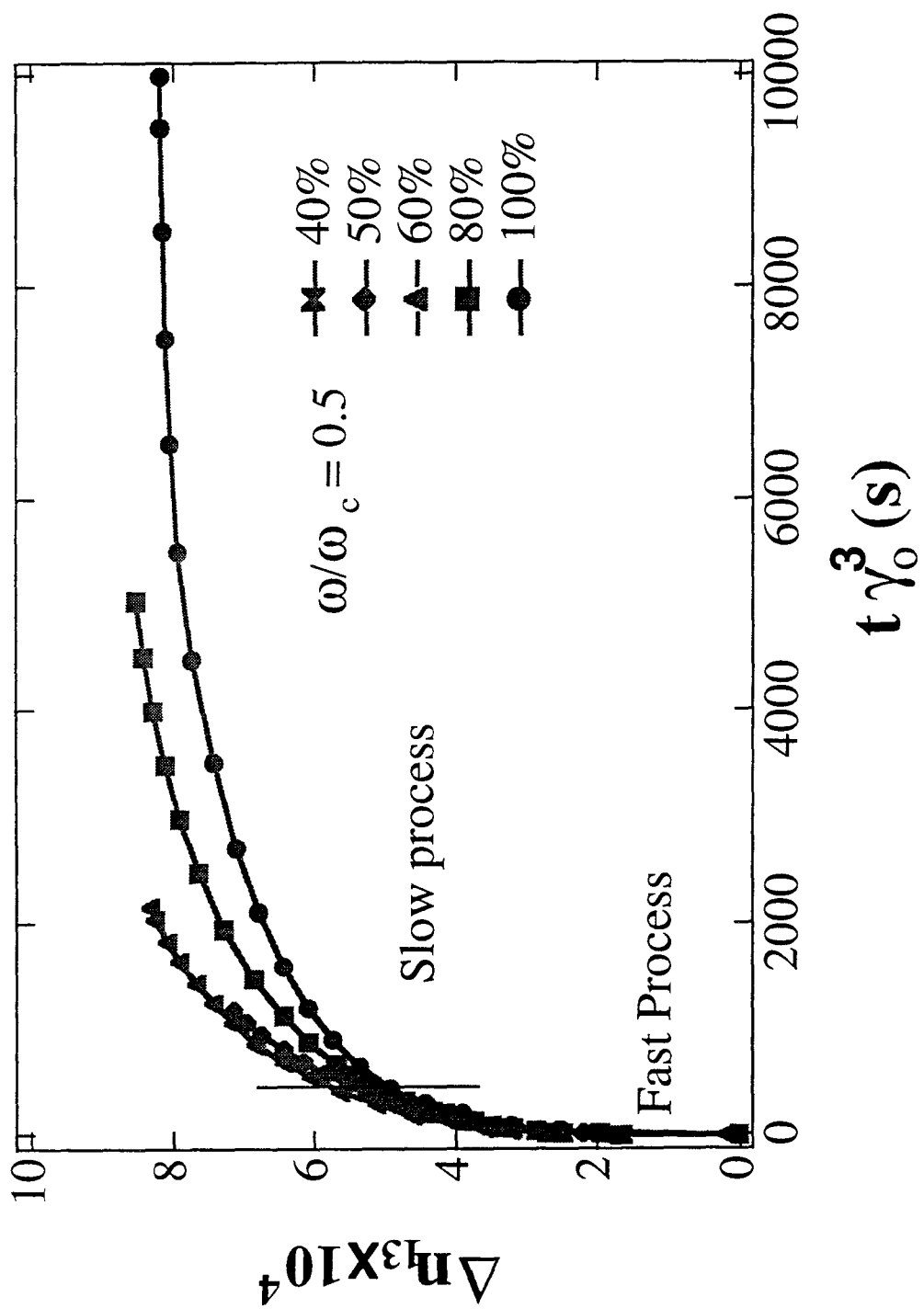
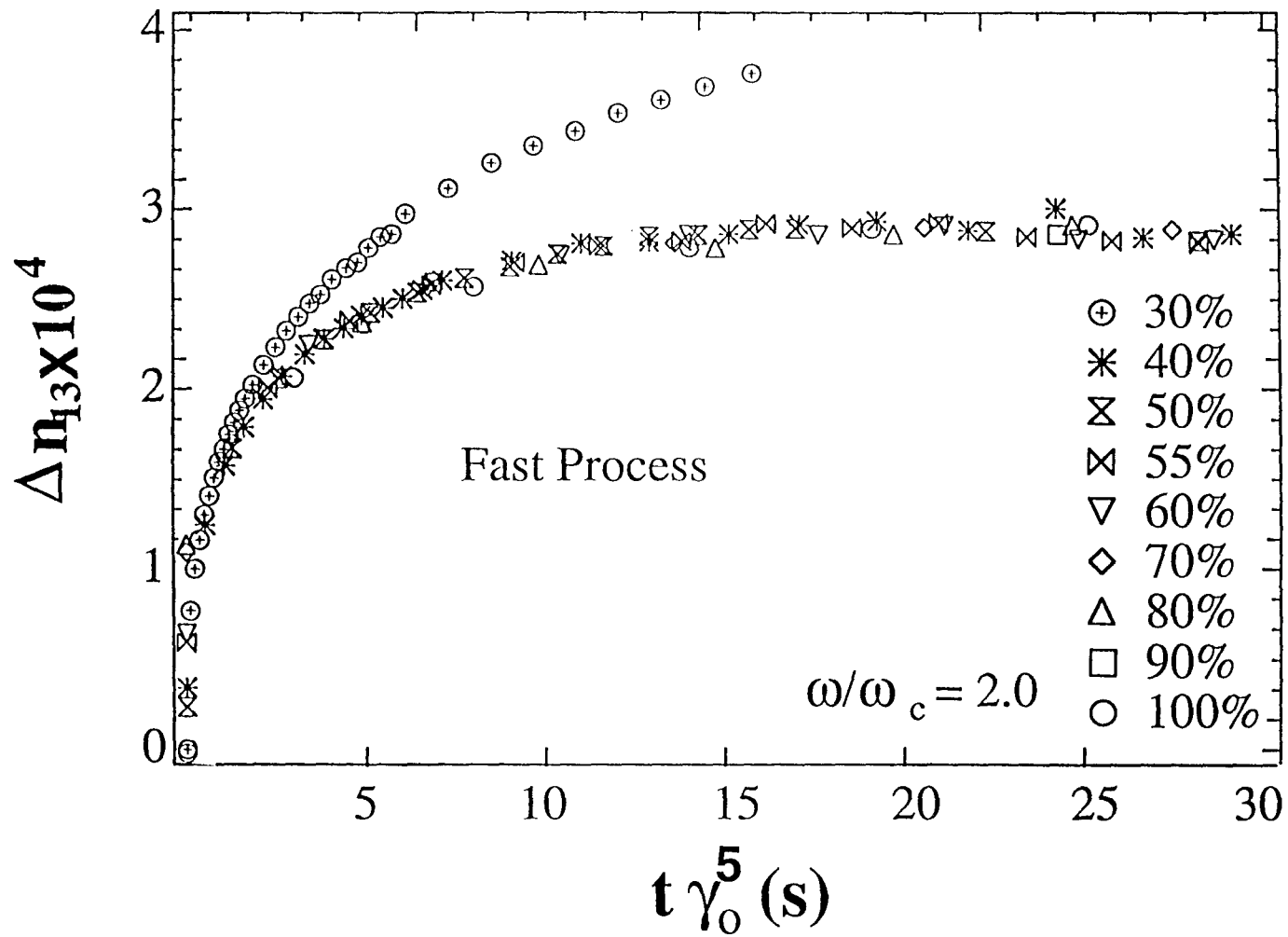


Fig.9b

Fig. 10a



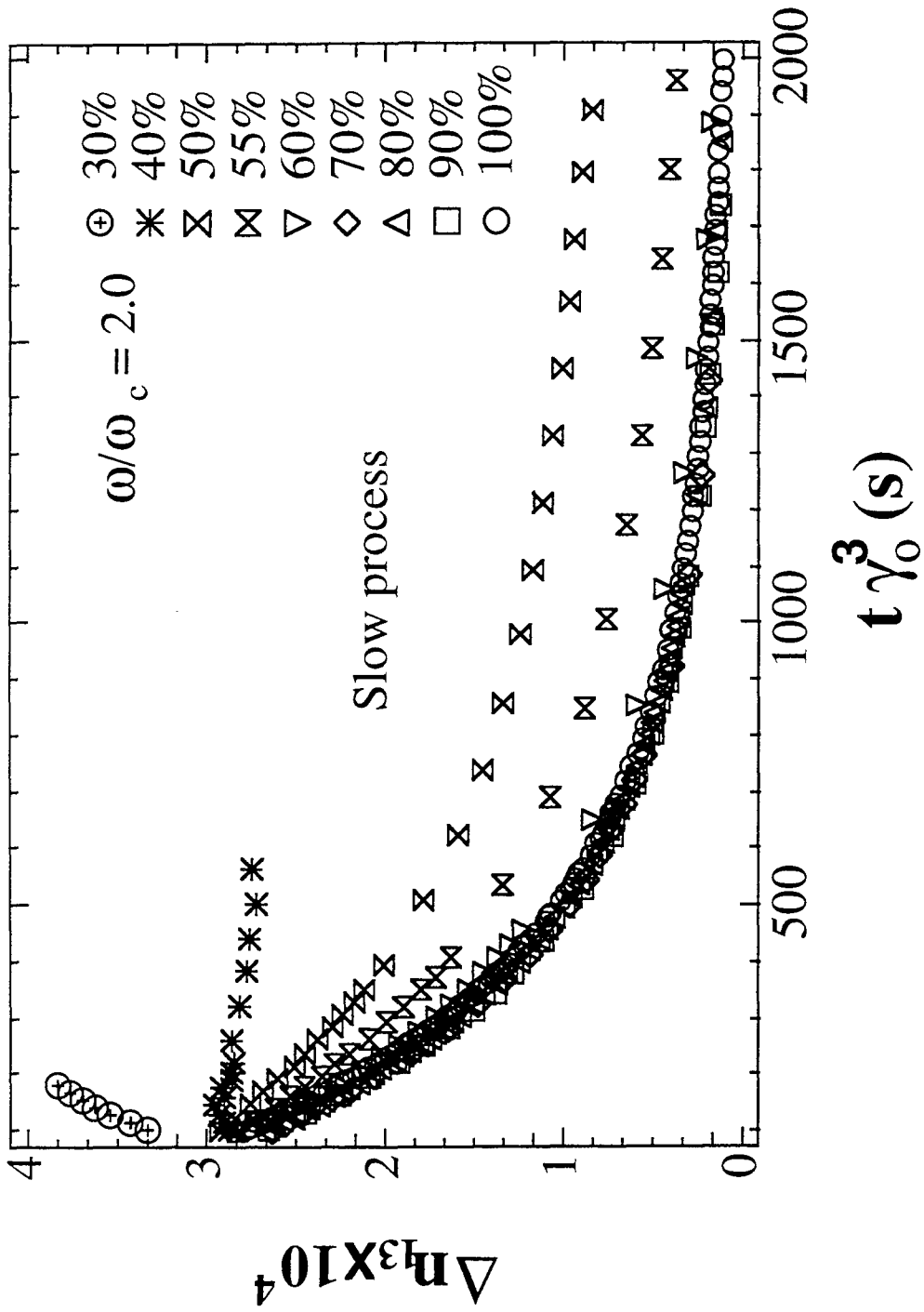


Fig.10b

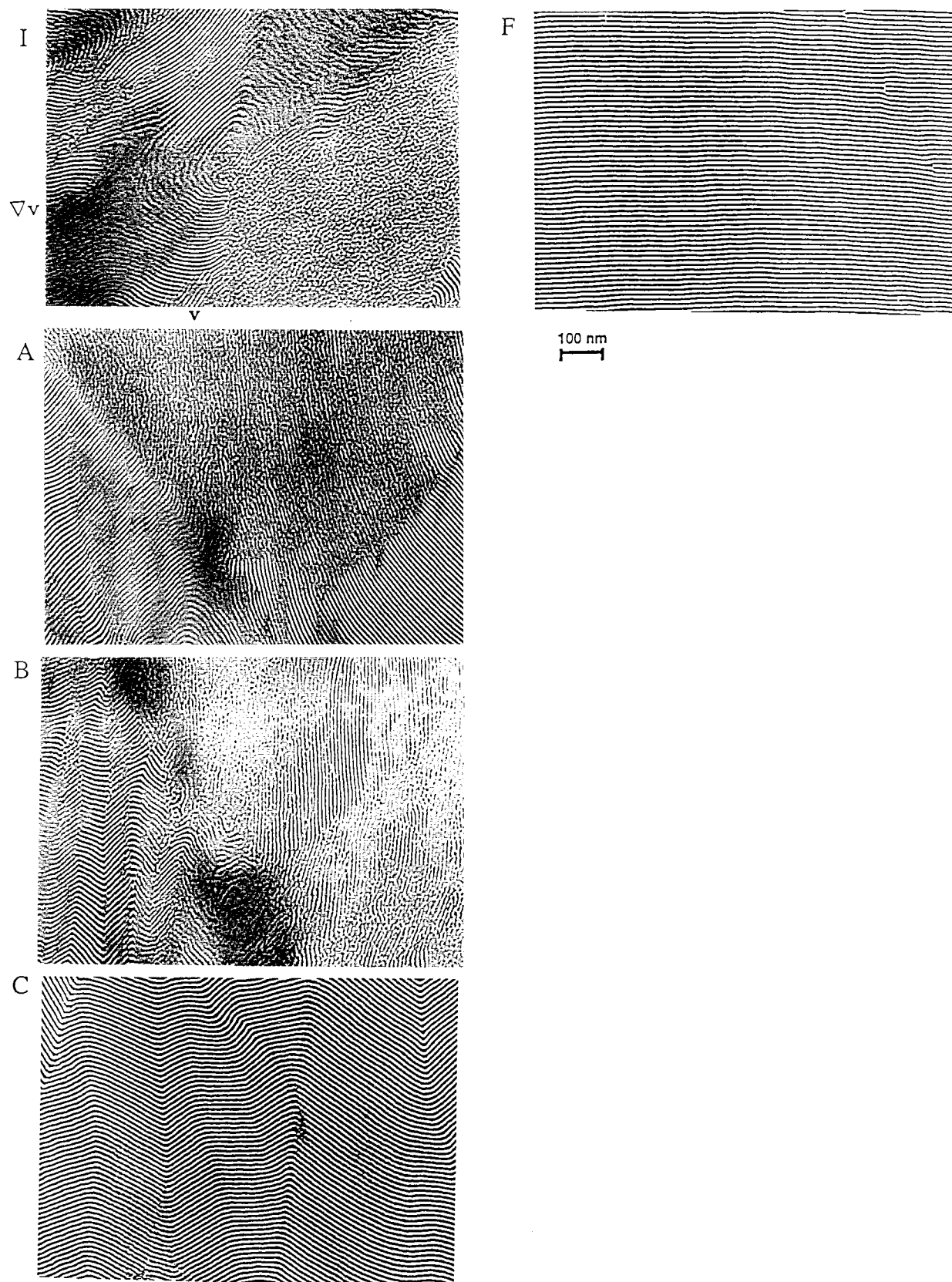


Fig.11

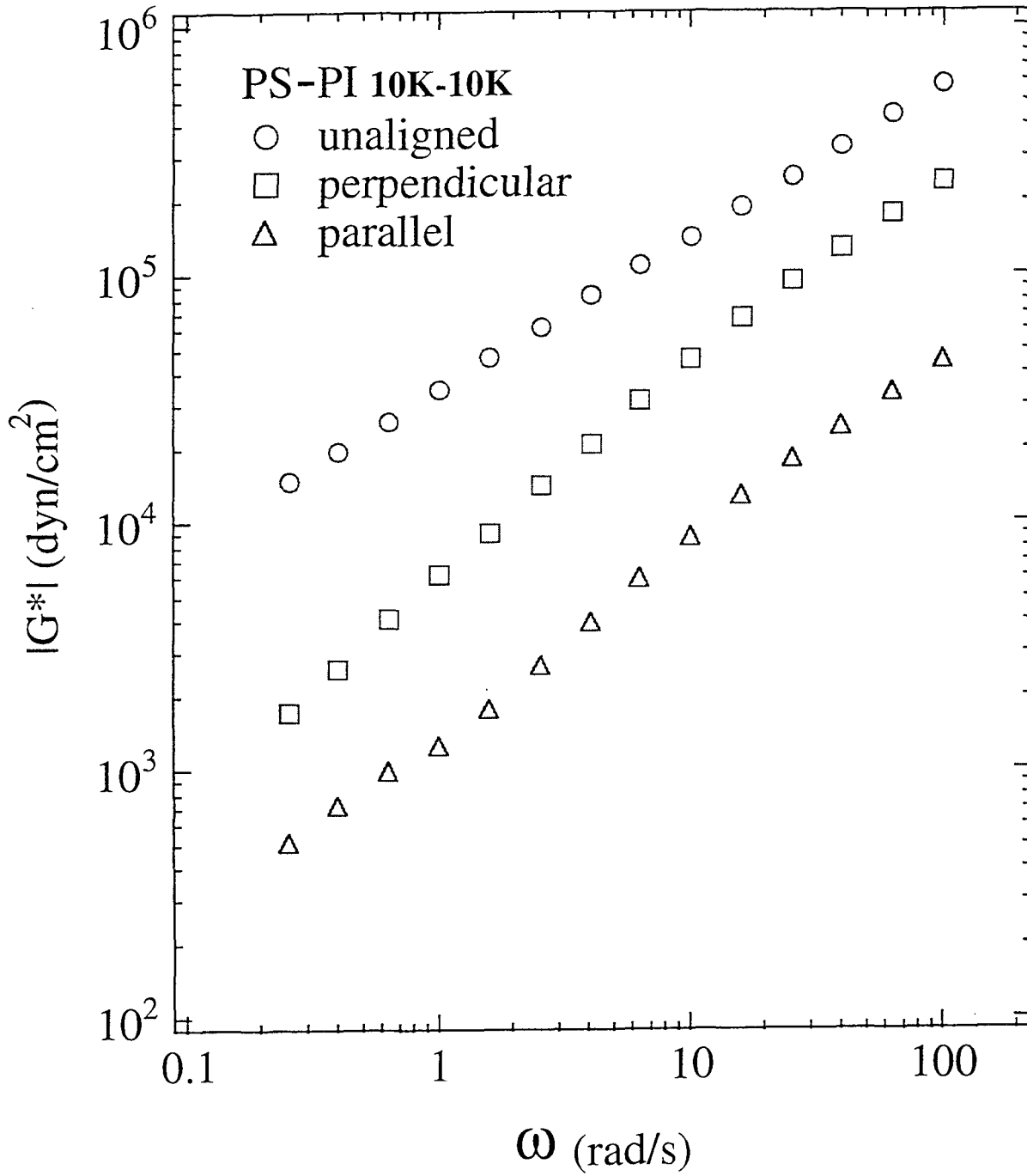
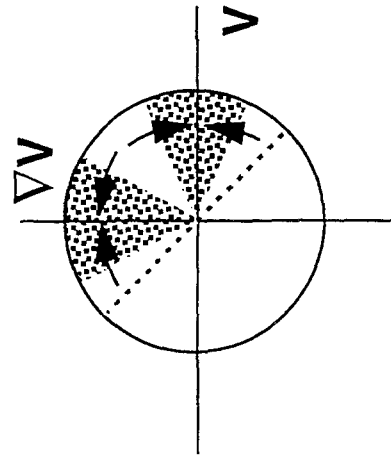
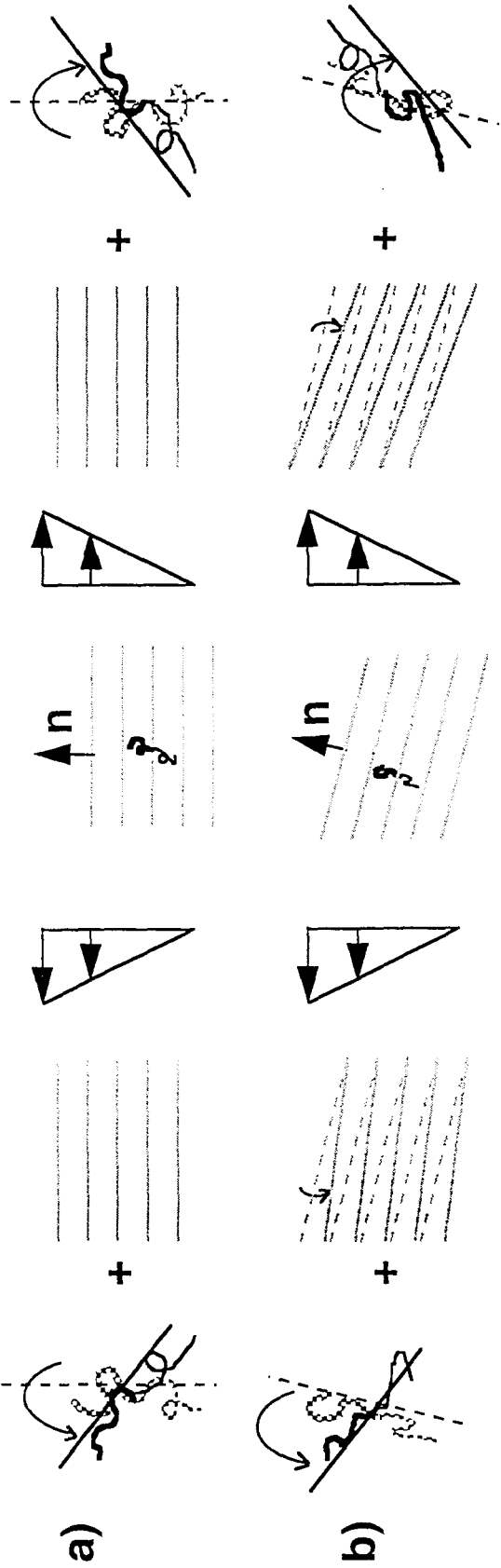


Fig.12



d)

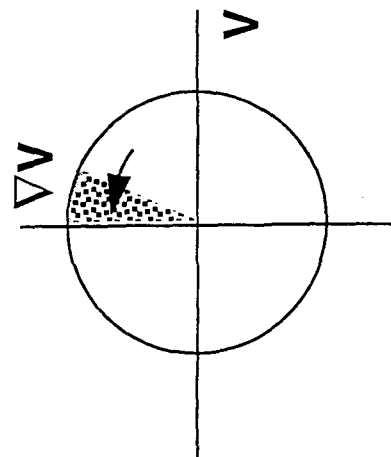


Fig.13

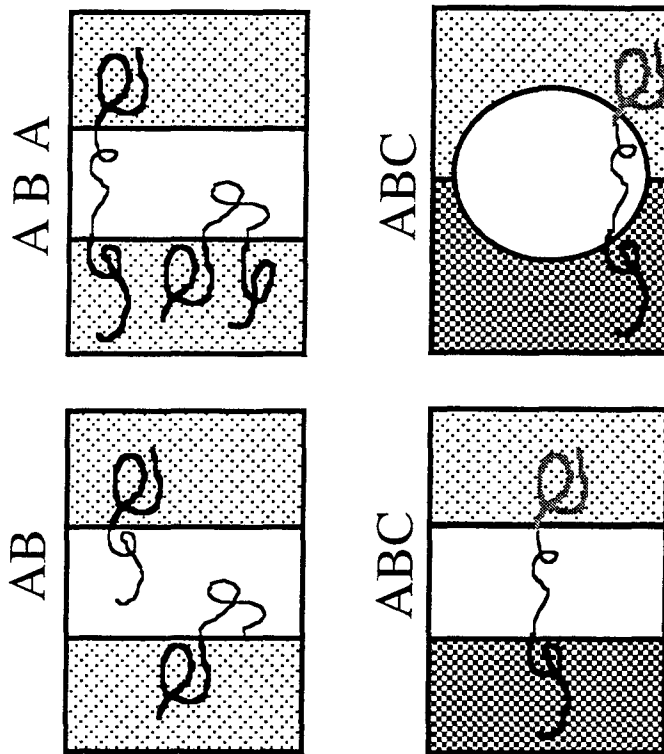


Fig.14

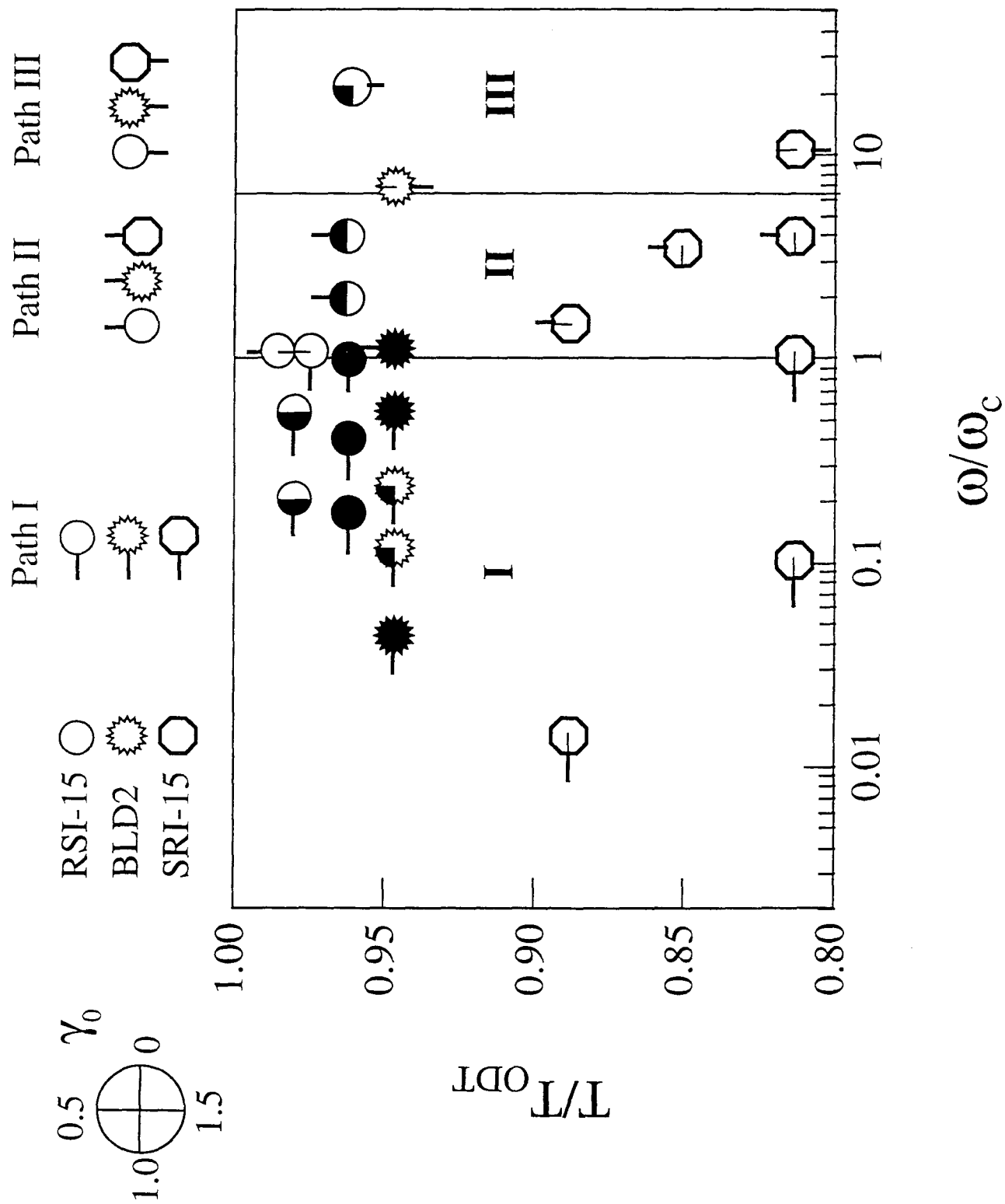
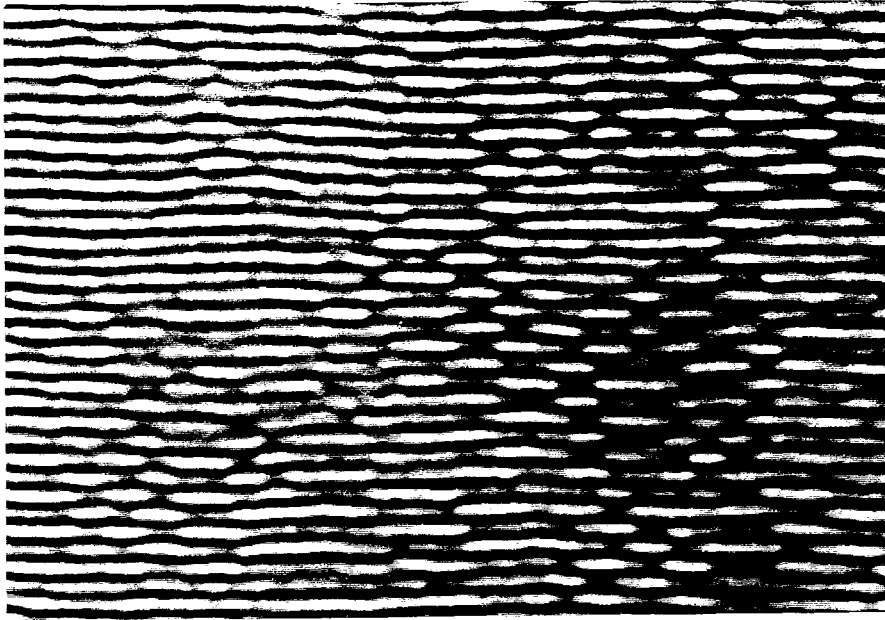
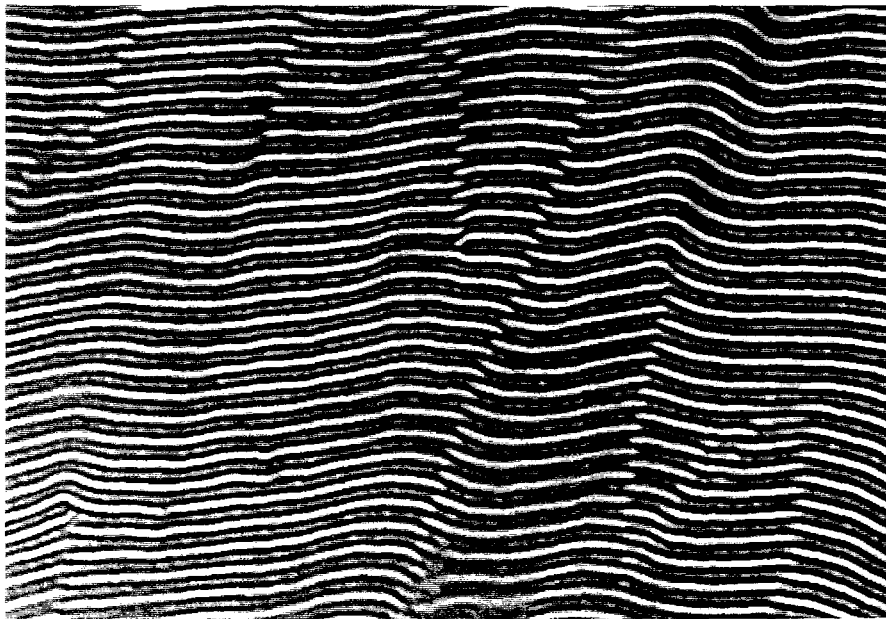


Fig.15



200nm



200nm



Fig.16

Chapter 2 PS-PI Diblock: Dynamics of Alignment and Structural Evolution

Abstract

In-situ rheo-optical methods are used to guide electron microscopy (TEM) and X-ray scattering (SAXS) studies of structure development during flow-induced alignment in a lamellar block copolymer melt (nearly symmetric polystyrene-polyisoprene diblock, $ODT \simeq 172^\circ\text{C}$). The progress of shear-induced alignment is recorded in real-time using flow birefringence; at selected points during alignment samples are taken for ex-situ characterization by TEM and SAXS along all three axes (\mathbf{v} , $\nabla\mathbf{v}$, $\nabla\times\mathbf{v}$) of the flow geometry. Three different trajectories are examined: perpendicular alignment and two qualitatively different routes to parallel alignment. At the highest frequencies, symmetry arguments explain the transient development of a bimodal texture en route to alignment of layers parallel to the planes of shear. At lower frequencies, larger scale relaxations introduce rearrangements out of the deformation plane that permit formation of lamellae perpendicular to the shear plane. These explain the change in character of the pathway to parallel alignment and the emergence of perpendicular alignment with decreasing frequency. For each trajectory in general, the initial ‘fast’ process enhances not only the projection of the orientation distribution that corresponds to the final state, but also increases other projections of the distribution; the late-stage ‘slow’ process eliminates these other projections and perfects a single alignment. For example, the highest frequency path to parallel alignment begins by transforming poorly organized regions into layers that are predominantly oriented along the parallel and transverse directions. The transition to the slow process is marked by the development of a characteristic texture in which tilt wall boundaries normal to the flow direction separate bands that form a repeating ‘chevron’ pattern (layers tilted up and down about the $\nabla\times\mathbf{v}$ axis). The coarsening of this pattern dominates the slow process during which the transverse projection is also eliminated.

1. Introduction

Self-assembly of block copolymers,¹⁻⁷ surfactants,⁸⁻¹¹ colloidal suspensions^{8,12} and proteins¹³ provides versatile means to create nanostructures with potential applications in biomaterials, optics and microelectronics. These materials form ordered structures on scales from a few to hundreds of nanometers. Monodisperse charged colloidal suspensions can assemble three-dimensional lattices.⁸ Surfactant systems form a variety of morphologies and can be used as precursors to prepare nanostructured solid materials.¹⁰ Similarly, block copolymers (BCPs) assemble a fascinating array of nanostructures. BCPs have the desirable feature that morphology can be systematically controlled by varying the number of blocks, their lengths and chemical compositions. For example, diblock copolymers can form cubic arrays of spheres, hexagonal arrays of cylinders, bicontinuous cubic phases or lamellae depending on the relative block lengths.¹ ABC triblock copolymers can assemble even more complex structures,¹⁴ such as helical strands surrounding cylinders embedded in a continuous matrix. Polymers also offer a level of control of dynamics that is desirable for scientific investigation and technological applications. Thus, block copolymers can clarify both the thermodynamics and dynamics of self-assembly phenomena that are analogous to those in a range of synthetic and biological systems, and provide routes to novel materials.

The dynamics of self-assembled nanostructures assume special importance in the context of producing functional macroscopic materials because self-assembly alone usually leads to polydomain structures. To achieve desired directional properties it is essential to control macroscale order. Active processing using applied fields can extend self-assembled order to macroscopic dimensions in BCP melts,^{1-5,15-41} colloidal suspensions¹² and surfactant systems.⁹ Flow has proven to be particularly efficient and versatile. In the case of block copolymers, flow-induced alignment was first discovered by Keller in an extruded BCP². Since then, other flow methods, including oscillatory and steady shear, and roll-casting⁴² have been applied to many kinds of self-assembled systems. We focus on oscillatory shear in this paper since it permits systematic investigation of the coupled effects of the rate and

amplitude of deformation in relation to the relaxation dynamics of the nanostructure. Since the discovery that large amplitude oscillatory shear at different frequencies could produce either “parallel” or “perpendicular” alignment (Figure 1),^{16,17} there has been particularly keen interest in the mechanism of selection of one orientation direction over the other. However, fundamental understanding of the mechanisms and dynamics of alignment remains elusive.

In situ, time-resolved experiments are revealing the richness of the structural evolution that can occur during flow-induced alignment of ordered block copolymers.^{17,23,26–28,34–37,39} For example, in situ x-ray scattering studies by Hashimoto and coworkers showed that shearing a lamellar block copolymer melt can produce bimodal orientation distributions with parallel and transverse populations.³⁹ And in situ neutron scattering measurements have shown that prolonged shearing can move lamellar block copolymer solutions through a predominantly perpendicular aligned state to a weakly ordered state with preferential parallel orientation.³⁷ These scattering studies have achieved a time resolution of a few minutes. Transient birefringence measurements provide an effective means to monitor faster alignment processes with a time resolution of a few milliseconds.^{23,26–28} The speed of these methods has proved useful in characterizing the rapid changes that occur in the early stages of the alignment process and for examining the effects of processing parameters on the rate and degree of alignment.

Three regimes of behavior in the present lamellar PS-PI have been distinguished based on their rheo-optical signatures (Fig. 2): the perpendicular regime previously identified in similar PS-PI diblocks and two distinct pathways to parallel alignment within the high frequency regime where parallel alignment had previously been observed. The body of in-situ results indicate a complex interplay of temperature, shearing frequency and strain amplitude in controlling the changes in the state of order and orientation during shearing. These have been summarized in a three-dimensional mapping of alignment behavior as a function of T/T_{ODT} , ω/ω'_c , and γ_o (Fig. 2)²⁸, where T_{ODT} is the order-disorder transition temperature, ω'_c is the frequency below which the ordered structure dominates the viscoelasticity of the

material (Figure 3), and γ_o is the strain amplitude of the sinusoidal shear.

Rheo-optical studies have shown that all three of these families of alignment trajectories start with a “fast” process (marked “F” in Fig. 2, top) that transforms the initial isotropic orientation distribution to an anisotropic distribution, followed by a later “slow” process (marked “S” in Fig. 2, top) that eliminates all but one orientation, either parallel or perpendicular.^{27,28} While these processes may be partially overlapping, they differ in time scale by over an order of magnitude, as well as showing pronounced differences in the strain-dependence of their respective rates.²⁸ The fast process of trajectories to perpendicular alignment and to parallel alignment at $\omega'_c < \omega < 10 \cdot \omega'_c$ produces an orientation distribution with a mix of perpendicular and parallel projections, but little transverse projection (positive Δn_{13} , Fig. 2, top, I and II). However, at very high shear frequencies, the nature of the fast process changes and produces an orientation distribution that consists of a mix of transverse and parallel projections (negative Δn_{13} , Fig. 2, top, III).

Now that distinct families of alignment pathways have been identified, the next step is to determine the nature of the fast and slow processes for each type of trajectory toward the goal of fundamentally understanding the effects of macromolecular design and processing parameters on the alignment behavior.

Ex-situ characterization methods have provided the majority of the structural information on flow induced alignment.^{2-4,16-21,24,25,33,38} Samples cooled and removed for characterization are amenable to TEM imaging and to SAXS or SANS studies in which the orientation distribution can be probed along each of the axes of the flow geometry. As a recent example, TEM imaging has revealed that samples with a bimodal parallel-transverse orientation distribution^{29-31,38,39} can contain a striking banded texture with large regions of the predominant parallel orientation punctuated by bands of transverse lamellae sandwiched between parallel tilt-wall boundaries.²⁹ Alternatively, this type of orientation distribution can correspond to islands of transverse orientation embedded in a matrix of parallel aligned material.³⁰ There is no in-situ method that can replace direct imaging of the nano- and microstructure. Ex-situ scattering along all three directions (\mathbf{v} , $\nabla\mathbf{v}$, $\nabla\times\mathbf{v}$) provided the

basis for the original identification of parallel and perpendicular alignment.¹⁶ More recently, this approach has clarified the evolution of structure during parallel alignment at very high frequencies (Type III)³¹, showing that the orientation distribution passes through a transient state characterized by a bimodal orientation distribution with coexisting parallel and transverse lamellae.

The detailed information gained by ex-situ characterization of texture (using TEM) and the orientation distribution (by SAXS or SANS) could provide insight into the nature of the distinct families of alignment trajectories, including their individual fast and slow processes. To establish the connection between structural changes and these individual processes, however, it is necessary to remove samples at known points in an overall alignment trajectory. To do so, one must have some in-situ probe of the progress of alignment in real time.

In this paper, we present such a detailed characterization of the evolution of microstructure during shear-induced alignment. We use in-situ birefringence measurements to identify selected points in the fast and slow processes and at the transition between them. Shearing is interrupted at the desired points and the inevitable relaxation of the structure upon cessation of flow is recorded before the samples are cooled and removed for ex-situ studies using TEM and SAXS. This approach is applied to each of the three families of alignment pathways for PS-PI described by Gupta et al.^{27,28} Following a brief description of the material and methods (Section 2), we present the structural changes that are observed by TEM and SAXS for the fast and slow processes in each of the three regimes (Section 3). Then we discuss the implications of these structural changes for the nature of alignment processes, examining existing concepts regarding alignment mechanisms and highlighting new insights that arise from the results.

2. Experimental Section

Materials: We used a nearly symmetric polystyrene-polyisoprene diblock copolymer with

$M_w \simeq 20$ kg/mol, and $\frac{M_w}{M_n} \leq 1.06$.⁴³ Rheological determination of the order-disorder transition temperature indicated $T_{ODT} \simeq 172^\circ\text{C}$.⁴⁴ The viscoelastic spectra for the present PS-PI material in the disordered state and the ordered, but unaligned state (Figure 3) are in accord with those reported in Gupta *et al.*²⁷ The frequency (ω'_c) associated with a crossover in the relaxation dynamics from being dominated by the macromolecular response to being dominated by the microstructural response is estimated to be $\omega'_c \approx 5$ rad/s at 120°C (corresponding to $\omega'_c \approx 2$ rad/s at 115°C). At shear frequencies above ω'_c parallel alignment is induced by prolonged sinusoidal shear of sufficiently large amplitude; at lower frequencies perpendicular alignment is induced.²⁷ The high frequency regime ($\omega > \omega'_c$) of parallel alignment consists of two regions in terms of the pathway that leads to the aligned state, as described above.

Optical-rheometry: Simultaneous, quantitative measurements of dynamic stress and birefringence were performed on a Rheometrics RSA II modified for rheo-optical measurements. Experimental details have been presented earlier.⁴⁵ Light propagating along the velocity gradient direction (axis 2) is used to probe the projection of the refractive index tensor in the plane formed by the flow direction (axis 1) and the vorticity axis (axis 3), *i.e.* $\Delta n_{13} = n_{11} - n_{33}$. For PS-PI diblocks, the birefringence is dominated by the form contribution resulting from the microphase-separated structure.⁴⁶⁻⁴⁸ Therefore, the evolution of the steady offset in $\Delta n_{13}^{(d)}(t)$ probes the orientation distribution of the lamellae (the 1,3-projection of the second moment tensor, as described in the Appendix of ref.²⁸).

Perpendicular alignment, with the lamellar normal ($\hat{\mathbf{u}}$) along the neutral direction ($\hat{\mathbf{u}} \parallel$ axis 3), corresponds to positive $\Delta n_{13}^{(d)}$ for PS-PI, since the form contribution has a higher index along the layers. For an orientation distribution biased along the transverse direction ($\hat{\mathbf{u}} \parallel$ axis 1) relative to the perpendicular direction, the 1,3-birefringence is negative. In the parallel orientation ($\hat{\mathbf{u}} \parallel$ axis 2), the lamellae are normal to the beam propagation direction (Figure 1), resulting in zero birefringence in the 1,3-plane for a perfectly aligned parallel state. While a final large, positive value of 1,3-birefringence

unambiguously reflects predominant perpendicular alignment, many states can give a final $\Delta n_{13}^{(d)}$ near zero. Therefore, final states with low $\Delta n_{13}^{(d)}$ have been interpreted in combination with the changes in the small strain dynamic moduli (G' , G'') and the SAXS patterns observed in samples removed at the end of the process^{27,28}; the resulting identification of parallel final states agreed with earlier structural studies using TEM and SAXS for a very similar polymer system¹⁸.

Shear-Induced Alignment and Preparation of Samples for Ex-Situ Characterization: Shear alignment experiments have been performed using prolonged, large amplitude oscillatory shear (LAOS). Here and in our previous studies^{27,28} the shearing is sinusoidal (rather than reciprocating). Before each alignment experiment, the sample is heated well into the disordered phase (180°C) and is allowed to equilibrate for 15-20 minutes to erase its previous thermal and deformation history. It is then cooled to the desired temperature in the ordered state and equilibrated for 15 minutes.⁴⁹ This procedure results in a reproducible initial condition, as confirmed by frequency sweep measurements using small-strains. To examine the structure present in this initial state, a sample was taken through the protocol above, then cooled to ambient temperature and removed from the cell without subjecting it to any shearing.

A temperature of 115°C was chosen for the present experiments; three frequencies were chosen that lie in each of the three alignment regimes shown in Fig. 2. The selected conditions are represented by the solid symbols in Fig. 2 and by the arrows on Fig. 3. The birefringence trajectories for each regime form a family of alignment transients as a function of strain: above a critical strain, a well-aligned state can be reached and the rate of the alignment process generally increases strongly with increasing strain amplitude (below the critical strain characteristic of a given temperature and frequency the system progresses to an anisotropic structure but then fails to evolve to a fully oriented one). The present experiments are conducted far enough from the boundaries between regimes that we can neglect the more complex effects of strain: at the boundary between the perpendicular and parallel regimes (I and II, Fig. 2), strain can flip the direction of alignment²⁶ and in

the boundary region between the two parallel alignment regimes II and III (Fig. 2), strain amplitude can change the character of the alignment trajectory from one to the other.²⁸

From each family of alignment trajectories we choose one for which the fast process is slow enough for us to reliably interrupt this process at a desired point. Along each of the three trajectories (one per regime), three points are chosen that represent roughly (A) the mid-point in the fast process, (B) the transition between the fast and slow processes and (C) mid-way through the slow process. We do not show the characterization of the final well-aligned state here since the SAXS results for each case have been published previously²⁸ and the TEM images are so uniform that they are essentially featureless over very large length scales in samples removed when the birefringence indicates the alignment process is complete. Ten samples were used for the TEM and SAXS measurements, representing the initial, unaligned state and points A, B, and C for three different trajectories (all at $T = 115^\circ\text{C}$: $\omega = 1, 4$ and 100 rad/s with $\gamma_o = 0.6, 0.7$ and 0.3 , respectively).

It is worth noting that the ex-situ experiments are subject to complications that are not present in our previous suite of rheo-optical experiments: variations in the samples⁴³ and in the temperature controller, uncertainties in the precise flow cell geometry, and possible distortion of the aligned structure during cooling and unloading. For the SAXS experiments performed with the beam along either the flow or vorticity directions, effects of cutting the sample could affect the results. Similarly, sample preparation can affect TEM results and are combined with the challenge of examining enough material to ensure that representative images are selected for interpretation. These complications are present in all studies that use ex-situ methods. A sample preparation guided by rheo-optical methods does assist in assessing the extent of structural relaxation after cessation of shearing and during cooling to ambient temperature. While the absence of a change in optical anisotropy does not rule out changes in structure, large changes in optical anisotropy give a valuable warning sign that structural changes must have occurred during relaxation and cooling. This information can influence how strongly we interpret the ex-situ results as representing the structure that actually existed during the flow-induced alignment process.

Substantial relaxation was observed when the fast process was interrupted (Figs. 5b, 9b and 14b); this suggests that the state of the harvested samples for point A of each trajectory have relaxed partially back toward an isotropic distribution and retain a lower degree of alignment than existed at the corresponding point during the alignment process. A more modest relaxation occurred when shearing was interrupted in the transition between the fast and slow processes (point B) and negligible relaxation was observed when the slow process was interrupted (e.g., point C). Beyond the three conditions used to prepare the samples for ex-situ characterization, we evaluated the magnitude of relaxation observed upon cessation of shearing for a wide range of shear frequency, strain amplitude and shearing time. At the early stages of the fast process (approximately half-way to point A), the 1,3-birefringence can relax to as little as half its magnitude just prior to cessation of shearing. The magnitude of the relaxation rapidly decreases as one moves through the fast process; the behavior shown for Points A and B in Figs. 5b, 9b and 14b are representative of the behavior found for many other alignment trajectories for each of the three families interrupted at times that were beyond the mid-point of the fast process. The relaxation processes typically take between 100 and 500 s.

The birefringence was also recorded during cooling from 115°C to room temperature; these changes were small compared to the relaxation upon cessation of shearing for point A of each trajectory. After cooling to room temperature, the samples were carefully removed from the shear sandwich tools and collected for TEM and SAXS measurements.

Small Angle X-ray Scattering: X-ray scattering patterns were collected using a Siemens Small Angle Scattering System that includes an Anton Paar HR-PHK high resolution pinhole optics system with a multiwire 2-D x-ray detector. The generator was a Rigaku RU-300 rotating anode operated at 40kV and 40 mA with a 0.2 mm x 2 mm filament set in the spot focus mode. The X-ray beam is collimated by a 100 μm diameter pinhole placed approximately 490mm from the focal spot. Another pinhole 300 μm in diameter is set 650mm from the focal spot. This second pinhole reduces the parasitic scattering from the first pinhole. The sample to detector distance is approximately 650mm. This arrangement

leads to an incident x-ray spot on the sample of a diameter about 0.2 mm. Samples are set on a micrometer holder that is adjusted to place the sample such that the incident beam strikes the sample completely. All samples were in the range of 0.6 to 0.8 mm in thickness. X-ray patterns were collected for either 10 or 30 minutes. The patterns were normalized for differences in thickness and collection time. Background scattering was negligible (less than 1% of the signal in the peaks). In fact, background scattering amounted to less than 1 or 2 counts per pixel per 30 minutes except very near the beam stop. Therefore, background corrections were ignored in these qualitative runs.

Transmission Electron Microscopy: For TEM, material is taken from the center of the sample. Typically a 1mm x 2mm piece is cut from the middle of the slab of material removed from the flow cell. The sample is cut into a shape such that the orientation of each of the axes of the flow (\mathbf{v} , $\nabla\mathbf{v}$, $\nabla\times\mathbf{v}$) is readily evident during specimen placement for microtoming. The sample is placed on the specimen carrier to achieve the desired orientation: for sections in the $(\mathbf{v}, \nabla\times\mathbf{v})$ - or (1,3)-plane, the sheet of material is glued down flat onto the mounting stub; for sections in $(\mathbf{v}, \nabla\mathbf{v})=(1,2)$ - or $(\nabla\mathbf{v}, \nabla\times\mathbf{v})=(2,3)$ -planes the sample is fastened to the stub edge-on using a sucrose solution. The chamber of the cryomicrotome (Reichert Ultra-cut S with Leica EM-FCS chamber) is held at a relatively low temperature of -160°C so that the structures in the material will remain rigid and so that relatively thin (30-35 nm) sections can be obtained. Our trimming protocol produces an asymmetric, trapezoidal face that allows us to keep track of the orientation of the sections relative to the previous shearing geometry. First, we cut $100\ \mu\text{m}$ into the sample to generate a clean face and avoid any surface artifacts. Then edges are cut on the right and left sides of the sample with a slight splay (5°) inward on each side; the parallel edges of the trapezoid are made by rotating the sample 90° and cutting straight edges ($\sim 250\ \mu\text{m}$) on each side. When the sample is rotated back, the long edge of the trapezoid is at the bottom and the shorter edge at the top. A Diatome diamond specimen trimmer is used for facing and trimming; a Micro Star Technologies 35° - angle diamond knife is used for sectioning. Sections are cut with 30-35 nm thickness, typically using a 0.05 mm/s cutting speed. Sections are placed on 300 mesh,

carbon coated grids. Samples are stained by exposing them to the vapor over OsO_4 crystals for 40 minutes. Images are recorded using a Phillips 420 (120 keV) microscope. During an imaging session, the orientation of the trapezoidal section relative to the alignment of the frame of the photograph is noted for each exposure. These notes are used to draw the orientation of the axes onto the images after prints are made. The cumulative uncertainty in recording the orientation of the images is less than $\pm 10^\circ$.

3. Results

Before describing the evolution of structure as alignment progresses, we first establish the initial condition that pertains to all three families of alignment trajectories. Then we describe the changes in microstructure and orientation distribution that occur along each of the three alignment trajectories in order of ascending frequency.

A. Initial Unaligned State

The unaligned sample was obtained by heating through the ODT to remove any effects of thermal history and prior deformation associated with molding and loading the sample, then cooling to the temperature used for all of the shear-induced alignment experiments, as described in the Experimental Section. It was imaged using sections taken in all three projections described above. No difference between the three directions was observed. The sample consists predominantly (roughly 70%) of poorly organized regions that have not formed well-defined layers (Figure 4).⁴⁹ These poorly organized areas may still be regarded as ordered in the sense that they show microphase segregation into styrene-rich and isoprene-rich domains on the same length scale that is observed in the well-organized regions. Layered domains also exist, and show a variety of defect structures, including some that are reminiscent of partially formed focal conics. Scattering results show that the initial structure is essentially isotropic. A slight anisotropy is evident in the scattering

pattern in the $(\nabla\mathbf{v},\mathbf{v})$ -plane. The orientation of this anisotropy does not coincide with any plausible surface-induced effect since it is at an oblique angle with respect to either parallel or perpendicular orientations (which could correspond to homogeneous or homeotropic surface alignment tendencies). Instead, we believe that this slight alignment could be induced during the procedure for removing the sample from the flow cell. In the interpretation of subsequent scattering patterns, we bear in mind that features of this magnitude could be artifacts caused simply by removing the sample from the flow cell.

B. Shear-induced alignment at $\omega < \omega'_c$: the path to perpendicular orientation

To monitor structure evolution during the perpendicular alignment process, shearing experiments were done at $\omega = 1$ rad/s and $T = 115^\circ\text{C}$ ($\omega \approx 0.5\omega'_c$, marked “ $\omega < \omega'_c$ ” in Figure 3). A series of alignment experiments using different strain amplitudes was performed to confirm that the behavior at this reduced frequency corresponds to that previously established for families of perpendicular alignment trajectories in this regime.²⁸ The behavior of the effective dynamic modulus during shearing and the buildup of the 1,3-birefringence are in accord with previous results.^{27,28} The effective storage modulus (G'_{eff}) shows a large drop upon the first cycle of LAOS, with the initial value of $G'_{eff}(1\text{rad/s}, \gamma_o)$ being approximately one fourth as large as the linear storage modulus of the unaligned material $G'_{unaligned}(1\text{rad/s})$; the effective storage modulus drops by roughly another factor of four during the alignment process (Figure 5a) The growth of the perpendicular projection of the orientation distribution is manifested in a monotonic increase in the 1,3-birefringence (Figure 5b). With increasing strain amplitude, the kinetics of alignment become more rapid; in particular, the time scale of the fast process decreases as γ_o^{-3} , as observed previously.²⁸ The largest birefringence we have ever observed for a perpendicular aligned PS-PI is $\Delta n_{max} \simeq 1 \times 10^{-328}$; in the time range reported here the highest value reached is roughly 85% of this value, suggesting a high, but imperfect degree of alignment.

For a trajectory that is representative of this whole family and affords a slow enough

initial rise in the 1,3-birefringence to allow us to capture a sample in the middle of the fast process, we choose a strain amplitude of $\gamma_o = 0.6$ (Figure 5c). The samples harvested for ex-situ characterization were prepared by shearing for 400, 1500 and 7000s at $\omega = 1$ rad/s and $\gamma_o = 0.6$, corresponding to 1,3-birefringence of 40%, 60% and 80% of the highest value we have ever observed. These three points lie (A) in the fast process, (B) in the transition region between the fast and slow processes, and (C) in the middle of the slow process of the perpendicular alignment trajectory. By recording the birefringence and effective modulus during shearing we confirmed that each of the three samples followed the same alignment dynamics as was established in the un-interrupted alignment experiment. Further, by recording the birefringence after cessation of shearing we gained information regarding potential differences in the structure of the static sample relative to the structure that existed in real-time during shearing (Figure 5b), as described in the Experimental section.

Point A along the Perpendicular Alignment Trajectory: At approximately the mid-point in the fast process the microstructure has a complex texture and an orientation distribution that is enriched in orientations that have their edges along the flow direction (Figure 6): parallel (indicated by the SAXS peaks in the $(\mathbf{v}, \nabla \mathbf{v})$ -plane), perpendicular (SAXS peaks in the $(\mathbf{v}, \nabla \times \mathbf{v})$ -plane) and all orientations in between (nearly uniform ring of SAXS intensity in the $(\nabla \mathbf{v}, \nabla \times \mathbf{v})$ -plane). In the TEM micrographs, the most noticeable change in microstructure with respect to the initial state is the increase in the proportion of material that is organized into layers. Images taken in the $(\mathbf{v}, \nabla \mathbf{v})$ -plane accord with an orientation distribution richer in parallel than transverse projections as indicated by the corresponding SAXS pattern; similarly, images in the $(\mathbf{v}, \nabla \times \mathbf{v})$ -plane show a stronger projection of perpendicular than transverse layers, in agreement with both the SAXS and 1,3-birefringence results.

Point B along the Perpendicular Alignment Trajectory: At approximately the transition between the fast and slow processes, the orientation distribution shows a distinct enhancement of the perpendicular projection, as indicated by the increased intensity of the peaks in the SAXS pattern in the $(\nabla \mathbf{v}, \nabla \times \mathbf{v})$ -plane (Figure 7). However, it is worth noting

that the parallel projection is still present (the intensity of the peaks in the $(\mathbf{v}, \nabla \mathbf{v})$ -plane and of the ring of intensity in the $(\nabla \mathbf{v}, \nabla \times \mathbf{v})$ -plane are similar at points B and A; they appear smaller in Figure 7 because the vertical scale has more than doubled). This type of scattering pattern has been reported in a similar system and interpreted a final well-aligned state¹⁹. The TEM images also show the growth of the perpendicular population: in the $(\mathbf{v}, \nabla \mathbf{v})$ -plane regions with layers lying in that plane have developed, appearing uniform grey in the TEM image; in both the $(\nabla \mathbf{v}, \nabla \times \mathbf{v})$ - and $(\mathbf{v}, \nabla \times \mathbf{v})$ -planes there are many domains with layers perpendicular to $\nabla \times \mathbf{v}$. Domain size has increased, especially along the velocity direction. Nevertheless, the texture is still riddled with defects and continues to contain some poorly organized regions (Figure 7).

Point C along the Perpendicular Alignment Trajectory: As the system evolves to the mid-point in the slow process, the perpendicular population continues to increase (stronger SAXS peak in Figure 8 than Figure 7) as indicated by the increase in 1,3-birefringence. The other projections that were enhanced during the fast process persist (peaks in the $(\mathbf{v}, \nabla \mathbf{v})$ -plane and of the ring of intensity in the $(\nabla \mathbf{v}, \nabla \times \mathbf{v})$ -plane have only slightly decayed relative to points B and A; they appear smaller because the peak intensity has doubled since point B). These projections are eliminated as the slow process reaches completion, indicated by their absence in the SAXS patterns of a perpendicular sample taken at the conclusion of the slow process²⁸. The TEM results show that by the mid-point in the slow process virtually all of the material is organized into layers. The images in the $(\mathbf{v}, \nabla \times \mathbf{v})$ -plane show a very high degree of alignment, in accord with the absence of a ring in the SAXS pattern for this projection. On the other hand, images in the $(\nabla \mathbf{v}, \nabla \times \mathbf{v})$ -plane accord with a predominant alignment along the perpendicular orientation, but one that still contains many defects. The misalignments evident in TEM images in this plane accord with the presence of the ring of intensity in the corresponding SAXS pattern. The defects have a distinctive appearance dominated by undulations in orientation, rather than sharp kinks. The fact that these defects are seen in the $(\nabla \mathbf{v}, \nabla \times \mathbf{v})$ -plane, but not in the $(\mathbf{v}, \nabla \times \mathbf{v})$ -plane indicate that they are anisotropic, with preferential alignment along the flow direction.

C. Shear-induced alignment at $\omega'_c < \omega < 10 \cdot \omega'_c$: one route to parallel orientation

Previous studies of lamellar PS-PI have shown that prolonged LAOS at frequencies above ω'_c induces parallel alignment.^{18,19,24,27,28} Rheo-optical studies revealed that this high frequency regime is actually composed of two regimes in terms of the *pathway* leading to the parallel alignment.^{27,28} In this section we deal with the trajectories that pass through transient states with a higher population of the perpendicular rather than transverse orientation (suggesting transient distributions with strong parallel and perpendicular projections) that occur at frequencies above, but fairly close to ω'_c . The following section describes structure evolution along the trajectories to parallel alignment that pass through transient states with greater populations of transverse than perpendicular projections (suggesting transient states with strong parallel and transverse components) that occur at frequencies far above ω'_c .

Parallel alignment above but close to ω'_c was performed at $\omega = 4$ rad/s and $T = 115^\circ\text{C}$ ($\omega \approx 2\omega'_c$, marked " $\omega > \omega'_c$ " in Figure 3). A series of experiments using different strain amplitudes was done to confirm that the behavior at this reduced frequency corresponds to the established family of parallel alignment trajectories in this regime.²⁸ The effective storage modulus (G'_{eff}) shows a modest drop immediately upon inception of LAOS, with the initial value of $G'_{eff}(4\text{rad/s}, \gamma_o)$ being approximately half the linear storage modulus of the unaligned material $G'_{unaligned}(4\text{rad/s})$; the effective storage modulus drops as much as an order of magnitude during the alignment process (Figure 9a). The time-trace of the 1,3-birefringence indicates that in the early stages of the process a perpendicular projection grows stronger than the transverse projection of the orientation distribution, giving rise to a large positive birefringence (Figure 9b). The late stage of the process brings the 1,3-birefringence back to zero, which has previously been shown by SAXS to correspond to a final state that is well-aligned parallel.²⁸ Increasing strain amplitude speeds the kinetics of alignment, as observed previously.

As a representative trajectory from this family, we choose a strain amplitude of $\gamma_o = 0.7$ (Figure 9b). The samples harvested for ex-situ characterization were prepared by shearing

for 22, 393 and 3121s at $\omega = 4$ rad/s and $\gamma_o = 0.7$, corresponding to (A) the middle of the fast process, (B) the transition region between the fast and slow processes, and (C) the middle of the slow process (Figure 9c). The birefringence and effective modulus observed during shearing confirmed that each of the three samples followed the same alignment dynamics as in an un-interrupted alignment experiment. The birefringence recorded after cessation of shearing was again used to monitor relaxation as described in the Experimental section.

Point A along the Parallel Alignment Trajectory above but near ω'_c : Moving from the initial condition to the mid-point of the fast process, there is an enhancement of the parallel projection (SAXS peaks in the $(\mathbf{v}, \nabla \mathbf{v})$ - and $(\nabla \mathbf{v}, \nabla \times \mathbf{v})$ -planes, Figure 10). The parallel layers coexist with projections of transverse (ring in $(\mathbf{v}, \nabla \mathbf{v})$ -plane SAXS) and perpendicular (ring in $(\nabla \mathbf{v}, \nabla \times \mathbf{v})$ -plane SAXS), but the perpendicular projection is the stronger of these (peaks in the $(\mathbf{v}, \nabla \times \mathbf{v})$ -plane SAXS) as indicated by the sign of the 1,3-birefringence. Electron micrographs show that large regions remain poorly organized, although these have diminished relative to the initial condition. Examination of many images shows no clear preferred orientation.

Point B along the Parallel Alignment Trajectory above but near ω'_c : The parallel projection grows strongly and the transverse projection is eliminated as the system proceeds to the transition from the fast to slow processes (compare SAXS patterns in Figure 11 to Figure 10 to see the growth of the peaks and decay of the ring of intensity in the $(\nabla \mathbf{v}, \mathbf{v})$ -plane, and the disappearance of the ring of intensity in the $(\mathbf{v}, \nabla \times \mathbf{v})$ -plane). At the same time, the perpendicular projection has also grown stronger, giving the hint of a second set of peaks in the $(\nabla \mathbf{v}, \nabla \times \mathbf{v})$ -plane and the growth of the peaks in the $(\mathbf{v}, \nabla \times \mathbf{v})$ -plane. The increase in the perpendicular projection and the elimination of the transverse projection give rise to the increase in the 1,3-birefringence moving from point A to point B (Figure 9b). The texture revealed by TEM shows a distinct reduction in the fraction of material that is poorly organized. Many parallel aligned domains are observed in the images in the $(\nabla \mathbf{v}, \mathbf{v})$ -plane. Electron micrographs in the $(\nabla \mathbf{v}, \nabla \times \mathbf{v})$ -plane show a complex mix of parallel, perpendicular and orientations between these two. Most of the field in the

$(\mathbf{v}, \nabla \times \mathbf{v})$ -plane appears featureless, indicative of parallel aligned regions; the regions that show lamellae edge-on tend to be close to the perpendicular alignment. All of these features of the TEM images accord well with the corresponding SAXS patterns.

Point C along the Parallel Alignment Trajectory above but near ω'_c : By the time the mid-point in the slow process is reached a strong parallel alignment has developed. From point B to point C, the alignment of domains that were nearly parallel has significantly improved, leading to a ten-fold increase in the intensity of the peaks in the SAXS patterns in the $(\nabla \mathbf{v}, \mathbf{v})$ - and $(\nabla \mathbf{v}, \nabla \times \mathbf{v})$ -planes (Figure 12). On this scale, the slight projection of perpendicular layers that remains is imperceptible (negligible SAXS intensity in the $(\mathbf{v}, \nabla \times \mathbf{v})$ -plane), in accord with the relatively small 1,3-birefringence that is left at point C. TEM images show parallel lamellae that are slightly undulating (see $(\nabla \mathbf{v}, \mathbf{v})$ - and $(\nabla \mathbf{v}, \nabla \times \mathbf{v})$ -images). Parallel lamellae are also indicated by the observation that over most of the sample the $(\mathbf{v}, \nabla \times \mathbf{v})$ -sections are so featureless that it is difficult to focus the electron microscope; the image shown is not representative of the whole sample, since pictures were taken where features were available to use to focus the image.

Note that we do not regard the structure at the mid-point of the slow process as “well-aligned”, a term we reserve for parallel states that have negligible 1,3-birefringence. The late stage of the shear alignment process eliminates the undulations from the lamellae, as manifested in sharper peaks in the SAXS patterns published earlier²⁸ and in the TEM micrographs of well-aligned parallel samples (Figure 13).

The early stages of this alignment trajectory may be related to the early stages of the flow process that leads to an initial enhancement of the perpendicular projection in reciprocating shear of a lamellar block copolymer solution³⁷. The TEM image in the $(\nabla \mathbf{v}, \nabla \times \mathbf{v})$ -plane of Figure 11 fits the description of undulations inferred from in-situ SANS results on a lamellar block copolymer solution³⁷ (although the undulations are not sharp enough to produce the previously reported splitting of the scattering peaks corresponding to the perpendicular population). However, the results of Wang et al. gave evidence of shear-induced disordering with time; whereas the present results suggest that the material remains ordered and

becomes better and better organized into lamellae and progressively aligned in the parallel direction (Figures 10-12). Here we must be careful in comparing in-situ and ex-situ results due to the uncertainties inherent in ex-situ studies: substantial changes can occur between the cessation of shearing and the time a sample is removed for characterization. Fortunately, previous studies have shown that pronounced structural changes tend to require long times. For example, recovery of order after shear-induced disorder in solvated lamellae took over 40 minutes, even when the process was sped by annealing at an elevated temperature relative to the shearing temperature.³⁷ And elimination of transverse bands in a primarily parallel biaxial texture of a lamellar diblock copolymer melt began on a timescale of 2 hours at a temperature approximately 50°C above T_g and was not complete after 168 hours.²⁹ The present samples were cooled through the glass transition after observing relaxations that occurred in the first few minutes after cessation of shearing, as described in the Experimental section; this time scale is short compared to that required for the reorganizations reported previously during annealing after cessation of flow. Thus, the progressive improvement in lamellar order and alignment shown in these TEM images and SAXS patterns is probably a good reflection of the structural evolution in situ. This supports an interpretation of the type (II) birefringence trajectories in terms of progressive parallel alignment,^{27,28} rather than progressive disordering.³⁷

D. Shear-induced alignment at $\omega'_c \ll \omega$: another route to parallel orientation

The last family of trajectories we examine is the pathway to parallel alignment at frequencies far above ω'_c .^{27,28} In this frequency regime, the orientation distribution evolves through transient states with stronger transverse than perpendicular projections on the way to parallel alignment. It has previously been inferred that the close correspondence between the time and strain dependence of the type (III) birefringence trajectories reported by Gupta et al.^{27,28} and the series of “four-spot” SAXS patterns reported by Zhang and Wiesner³¹ in this same frequency regime might indicate that an orientation distribution

with distinct transverse and parallel populations gives rise to the negative 1,3-birefringence that is observed in this family of alignment trajectories.²⁸

Parallel alignment at high shearing frequency ($\omega'_c \ll \omega$) was performed at $\omega = 100$ rad/s and $T = 115^\circ\text{C}$ (corresponding to $\omega \approx 50\omega'_c$ shown by the arrow marked “ $\omega \gg \omega'_c$ ” in Figure 3). The mechanical and optical signatures of these trajectories show that they do belong to the high-frequency parallel alignment family reported previously by Gupta et al.²⁸ The initial drop in the effective storage modulus (G'_{eff}) upon inception of LAOS is relatively small compared to results at lower frequencies, with the initial value of $G'_{eff}(100\text{rad/s}, \gamma_o)$ being approximately 75% of the linear storage modulus of the unaligned material $G'_{unaligned}(100\text{rad/s})$. The effective storage modulus drops as much as an order of magnitude during the alignment process, like the behavior for parallel alignment close to ω'_c (Figure 14a). It is interesting to note that the stress-strain behavior during the two distinct parallel alignment processes are similar in spite of the dramatic differences between the two transient orientation distributions.²⁸ The 1,3-birefringence indicates that in the early stages of the process a *transverse* projection grows stronger than the perpendicular one, giving rise to a large *negative* birefringence (Figure 14b). The late stage of the process brings the 1,3-birefringence back to zero, which has previously been shown by SAXS to correspond to a final state that is well-aligned parallel.²⁸ The rate of the alignment process increases with strain amplitude, as observed previously.

The highest strain amplitude used in this series ($\gamma_o = 0.7$) is dictated by the onset of very subtle melt fracture. We find that at modestly higher strains ($\gamma_o \geq 0.8$) the time dependence of the effective modulus changes: it undergoes an initial drop and flattening out, but then enters a period in which the modulus gradually declines and does not plateau even after hours of shearing. At the same time the transmittance of the sample gradually declines. This behavior has proven to be an indicator that fissures will eventually develop in the sample, even though this macroscopic manifestation of melt fracture only occurs at much later times (many hours after the onset of the gradual decline of G_{eff}). If shearing is stopped prior to the formation of fissures, the linear modulus gradually increases with time.

We believe that the effective modulus during shear and gradual recovery of G' after shearing reported by Pinheiro et al. may indicate the presence of this subtle form of incipient melt fracture³⁸.

As a representative trajectory from this family that has a slow enough initial rise to allow us to capture a sample in the middle of the fast process, we use $\gamma_o = 0.3$ (Figure 14c). The samples harvested for ex-situ characterization were prepared by shearing for 137, 900 and 4900 s at $\omega = 100$ rad/s and $\gamma_o = 0.3$; as before, these points are selected because they lie in (A) the middle of the fast process, (B) the transition between the fast and slow processes, and (C) the middle of the slow process (Figure 14b). As previously, the birefringence and effective modulus recorded during the alignment process confirmed that each each of the three samples followed the same dynamics as in an un-interrupted experiment. The birefringence observed during the relaxation after cessation of shearing (see Experimental section) again indicated that appreciable relaxation only occurs when the fast process is interrupted. As in the preceding two cases, the birefringence recorded during cooling to room temperature did not indicate significant changes. After cooling to room temperature, the samples were collected for TEM and SAXS measurements.

Point A along the Parallel Alignment Trajectory far above ω'_c : Between the initial condition and the mid-point in the fast process a bimodal orientation distribution develops (Figure 15): a strong parallel component (indicated by the SAXS peaks in both the $(\nabla\mathbf{v},\mathbf{v})$ - and $(\nabla\mathbf{v},\nabla\times\mathbf{v})$ -planes) and a *transverse* component (SAXS peaks in both the $(\nabla\mathbf{v},\mathbf{v})$ - and $(\mathbf{v},\nabla\times\mathbf{v})$ -planes). The texture in the sample is quite complex, but it clearly shows a dramatic reduction in the amount of material that is in a poorly organized state (TEM images, Figure 15). In many domains the layers show good continuity, but in others the layers are discernible, but perforated by many local defects on the scale of one or a few lamellae.

Point B along the Parallel Alignment Trajectory far above ω'_c : Moving forward to the transition from the fast to the slow process, there is a dramatic growth in the parallel population and a slight increase in the transverse projection (see the intensities

of the corresponding SAXS peaks in Figure 16 compared to Figure 15). The increase in the transverse component is in accord with the increasingly negative 1,3-birefringence developed between points A and B (Figure 14b). The microstructure in the sample shows extended domains in which the mean orientation is parallel, but the layers are tilted up and down in the velocity direction making a ‘chevron’ pattern when viewed down the vorticity axis (an example is shown in the left side of the TEM image in the $(\nabla\mathbf{v},\mathbf{v})$ -plane). This defect pattern is not seen in TEM images taken in the other two projections. Thus, the tilt-walls are preferentially aligned normal to the flow direction. Electron micrographs show a distribution of tilt angles across the boundaries, in accord with seeing arcs of intensity in the $(\nabla\mathbf{v},\mathbf{v})$ -plane SAXS pattern along the $\nabla\mathbf{v}$ -direction. In addition, there are domains in which the orientation is close to transverse (e.g., right side of the $(\nabla\mathbf{v},\mathbf{v})$ -image and the left side of the $(\mathbf{v},\nabla\times\mathbf{v})$ -image).

At Point B, the 1,3-birefringence indicates that the transverse population is at its maximum. In a sense, this represents the strongest bimodal character (parallel-transverse) that the system ever passes through on its way to parallel alignment. However, the texture at this point does not correspond to the ‘kink band’ texture (sharp tilt boundaries between parallel regions and transverse bands) that is observed in the analogous bimodal distribution in a much higher molecular weight lamellar diblock (PS-PEP 40k-70k g/mol)²⁹. Instead there are transverse domains coexisting with poorly organized regions and with overall parallel regions containing ‘chevron’ bands. This is reminiscent of the texture of transverse islands in a matrix of parallel material reported by Hudson for a lamellar diblock sheared in this regime ($\omega \gg \omega'_c$)³⁰.

Point C along the Parallel Alignment Trajectory far above ω'_c : During the first part of the slow process, the transverse projection is distinctly reduced, while the parallel projection is strongly enriched (Figure 17). The drop in the transverse component correlates with the reduced magnitude of the negative 1,3-birefringence at point C relative to B (Figure 14b). TEM images show that essentially all of the material is now well organized into layers. The characteristic ‘chevron’ pattern of defects dominates the images in the

$(\nabla\mathbf{v},\mathbf{v})$ -plane, but with a length scale that is dramatically longer than was evident at point B along this trajectory. The images in the $(\nabla\mathbf{v},\nabla\times\mathbf{v})$ - and $(\mathbf{v},\nabla\times\mathbf{v})$ -planes accord with predominant parallel alignment.

Note that this state of alignment corresponds roughly to the mid-point in the slow process; we do not regard it as a well-aligned state. Samples taken after the 1,3-birefringence has returned to zero show much narrower SAXS peaks²⁸ and no longer show tilt boundaries in TEM images (a representative image is shown in Figure 13).

Comparing the degree of alignment at roughly the middle of the slow process (point C) for each of the three trajectories, it is clear that the uniformity of orientation increases as one moves to higher frequency regimes. This qualitative trend agrees with previous descriptions of final states of alignment in PEP-PEE¹⁶ and PS-PI^{18,19} lamellar melts.

4. Discussion

In the intense effort to understand the physics of flow-induced alignment of lamellar block copolymers, progress toward the goal of determining the mechanisms of alignment has been limited. Dating back to the early work of Keller and Hadziioannou, the concepts of grain rotation, anisotropic viscoelasticity, selective melting and defect migration have been considered^{3,4,18}. Since the discovery of perpendicular alignment, the selective melting hypothesis has taken on a special role in explaining the development of perpendicular alignment under conditions close to the ODT.¹⁶ The idea that the system moves into a configuration that minimizes its modulus has been advocated as the means of selecting one orientation over another^{3,24}. It has also be acknowledged that two or more mechanisms may act in combination to produce alignment.^{4,18} However, direct evidence of these mechanisms and their relative importance in flow-induced alignment has been lacking. Consequently, there is insufficient fundamental basis for predicting the direction, degree and dynamics of the alignment process.

Recent rheo-optical results have provided powerful evidence that during the course of

shearing there is a transition in the character of alignment, as though one process overtakes another in importance.²⁸ Three alignment regimes were established for PS-PI cooled from $T > T_{ODT}$ directly to the temperature at which shear-induced alignment is performed (Fig. 2): (I) perpendicular alignment ($\omega < \omega'_c$), (II) parallel alignment via orientation distributions with strong perpendicular and parallel projections ($\omega'_c < \omega < 10 \cdot \omega'_c$), and (III) parallel alignment via orientation distributions richer in transverse and parallel projections ($10 \cdot \omega'_c < \omega$). The distinct strain dependencies of rates of the fast and slow processes and the qualitative difference between the orientations they induce in each of the three regimes strongly suggested that the physics for the distinct processes were different. However, it was not possible to infer from the rheo-optical results what the distinct mechanisms might be.

The present results provide valuable complementary information that may highlight the key physics associated with the fast and slow processes. In particular, the electron micrographs reveal how the texture evolves as one moves through each stage of the three types of alignment trajectories.

A. Evolution of Microstructure

A general feature that emerges from the TEM images is that the fast process of all three trajectories is largely responsible for the formation of layers from poorly organized material. From the SAXS results it is clear that the population of layers that is created is not isotropic—but neither is it unimodal. In general, the orientations that are enhanced in the fast process share a common tangent: for example, the fast processes of trajectory types (I) and (II) enhance orientations that have lamellae tangent to the \mathbf{v} direction, while the fast process of a type (III) trajectory creates layers with edges along $\nabla \times \mathbf{v}$. As the trajectory reaches the transition from the fast to the slow process, a distinctive texture develops for each trajectory: at the end of the fast process in trajectory (I) the texture viewed in the $(\nabla \mathbf{v}, \nabla \times \mathbf{v})$ -plane consists of well-organized layered domains separated by bands of poorly organized material; in (II) the layers meander fairly gently in the $(\nabla \mathbf{v}, \nabla \times \mathbf{v})$ -plane, and

in (III) the microstructure viewed in the $(\nabla\mathbf{v},\mathbf{v})$ -plane includes residual poorly organized regions, transverse domains and large regions with mean orientation in the parallel direction, which contain tilt walls that are oriented normal to the flow direction, forming a ‘chevron’ pattern.

The slow process generally appears to coarsen the structure that exists once most of the material has been converted to well-organized layers; it is during this process that the range of orientations that were enriched during the fast process is selectively winnowed down to a single orientation.

The path to perpendicular alignment (family (I), $\omega < \omega'_c$) begins with the enhancement of perpendicular and parallel layers and the orientations in between during ‘fast process’. While perpendicular layers are enhanced during the whole process, parallel layers are eliminated in the later stages. The first half of the slow process is responsible for the elimination of residual bands of poorly organized texture that separate lamellar domains at the end of the fast process. Relatively isolated poorly organized islands seem to persist at the mid-point of the ‘slow process’ even in regions with a strong overall perpendicular alignment.

Like the trajectory to perpendicular alignment, the pathway to parallel alignment at modestly high frequency (family (II), $\omega'_c < \omega < 10 \cdot \omega'_c$) begins with the build-up of perpendicular and parallel layers and the orientations in between, while no creation of transverse layers is observed. But in this process, the parallel projection grows more quickly than the perpendicular. The subsequent ‘slow process’ narrows the orientational distribution towards parallel alignment by eliminating poorly organized regions and reducing the angular variations associated with the undulating domain texture.

In family (III) trajectories (very high-frequency route to parallel, $\omega'_c \ll \omega$), the ‘fast’ process transforms poorly organized material to layers that are predominantly aligned along the parallel and transverse directions, but not along orientations between the two. This is the only one of the three families of trajectories that shows distinctly bimodal transient states. As most of the poorly organized regions are transformed to lamellae, the transition to the ‘slow’ process is marked by the development of a characteristic texture in regions of

average orientation along the parallel direction, with bands tilted about the vorticity axis to form ‘chevron’ patterns. The coarsening of this pattern appears to dominate the slow process, during which the transverse projection is also eliminated. At the end of the slow process a well-aligned “single-crystal-like” state is achieved.

These observations build a much clearer picture of the evolution of shear-induced alignment processes than was previously possible from the transient rheo-optical results that established the families of trajectories or from structural studies that did not have a context for relating the sample points to their corresponding positions along a given alignment trajectory.

B. Implications Regarding Alignment Mechanisms

There are three mechanisms of flow-induced alignment that have been frequently mentioned in the literature: selective melting, defect migration and grain rotation. Therefore, we first comment on the implications of the TEM and SAXS results regarding the existence and importance of these three mechanisms. Then we comment on a process that is strongly indicated by each sequence of TEM images, but which appears not to have been considered previously: selective *creation* of lamellae from ordered, but poorly organized material. Finally, some suggestions regarding future theoretical work will be discussed.

From the progression of local structure seen in the TEM images, there is no evidence of selective lamellar melting or flow-induced disordering. This is particularly significant in relation to the perpendicular alignment trajectory, since the selection of perpendicular alignment has been attributed to flow-induced disordering followed by ordering under the influence of shear, which produces perpendicular lamellae. Since melting is most likely to play a role when the amount of unfavorably oriented material is greatest, it would produce a rapid growth of the perpendicular alignment at the early stage of the process, while depleting (or leaving unchanged) other orientations. The observed texture at points A and B and the corresponding orientation distributions indicated by SAXS fail to show evidence of such a

highly selective mechanism.

A number of images do suggest that defect migration plays a role, especially in the later stages of the alignment process. One example is the disappearance of the bands of poorly organized material separating well-ordered lamellar domains during parallel alignment close to ω'_c (type (II) trajectory). This could indicate that the boundary between the two types of regions moves in the direction of the poorly organized material, which disappears when the boundaries on each side meet. An even more compelling example is the coarsening of the ‘chevron’ texture during parallel alignment at very high frequencies (type (III) trajectory). If tilt walls on either side of a relatively steeply tilted band moved together and annihilated, the process could produce the observed increase in the spacing between and reduction in the misalignment angle across tilt walls that occurs between points B and C along this type of trajectory.

Ex-situ methods are not well suited to confirming or negating grain rotation. However, the general observation that extended domains of well-defined lamellae develop as a result of the alignment process suggests that *if* grain rotation plays a role: in the fast process it would correspond to rotation of a domain of well-organized layers within a matrix that has a large amount of poorly organized material; in the slow process ‘grains’ that have formed might reorient in a cooperative manner with adjacent regions that are also well-organized, but differently oriented with respect to the flow. To date the most direct evidence of grain rotation comes from the rheo-optical signature of the low frequency ($\omega < \omega_d$) alignment process in a PEP-PEE lamellar diblock.²³ Although such a regime has been reported in specially annealed PS-PI diblocks and in both annealed and unannealed PEP-PEE diblocks, it is not observed in PS-PI that is simply heated through the ODT to erase prior thermal and flow history and then cooled to the shearing temperature. Although it is beyond the scope of the present study, future work on the effects of annealing on the trajectories of alignment in PS-PI at very low frequency may provide additional information on the role of grain rotation in producing the low frequency pathway to parallel alignment.

In all three trajectories explored here, shearing appears to play a role in converting

poorly organized material into well-defined lamellae. The selectivity of this re-organization process appears to direct the initial development of the orientation distribution during the fast process. The reorganization process has a particularly interesting feature in the very high frequency regime: it produces mainly parallel and transverse lamellae.

Bimodal transverse-parallel distributions have been attributed to entanglement and strong segregation³¹; and it has been asserted that parallel alignment is simply controlled by the loss tangent, implying that one type of trajectory applies to all routes to parallel alignment³³. The present results indicate that these bimodal distributions also occur in non-entangled polymers and in weak segregation, and that they correspond to type (III) trajectories to parallel alignment ($\omega \gg \omega'_c$), but not to type (II) trajectories to parallel alignment ($\omega'_c < \omega < 10 \cdot \omega'_c$). As to the mechanism responsible for the bimodal distribution, the creation of transverse domains has been attributed to alignment of entangled chains along the flow direction. However, this is unlikely to be an adequate explanation, since the bimodal distribution can occur at small strain amplitudes (as small as $\gamma_o = 0.1$) in both entangled and unentangled systems. At small strain amplitudes, segmental orientation is hardly perturbed, and its orientation is along the extensional axis of the shear (45° with respect to the flow direction). Thus, a more general explanation is needed. Here we present a mechanism that overcomes these deficiencies and applies to a wide range of systems so long as $\omega \gg \omega'_c$.⁵⁰ This explanation requires only a symmetry argument and the distortion of chain conformation to explain the simultaneous creation of both transverse and parallel orientations during the fast process.

The key feature is that the shear frequency is so high that chain conformation cannot relax; and larger scale-structures that require the motion of many chains certainly cannot relax. Under these conditions, symmetry arguments may give insight into the physics of the alignment process. The orientations that are affected the same way by forward and reverse cycles, and consequently have the possibility of being progressively reinforced, have fore-aft symmetry (Fig 18A). And since the structure has insufficient time to relax, the motion imposed by the deformation in the $(\nabla \mathbf{v}, \mathbf{v})$ -plane should dominate over out-of-plane

rearrangements. This leaves two orientations that could potentially be reinforced by multiple cycles of high frequency shearing: transverse and parallel (Fig 1). Of course, this does not imply that both projections will be reinforced, but this simple symmetry argument can explain why intermediate orientations between these two, as well as orientations with normals out of the $(\nabla\mathbf{v},\mathbf{v})$ -plane are *not* created.

The observation that a substantial transverse population forms, in spite of the fact that this orientation is the most unstable when subjected to shear, suggests that the mechanism for converting poorly organized domains into well-defined lamellae contributes approximately equally to the two possible orientations that could be reinforced. Simultaneous with this organization process, which creates both transverse and parallel domains, is a mechanism that converts the unstable transverse domains to the more stable parallel orientation. The former mechanism dominates at the beginning, since the initial state is largely composed of poorly organized domains; the latter dominates at long times, when most of the material exists in well-organized lamellae in either nearly transverse or nearly parallel orientation.

Here we suggest one possible mechanism for creation of parallel and transverse lamellae that emphasizes the special feature of high frequencies $\omega \gg \omega_c$: the distortion of chain conformation. In particular, the effects of shear on the lamellar orientation and on chain conformation tend to produce deviations from the equilibrium structure in which chains are on average oriented transverse to the lamellae. Layers that are either transverse or parallel are affected equally by forward and reverse shearing, so their orientation tends to remain unchanged. Layers that deviate from these orientations are swept into them due to the asymmetric effects of forward and reverse half-cycles of shear. For lamellae whose normal lies in the $(\nabla\mathbf{v},\mathbf{v})$ -plane and within $\pm 45^\circ$ of the flow direction, the half cycle that would tend to rotate the layers away from transverse alignment also extends chains away from the layer normal, tending to resist rotation (Fig 18B). Instead of responding the same way to forward and reverse cycles, layers with orientation in this range would tend to rotate toward transverse alignment (Fig 18C). For lamellae whose normal lies in the $(\nabla\mathbf{v},\mathbf{v})$ -plane, but within $\pm 45^\circ$ of the gradient direction, the half cycle that tends to rotate layers toward

parallel alignment imposes a distortion of chain orientation from the layer normal that reinforces reorientation. This produces an asymmetry with respect to forward and reverse cycles that would progressively reinforce parallel alignment (Fig 18D). Given the isotropic initial structure, equal populations of each family of local initial orientations would exist, so shearing could lead to approximately equal production of transverse and parallel lamellae from the initial poorly organized material.

The trajectories to parallel alignment at moderately high frequencies ($\omega_c < \omega < 10 \cdot \omega_c$) involve a transition in behavior: here the initial fast process is less selective (enhancing a range of orientations, rather than just two) and has different symmetry (selecting layers with normals that lie in the $(\nabla\mathbf{v}, \nabla \times \mathbf{v})$ -plane rather than the $(\nabla\mathbf{v}, \mathbf{v})$ -plane). This is a natural consequence of moving to frequencies that are low enough to allow relaxations on the scale of the whole chain or even the nanostructure (the time scale of the deformation approaches the single chain relaxation time). These relaxations can produce out-of-plane reorganizations of structure that avoid higher energy distortions in the plane (such as the creation of transverse layers). In particular, all of the orientations that are enhanced during the fast process of this trajectory have the property that their layer spacing is not altered by a shearing deformation. From this distribution, the slow process winnows out all but the parallel alignment. This would be in accord with a final selection of orientation at all frequencies $\omega > \omega_c$ based on the viscoelastic contrast between the styrene-rich and isoprene-rich layers.²⁴

As frequency is lowered further, the progression of behavior continues: the fast process of the perpendicular alignment trajectory again has the type of selectivity observed in the intermediate trajectory to parallel alignment. What changes is the selectivity of the slow process. In the frequency regime where the nanostructure dominates ($\omega < \omega_c$), the selection of perpendicular alignment can be explained by the coupling of shear to composition fluctuations, which destabilizes the parallel orientation relative to perpendicular.^{6,11}

As has been previously noted, the theoretical literature is mainly devoted to the relative stability of monodomains with different orientation with respect to the flow geometry.^{5,15,22,40,41} Since the rate, degree and direction of alignment are determined by

the way the orientation distribution evolves dynamically from the complex initial texture to a well-aligned material, consideration of the stability of the ultimate microstructure alone is not enough. Guided by the TEM and SAXS results, it may be possible to break the overall alignment process into parts that are tractable by analysis or simulation. For example, the conversion of poorly organized material into lamellae might be treated as an individual part; future work might examine how this reorganization proceeds at very high frequencies where chain dynamics may play an important role and contrast this high frequency process to the reorganization into lamellae at low frequencies where nanostructural dynamics, including fluctuations, dominate the flow behavior. The TEM images also suggest specific types of defect migration that might be investigated theoretically. For example, in the very high frequency regime, the evolution of ‘chevron’ patterns of defects under the influence of oscillatory shear might be tractable, giving insight into the slow process of the type (III) trajectories to parallel alignment. The new information on the evolution of microstructure at well defined stages in the alignment process may present opportunities in modeling and simulation, which in turn could yield valuable insights to guide the unified design of materials and processing conditions to exploit flow induced alignment.

5. Conclusion

The combination of real-time in-situ rheo-optical methods, with ex-situ small-angle x-ray scattering and transmission electron microscopy for nano-, micro-, and macroscopic observations, reveals the structural evolution during flow-induced alignment of a model diblock copolymer through different trajectories. By spanning the range of length and time scales involved, we can observe the cascade of structural changes: the formation of layers from poorly organized regions; the creation, growth, coarsening, and deformation of domains; the generation and elimination of defects, and the perfection of well-aligned ‘single-crystal-like’ order. These results enable us to re-evaluate numerous proposed mechanisms of block copolymer alignment that have been put forward over the past two decades.^{3,4,1,5,15–41}

For example, in the PS-PI system, we find no evidence of selective melting or flow-induced disordering; instead, results suggest selective creation of well-defined lamellae from poorly organized regions, particularly in the initial fast processes of various alignment trajectories. Observations of different types of defects and their anisotropic arrangement during the fast and slow processes of each trajectory, make the general concept of defect dynamics more specific in terms of both the type of defects involved and the dynamic regime where they are important. For example, partially formed focal conic defects appear in the initial ordered, but unaligned block copolymer lamellae and disappear during the fast processes of each trajectory. In the slow process of each trajectory the majority of the material exists in well-defined layers and these form different types of defects in each of the three trajectories. For example, in the very high frequency path to parallel alignment the late stage of the process appears to be controlled by coarsening of “chevron” patterns of tilt-walls that are oriented normal to the flow direction.

Recently, shear-induced parallel-transverse orientation distributions have been observed in disparate systems.^{30,31,38,39} This surprising texture has attracted considerable interest. It has been asserted that this type of structure is characteristic of parallel or strongly segregated, entangled polymers.³¹ However, the present results show that this type of microstructure, manifested by four-spot scattering patterns in the $(\mathbf{v}, \nabla\mathbf{v})$ -plane, is particular to the very high frequency regime, and occurs in both unentangled and entangled polymers in both weakly and strongly segregated states. Indeed, the common feature of all reports of the parallel-transverse bimodal structure is that the materials were subjected to oscillatory shearing in the very high frequency regime ($\omega'_c \ll \omega$). From this insight, we have suggested a mechanism for simultaneous creation of transverse and parallel lamellae in the fast process of the high frequency trajectory to parallel alignment.⁵⁰ This mechanism invokes only symmetry arguments and the role of conformational distortion of the chains when subjected to rapid deformations.

Information on the microstructural nature of the initial fast process and subsequent slow process of each trajectory provides greater insight into the distinct physics involved

in each of three alignment regimes. In turn, more specific physical concepts may provide a guide for modeling and simulation of dynamic processes during shear: it appears reasonable to break each type of trajectory down into processes that dominate at different stages (e.g., early vs. late), which could be integrated together to describe the whole alignment trajectory. Based on the success of this experimental approach in clarifying the dynamics of the present lamellar diblock, it is being extending to other nanostructures, including various diblock copolymers and the elaborate structures formed by ABC triblock copolymers. The combination of rapid in-situ measurements with detailed ex-situ structural characterization has the potential to uncover the physics of flow-induced alignment in a wide-range of self-assembled materials.

REFERENCES

1. Bates, F.S.; Fredrickson, G.H. *Annu. Rev. Phys. Chem.* **1990**, *41*, 525.; Bates, F. S. *Science* **1991**, *251*, 898.; Bates, F.S.; Fredrickson, G.H. *Annual Rev. Mater. Sci.* **1996**, *it 26*, 501; Colby, R.H. *Curr. Opin. Coll. Int. Sci.*, **1996**, *1*, 454.
2. Keller, A.; Pedemonte, E.; Willmouth, F.M. *Colloid Polym. Sci.* **1970**, *238*, 25.; Folkes, M.J.; Keller, A.; Scalisi, F.P. *Colloid Polym. Sci.* **1973**, *251*, 1.
3. Hadziioannou, G.; Mathis, A.; Skoulios, A. *Colloid Poly. Sci.* **1979**, *257*, 136; Hadziioannou, G.; Mathis, A.; Skoulios, A. *Macromolecules* **1982**, *15*, 258.
4. Morrison, F. A.; Winter, H. H. *Macromolecules.* **1989**, *22*, 3533.; Morrison, F. A.; Winter, H.H.; Gronski, W.; Barnes, J. D. *Macromolecules.* **1990**, *23*, 4200.
5. Cates, M. E. ; Milner, S. T. *Phys. Rev. Lett.* **1989**, *62*, 1856; Bruinsma, R.; Rabin, Y. *Phys. Rev. A* **1992**, *45*, 994; Goualian, M. ; Milner, S. T. *Phys. Rev. Lett.* **1995**, *74*, 1775.
6. M. Goualian, S. T. Milner, *Phys. Rev. Lett.* **74**, 1775 (1995); G. H. Fredrickson, *J. Rheol.* **38**, 1045 (1994).
7. J. T. Chen, E.L. Thomas, C. K. Ober, G. P. Mao, *Science* **273**, 343 (1996); S. I. Stupp, V. LeBonheur, K. Walker, L. S. Li, K. E. Huggins, M. Keser, A. Amstutz, *Science* **276**, 384 (1997); S. Kanaoka, R. H. Grubbs, *Macromolecules* **28**, 4707 (1995); X. L. Chen, S. A. Jenekhe, *Macromolecules* **29**, 6189 (1996); M. Park, C. Harrison, P. P. Chaikin, R. A. Register, D. H. Adamson, *Science* **276**, 1401 (1997).
8. W. M. Gelbart, A. Benshaul, *J. Phys. Chem.* **100**, 13169 (1996); J. Liu, A. Kim, L. Q. Wang, B. J. Palmer, Y. L. Chen, P. Bruinsma, B. C. Bunker, *Adv. Coll. Int. Sci.* **69**, 131 (1996); P. Pieranski, *Contemp. Phys.* **24**, 25 (1983); J. M. Jethmalani, W. T. Ford, *Chem. Mater.* **8**, 2138 (1996).
9. W. Richtering, G. Schmidt, P. Lindner, *Coll. Polym. Sci.* **274**, 85 (1996); U. Olsson,

- K. Mortensen, *J. Phys. II* **5**, 789 (1995); O. Diat, D. C. Roux, F. Nallet, *J. Phys. II* **3**, 1427 (1993); L. Soubiran, C. Coulon, P. Sierro, D. Roux, *Europhysics Lett.* **31**, 243 (1995); C. R. Safinya, E. B. Sirota, R. F. Bruinsma, C. Jeppesen, R. J. Plano, L. J. Wenzel, *Science* **261**, 588 (1993).
10. N. K. Raman, M. T. Anderson, C. J. Brinker, *Chem. Mater.* **8**, 1682 (1996); Q. Hue, R. Leon, P.M. Petroff, G.D. Stucky, *Science* **268**, 1324 (1995); E. Evans, H. Bowman, A. Leung, D. Needham, D. Tirrell, *Science* **273**, 933 (1996); K. M. McGrath, C. J. Drummond, *Coll. Polym. Sci.* **274**, 612 (1996).
 11. R. Bruinsma, Y. Rabin, *Phys. Rev. A* **45**, 994 (1992).
 12. W. D. Dozier, P. M. Chaikin, *J. Physique* **43**, 843 (1982); J. Liu, D. A. Weitz, B. J. Ackerson, *Phys. Rev. E* **48**, 1106 (1993).
 13. M. R. Ghadiri, *Adv. Mater.* **7**, 675 (1995); W. Frey, W. R. Schief, D. W. Pack, C. T. Chen, A. Chilkoti, P. Stayton, V. Vogel, F. H. Arnold, *Proc. NAS US* **93**, 4937 (1996).
 14. U. Krappe, R. Stadler, I. Voigt-Martin, *Macromolecules* **28**, 4558 (1995); J. Bechmann, C. Auschra, R. Stadler, *Macromol. Rapid Commun.* **15**, 67 (1994); Z. Wei, Z.-G. Wang, *Macromolecules* **28**, 7215 (1995).
 15. Fredrickson, G. H. *J. Rheol.* **1994**, *38*, 1045.
 16. Koppi, K.; Tirrel, M.; Bates, F.S.; Almdal, K, Colby, R.H. *J. Phys. II* **1992**, *2*, 1941.
 17. Koppi, K.; Tirrel, M.; Bates, F.S. *Phys. Rev. Lett.*, **1993**, *70*, 1449.
 18. Winey, K. I.; Patel, S. S.; Larson, R. G.; Watanabe, H. *Macromolecules* **1993**, *26*, 2542.
 19. Winey, K. I.; Patel, S. S.; Larson, R. G.; Watanabe, H. *Macromolecules* **1993**, *26*, 4373.
 20. Larson, R. G.; Winey, K. I.; Patel, S. S.; Watanabe, H. *Rheol. Acta* **1993**, *32*, 245.
 21. Riise, B.L.; Fredrickson, G.H.; Larson, R.G.; Pearson, D.S. *Macromolecules*, **1995**, *28*,

7653.

22. Amundson, K.; Helfand, E.; Quan, X.; Hudson, S. D.; Smith, S. D. *Macromolecules* **1994**, *27*, 6559.
23. Kannan, R. M.; Kornfield, J. A. *Macromolecules* **1994**, *27*, 1177.
24. Patel, S. S.; Larson, R. G.; Winey, K. I.; Watanabe, H. *Macromolecules* **1995**, *28*, 4313.
25. Zhang, Y.; Wiesner, U.; Spiess, H. W. *Macromolecules* **1995**, *28*, 778.
26. Gupta, V. K.; Krishnamoorti, R.; Kornfield, J. A.; Smith, S. D. *Macromolecules* **1996**, *29*, 1359.
27. Gupta, V. K.; Krishnamoorti, R.; Kornfield, J. A.; Smith, S. D. *Macromolecules*, **1995**, *28*, 4464.
28. Gupta, V. K.; Krishnamoorti, R.; Chen, Z.-R.; Kornfield, J. A.; Smith, S. D.; Satkowski, M. M.; Grothaus, J. T. *Macromolecules*, **1996**, *29*, 875.
29. Polis, D. L.; Winey, K. I. *Macromolecules*, **1996**, *29*, 8180.
30. S. D. Hudson, K. R. Amundson, H. G. Jeon, S. D. Smith, *Mat. Res. Soc. Bulletin* **20**, 42 (1995)
31. Zhang, Y.M.; Wiesner, U. *J. Chem. Phys.*, **1995**, *103*, 4784.
32. Zhang, Y.; Wiesner, U.; Yang, Y.; Pakula, T.; Spiess, H.W. *Macromolecules*, **1996**, *29*, 5427.
33. Zhang, Y.; Wiesner, U. *J. Chem. Phys.*, **1997**, *106*, 2961.
34. Morrison, F.A.; Mays, J.W.; Muthukumar, M.; Nakatani, A.I.; Han, C.C. *Macromolecules*, **1993**, *26*, 5271.
35. Nakatani, A.I.; Morrison, F.A.; Douglas, J.F.; Mays, J.W.; Jackson, C.L.; Muthukumar, M.; Han, C.C. *J. Chem. Phys.*, **1996**, *104*, 1589.

36. Balsara, N.; Hammouda, B.; Kesani, P. K.; Jonnalagadda, S. V.; Straty, G. C. *Macromolecules* **1994**, *27*, 2566; N. P. Balsara and B. Hammouda, *Phys. Rev. Lett* **1994**, *72*, 360.
37. Wang, H.; Kesani, P.K.; Balsara, N.P.; Hammouda, B. *Macromolecules* **1997**, *30*, 982.
38. Pinheiro, B.S.; Hajduk, D.A.; Gruner, S.M.; Winey, K.I. *Macromolecules*, **1996**, *29*, 1482.
39. Okamoto, S.; Saijo, K.; Hashimoto, T. *Macromolecules*, **1994**, *27*, 5547.
40. Amundson, K.; Helfand, E.; Davis, D. D.; Quan, X.; Patel, S. S.; Smith, S. D. *Macromolecules* **1991**, *24*, 6546.; Amundson, K.; Helfand, E.; Quan, X.; Smith, S. D. *Macromolecules* **1993**, *26*, 2698.
41. Amundson, K.; Helfand, E. *Macromolecules*, **1993**, *26*, 1324.
42. R. J. Albalak, E. L. Thomas, *J. Polym. Sci.: Polym. Phys. Ed.* **31**, 37 (1993).
43. The rheo-optical results presented here and in our earlier papers²⁶⁻²⁸ are from the same batch of PS-PI. In the previous studies only one aliquot from this batch was used for a whole suite of rheo-optical experiments. Here various samples are loaded, processed and removed for ex-situ characterization, therefore a series of aliquots from the same batch of polymer are used. Since small variations in the ODT were previously detected from aliquot to aliquot taken from the same batch of polymer,^{27,28,44} rheo-optical characterization of each loading was used to confirm that it behaved in accord with all other samples in the series.
44. We performed a temperature sweep at a rate of 1°C/min and in steps of 1°C. At each temperature the dynamic moduli were measured using oscillatory shear at 10 rad/s and 2% strain. At T_{ODT} , both G' and G'' exhibited a steep decrease, which was more pronounced for G' . Similar determination revealed a typical hysteresis behavior upon cooling with the transition temperature a few degrees lower than that during heating.

For yet unknown reasons, we observed T_{ODT} of 172°C and 164°C for two different aliquots of the same polymer batch. All ten aliquots used for the experiments reported in this paper had ODTs between 170 and 172°C.

45. Kannan, R. M.; Kornfield, J. A. *Rheo. Acta* **1992**, *31*, 535; Kannan, R. M.; Kornfield, J. A.; Schwenk, N.; Boeffel, C. *Macromolecules* **1993**, *26*, 2050.
46. Lodge, T. P.; Fredrickson, G. H. *Macromolecules* **1992**, *25*, 5643.
47. Allan, P., Arridge, R. G. C.; Ehtaiatkar, F.; Folkes, M. J. *J. Phys. D: App. Phys.*, **1991**, *24*, 1381.
48. It has been suggested that under certain flow conditions the intrinsic birefringence could dominate over the form birefringence in the present PS-PI,³³ since the theoretical basis for expecting the form contribution to dominate⁴⁶ gives a form birefringence that is only approximately three times the intrinsic birefringence and is based on a static sample. However, experimental evidence indicates that the form effect is over an order of magnitude larger than the intrinsic birefringence even during shearing. One piece of evidence comes from comparison to a system in which the intrinsic birefringence is known to dominate: PEP-PEE.²³ In this system the intrinsic contributions of the two blocks reinforce each other, whereas the two tend to cancel in PS-PI. This trend holds for both flow-induced anisotropy and anisotropy associated with the tendency of chains to align normal to lamellar interfaces. Thus, the birefringence of PEP-PEE tends to provide an upper bound on the intrinsic contribution to the birefringence in PS-PI. The 1,3-birefringence of well-aligned perpendicular PEP-PEE is less than 1/20 as large as that of similarly aligned PS-PI; this suggests that the intrinsic component of the birefringence of PS-PI is less than 5% of its form birefringence. Another piece of evidence comes from the magnitude of the birefringence that can be attributed to flow-induced segmental anisotropy. Since the oscillatory stress has similar amplitude throughout the alignment processes,²⁷ the stress-induced intrinsic contribution to the displacement of

the 1,3-birefringence $\Delta n_{13}^{(d)}$ must remain of the same order of magnitude through the process. Its magnitude can be inferred by the value of $\Delta n_{13}^{(d)}$ observed during shearing when the sample is well aligned: at the conclusion of the alignment process this value is less than 0.1% of the magnitude of $\Delta n_{13}^{(d)}$ observed during the transient stages of the process (see ref.²⁸, Figure 4a for γ_o of 0.9 and 1.0 and Figure 6a for γ_o of 0.6; and in this article see Figure 9b for $\gamma_o = 1.1$ and Figure 14b for $\gamma_o = 0.5$ and 0.7). This suggests that the flow-induced anisotropy of the chains produces a 1,3-birefringence contribution that has a magnitude less than 1/1000 of the form birefringence associated with the evolution of the lamellar orientation distribution.

49. To evaluate the effect of equilibration time on the initial state, we examined TEM micrographs of a sample which was annealed at 115°C for 24 hours, and compared them with TEM micrographs of a sample that was annealed for 15 min (see Figure 4). Surprisingly, almost no difference was found in terms of their textures, morphologies, and percentages of poorly organized material. We observed that annealing time did not change the alignment trajectory. A small effect can be detected in the rate of orientation, with longer annealing time producing slightly faster alignment.
50. Chen, Z.-R.; Kornfield, J. A.; Smith, S. D.; Grothaus, J. T.; Satkowski, M. M. *Science*, **1997**, *277*, 1248.

FIGURES

Fig. 1. Schematic diagram of the three principal lamellar orientations. (a) perpendicular; (b) transverse; (c) parallel.

Fig. 2. Three families of alignment trajectories are observed for PS-PI lamellae that have been heated through the ODT to erase their thermal and flow history, then cooled to a particular temperature in the ordered state where flow-induced alignment is performed: (I) perpendicular alignment at $\omega < \omega'_c$; (II) parallel alignment at frequencies above, but close to ω'_c ; and (III) parallel alignment at $\omega \gg \omega'_c$. Each regime has a qualitatively different signature in the transient 1,3-birefringence during alignment (top row). The range of temperatures, frequencies and strain amplitudes over which each type of alignment trajectory is observed is represented on a three-dimensional plot²⁸, where the third dimension of strain is indicated inside the open symbols (see dial in the lower left of the graph). Filled symbols show the conditions used in the present study (see Figs. 5a, 9a and 14a for range of strain amplitudes). Conditions shown lead to a well-aligned state (see text) in less than ten hours. Two symbols directly atop one another represent different alignments or trajectories at identical temperature and frequency, but different strain amplitude.

Fig. 3. The storage modulus of the disordered and ordered, unaligned states for the present PS-PI diblock. Although the disordered state results lie in the terminal regime for all experimentally accessible frequencies, the critical frequency ω'_c can be estimated by comparison to materials for which the disordered and ordered state data converge. The arrows above the data points indicate the reduced frequencies that are used for the shear-induced alignment experiments and are labeled according to the flow alignment regime to which they belong (see text).

Fig. 4. Structure of the initial condition as characterized by TEM and SAXS.

Fig. 5. Evolution of the dynamic moduli and birefringence during perpendicular alignment driven by oscillatory shearing at $\omega = 1$ rad/s at $T = 115^\circ\text{C}$: **a)** effective dynamic storage modulus during shearing with large strain amplitude ($\gamma_o \geq 0.4$) compared to the linear storage modulus observed at the same frequency but with sufficiently small strain (indicated by the arrow on the left for the unaligned initial state and on the right for a well-aligned perpendicular state), **b)** growth of the 1,3-birefringence with time during the same experiments as in part a), and **c)** birefringence during and upon cessation of shearing for samples prepared for ex-situ studies.

Fig. 6. Structure at Point A along the perpendicular alignment trajectory shown in Figure 5b as revealed by TEM and SAXS. The scale for SAXS intensity can be quantitatively compared to Points B and C for this trajectory.

Fig. 7. Structure at Point B along the perpendicular alignment trajectory shown in Figure 5b as revealed by TEM and SAXS. The scale for SAXS intensity can be quantitatively compared to Points A and C for this trajectory.

Fig. 8. Structure at Point C along the perpendicular alignment trajectory shown in Figure 5b as revealed by TEM and SAXS. The scale for SAXS intensity can be quantitatively compared to Points A and B for this trajectory.

Fig. 9. Evolution of the dynamic moduli and birefringence during parallel alignment driven by oscillatory shearing at $\omega = 4$ rad/s at $T = 115^\circ\text{C}$: **a)** effective dynamic storage modulus during shearing with large strain amplitude ($\gamma_o \geq 0.5$) compared to the linear storage modulus observed at the same frequency but with sufficiently small strain (indicated by the arrow on the left for the unaligned initial state and on the right for a well-aligned perpendicular state), **b)** growth of the 1,3-birefringence with time during the same experiments as in part a), and **c)** birefringence during and upon cessation of shearing for samples prepared for ex-situ studies.

Fig. 10. Structure at Point A along the parallel alignment trajectory shown in Figure 9b as revealed by TEM and SAXS. The scale for SAXS intensity can be quantitatively compared to Points B and C for this trajectory.

Fig. 11. Structure at Point B along the parallel alignment trajectory shown in Figure 9b as revealed by TEM and SAXS. The scale for SAXS intensity can be quantitatively compared to Points A and C for this trajectory.

Fig. 12. Structure at Point C along the parallel alignment trajectory shown in Figure 9b as revealed by TEM and SAXS. The scale for SAXS intensity can be quantitatively compared to Points A and B for this trajectory.

Fig. 13. TEM image of a well-aligned parallel sample. Sample prepared by prolonged shearing at $T = 115^\circ\text{C}$, $\omega = 100$ rad/s, and $\gamma_o = 70\%$. This image is taken in the $(\nabla\mathbf{v}, \nabla\times\mathbf{v})$ -plane. Although some defects do persist in this plane, large areas show uniform parallel alignment; in the $(\mathbf{v}, \nabla\mathbf{v})$ -plane even fewer defects are observed.

Fig. 14. Evolution of the dynamic moduli and birefringence during parallel alignment driven by oscillatory shearing at $\omega = 100$ rad/s at $T = 115^\circ\text{C}$: **a)** effective dynamic storage modulus during shearing with large strain amplitude ($\gamma_o \geq 0.2$) compared to the linear storage modulus observed at the same frequency but with sufficiently small strain (indicated by the arrow on the left for the unaligned initial state and on the right for a well-aligned perpendicular state), **b)** growth of the 1,3-birefringence with time during the same experiments as in part a), **c)** birefringence during and upon cessation of shearing for samples prepared for ex-situ studies, and **d)** loss tangent during shearing.

Fig. 15. Structure at Point A along the parallel alignment trajectory shown in Figure 14b as revealed by TEM and SAXS. The scale for SAXS intensity can be quantitatively compared to Points B and C for this trajectory.

Fig. 16. Structure at Point B along the parallel alignment trajectory shown in Figure 14b as revealed by TEM and SAXS. The scale for SAXS intensity can be quantitatively compared to Points A and C for this trajectory.

Fig. 17. Structure at Point C along the parallel alignment trajectory shown in Figure 14b as revealed by TEM and SAXS. The scale for SAXS intensity can be quantitatively compared to Points A and B for this trajectory.

Fig. 18. The role of chain distortion in the development of the bimodal transverse-parallel texture en route to parallel alignment at very high frequencies ($\omega \gg \omega_c$). The extensional component of shear affects chain conformation as shown schematically by the solid chains (deformed) compared with the dotted chains (undeformed). Convection of the layers produces a reorientation indicated by the solid lines (deformed) versus the dotted lines (undeformed). A. Transverse layers are affected the same way by forward and reverse cycles, so there is no tendency to reorient. A similar argument applies to the parallel orientation. B. Layers tilted away from the transverse orientation are *not* affected the same way by forward and reverse shear. If their normal \mathbf{n} is tilted down relative to the flow direction of a forward cycle, then the distortion of the chains is stronger in the forward than in the reverse direction; consequently, the net effect of a full cycle is to promote reorientation toward transverse alignment. C. Thus, layers with \mathbf{n} in the blue shaded sector will tend to evolve toward transverse alignment ($\mathbf{n} // \mathbf{v}$). D. The same reasoning applies to orientations tilted in the opposite direction relative to transverse, so they will also tend to evolve toward transverse alignment (blue shaded region). Similarly, orientations tilted away from parallel alignment would progressively rotate into parallel (green shaded regions).

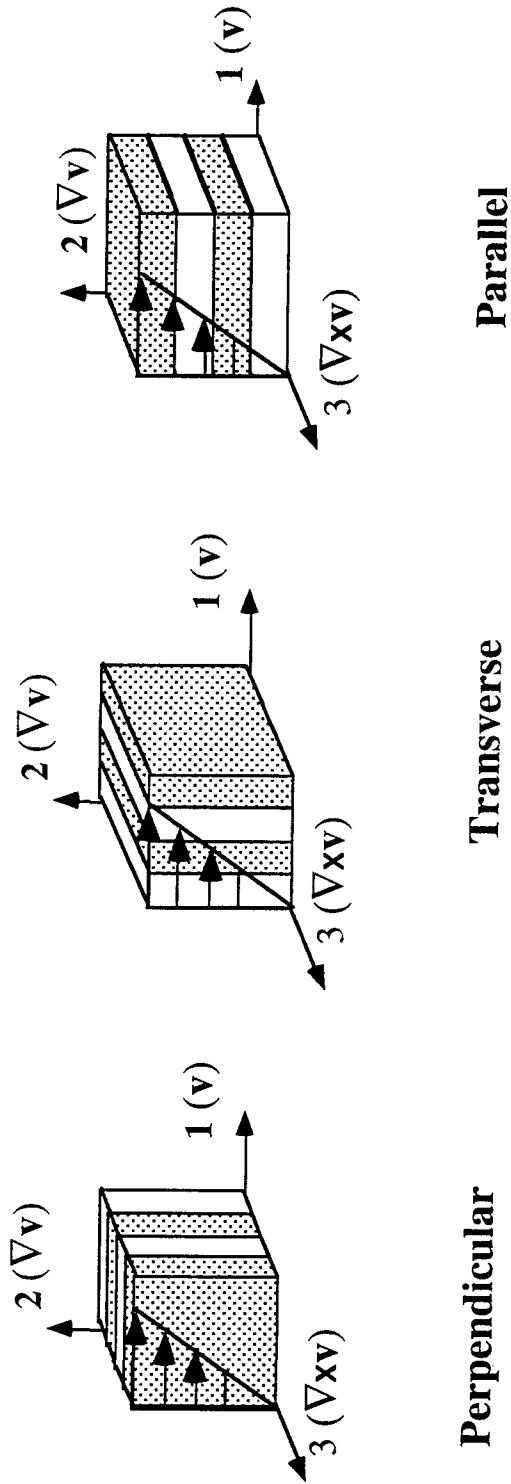


Fig. 1

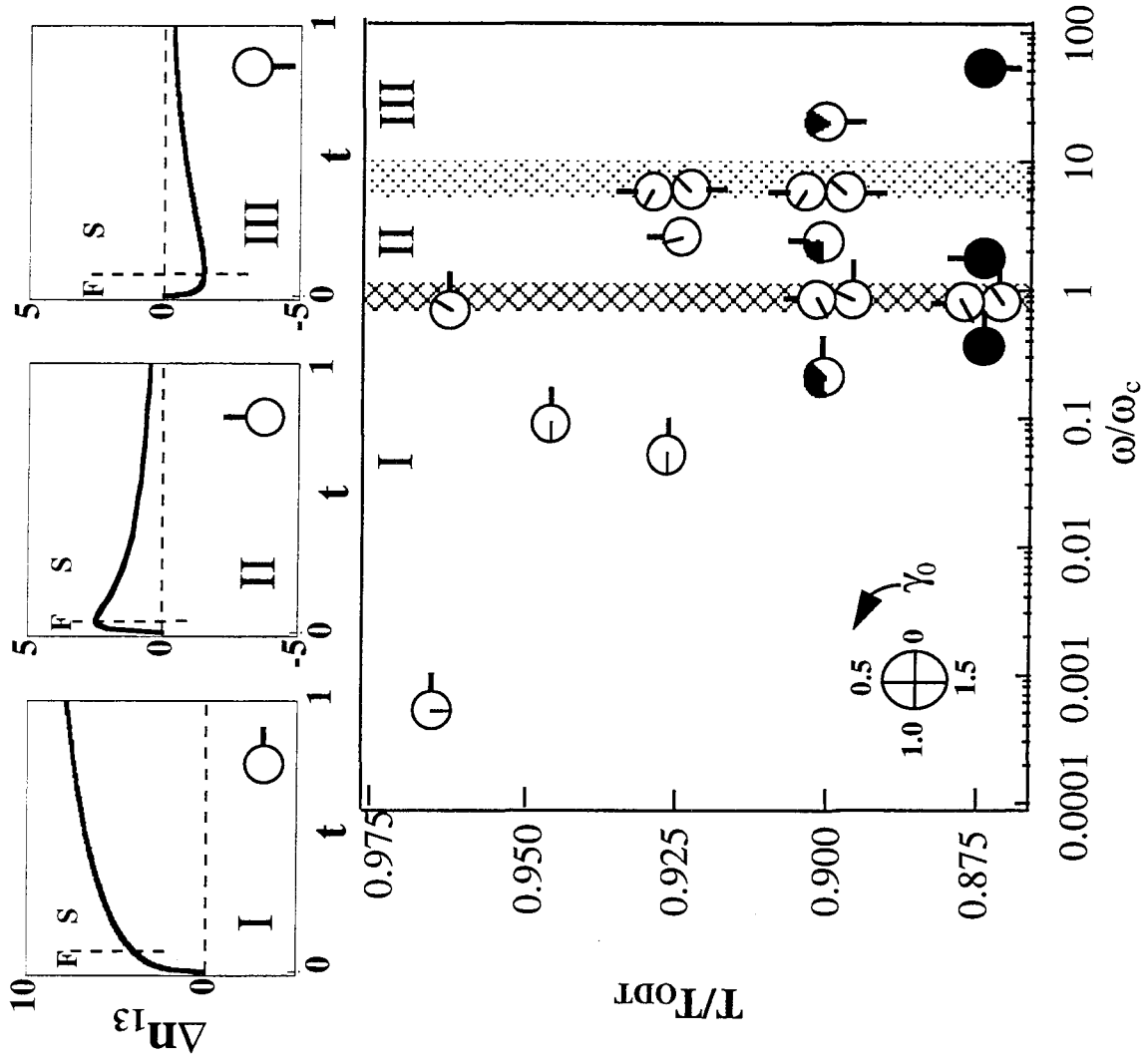
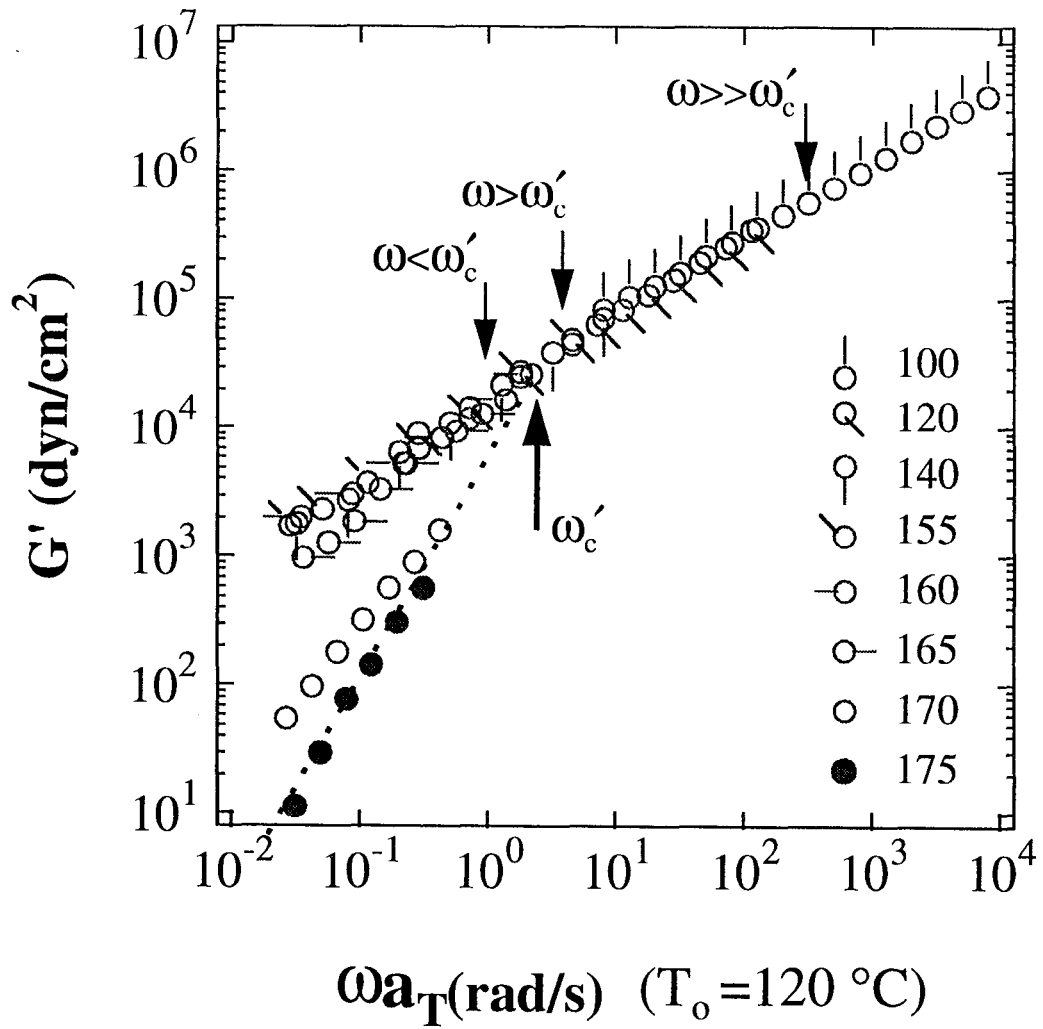


Fig.2

Fig. 3



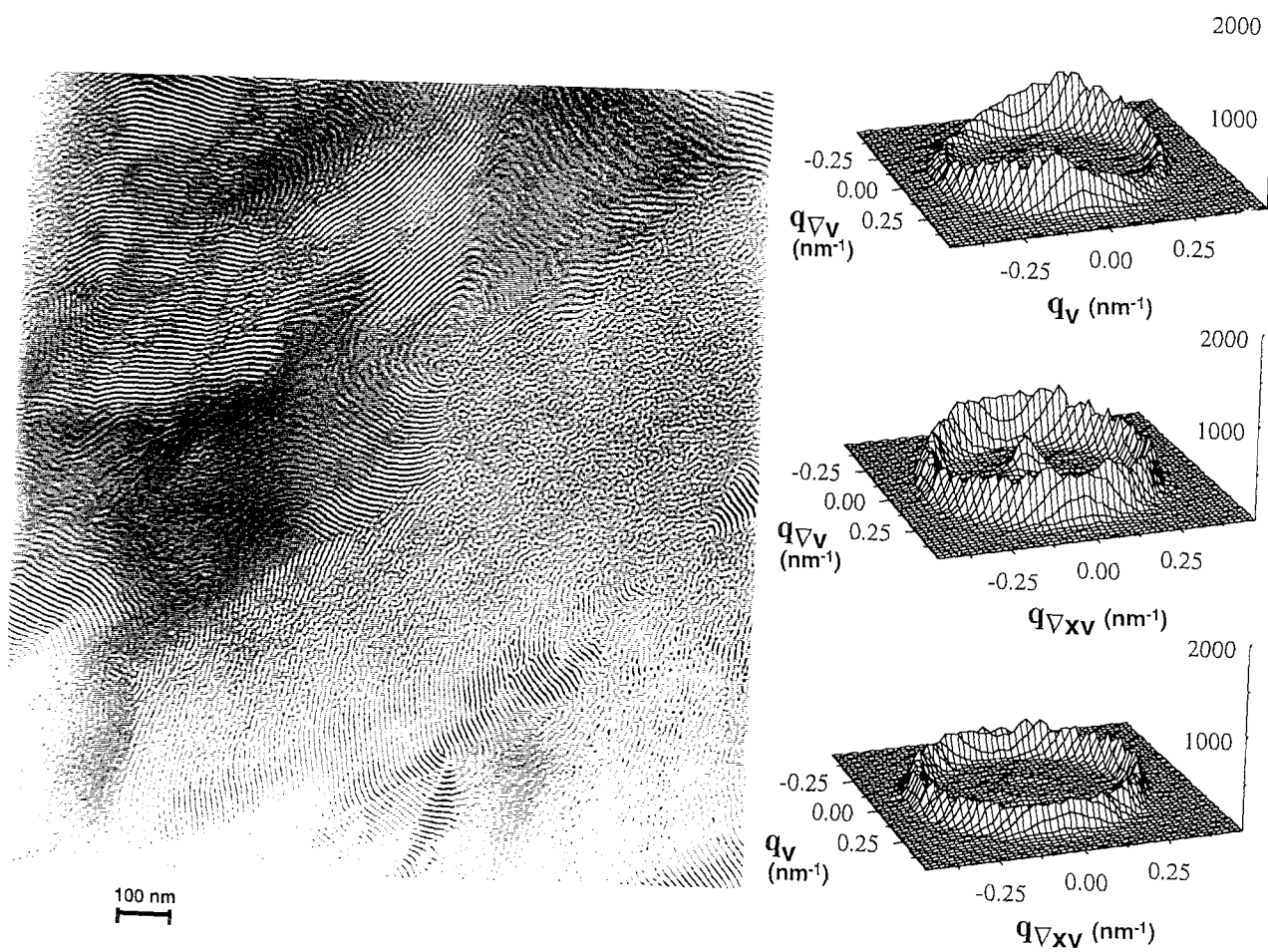


Fig.4

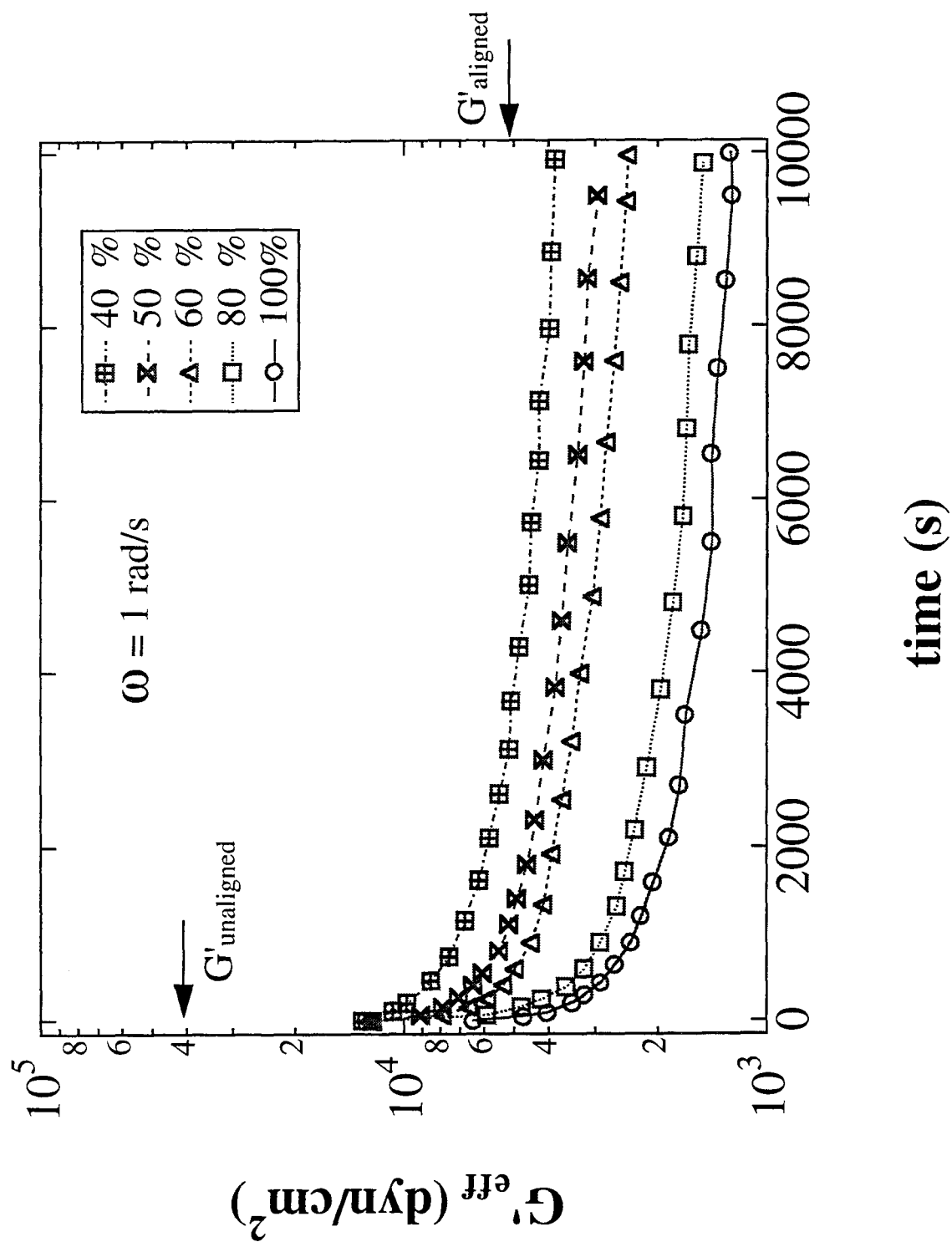


Fig. 5a

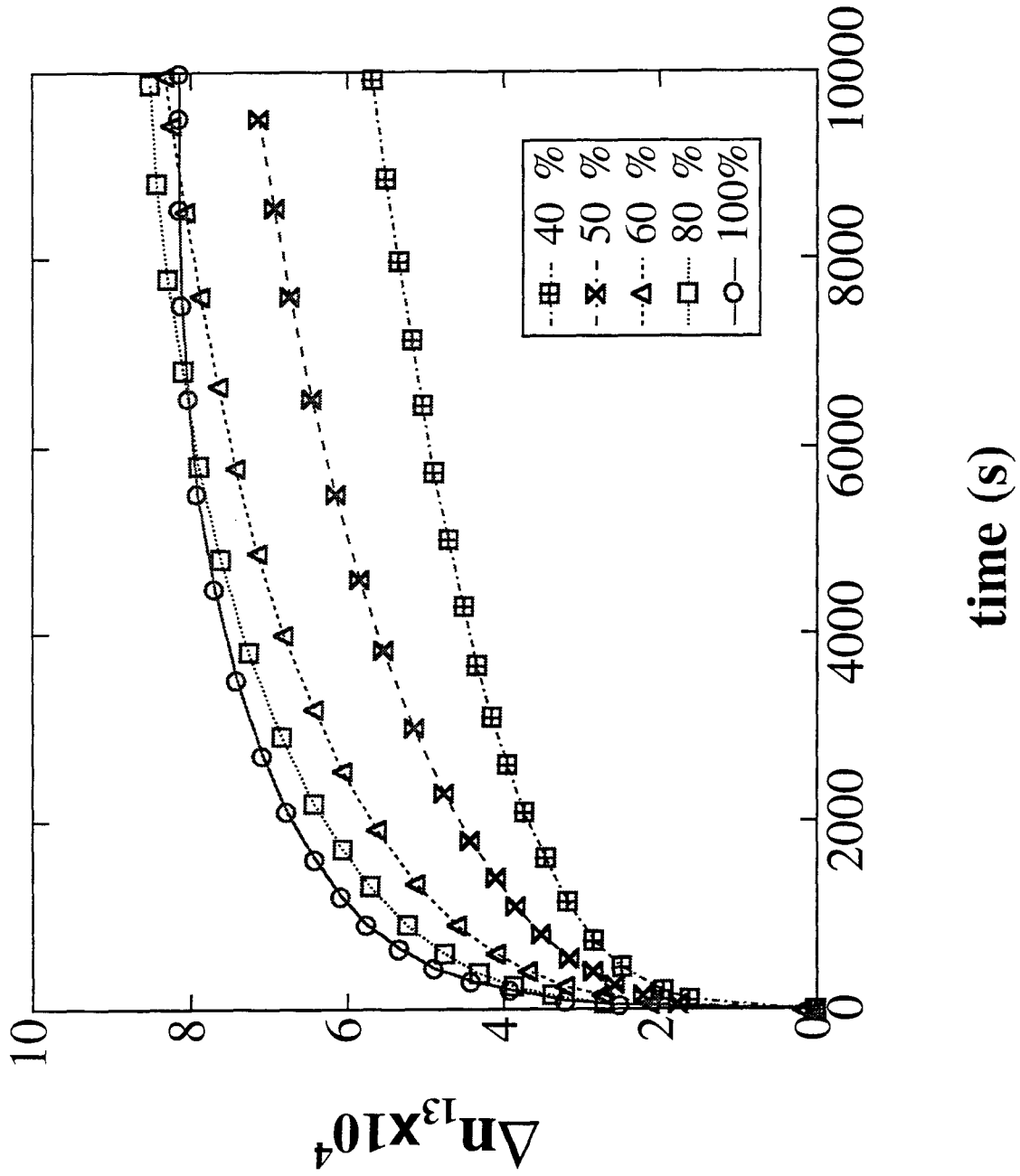


Fig. 5b

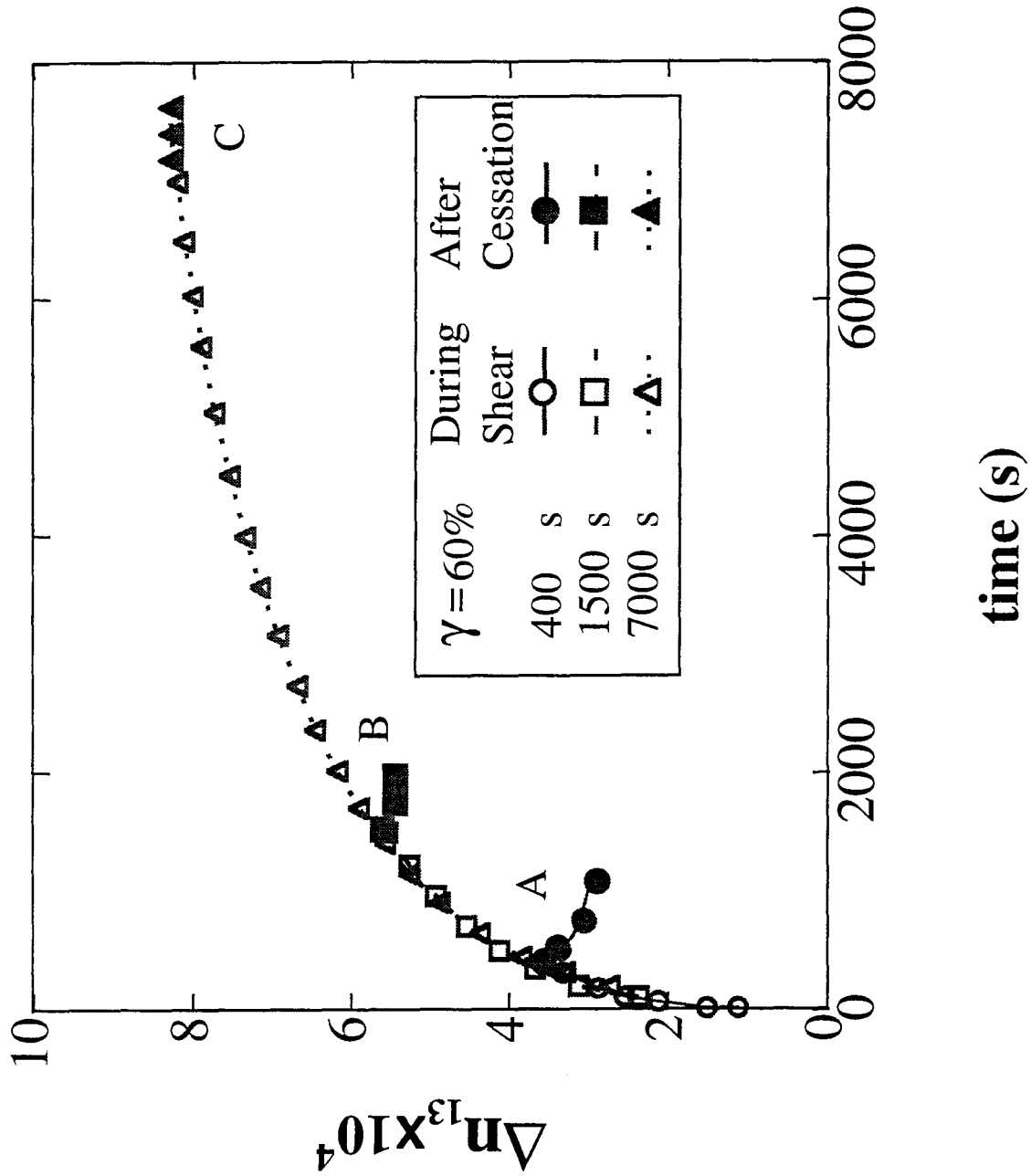


Fig. 5c

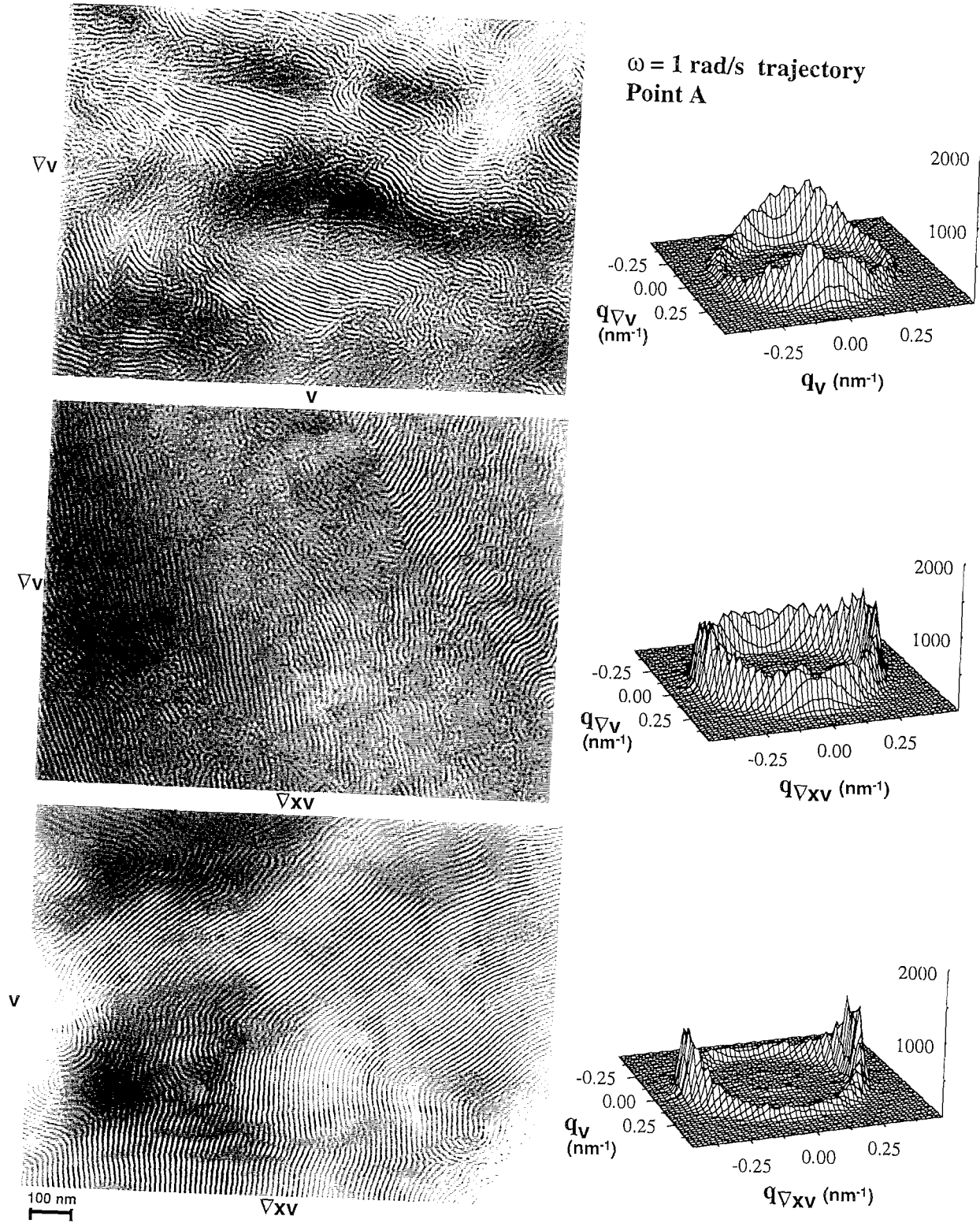


Fig.6

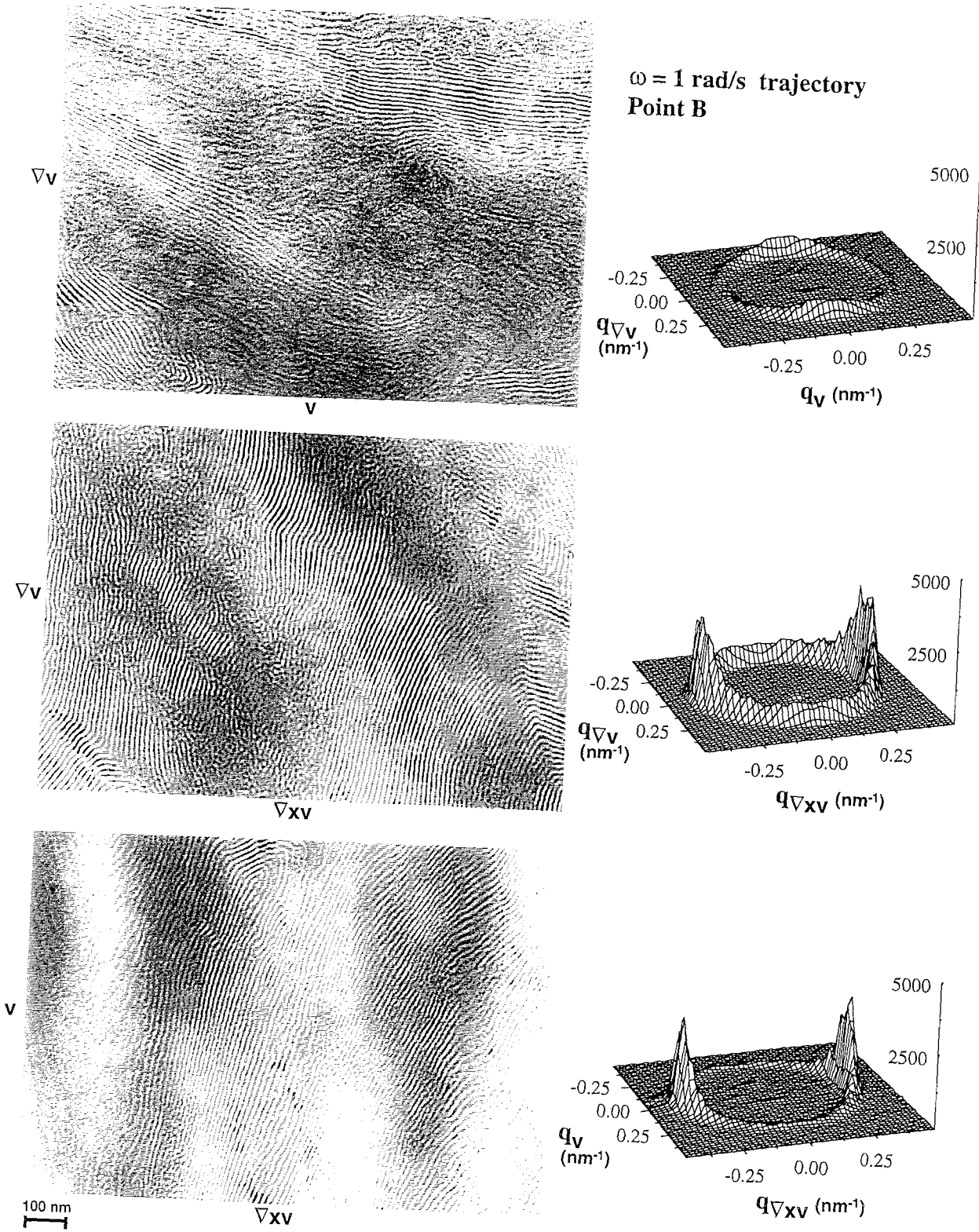


Fig.7

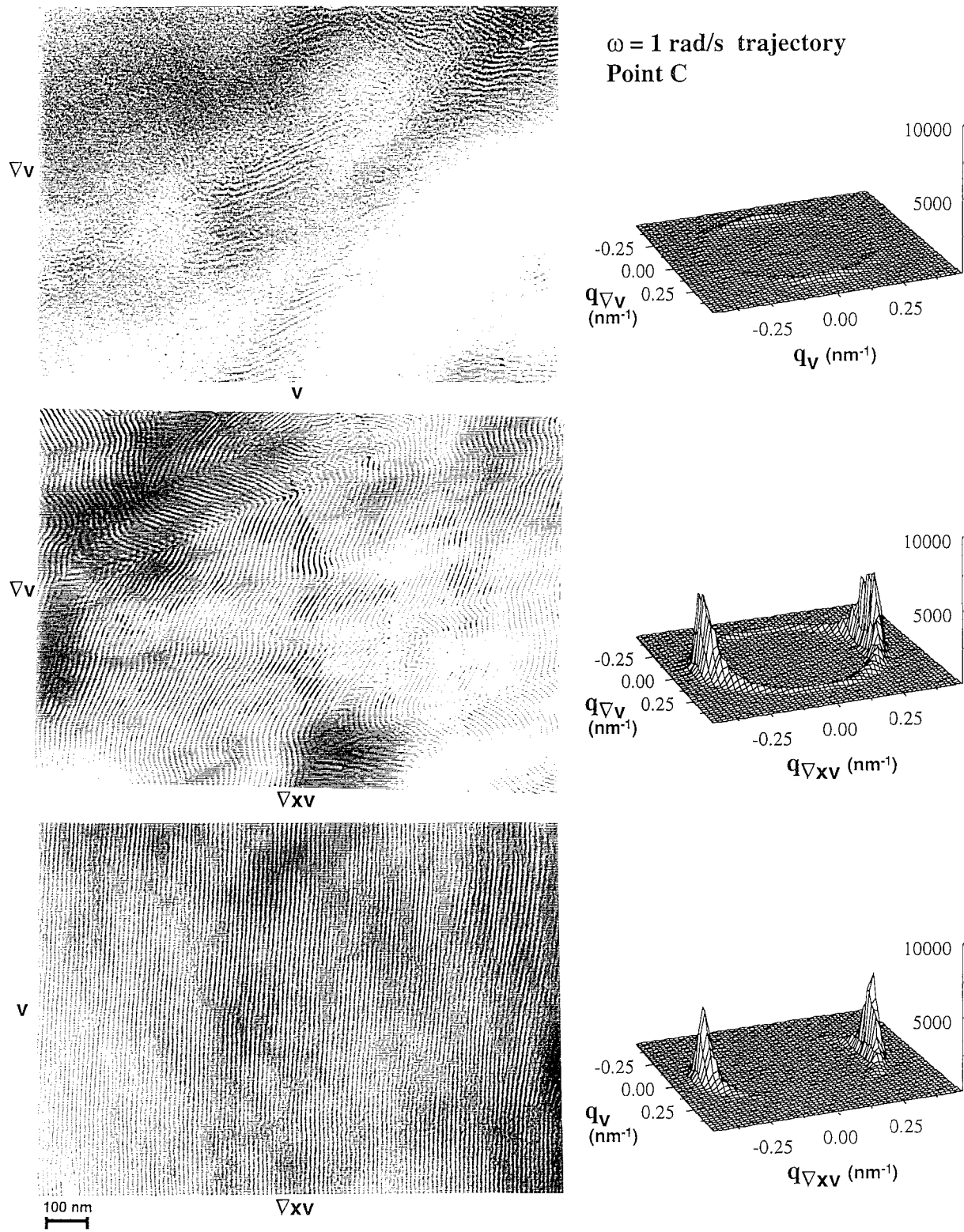


Fig.8

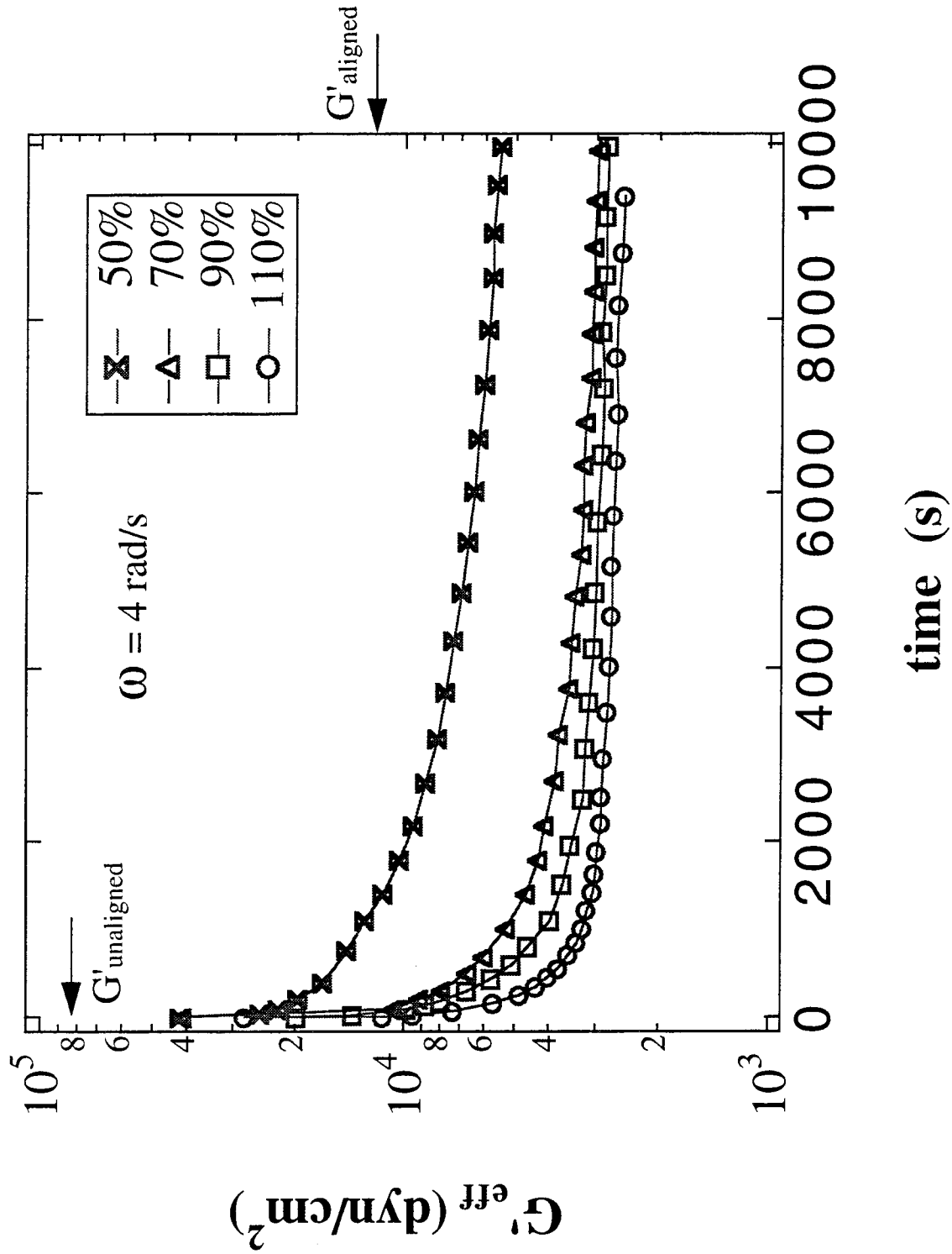


Fig.9a

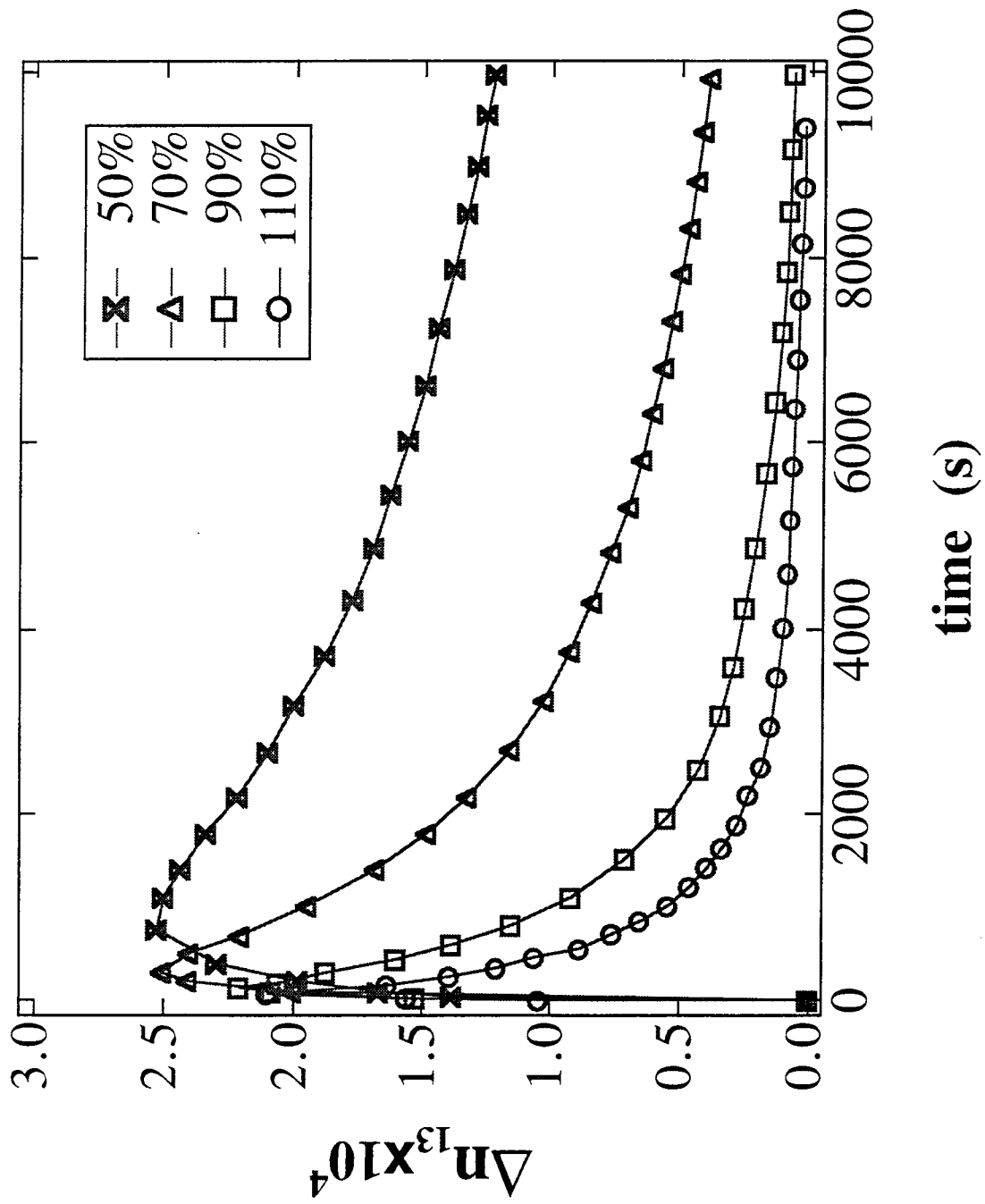
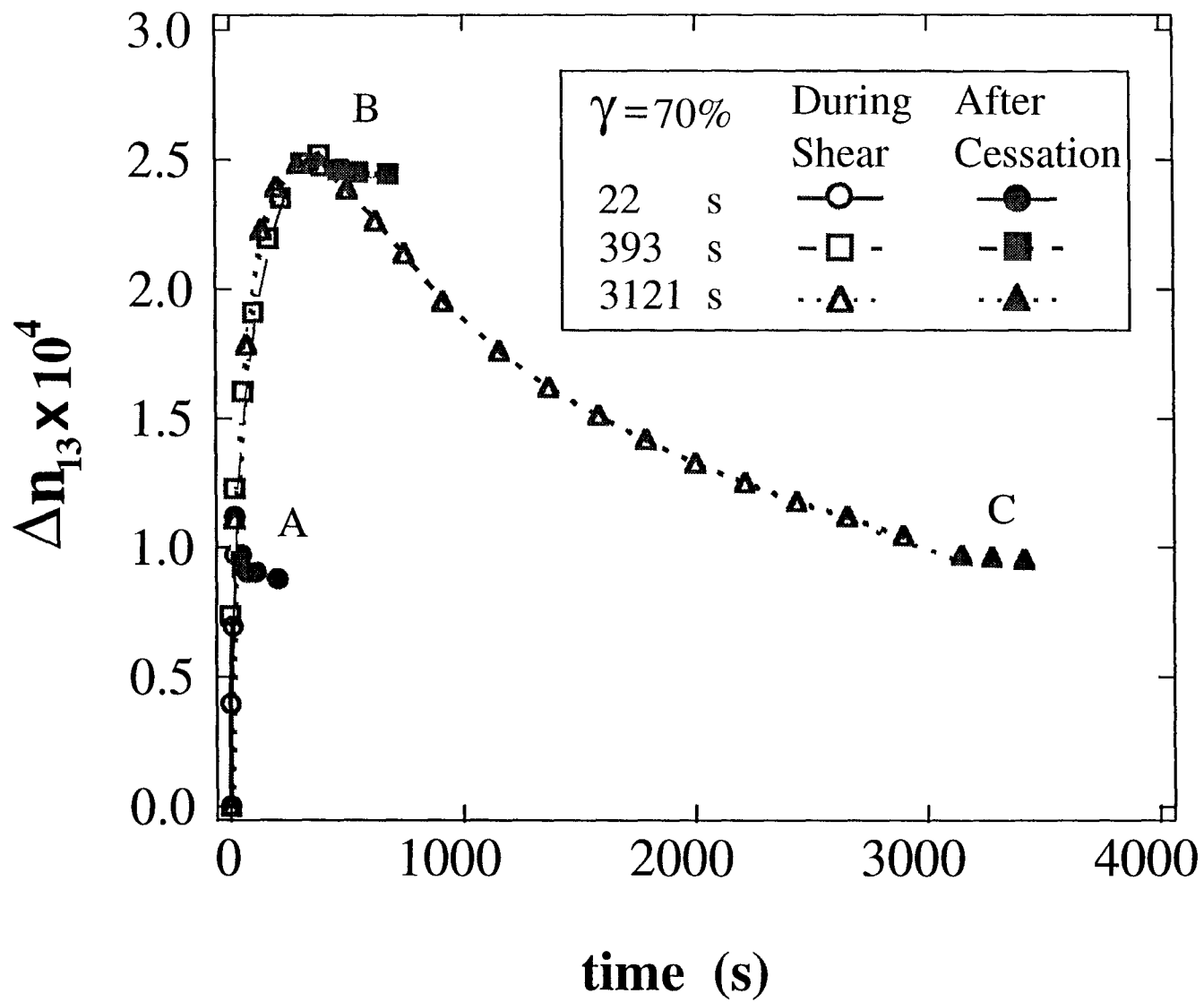


Fig.9b



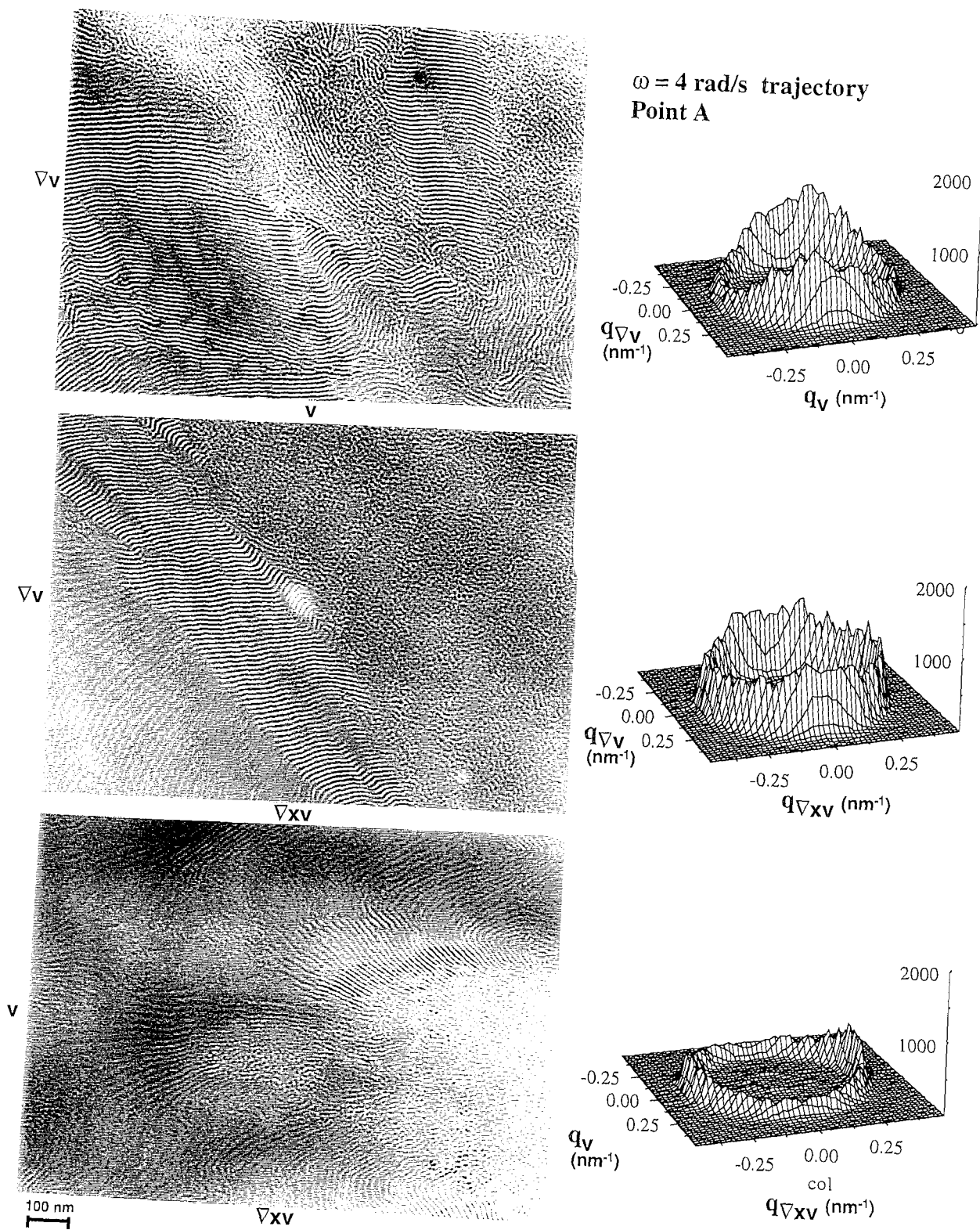


Fig.10

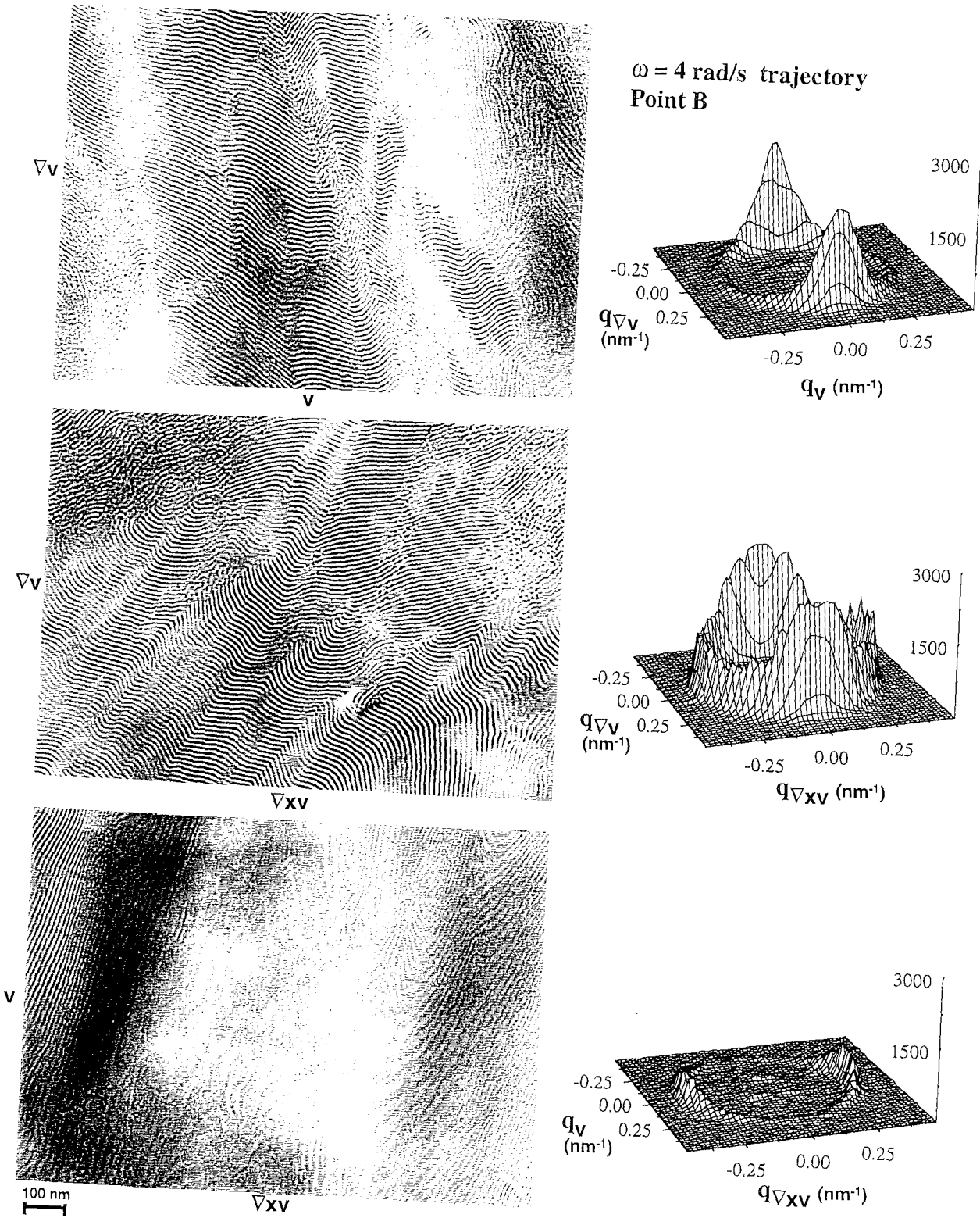


Fig.11

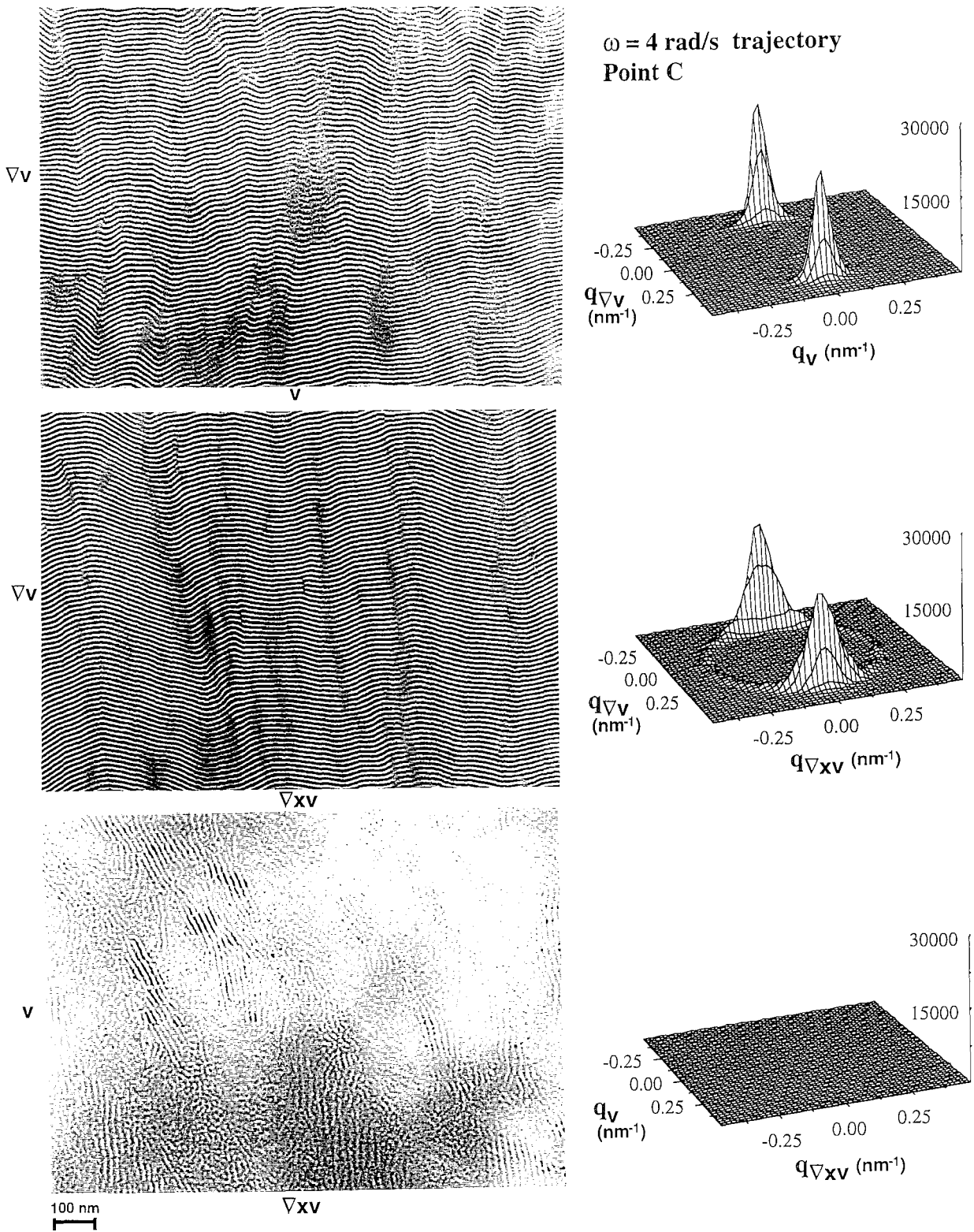


Fig.12

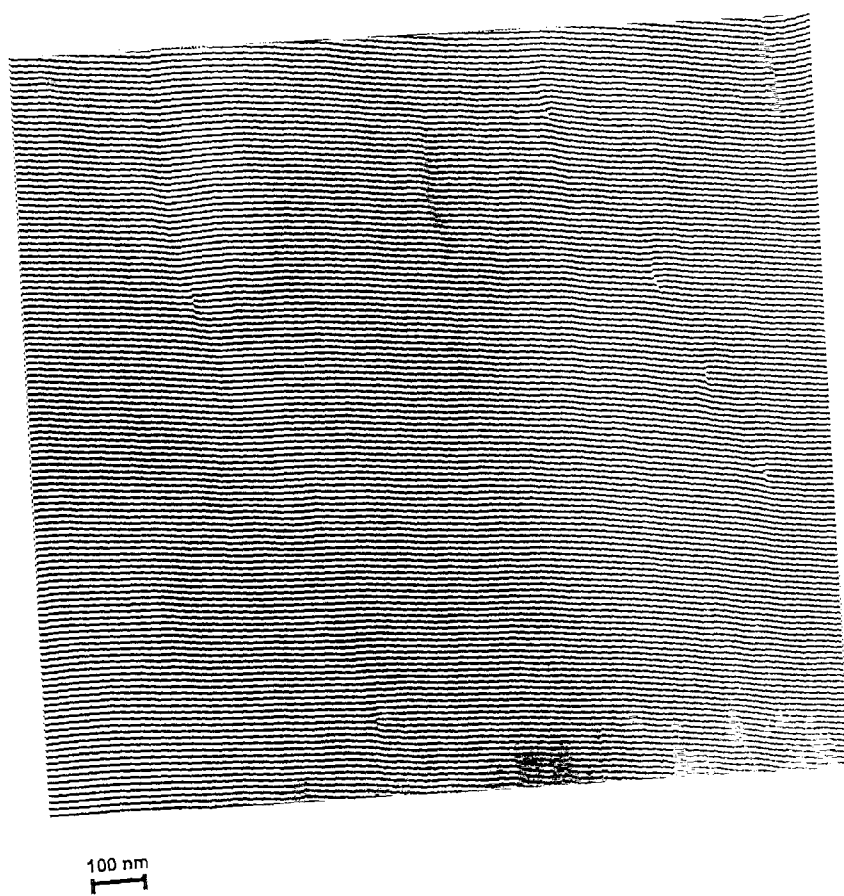


Fig.13

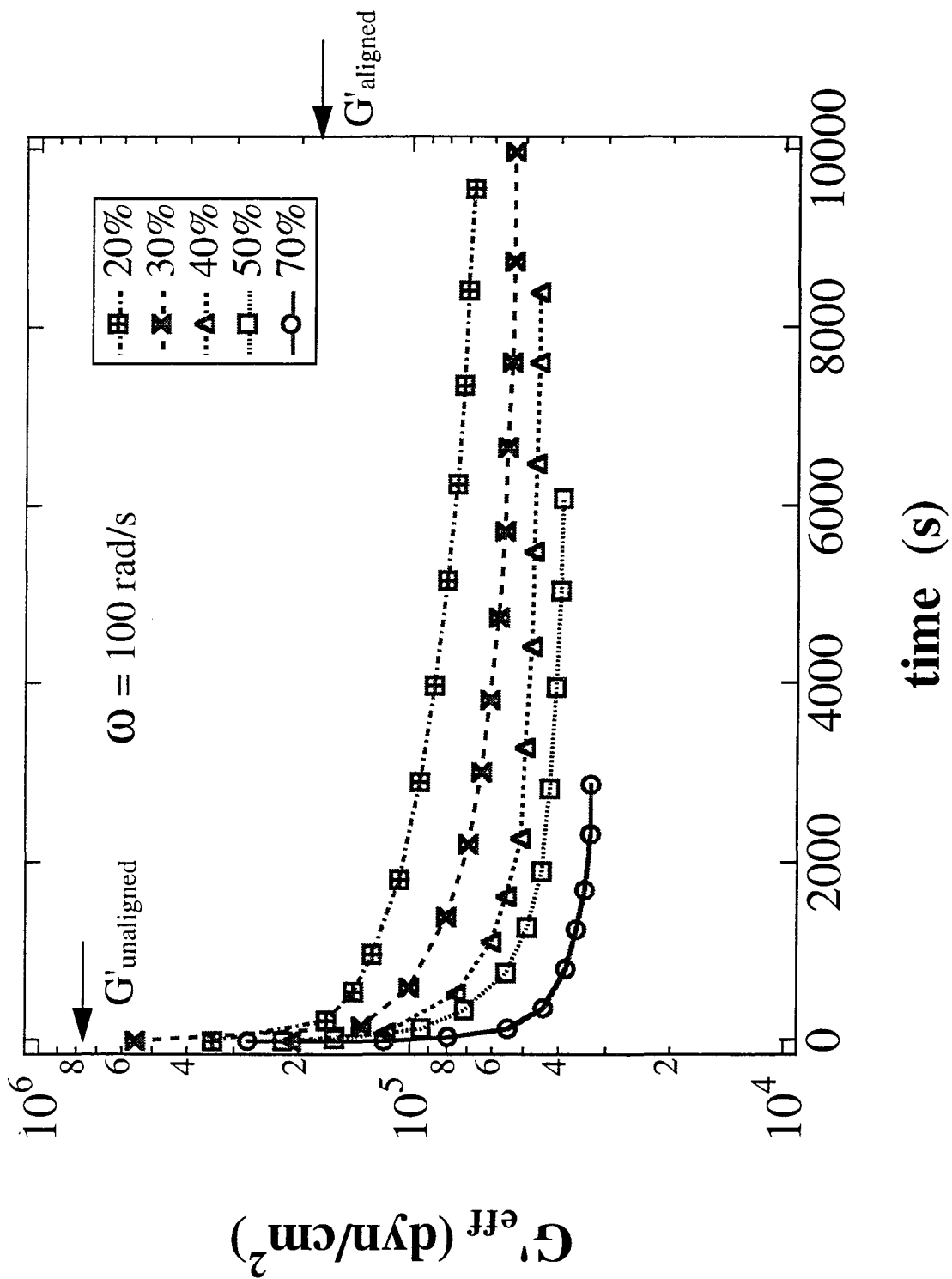


Fig. 14a

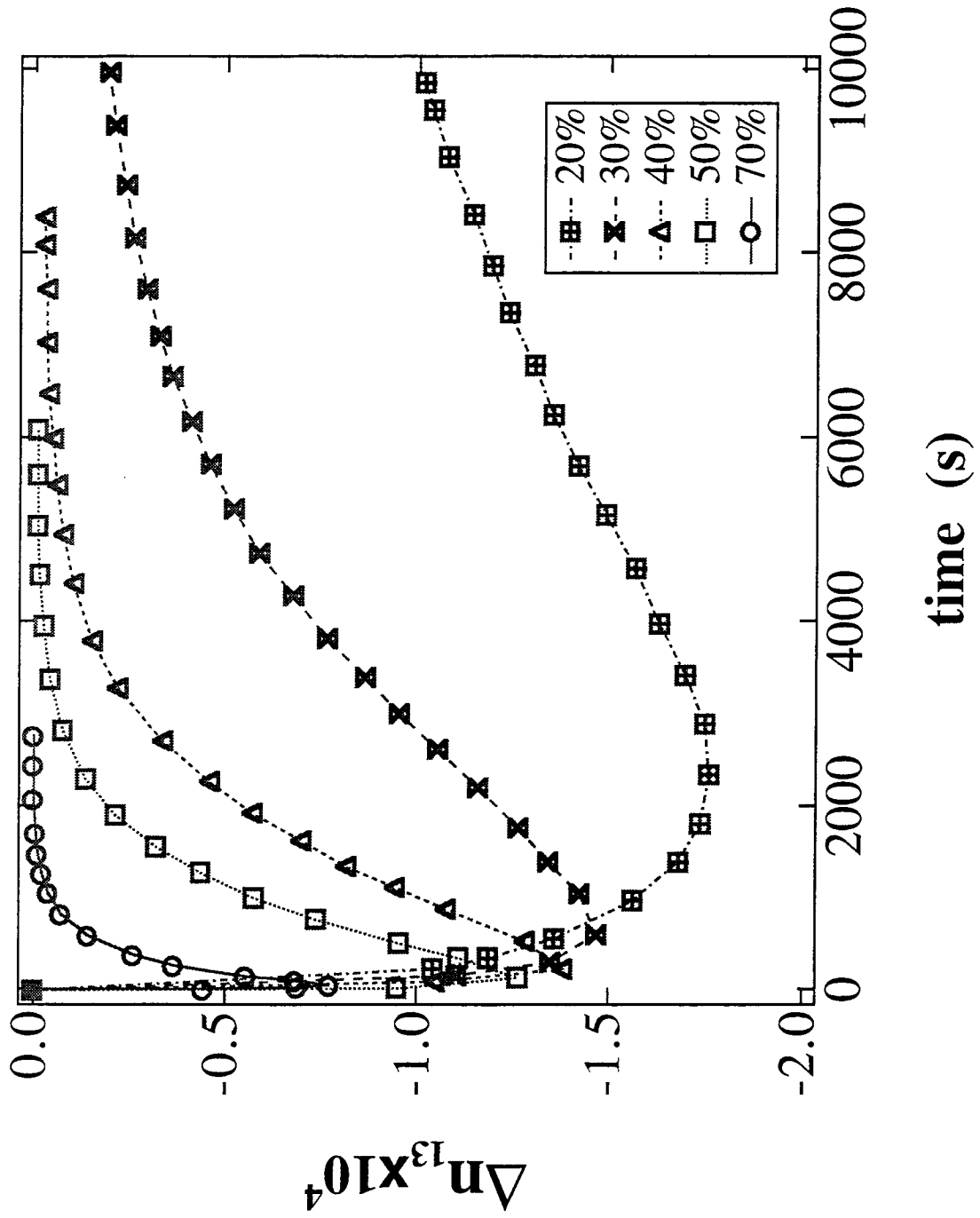


Fig. 14b

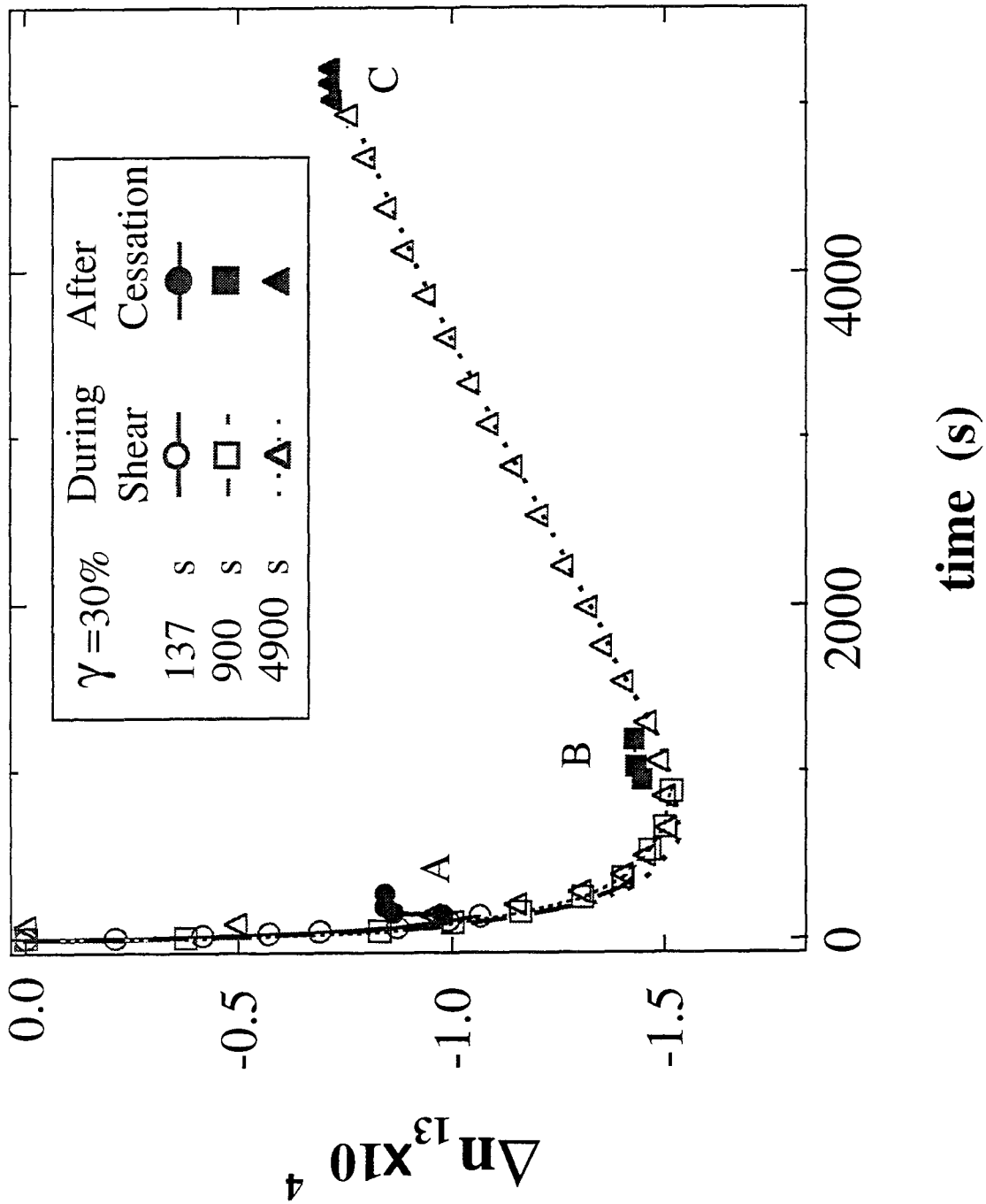


Fig. 14c

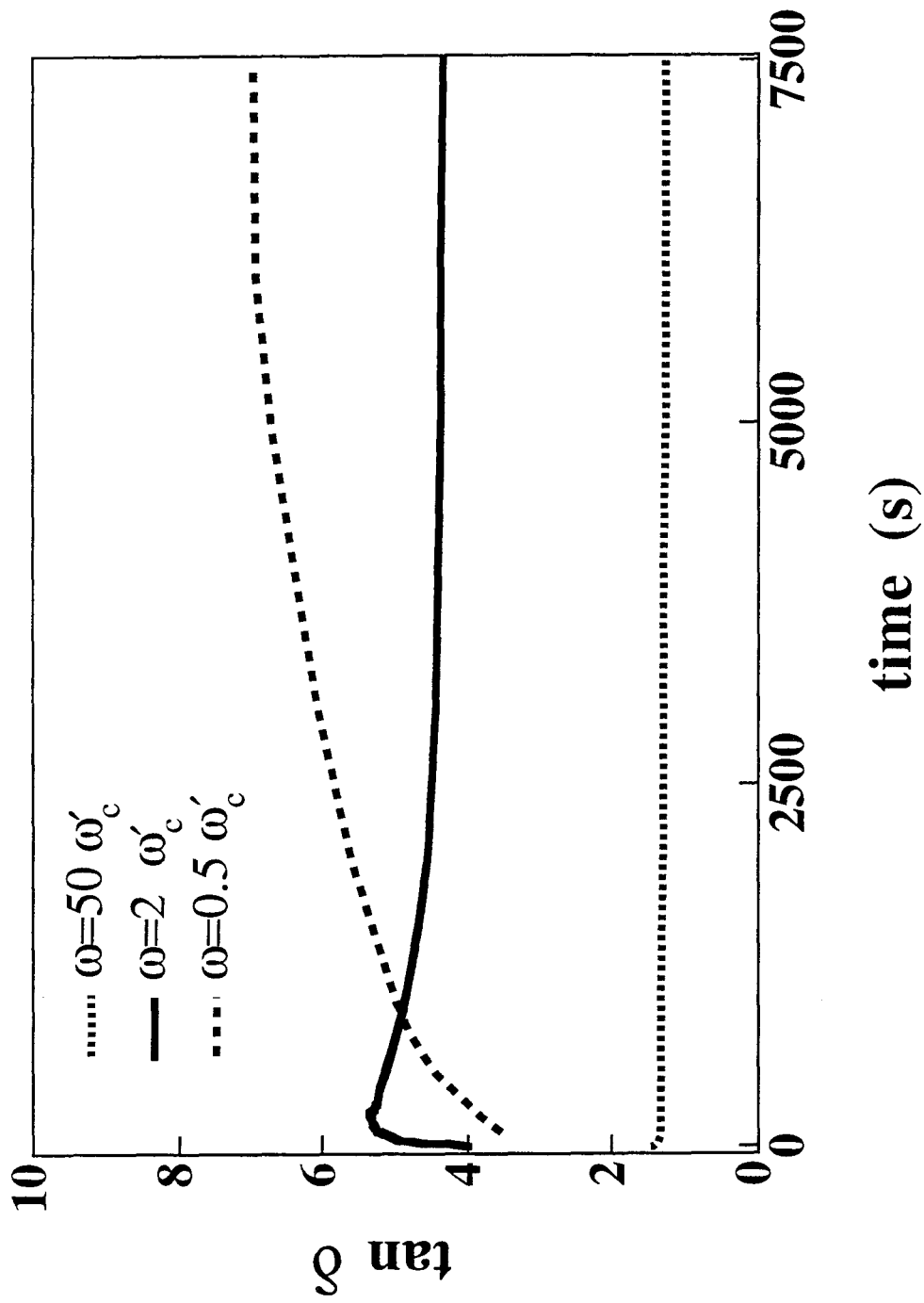


Fig.14d

$\omega = 100$ rad/s trajectory
Point A

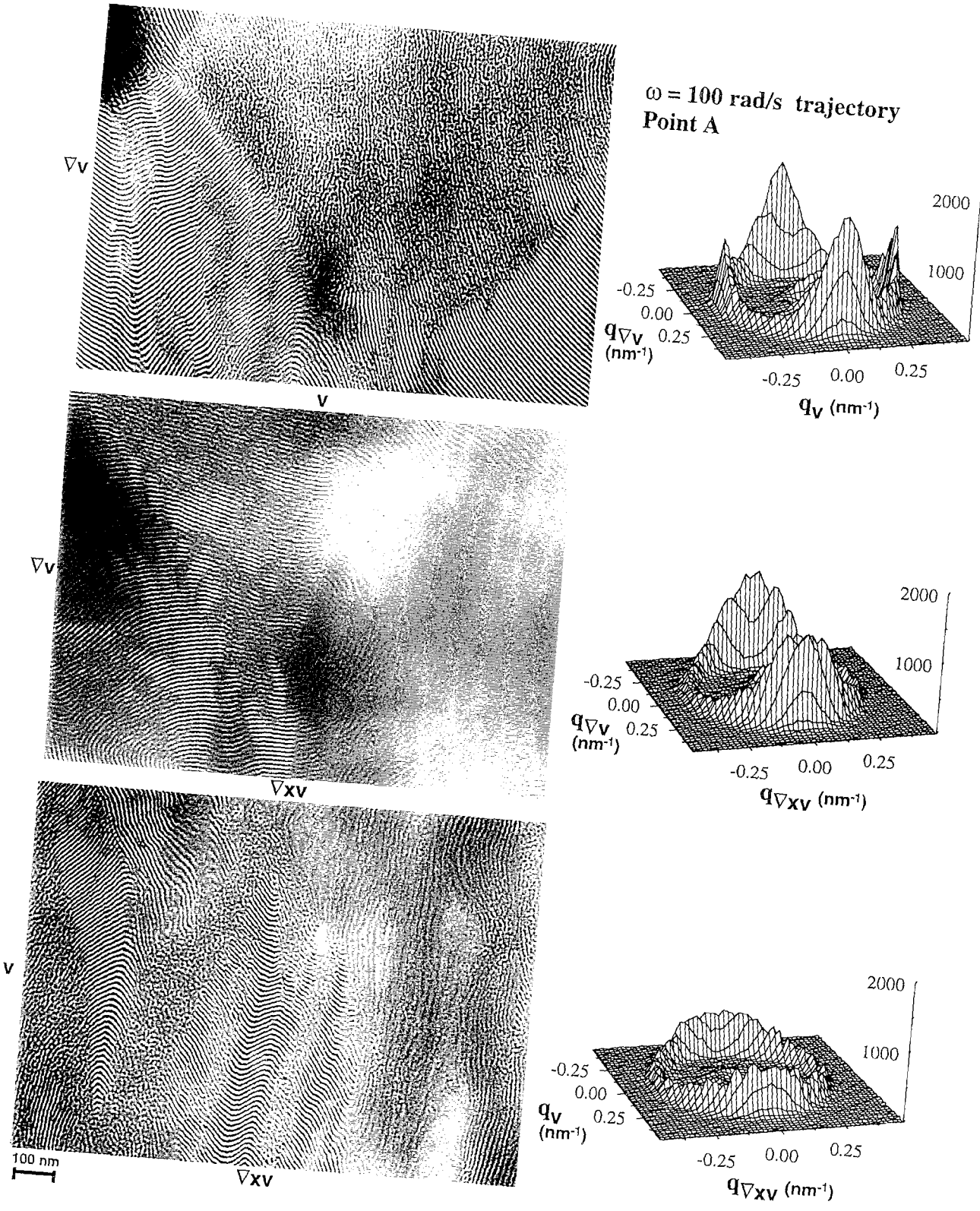


Fig.15

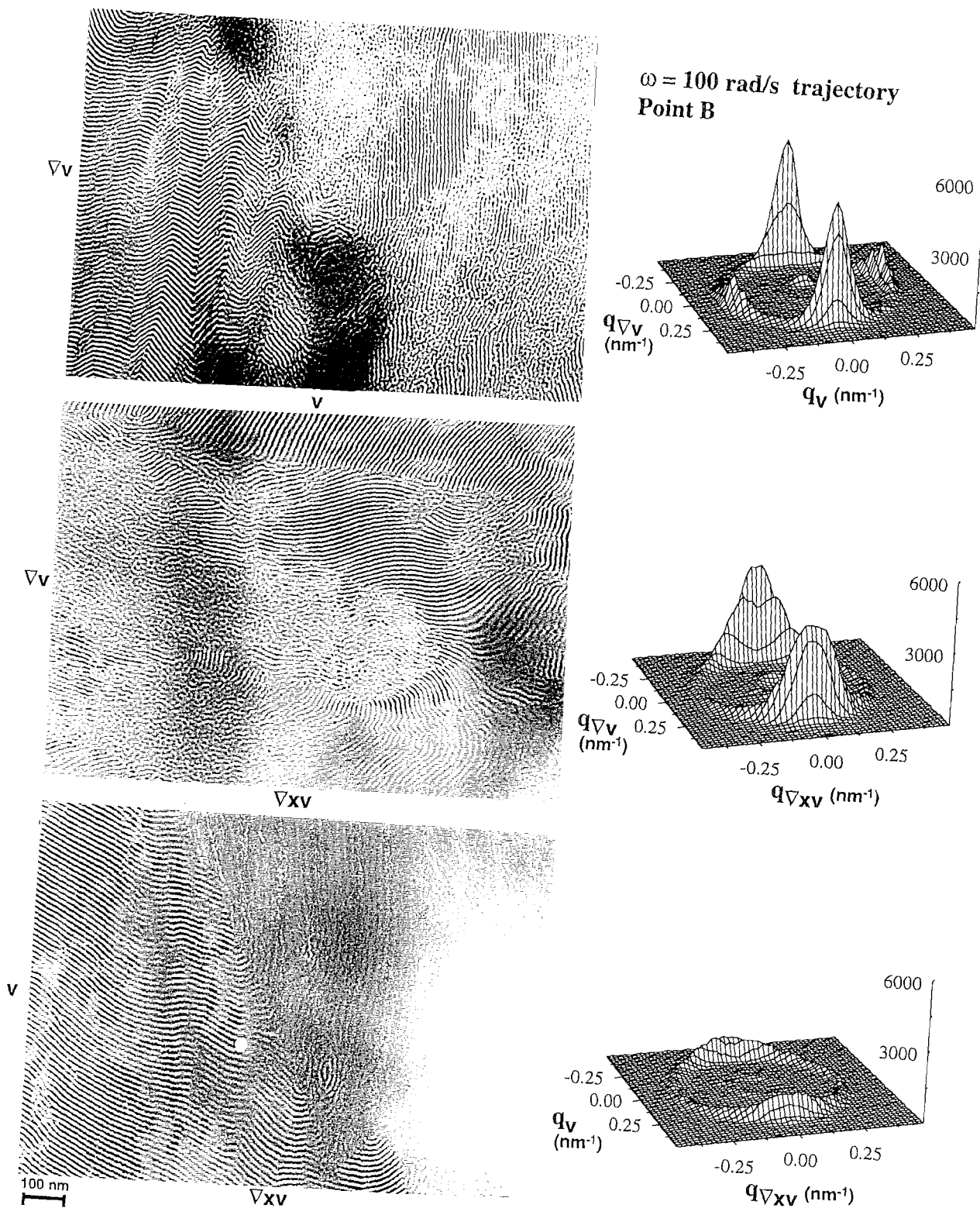


Fig.16

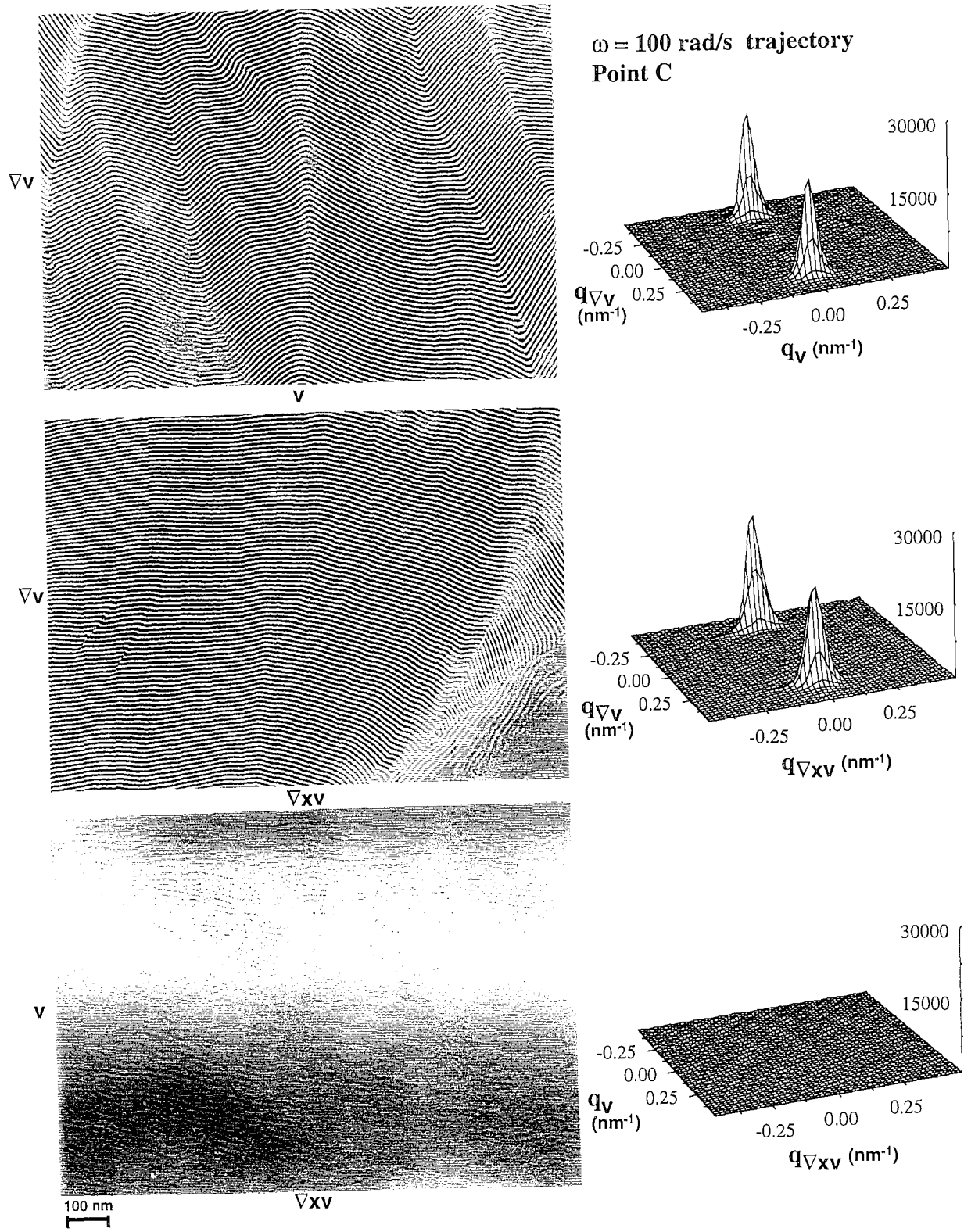


Fig.17

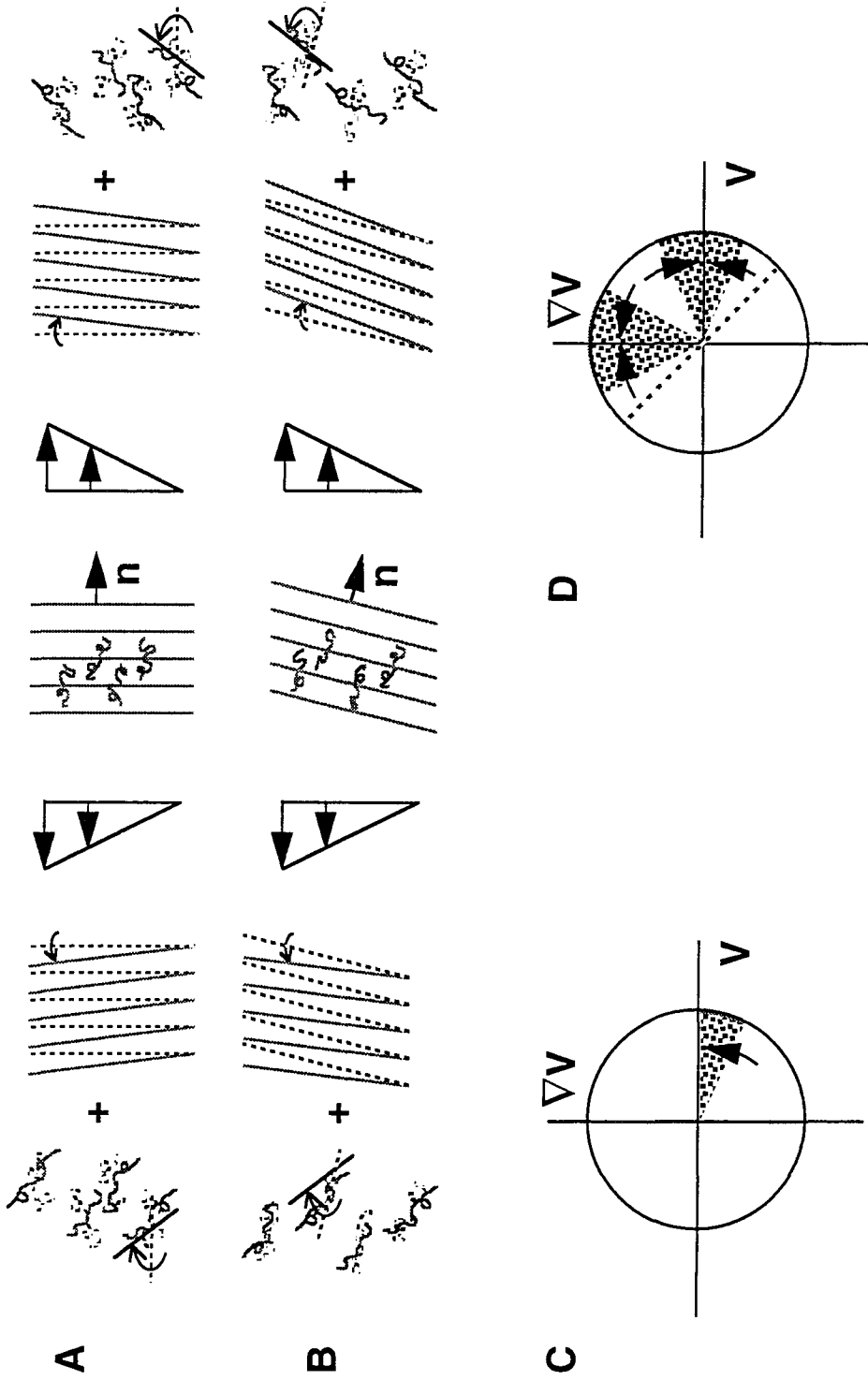


Fig.18

Chapter 3 ABC Triblocks: Phase Behavior and Shear Orientation

Abstract

ABC triblock copolymers can form a fascinating array of nanostructures and correspondingly exhibit complex phase behavior and dynamics. In this chapter, phase behavior and the effect of shear flow of a model ABC triblock system is described. The polymers are composed of styrene (S), isoprene (I), and a random copolymer segment of styrene and isoprene (R). They can be synthesized anionically in all three different permutations: SIR, RSI, and SRI. Here we examine polymers with equal length blocks and 50:50 S:I composition of the R block. Molar masses range from 15,000 g/mol per block (15K-15K-15K) to 35,000 g/mol per block (35K-35K-35K). In-situ rheo-optical methods are combined with ex-situ TEM and SAXS to examine the shear orientation behavior and phase transitions. Four types of morphologies were found: nearly symmetric or asymmetric two-phase lamellae (L2), two-phase hexagonal cylinders (H), bicontinuous cubic structure Ia3d (G), and three-phase lamellae (L3). The L3 phase of SIR-35 consists of repeating stacks of [I-S-I-R]. The I layers are observed to be continuous; while the intermediate layers are composed of alternating sections of S and R. When there is S on one side of an I layer, there is R on the other side. Thus, the defects represented by an S/R junction within a given layer are correlated with R/S defects on the layers just across the adjacent I layers. As these defects annihilate upon annealing, long range correlations produce striking patterns, including those that resemble a ships wake. Analogous defects are observed in RSI-35, but with S as continuous layers. However, these defects are not observed in SRI-35, in which all layers are nearly defect-free.

Oscillatory shear can induce global alignment of these nanostructures. For PS-PI-type two-phase lamellae, whether they are symmetric (SRI-20, SRI-15) or asymmetric (RSI-15, RSI-16B), whether they are formed by diblocks or two-phase separated ABC triblocks, the selection of parallel or perpendicular alignment and their pathways towards final aligned states are the same: perpendicular in Regime I ($\omega < \omega'_c$) and parallel in both Regime II ($\omega > \omega'_c$) and Regime III ($\omega \gg \omega'_c$). At $\omega \simeq \omega'_c$ the direction of alignment depends on strain amplitude: below a particular strain amplitude γ_c , perpendicular alignment is induced; above γ_c , the final orientation is parallel; at ω'_c and γ_c , a novel trajectory was discovered. As to ABA-type two-phase layers (SIR-20), only perpendicular alignment is induced. Only parallel alignment was found in the L3 phase of all samples (SRI-35, SIR-35, and RSI-35) so far. The H phase (both soft and hard cylinders) can be aligned along the velocity direction using shear. Shear-induced phase transitions were observed: in the temperature range within which the G phase of ISR-20 is most stable, shearing converts this bicontinuous cubic phase back to the hexagonal cylinder phase. Depending on shear frequency, either shear-induced alignment or shear-induced disordering was observed in the H phase of SIR-18B.

1. Introduction

Recent discoveries of a fascinating array of nanostructures^{1–10} present exciting possibilities for materials design. The versatility of ABC triblocks in creating new nanostructures results from the competition among the interaction parameters⁷. Thus, new morphologies can be formed simply by permutation of blocks, without changing the length and composition of each block. With a fixed sequence of blocks, varying the relative length of the blocks moves the systems through a range of different nanostructures.^{1,3}

In order to investigate the rich physics associated with this new frontier of materials science—such as the thermodynamics and mechanisms of the formation of interesting three-phase morphologies from disordered and/or two-phase states, shear-induced phase transitions and alignment, and defect dynamics—a model system has been designed. This model system consists of blocks of styrene (S), isoprene (I), and a random (R) copolymer of styrene and isoprene. S/I/R blocks can be connected in any order, by sequential addition of monomer to a living anionic polymerization, producing a narrow molecular weight distribution. The relative magnitude of the interaction parameters can be tuned as a continuous variable by changing styrene content in the random block. Further, a series of polymers that have progressively larger interaction parameters can be prepared by randomly hydrogenating the isoprene units to different extents from a single prepolymer (fixing the overall length, relative length of the three blocks, and the ratio of the interaction parameters). As a starting point, a series of triblocks with equal length blocks (S:I:R=1:1:1) and no hydrogenation have been investigated.

In this chapter, I present the phase behavior and shear orientation of sets of samples with three different permutations of the blocks SRI, SIR, and RSI. Four sets of samples with different block lengths are used to span a wide range of the repulsion between the blocks. Rich phase behaviors of these model triblock copolymers and the effect of molecular weight, temperature, and permutation will be described, followed by discussion of shear orientation of these different morphologies and shear-induced phase transitions.

2. Experimental Section

Materials: Model ABC triblock polymers are synthesized via anionic polymerization.¹¹ The three blocks are pure styrene, pure isoprene, and a random copolymer block of styrene and isoprene. All three blocks are of approximately of equal length, and the composition of the random block is about 50% styrene. Molecular weight for each block ranges from 15 Kg/mol (15K-15K-15K) to 35 Kg/mol (35K-35K-35K) (Table 1).

Table 1

Sample	Molar Mass (kg/mol)		Overall Styrene Content (% wt)
	First Block	Total	
SRI-35	35	156	44%
SIR-35	34	176	51%
RSI-35	46	132	52%
SRI-25	26	122	55%
SIR-25	23	110	54%
RSI-25	26	94	58%
SIR-20	19	68	55%
SRI-20	18	67	53%
RSI-20	27	79	53%
SRI-15	16	61	50%
SIR-15	17	52	46%
RSI-15	N/A	64	44%
RSI-16B	4:1=RSI-15:RSI-20		
RSI-19B	1:4=RSI-15:RSI-20		
SIR-18B	1:1=SIR-15:SIR-20		

Preparation of Samples for Structure Characterization: Samples for rheo-optical characterization and shear-induced alignment experiments are prepared as follows: the

polymer was dissolved in toluene with antioxidant (1% of polymer weight), and vacuum dried for at least 24 hours at 120°C.

Three types of samples are prepared for TEM and SAXS: solvent cast, shear aligned, and aligned-and-annealed. The solvent cast samples are prepared by adding antioxidant (1% of polymer weight) in toluene solution, evaporating the solvent slowly, vacuum drying for at least 24 hours at 120°C, and annealing at 110°C for 4 to 10 days. The shear aligned samples are obtained by loading the material in the flow cel, heating through the ODT if it is accessible, cooling to the desired temperature for shearing, shear aligning as desired for each sample, then cooling the aligned samples to room temperature and removing them from the flow-cell very carefully to avoid any extra deformation. The aligned-and-annealed samples are prepared by annealing sheared samples in the vacuum oven at a selected temperature for a specific period of time.

In-situ Monitoring of Phase Transitions: An RSA II rheometer equipped with an optical train is used for monitoring phase transitions. Two types of rheological experiments are performed: (1) temperature sweep at fixed frequency and (2) frequency sweep at fixed temperature. Using temperature sweep experiments, phase transitions of block copolymers can be evaluated by measuring the dynamic moduli at a low frequency over a range of temperatures: a change in morphology often results in an abrupt change in dynamic mechanical properties. The frequency dependence of the dynamic moduli at a given temperature provides information regarding the state of the samples; for example, the disordered state shows terminal behavior at low frequencies, the cubic phase shows solid-like elastic character, and unaligned lamellae show nearly power-law behavior at low frequencies ($G' \propto \omega^{0.5 \pm 0.1}$ and $G'' \propto \omega^{0.5 \pm 0.1}$). Birefringence is used for monitoring the state and morphology of BCPs, since zero birefringence could be the disordered state and some ordered states (such as bicontinuous cubic), and non-zero could mean other states (e.g., aligned cyliders and perpendicular lamellae).

Thus, in this work, both rheological and optical methods are applied for monitoring phase transitions. Five steps are applied to monitor and assign a phase state for most samples

investigated in this chapter: (1) conduct temperature sweep experiments using at least two frequencies for as-loaded samples to detect any discontinuity in their dynamic moduli; (2) run frequency sweep experiments at temperatures of interest (identified by the temperature sweep experiment) to detect the rheological signature of the material's state, and to assign possible phase states; (3) perform a shear alignment experiment to observe the optical trace of the process and measure the saturated value of the 1,3-birefringence; (4) perform temperature sweep experiments for these pre-aligned samples and measure the dynamic moduli and birefringence simultaneously for additional information on phase transitions; and (5) remove samples after selected thermal and flow histories for characterization by SAXS and TEM. Later in this article, we will refer this sequence of experiments as the 5-step procedure.

Characterization of Shear-Induced Alignment: A combined experimental approach was applied for this research, which includes an in-situ probe of alignment (rheo-optical methods) and ex-situ transmission electron microscopy (TEM) and small-angle x-ray scattering (SAXS) for structural characterization. Real-time monitoring using simultaneous, quantitative measurements of dynamic stress and birefringence was performed with a modified Rheometrics RSA II. Experimental details have been presented in Chapter 2. Light propagating along the velocity gradient direction (axis 2) is used to probe the projection of the refractive index tensor in the plane formed by the flow direction (axis 1) and the vorticity axis (axis 3), *i.e.* $\Delta n_{13} = n_{11} - n_{33}$. For these ABC triblock copolymers, the birefringence is dominated by the form contribution resulting from the microphase-separated structure. Therefore, the evolution of the steady offset in $\Delta n_{13}^{(d)}(t)$ probes the orientation distribution of nanostructures (the 1,3-projection of the second moment tensor, as described in Chapter 2). When the 1,3-birefringence reaches a saturated value, it often indicates that a well-aligned state has been reached. These shear aligned samples are used for characterization of their morphology using TEM and SAXS.

For TEM, material is taken from the center of the sample. Typically a 1mm x 2mm piece is cut from the middle of the slab of material removed from the flow cell. The sample

is cut into a shape such that the orientation of the flow geometry (\mathbf{v} , $\nabla\mathbf{v}$, $\nabla\times\mathbf{v}$) is readily evident during specimen placement for microtoming as described in Chapter 2. Microtoming is performed at a relatively low temperature of -160°C (Reichert Ultra-cut S with Leica EM-FCS chamber) and relatively thin (30-35 nm) sections are obtained. Samples are stained by exposing them to the vapor over OsO_4 crystals for 15 to 40 minutes. Images are recorded using a Phillips 420 (120 keV) microscope. During an imaging session, the orientation of the trapezoidal section relative to the alignment of the frame of the photograph is noted for each exposure. These notes are used to draw the orientation of the axes onto the images after prints are made. The cumulative uncertainty in recording the orientation of the images is less than $\pm 10^{\circ}$. In micrographs, dark regions consist of isoprene which is reacted with OsO_4 , white areas consist of styrene, and gray domains could either consist of the R block, or mixtures of R and I, or of R and S.

X-ray scattering patterns were collected using a Siemens Small Angle Scattering System that includes an Anton Paar HR-PHK high resolution pinhole optics system with a multiwire 2-D x-ray detector as described in Chapter 2. All samples were in the range of 0.6 to 0.8 mm in thickness. X-ray patterns were collected for either 10 or 30 minutes. The patterns were normalized for differences in thickness and collection time. Background scattering was negligible (less than 1% of the signal in the peaks).

3. Phase Behaviors

Morphologies of four series of symmetric ABC triblock copolymers and their blends are summarized in Fig. 1. For most of these samples, the 5-step procedure which has been described in the experimental section was applied to determine their phase behaviors. For the highest molar mass samples (25Kg/mol per block and above), only TEM or/and SAXS were used to identify their morphologies, because the kinetics of their phase transitions was too slow to observe by in-situ monitoring. As revealed by either the 5-step procedure or by TEM only, we found the following four morphologies: nearly symmetric or asymmetric two-

phase lamellae (L2), two-phase hexagonal cylinders (H), bicontinuous cubic structure Ia3d (G), and three-phase lamellae (L3) (Fig. 2abcd). Starting with the SRI permutation of the blocks, I will discuss samples with descending block length (35, 25, 20, and 15Kg/mol per block), and then move to the SIR and RSI samples. Finally I will comment on the combined effect of temperature and molecular weight on phase behavior.

For the sample that has the random copolymer block in the middle (SRI) and has the highest molecular size (35K g/mol per block), i.e. SRI-35, we observed a well-defined L3 phase at temperatures lower than 140°C, based on the TEM micrographs of both an aligned sample (aligned at 140°C) and an aligned-and-annealed sample (aligned at 140°C, and then annealed at 120°C for one week). This four-layer three-phase structure is clearly seen to have a [S-R-I-R] repeating sequence. The L2 phase was observed 170°C; and the R block appears to be miscible with the I block in this phase, since the dark layers observed by electron microscopy are thicker than the light ones. We have observed the coexistence of H with a small percentage of G in an aligned sample that was heated to 250°C for about 30 minutes. Although it is difficult to tell if the G phase is tricontinuous or bicontinuous from limited TEM micrographs, we rule out a tricontinuous cubic structure, since the G phase exists at temperatures higher than those for the H phase, in which the R and S blocks are already miscible. A bicontinuous cubic structure Ia3d (G) coexists with a small amount of H in an aligned sample (aligned at 250°C for 5 hours). Thus the coexistence of two morphologies is probably the consequence of slow kinetics of phase transition from H to G rather than any chemical changes of the material, such as decomposition or crosslinking. To verify this explanation, we annealed these samples at lower temperatures (170°C for 5 days and 140°C for 5 days) and L2 and L3 were recovered respectively.

As molecular size moves downward, for SRI-25 we observed two-phase lamellae even at the lowest experimental temperatures (limited by the highest T_g of the sample), even when the sample was annealed for a week at 140°C and 120°C respectively. Nearly symmetric lamellae are formed, since the black and white layers have almost equal thickness in the TEM micrographs: this may suggest that the middle block R is partially miscible with both

S and I blocks. With increasing temperature it appears that the morphology changes from L2 to H to G. This is based on electron micrographs of the following samples. A material that was aligned by shearing for five hours at 220°C, then rapidly cooled to room temperature showed coexisting L2 and H phases. When this sample was further treated by annealing under vacuum at 250°C for 30 minutes it showed coexisting H and G phases (Fig. 3). Thus the TEM micrographs suggest that there are order-order transitions around 220°C (from L2 to H) and 250°C (from H to G) as SRI-25 is heated from below 140°C to above 250°C. Unfortunately, these transition temperatures could not be established rheologically, since the kinetics of the phase transitions of SRI-25 and SRI-35 are too slow to allow real-time rheological or rheo-optical monitoring. For the sample with shorter block length SRI-20, only the L2 phase was observed; no phase transitions were detected by either rheo-optical methods or TEM and SAXS from 110°C to 280°C. Using the 5-step procedure, we identified one phase transition in the sample with shortest block length, i.e. SRI-15. The order-disorder transition (ODT) from L2 occurs around 135°C (T_{ODT}).

Samples with the SIR permutation have predominately lamellar structure throughout the temperature range from 110°C to 280°C. For SIR-35, there is an order-order transition (OOT) from the L2 phase to the L3 phase as the sample is cooled through 210°C as revealed by temperature sweep experiments and TEM micrographs. At elevated temperature, the R and S blocks are miscible as indicated by thicker light layers than dark ones in the micrographs of the L2 phase. When the sample cools down below 210°C, phase separation occurs between R and S blocks. The three microphase segregated structure has an L3 morphology with an [S-I-R-I] repeat. All samples of this morphology contain a distinct type of defect that is indicative of an L2 [I-(S/R)] to L3 [S-I-R-I] phase transition. The L3 phase contains continuous I-layers (that already existed in the L2 phase), but their intermediate layers have S-regions and R-regions, which correlate with R-regions and S-regions respectively on the other side of the adjacent isoprene layers (Fig. 2d). We call the breaks in the R (or S) layers “correlated perforations” (Fig. 4). To our knowledge, this is the first time that this unique type of defect has been found. As these defects annihilate

upon annealing below 210°C, long range correlations produce striking patterns, including those that resemble a ship's wake (Fig. 5ab). Analogous defects are observed in RSI-35, but with S as continuous layers. However, these defects are not observed in SRI-35, in which all layers are nearly defect-free. A possible explanation for the difference is illustrated in schematic diagrams (Fig. 6abc) of order-order transitions from two-nanophase to three-nanophase segregations.

As the molecular size decreases, we observed only the L2 phase for the whole range of temperature (110-280°C) in SIR-25; the ODT is still not accessible. The 5-step procedure revealed an ODT from L2 at 220°C for SIR-20. In the following section, I will demonstrate how this 5-step procedure applies to this sample in detail. SIR-15 has the lowest molecular weight, and we are not able to observe any well-defined structure. We suspect the anticipated ODT for this sample is below the T_g of styrene-rich phase. As long as phase separation occurs locally, the styrene-rich phase that forms is rigid at that temperature and prevents further self-organization of the material. Indeed, we observed a very poorly phase-separated state (Fig. 2e). In order to test this idea, a blend consisting of equal amounts of SIR-20 and SIR-15 is prepared. By the 5-step procedure, the phase transition from hexagonal cylinder to disorder is detected around 154°C. This is the only material we have in this research that has styrene cylinders in an isoprene-rich matrix, which suggests that the I and R blocks are mixed in the continuous microphase (Fig. 2b).

Rich thermodynamics and phase transitions have been observed in RSI samples. Similar to SIR-35, correlated perforations exist in the three-phase lamellae of RSI-35. The L3 and L2 phases coexist at 140°C, and this mixed state converts to the L3 phase after prolonged annealing at 120°C for a week (Fig. 7ab). Two-phase lamellae have been observed at 180°C and 200°C. The G phase was observed at 250°C (Fig. 2c). Only the H phase with isoprene (dark) cylinders in a styrene rich S/R (gray) matrix exists over the whole range of temperature for RSI-25. Revealed by the 5-step procedure, RSI-20 has an order-order transition from the H phase (isoprene cylinders) to a G phase at T_{OOT} (220°C). This G phase is disordered above 265°C. On the other hand, the phase transition from G to H can

be induced by shearing as well. These interesting shear related phenomena will be discussed in a separate section. The shortest sample RSI-15 has ODT around 140°C; an asymmetric L2 phase (Fig. 2a) is observed below T_{ODT} , in which the R and I blocks are miscible with each other. To investigate the effect of blending, we prepared blends of RSI-15 and RSI-20. For the RSI-16B consisting of 80% of RSI-15, a L2 phase is observed with a slightly higher T_{ODT} . The blend RSI-19B consisting of 20% of RSI-15 has similar phase behavior to that of RSI-20 with slightly lower T_{OOT} and T_{ODT} .

In examining the combined effect of molecular size and temperature on morphologies, we use $\chi_{SI}N_{total}$ which is the product of the interaction parameter of polystyrene and polyisoprene and the total molecular weight of the sample. Since many equations have been suggested to correlate the effect of temperature with χ_{SI} , we use one suggested by Bates et al.³⁴ for the convenience of comparing our results with their phase diagram of the PS-PI diblock system. For all three permutations, the L3 phase occurs only when $\chi_{SI}N_{total}$ is about 40 or above, while the disordered state occurs when $\chi_{SI}N_{total}$ is less than approximately 12.5. This may explain why SIR-15 is disordered, since $\chi_{SI}N_{total}$ is too small (below 12); and why SRI-25, SIR-25, and RSI-25 do not have the L3 phase. At intermediate $\chi_{SI}N_{total}$, the complexity of phase behavior is at least comparable with that of PS-PI diblock copolymer melts.³⁴

The effect of permutation of the S/I/R blocks probably plays a role as well,^{6,7} even for the two-phase morphologies. We found that the phase behavior of one permutation is quite different from that of the others. For example, SRI-20 has phase and flow behaviors similar to those of symmetric PS-PI diblock copolymers,³⁴ SIR-20 behaves like ABA-type PS-PI-PS lamellae, while RSI-20 has both H and G phases. SRI-25 has at least three types of morphologies (L2, H, and G), SIR-25 has only the L2 phase, while RSI-25 has only the H phase. Unfortunately, it is difficult to differentiate the effects of permutation from that of $\chi_{SI}N_{total}$ from the results obtained from samples investigated here. Even for samples with the same permutation, we are not able to have a concrete conclusion regarding the effect of $\chi_{SI}N_{total}$. The complex phase behavior could be the consequence of small variations in

relative block lengths and in the composition of the random block. Indeed as shown in Table I, the samples we used in this research are not exactly symmetric, nor do they have exactly 50% styrene units. However, we can still explain the observed results based on a very basic phase diagram. When two adjacent blocks are miscible, these triblocks behave similar to asymmetric diblock copolymers, with chain length ratio of approximately 1:2. This composition is near the border of lamellae and hexagonal cylinders. Thus slight variations in the relative block length would result in different phase behavior. The greater the total length of two miscible blocks, the better the chance that the H phase will be formed. Such an effect has been observed in the blends of RSI-15 (L2) and RSI-20 (H below 220°C): the morphology moves from the L2 phase of a 4:1 blend (SI-16B) to the H phase of a 1:4 blend (RSI-19B). At higher temperature, the H phase could also undergo a transition to the bicontinuous cubic structure before disorder, in accord with the order-order transition of RSI-20 at 220°C.

4. Effect of Shear Flow: Shear Orientation and Shear-Induced Phase Transitions

This section deals with shear orientation of two-phase lamellae and hexagonal cylinders, which are the most common morphologies in these systems. An additional reason that these two-phase morphologies will be the main subject is that they usually have accessible ODT, which allows the best control of initial conditions by heating over ODT to erase the flow and thermal histories. Samples that have the L3 phase do not have accessible ODT, thus it is difficult to control the initial condition before applying shear deformation, since these samples can be aligned during pressing and loading them in the flow cell. This limitation prevents us from making any conclusive comments regarding alignment behaviors of the L3 phase.

Regarding the two-phase lamellae, we have studied the flow-induced structural evolution of a nearly symmetric PS-PI diblock copolymer in Chapter 2. Three different trajectories of alignment has been identified in three different regimes (Regime I, III and III).^{25,26,35} On

the other hand, ABA-type triblock copolymers exhibit very different flow behaviors than AB diblocks.^{16,22} Shear-induced alignment of hexagonal cylinders has been investigated and hard cylinders in a soft matrix have attracted the most attention. As presented in the previous section, both AB-type and ABA type two-phase lamellae, and both soft (isoprene-rich) and hard (styrene-rich) cylinders have been observed in S/I/R triblock copolymers. Thus investigation of shear orientation of two-phase structures formed by S/I/R triblock copolymers provides an opportunity to test basic concepts which have been proposed previously and provides answers to questions raised regarding ABC-triblocks. For example, do asymmetric AB-type two-phase lamellae behave differently than symmetric AB diblock lamellae? Do they behave like PEP-PEE-type or PS-PI-type lamellae? Do ABA-type lamellae formed by SIR-20 behave similar to SIS triblocks or PEP-PEE-PEP triblocks? Does the L3 phase behave like an AB-type or ABA-type L2 phase or neither of them? Is there any difference in alignment behavior between soft cylinders and hard cylinders? etc. In the following, we present the alignment behavior of the ABA-type L2 phase, the AB-type symmetric and asymmetric L2 phases, and the L3 phase. As to hexagonal cylinders, I will focus on alignment and the order-order phase transitions induced by oscillatory shear.

A. ABA-Type Two-Phase Lamellae

Before discussing shear-induced orientation, here the 5-step procedure is illustrated to identify the phase behavior of SIR-20. The first step (a temperature sweep experiment) is presented in Fig. 8a. Both storage and loss moduli drop at around 220°C (if no discontinuity were detected, another temperature sweep with lower shear frequency would be necessary). The second step (frequency sweep experiments at different temperatures) verifies that this phase transition is the ODT, since terminal behavior, i.e. $G'(\omega) \propto \omega^2$, is observed in Fig. 9. The slope of $\log G'$ vs. $\log \omega$ in the ordered state is about 0.7, which suggests a possible lamellar morphology. This sample is then subject to a large amplitude oscillatory shear (the third step), and the rheological and optical responses (Fig. 10) are recorded.

The fourth step is recording the optical trace during the process of heating the pre-aligned sample (Fig. 8b), which could be carried out either the same way as a temperature sweep experiment or simply heating without rheological monitoring. The 1,3-birefringence drops at around 220°C, consistent with the simultaneous rheological response and with the rheological signature in the first step. In contrast to a previous report regarding PS-PI solutions,³⁶ there is no difference in T_{ODT} between aligned and unaligned samples. From the magnitude of the 1,3-birefringence, we can get a rough idea about the possible morphology. A sheared sample was quenched to room temperature for TEM and SAXS. We noted that the aligned sample showed a much better defined morphology in TEM micrographs than did the simple solvent-cast material.

The characteristic frequency ω'_c is determined as 0.3 rad/s at the reference temperature of 130°C (Fig. 9). Shear orientation experiments were performed both below and above ω'_c (from $0.1\omega'_c$ to $10\omega'_c$; see arrows in Fig. 9) at various temperatures (130°C to 180°C) and strain amplitudes ($\gamma_o = 0.2$ to 1). Only perpendicular alignment was induced by all shearing conditions: parallel alignment was not induced even at frequencies higher than ω'_c . This behavior is different from AB-type diblock copolymers such as PS-PI presented in Chapter 2, and other ABC triblock two-phase lamellae (see next section). Indeed, similar flow-alignment behavior has been observed in an ABA-type triblock copolymer polystyrene-polyisoprene-polystyrene (SIS).¹⁶

We performed alignment experiments with the same reduced frequency ($\omega a_T = 1$ rad/s, $T_0 = 130^\circ\text{C}$) and the same strain amplitude ($\gamma_o = 0.7$) at five different temperatures from 130°C to 170°C (Fig. 10). A common feature is that shearing produces a rapid rise in birefringence followed by a slow saturation to about 7×10^{-4} to 8×10^{-4} . The higher the temperature, the lower the saturation value of the birefringence. This is probably due to weaker segregation at elevated temperatures. The rate of alignment, on the other hand, increases dramatically at higher temperatures. At 130°C, after ten thousand seconds of shearing, birefringence barely reaches the plateau; while at 170°C, alignment is complete within one thousand seconds. Dynamic moduli were reduced after shear alignment (Fig. 11),

similar to AB diblock copolymers.³⁵

The final aligned states were verified by SAXS patterns and TEM micrographs. For example, after shearing at $T = 140^\circ\text{C}$, $\omega = 50$ rad/s, and $\gamma_o = 0.3$ for an hour, well-defined perpendicular layers have been observed in TEM. There are two sharp spots along the vorticity direction in SAXS patterns both in $(\mathbf{v}, \nabla \times \mathbf{v})$ - and $(\nabla \mathbf{v}, \nabla \times \mathbf{v})$ -planes, and there is almost no scattering intensity in the $(\mathbf{v}, \nabla \mathbf{v})$ -plane (Fig. 12).

It is still not clear why they behave differently than AB-type lamellae. The most significant difference between AB-type and ABA-type lamellae is chain conformation. In ABA-type lamellae, two different chain conformation are possible, i.e. bridges and loops. In the bridge conformation, two end-blocks are in two different A layers which are separated by a B layer; while in the loop conformation, two end-blocks are in the same A layer. In AB-type lamellae, such as PS-PI lamellar diblocks (and SRI-20 and SRI-15, see next section), there are no bridges. Thus, the presence of bridge conformations could be responsible for the absence of parallel alignment of SIS-type triblocks. Unfortunately the simple argument of this fact is not enough to explain the difference. In fact, a recent study suggest that bridge conformation can prevent perpendicular alignment, since only parallel alignment was induced for in PEP-PEE-PEP while PEP-PEE can be aligned both parallel and perpendicular.

B. AB Diblock Lamellae: Symmetric and Asymmetric

Two-phase lamellae formed by the SRI triblock copolymers could be viewed as a nearly symmetric AB-type lamellae if the center block R is partially miscible with both end-blocks S and I; while lamellae formed by RSI permutation would resemble asymmetric AB-type lamellae when the two adjacent blocks R and S are miscible. To address questions raised in the beginning of this section, I will discuss the shear orientation of nearly symmetric L2 phases in SRI-20 and SRI-15, and compare them with asymmetric L2 phases in RSI-15 and RSI-16B.

SRI-20 has an L2 phase up to above 280°C , and there is no phase transition in the

temperature range from 110°C to 280°C as detected by the 5-step procedure. Thus flow-induced alignment experiments have been performed in a wide range of temperatures from 115°C to 200°C. Shear frequencies range from 1 to 100 rad/s. Both parallel and perpendicular alignment are induced by oscillatory shear and monitored by real-time rheo-optical measurements. SAXS and TEM results verified the rheo-optical observations of parallel alignment: uniform and well-defined layers are seen in TEM micrographs, and the SAXS pattern has two sharp peaks along the velocity gradient direction in planes of $(\mathbf{v}, \nabla\mathbf{v})$ and $(\nabla\mathbf{v}, \nabla\times\mathbf{v})$ (Fig. 15). Similar to diblock copolymers, dynamic moduli are much lower in the parallel aligned sample than the freshly loaded sample. (Since the T_{ODT} is not accessible, the thermal and flow histories of the sample can not be erased. It is impossible to precisely compare the dynamic moduli of unaligned state with aligned state, since loading the sample could have induced alignment and reduced the dynamic moduli quite significantly already.) From the TEM images, the structure of SRI-20 consists of nearly symmetric two-phase layers. The center block R is probably mixed partially into both I-rich and S-rich layers. Thus the concentration profile would be close to weakly-segregated PS-PI diblock copolymer melts. This may explain the similar alignment behavior of SRI-20 to PS-PI diblocks (perpendicular at low shear frequencies and parallel alignment at higher shear frequencies). However, we are not able to determine ω'_c since the ODT is not accessible (higher than 280°C), thus are not able to assign alignment regimes (Regimes I, II, and III) for this material.

A low molecular weight analogue, SRI-15, has the desirable feature of an accessible ODT with the same nearly symmetric two-phase lamellar structure. The ODT occurs around 235°C and ω'_c is 2 rad/s at 120°C or 10 rad/s at 140°C (Fig. 13a). When we perform shear-induced alignment at frequencies below, above but close and much higher than ω'_c , three distinct alignment regimes are identified based on their optical signatures (Fig. 14), i.e. Regimes I, II, and III. The correspondence between these optical signatures with TEM and SAXS has been established in Chapter 2 for PS-PI diblock copolymers. We expect that these correlations still hold; therefore, we assign alignment regimes based on rheo-optical signature only. The results are the same as those of a symmetric PS-PI diblock copolymer

described in Chapter 2. For example, perpendicular alignment (Regime I) is induced at 180°C and 1 rad/s ($\ll \omega'_c$), and at 140°C and 1 rad/s ($0.1 \omega'_c$) as shown in Fig. 14a. Parallel alignment is induced at 140°C and 40 rad/s ($4 \omega'_c$) through a transient positive 1,3-birefringence (Regime II). Another path to parallel alignment was observed at very high shear frequency 100 rad/s at 140°C ($10 \omega'_c$) through a negative transient 1,3-birefringence (Regime III) (Fig. 14b, Fig. 15).

At frequencies close to ω'_c , strain-induced flipping was observed: when the strain amplitude is below a specific value (γ_c), perpendicular alignment is induced (similar to Regime I); while parallel alignment is induced (Regime II) at higher strain amplitude ($> \gamma_c$). A novel trajectory was found at a specific condition: $\omega = \omega'_c$, $\gamma_o = \gamma_c$. For example, at 140°C, 10 rad/s (ω'_c), and 100% (γ_c), 1,3-birefringence increases rapidly at the very beginning of oscillatory shear, reaches a maximum value (the same as the “fast process” in Regime II), and drops slightly (the same as the beginning of “slow process” in Regime II); then instead of inducing parallel alignment, manifested by decreasing 1,3-birefringence to nearly zero, further shearing induces perpendicular alignment, since the 1,3-birefringence increases steadily (like the fast and slow processes in Regime I), and finally reaches a saturated value equivalent to those observed in Regime I (Fig. 14c). The discovery of this novel trajectory suggests that shear-induced alignment consists of combinations of different “fast processes” and “slow processes” depending on the shear conditions.

So far, we have found that symmetric two-phase lamellae in AB-type block copolymers such as PS-PI, SRI-20, and SRI-15 behave similarly under oscillatory shear (Fig. 16). Next we determine whether asymmetric lamellae will behave like their symmetric counterparts. Using the 5-step procedure, the phase behaviors of RSI-15 and RSI-16B were characterized. Both of these samples have the desired feature of a readily accessible ODT. RSI-15 has an ODT at 138°C from the L2 phase. The R and I blocks are miscible, since TEM with OsO_4 staining shows the dark layers are thicker than the light layers. The characteristic frequency ω'_c is 5 rad/s at 120°C. A comprehensive set of experiments has been explored and the shear-induced alignment behavior is the same as symmetric lamellae: three alignment

regimes (Regime I, II, and II), strain-induced flipping in the vicinity of ω'_c , etc. (Fig. 13ab) Only selected experimental points are mapped in Fig. 16 for clarity. RSI-16B has an ODT at 140°C and a ω'_c of 18 rad/s at 120°C. These AB-type asymmetric lamellae also have thick R/I (dark) layers and thin S (light) layers. Again, as plotted in Fig. 16, these asymmetric lamellae behave like symmetric lamellae. Thus, we can conclude that for PS-PI-type lamellae, whether they are symmetric or asymmetric, whether they are formed by diblock copolymers or two-phase separated ABC triblock copolymers, the selection of parallel or perpendicular alignment and their pathways towards final aligned states are similar.

We have noted that it has been proposed that the selection of parallel and perpendicular alignment is dictated by the one with “minimum dynamic moduli”. In all the samples we studied in this thesis, the absolute values of the linear dynamic moduli are lower in parallel aligned states than perpendicular aligned ones in the frequency range of study (Fig. 17). Thus, we further conclude that the cascade dynamic responses of polymer chains and nanostructures determines the selection of the alignment direction, not the minimum dynamic moduli.

C. Three-Phase Lamellae: Shear Orientation and Defect Dynamics

For all three samples that have three-nanophase-separated lamellar structure (SRI-35, SIR-35, and RSI-35), global alignment is induced by oscillatory shear or simple pressing-and-annealing. So far only parallel alignment has been found in all of these samples. For example, parallel alignment of the L3 phase of SRI-35 is induced at 140°C, 10 rad/s, and 50% strain amplitude. Dynamic moduli decrease gradually during shearing (Fig. 18a). The linear dynamic moduli of the aligned sample are lower than those of the as-loaded sample (Fig. 18b). TEM micrographs indicate a well-defined three-phase structure (Fig. 19). Parallel alignment has also been induced in RSI-35 when oscillatory shear was applied at 140°C, 10 rad/s, and 100% strain amplitude, and similar rheological responses were observed to SRI-35 (Fig. 20ab and Fig. 7ab). Parallel alignment of these L3 phases has also

been achieved simply by pressing-and-annealing experiments. We press these samples at around 120°C, and then anneal them at 140°C for a week. TEM micrographs indicate that almost the same degree of parallel order was induced by pressing and annealing as those by oscillatory shear. We noted that without prolonged annealing, only a relatively small degree of parallel order can be achieved by pressing.

As SIR-35 has an OOT from the L3 phase to the L2 phase approximately at 210°C (Fig. 21), shear-induced alignment experiments were conducted in both the L2 and L3 phases. Shear-induced alignment of this L3 phase is similar to those of SRI-35 and RSI-35. For example, when oscillatory shear is applied at 180°C, 10 rad/s, and 100% strain amplitude, the effective dynamic moduli decrease, while the 1,3-birefringence follows a trajectory that belongs to Regime II (Fig. 22). The linear dynamic moduli are reduced after flow processing (Fig. 23). Parallel layers with correlated perforation are observed with electron microscopy (Fig. 24). The alignment process at lower temperature (140°C) is similar to those at 180°C as revealed by rheology and TEM (Fig. 25ab).

Flow processing of the L2 phase of SIR-35 at 230°C, 1 rad/s, and 100% strain amplitude results in parallel alignment. As mentioned before, layers with correlated perforations were observed when we cooled this aligned sample to room temperature before TEM characterization. We believe that only two-phase layers exist above the OOT (210°C) when the R and S blocks are miscible. The cooling process gives the R and S blocks an opportunity to undergo a local segregation. This idea is confirmed as we anneal these samples at temperatures which are high enough for a phase transition to occur kinetically but still below 210°C. The annealing temperatures we used are 120°C, 140°C, and 160°C respectively. As these correlated perforation type defects annihilate, long range correlations are produced. The higher the temperature, the faster the annihilation process. After one or two hours of annealing at 160°C or one day at 140°C, the length scale of perforation increases almost an order of magnitude, and striking patterns, including those that resemble a ship's wake were observed. The slow kinetics of annihilation at 120°C provide an opportunity to observe the emergence of these patterns and the changes of the length scale between

perforation defects (Fig. 26ab, and 27ab).

In an attempt to eliminate these correlated perforations, a shearing-while-cooling experiment was performed from 220°C to 180°C at the rate of 0.25°C per minute, and from 180°C to 140°C at 0.5°C per minute, all at 1 rad/s, 100% strain amplitude. Unfortunately, the resulting material has a similar defect texture as one that was sheared at 230°C and annealed at 140°C. Thus, we conclude that well-defined three-phase layers can be formed only when the two adjacent blocks are miscible in the two nanophase structure (Fig. 6a) before further segregation from L2 to L3. If the two end-blocks are miscible in a L2 phase before segregation to a L3 phase (Fig. 6bc), perforation-type defects exist and they are not easy to eliminate.

D. Hexagonal Cylinders: Alignment and Phase Transitions

The hexagonal cylindrical morphology has been identified for samples SRI-25, SIR-18B, RSI-25, RSI-20, and RSI-19B. Two-types of cylinders exist, i.e. either styrene-rich hard cylinders or isoprene-rich soft cylinders. We have found that all these cylinders can be aligned along shear velocity direction. For example, we align the cylindrical structure of SIR-18B along the velocity direction of oscillatory shear at 120°C, 1 rad/s, and 100% strain amplitude, as indicated by the rheo-optical signature and TEM observations (Fig. 2b). This is consistent with previous studies of hard cylinders. On the other hand, TEM micrographs show that in the H phase of RSI-20, the cylinders consist of isoprene, which is softer than the matrix consisting of R and S. Thus, cylinder orientation is independent on the relative rigidity of matrix and cylinders. As an example of shear orientation of hexagonal cylinders, in the following, I will begin with the identification of phase transitions of RSI-20, followed by the kinetics of alignment, including the effects of temperature and strain amplitude.

For RSI-20, different nanostructures exist depending on the temperature and shearing conditions. Temperature sweep experiments showed the initial gradual decrease in dynamic moduli followed by a jump of more than one order of magnitude at about 220°C, and finally

a drop of more than three orders of magnitude around 265°C (Fig. 28a). This implies phase transitions around these temperatures.

Information regarding the phase transitions was obtained also from the optical measurements. We aligned a sample at $T = 140^\circ\text{C}$, $\omega = 10$ rad/s, $\gamma_o = 1$ until the birefringence reached a plateau. Then the aligned sample was heated from 140°C to 275°C. The 1,3-birefringence decreased gradually at the beginning, and then dropped rapidly around 220°C to almost zero. It is interesting to notice that a small birefringence appeared and then quickly disappeared around 265°C (Fig. 28b). Comparison of results from both rheological and optical measurements suggests that there is an order-order transition around 220°C, from one structure that has large birefringence to another structure that has almost zero birefringence and a much larger modulus than the lower temperature phase. Between 140°C and 220°C, since this aligned state has a birefringence of about 3.7×10^{-4} , lower than that of lamellar structures of the same chemical composition (presented earlier in SRI-20 and SIR-20) at comparable temperature. Therefore, we expected a cylinder or other structure rather than lamellae up to 220°C. Above 220°C, we expected a cubic structure from the birefringence (zero) and higher dynamic moduli. At around 265°C, there is a phase transition again. We suspected that the polymer is disordered at temperatures higher than 265°C, since dynamic moduli are so low. Additional rheological experiments (frequency sweeps above 265°C) confirmed a disordered state, since terminal behavior was observed. TEM and SAXS confirmed the order-order transition at around 220°C from the H phase to the G phase (Fig. 29 and Fig. 30).

Flow alignment experiments in the H phase were conducted at various conditions in the temperature range from 140°C to 220°C. Similar behaviors were observed. As an example, here we present one alignment process at $T = 180^\circ\text{C}$, $\omega = 100$ rad/s, and $\gamma_o = 80\%$ (Fig. 31ab). The dynamic moduli drop rapidly at the beginning and flatten out after about 20 s. At the same time, the 1,3-birefringence builds up quickly, and reaches a plateau within 50 seconds. The process is so quick that scattering methods (which require tens of seconds per scattering pattern for in-situ SAXS and SANS) would not be able to monitor the structural

evolution at this condition. The effect of strain amplitude was investigated (Fig. 32a) by monitoring the birefringence. At 180 °C, 20 rad/s, alignment took a few seconds to complete when $\gamma_o = 160\%$, while at lower strain amplitude ($\gamma_o = 80\%$), alignment is finished in about 400 s. At $\gamma_o = 20\%$, the birefringence reaches only one fourth of the saturated value after 500 s of shearing, and many hours are needed to reach the final aligned state. This highly non-linear effect of strain amplitude (the alignment time needed to reach a half of the final saturated birefringence varies with strain approximately as γ_o^{-3}) was observed earlier during the alignment of diblock lamellar structures.²⁶

Higher rates of alignment were observed at elevated temperatures (Fig. 32b). For example, at the same strain amplitude ($\gamma_o = 1$) and the same reduced frequencies ($\omega a_T = 1 \text{ rad/s}$, $T_0 = 140^\circ\text{C}$), alignment is faster at 180°C than at 140°C. The higher the temperature, the lower the saturated birefringence of well-aligned states (at final aligned state after shearing for thousands of seconds, the final 1,3-birefringence is higher at 140°C than in 180°C). This is similar to the trend observed in lamellar structures of SIR-20. Note that more than 500 s of shearing is needed to complete the alignment at these two conditions.

An interesting phenomenon occurred when we applied a large strain shear to RSI-20 at 230°C. Instead of zero birefringence as we expected for a bicontinuous cubic structure, we observed a birefringence build-up similar to those at 140°C and 180°C. The birefringence is saturated within a few hundreds seconds. In-situ rheological characterization was used to compare the small-strain-amplitude dynamic moduli (Fig. 33). For an unaligned sample at temperatures below 220°C, the storage modulus is almost independent of shear frequency, which is consistent with previous theoretical predictions and experimental results on cubic ordered phases. In contrast, the storage modulus of the aligned sample

Aligned samples were quickly cooled to room temperature for ex-situ characterization using SAXS and TEM. For samples that were aligned and then quenched rapidly to room temperature, TEM micrographs and SAXS patterns always show uniform hexagonal cylinders (Fig. 29). Sharp six-spot patterns were observed when the x-ray beam was sent along the velocity direction. If aligned cylinders were heated to above 220°C, and allowed

to anneal until the 1,3-birefringence dropped to zero, then cooled to room temperature, we observed a bicontinuous cubic structure in TEM micrographs and SAXS patterns (Fig. 30). An eight-spot pattern observed in the $(\nabla\mathbf{v}, \nabla\times\mathbf{v})$ -plane (Fig. 29b) resembles the hexagonal-to-cubic phase transition by Shultz et al.,³³ and a ten-spot pattern in $(\nabla\mathbf{v}, \mathbf{v})$ -plane (Fig. 29b) is the same as those observed by Foster et al.³⁴ Therefore, we assign this structure as a twinned Ia3d as well.

While heating can transform aligned hexagonal cylinders of RSI-20 into a bicontinuous cubic structure Ia3d, oscillatory shear can reverse this process. We observed an H phase from the X-ray pattern and TEM in a sample that was quenched to room temperature after shearing at 235°C. In addition to this shear-induced OOT, a transition from shear-induced alignment to shear-induced disordering has been discovered in SIR-18B. At 120°C and $\gamma_o = 100\%$, shear-induced alignment occurs at a shear frequency of 1 rad/s (Fig. 2b), while shear-induced disordering occurs at 100 rad/s as revealed by both rheo-optical monitoring and electron microscopy (Fig. 34).

5. Conclusions

In this chapter, rich thermodynamics and dynamics of ABC triblock copolymers have been revealed using a S/I/R model system. Dramatic changes of morphology and alignment behavior can be induced simply by switching the permutation of the blocks, by increasing/decreasing molecular size, and by changing experiment conditions such as thermal and shear history.

We have observed phase transitions from three-nanophase to two-nanophase, from two-nanophase to one phase (disordered) states, and from one nanostructure to another within the two-nanophase state. For example, SRI-35 is in a three-nanophase state at 140°C and a two-nanophase state at 180°C; while SRI-20 is in the two-nanophase state throughout the whole temperature range (100°C to 280°C), but has order-order transitions from L2 to H, and to G phases during heating. Both thermotropic and shear-induced phase transitions

are identified. Transitions from shear-induced alignment at low frequency to shear-induced disordering at high frequency of a stable H phase (SIR-18B) is the first observation of this type in hexagonal cylinder BCPs. Extensive studies of shear-induced alignment are conducted for lamellar structures: AB-type, ABA-type, and three-nanophase lamellae. For AB-type lamellae, similar alignment behaviors have been revealed: Regimes I, II, and III, and strain effect on kinetics. Thus, we have concluded that it is a cascade of dynamic responses that determines the selection of alignment orientations and trajectories: it applies to a symmetric PS-PI diblock lamellae, it applies to a nearly symmetric AB-type triblock lamellae (SRI-15), it applies to an asymmetric AB-type triblock lamellae (RSI-15), and it also applies to AB-type triblock lamellar BCPs with bimodal molecular weight distribution (RSI-16B). Only perpendicular alignment is induced in all frequency ranges for an ABA-type triblock lamellae (SIR-20), possibly due to the different chain conformations. Only parallel alignment has been observed in three-nanophase lamellae so far. It is not clear if pressing during sample loading plays a role. Indeed, Reasonably aligned samples can be prepared just by pressing and annealing above T_g . We noted that it is much easier to identify phase structures if samples are aligned. For example, it is difficult to distinguish three-nanophase from two-nanophase structures during imaging for a solvent-cast sample (Fig. 35).

To understand the formation of three-nanophase structures from two-nanophase precursor in ABC triblock copolymer melts, we have examined two situations: a) two adjacent blocks (A/B or B/C) are miscible in two-nanophase state and b) two end-blocks are miscible in two-nanophase precursor. Well-defined three-nanophase lamellae can be formed only from precursors (A/B)-C or A-(B/C), e.g. SRI-35. A new type of defects (correlated perforations) is discovered (SIR-35), and it is very difficult to eliminate them. This discovery provides insight into the design of three-nanophase structures and kinetic pathways of phase transitions from two-nanophase to three-nanophase states.

Appendix:

Table of Shift Factors

Temp (°C)	SIR-20	SRI-15	RSI-15	RSI-16B
100			5.88	7.14
105			3.29	
110			2.18	2.57
115			1.53	
120	1	1	1	1
125		0.63	0.706	
130	0.316	0.41	0.529	0.464
135		0.29	0.324	0.357
140	0.124	0.21	0.194	0.229
145			0.141	0.157
150	0.05	0.11	0.0941	
155			0.0647	
160	0.0224			
170	0.0113	0.045		
180	0.00632			
190	0.00363	0.02		
195	0.00284			
200	0.00221			
205	0.0019			
210	0.00158	0.011		
215	0.00133			
220	0.00104			
225	0.000885			
230	0.000695	0.0067		
235		0.0058		
240	0.000474	0.005		
245		0.0044		

REFERENCES

1. Krappe, U. ; Stadler, R.; Voigt-Martin, I. *Macromolecules* **1995**, **28**, 4558; *ibid* **1995**, **28**, 7583.
2. Abetz, V.; Stadler, R. *Macro. Symp.* **1997**, **113**, 19. Stadler, R.; Auschra, C.; Beckmann, J.; Krappe, U.; Voigtmartin-I. *Macromolecules* **1995**, **28**, 3080.
3. Matsushita, Y.; Nomura, M.; Watanabe, J.; Mogi, Y.; Noda, I. *Macromolecules* **1995**, **28**, 6007; Mogi, Y.; Nomura, M.; Kotsuji, H.; Ohnishi, K.; Mori, K.; Matsushita, Y.; Noda, I. *Macromolecules* **1994**, **27**, 1994; Matsushita, Y.; Tamura, M.; Noda, I. *Macromolecules* **1994**, **27**, 3680; Mogi, Y.; Mori, K.; Matsushita, Y.; Noda, I. *Macromolecules* **1992**, **25**, 5412; Mogi, Y.; Kotsuji, H.; Kaneko, Y.; Mori, K.; Matsushita, Y.; Noda, I. *Macromolecules* **1992**, **25**, 5408.
4. Gido, S.P.; Schwark, D.W.; Thomas, E.L.; Goncalves, M.D. *Macromolecules* **1993**, **26**, 2636.
5. Dormidontova, E.E.; Khokhlov, A.R. *Macromolecules* **1997**, **30**, 1980.
6. Breiner, U.; Krape, U.; Abetz, V.; Stadler, R. *Journal of Macromolecular Chemistry and Physics* **1997**, **198-4**, 1051; Bechmann, J.; Auschra, C.; Stadler, R. *Macromol. Rapid Commun.* **1994**, **15**, 67; Balsamo, V.; Vongyldenfeldt, F.; Stadler, R. *Journal of Macromolecular Chemistry and Physics* **1996**, **197-10**, 3317; Breiner, U.; Krappe, U.; Stadler, R. *Macromol. Rapid Commun.* **1996**, **17-8**, 567; Auschra, C.; Stadler, R. *Macromolecules* **1993**, **26**, 2171
7. Wei,Z.; Wang, Z.-G. *Macromolecules* **1995**, **28**, 7215.
8. Kane, L.; Spontak, R.J. *Macromolecules* **1994**, **27**, 1267.
9. Werner, A.; Fredrickson, G. H. *Journal of Polymer Science: Part B: Polymer Physics* **1997**, **35-5**, 849; Wang, Z.-G.; Chang, C.; Unpublished results.

10. Abetz, V.; Stadler, R.; Leibler, L. *Polymer Bulletin* **1996**, **37**, 135 Neumann, C.; Abetz, V.; Stadler, R. *Polymer Bulletin* **1996**, **36**, 43
11. Ashraf, A.; Smith, S.D. submitted
12. Milner, S.T.; Witten, T.A.; *Macromolecules* **1992**, *25*, 5495; Zhulina, E.B.; Halperin, A. *Macromolecules* **1992**, *25*, 5730; Masten, M.W.; Schick, M. *Macromolecules* **1994**, *27*, 187; Matsushita, Y.; Nomura, M.; Noda, I.; Imai, M. *Physica B* **1995**, *213*, 697.
13. Keller, A.; Pedemonte, E.; Willmouth, F.M. *Colloid Polym. Sci.* **1970**, *238*, 25.; Folkes, M.J.; Keller, A.; Scalisi, F.P. *Colloid Polym. Sci.* **1973**, *251*, 1.
14. Hadziioannou, G.; Mathis, A.; Skoulios, A. *Colloid Poly. Sci.* **1979**, *257*, 136; Hadziioannou, G.; Mathis, A.; Skoulios, A. *Macromolecules* **1982**, *15*, 258.
15. Morrison, F. A.; Winter, H. H. *Macromolecules*. **1989**, *22*, 3533.; Morrison, F. A.; Winter, H.H.; Gronski, W.; Barnes, J. D. *Macromolecules*. **1990**, *23*, 4200.
16. Riise, B.L.; Fredrickson, G.H.; Larson, R.G.; Pearson, D.S. *Macromolecules*, **1995**, *28*, 7653.
17. Amundson, K.; Helfand, E.; Quan, X.; Hudson, S. D.; Smith, S. D. *Macromolecules* **1994**, *27*, 6559.
18. Morrison, F.A.; Mays, J.W.; Muthukumar, M.; Nakatani, A.I.; Han, C.C. *Macromolecules*, **1993**, *26*, 5271.
19. Amundson, K.; Helfand, E.; Davis, D. D.; Quan, X.; Patel, S. S.; Smith, S. D. *Macromolecules* **1991**, *24*, 6546.; Amundson, K.; Helfand, E.; Quan, X.; Smith, S. D. *Macromolecules* **1993**, *26*, 2698.
20. Amundson, K.; Helfand, E. *Macromolecules*, **1993**, *26*, 1324.
21. Allan, P., Arridge, R. G. C.; Ehtaiatkar, F.; Folkes, M. J. *J. Phys. D: App. Phys.*, **1991**, *24*, 1381.

22. Tepe, T.; Hajduk, D.A.; Hillmyer, M.A.; Wiemann, P.A.; Tirell, M.; Bates, F.S.; Almdal, K.; Mortensen, K. *J. Rheology* **1997**, *41*, 1147.
23. Lee, H. H.; Register, R. A.; Hajduk, D. A. ; Gruner, S. M. *Polymer Engineering and Science* **1996**, *36-10*, 1414.
24. Scott, D.B.; Waddon, A.J.; Lin, Y.-G.; Karasz, F.E.; Winter, H.H. *Macromolecules* **1992**, *25*, 4175.
25. Chen, Z.-R.; Kornfield, J. A.; Smith, S. D.; Grothaus, J. T.; Satkowski, M. M. *Science*, **1997**, *277*, 1248.
26. Chen, Z.-R.; Issaian, A.M.; Kornfield, J. A.; Smith, S. D.; Grothaus, J. T.; Satkowski, M. M. *Macromolecules*, **1997**, *30*, 7096.
27. Gido, S.P.; Thomas, E.L. *Macromolecules* **1997**, *30*, 3739; *ibid* **1994**, *27*, 849; *ibid* **1993**, *26*, 4506.
28. Laurer, J.H.; Hajduk, D.A. Fung; J.C.; Sedat, J.W.; Smith, S.D. *Macromolecules* **1997**, *30*, 3938.
29. Allan, P., Arridge, R. G. C.; Ehtaiatkar, F.; Folkes, M. J. *J. Phys. D: App. Phys.*, **1991**, *24*, 1381.
30. Hongladarom, K.; Burghardt, W.R.; Baek, S.G.; Cementwala, S.; Magda, J.J. *Macromolecules* **1993**, *26*, 772.
31. Hashimoto, T.; Shibayama, M.; Kawai, H. *Macromolecules* **1980**, *13*, 1237; Mayes, A.M.; Olvera de la Cruz, M. *J. Chem. Phys.* **1991**, *95*, 4670.
32. Watanabe, H. *Macromolecules* **1995**, *28*, 506.
33. Schultz, M.F. et al. *Phys. Rev. Lett.*, **1994**, *73*, 86.
34. Foster, S. et al. *Macromolecules*, **1994**, *27*, 6922; Khandpur, A.K. et al. *Macromolecules*,

1995, 28, 8796

35. Chen, Z.-R.; Kornfield, J.A. *Polymer*, in press
36. Balsara, N.P.; Da, H.J.; Watanabe, H.; Sato, T.; Osaki, K. *Macromolecules*, **1996**, 29, 3507

FIGURES

Fig. 1. Schematic representation of morphologies of 12 different S/I/R triblock copolymers and three different blends. The vertical coordinate $\chi_{SI}N_{total}$ is the product of the total molecular weight of the triblock sample and the Flory-Huggins interaction parameter of polystyrene and polyisoprene.³⁴ The black area within the triangle in the bottom of each figure schematically indicates that nearly equal lengths for the three blocks were used in all these triblock copolymers. The morphology observed as a function of $\chi_{SI}N_{total}$ is represented schematically by vertical bars of different types that are assigned to the following morphologies: L3 (three-microphase lamellae), L2 (two-microphase lamellae), H (hexagonal cylinders), and G (bicontinuous cubic Ia3d). For samples SRI-35, SRI-25, SIR-25, RSI-35, and RSI-25, only limited data are available to plot in the diagram. See the text for details.

Fig. 2. Representative morphologies of S/I/R triblock copolymers. (a) Two-microphase lamellae (L2) by RSI-15; (b) Hexagonal cylinders (H) by a blend (SIR-1B); (c) Bicontinuous cubic Ia3d (G) structure by a RSI-35 sample quenched from 250°C; (d) Solvent-cast three-nanophase-separated lamellae by SIR-35 after annealing at 110°C for 4 days; and e) disordered structure of solvent-cast SIR-15.

Fig. 3. Coexistence of hexagonal cylinders and bicontinuous cubic Ia3d structure by a SRI-25 sample.

Fig. 4. Correlated perforations in SIR-35 that was rapidly cooled after shearing for 4 hours at 230°C, 1 rad/s, and 100% strain. View in (a) the plane of velocity gradient and vorticity and (b) the plane of velocity and vorticity.

Fig. 5. Correlated perforations in three-phase lamellae of SIR-35. The sample was annealed at 140°C for 3 days after shearing at 230°C, 1 rad/s, and 100% strain amplitude for 4.5 hours. View in (a) the plane of velocity gradient and vorticity and (b) the plane of velocity and vorticity.

Fig. 6. Schematics for the formation of three-phase lamellae from two-phase lamellae of (a) SRI-35, (b) (c) SIR-35, and (c) RSI-35.

Fig. 7. (a) Two-phase and three-phase lamellae coexist in a quenched sample of RSI-35 after aligned at 140°C, 10 rad/s, and 50% strain amplitude for 10 hours. (b) After it is annealed for a week at 120°C, this aligned sample converts fully to the three-nanophase structure.

Fig. 8. Characterizing the order-disorder transition of SIR-20 (a) using a temperature-sweep experiment and (b) by monitoring the birefringence drop during heating of a pre-aligned sample.

Fig. 9. Determination of ω'_c of SIR-20 lamellae (L2). Arrows indicate the reduced frequencies under which shear experiment were performed.

Fig. 10. Effect of temperature on the kinetics of alignment of two-microphase lamellae of SIR-20. Higher shear frequencies are applied at higher temperature to keep a nearly constant reduced frequency.

Fig. 11. Dynamic moduli of SIR-20 before and after shearing at 170°C.

Fig. 12. High orientational order and low defect density observed in aligned SIR-20 by SAXS and TEM.

Fig. 13. Determination of ω'_c for two-microphase lamellae. Arrows indicate the reduced frequencies under which shear experiments were performed. I, II, and III represent the alignment regimes defined in Chapters 1 and 2. (a) SRI-15, (b) RSI-15, (c) RSI-16B. See Table 2 for the shift factors.

Fig. 14. Shear-induced alignment behavior of two-microphase lamellae of SRI-15: (a) Perpendicular alignment in Regime I ($\omega < \omega'_c$); (b) Parallel alignment in Regime II ($\omega > \omega'_c$) and Regime III ($\omega \gg \omega'_c$); (c) A novel trajectory in the boundary of Regime I and Regime II at a specific shearing condition: $\omega = \omega'_c$ and $\gamma_o = \gamma_c$. The first half of the trajectory (from I to M) is similar to those in Regime II; the second half (from M to F) follows the path similar to those in Regime I. The dashed line (from M to F') represents the path if it were parallel alignment in Regime II (from I to M, and M to F') (reproduced from Chapter 1)

Fig. 15. A well-aligned parallel state: SAXS patterns and TEM micrograph of aligned SRI-20.

Fig. 16. Flow-alignment behaviors of two-nanophase-separated lamellar ABC triblocks. Three alignment regimes exist for all AB-type block copolymers studied in this thesis: perpendicular alignment in Regime I ($\omega < \omega'_c$), parallel alignment in Regime II ($\omega > \omega'_c$) and in Regime III ($\omega \gg \omega'_c$). Strain-induced flipping was observed also in these samples as indicated by the pairs of symbols on top of each other. In order to avoid crowdedness, only representative results are mapped.

Fig. 17. Linear complex dynamic moduli of unaligned, parallel, and perpendicular aligned two-phase AB-type diblock melts. The absolute values of complex dynamic moduli are the lowest for parallel alignment in the whole range of frequency for all samples examined: (a) RSI-15, (b) BLD2, and (c) SRI-15.

Fig. 18. (a) Effective dynamic moduli decrease during alignment of SRI-35, (b) dynamic moduli before and after shearing for 13 hours at 140°C, 10 rad/s, and 50% strain.

Fig. 19. Three-nanophase-separated lamellae of SRI-35. Samples are aligned at 140°C, 10 rad/s, and 50% strain for 13 hours.

Fig. 20. (a) Effective dynamic moduli decrease during alignment of RSI-35, (b) dynamic moduli before and after shearing for 10 hours at 140°C, 10 rad/s, and 100% strain.

Fig. 21. Order-order transition from two-phase lamellae to three-phase lamellae during cooling as detected by rheological measurement for SIR-35.

Fig. 22. (a) Effective dynamic moduli decrease during alignment of SIR-35 in the three-nanophase state, (b) birefringence trace during shear.

Fig. 23. Dynamic moduli of SIR-35 before and after shearing for 2000 seconds at 180°C, 10 rad/s, and 100%.

Fig. 24. Three-nanophase-separated lamellae of SIR-35 after shearing at 180°C, 10 rad/s, and 100% for 2000 seconds.

Fig. 25. Texture in three-nanophase-separated lamellae of SIR-35 after shearing at 140°C, 10 rad/s, and 50% strain amplitude for 13 hours. (a) Correlated perforation defects, and (b) more complex defects are observed in this aligned sample.

Fig. 26. Correlated perforations in three-phase lamellae of SIR-35. The sample was annealed at 120°C for 3 days after shearing at 230°C, 1 rad/s, and 100% for 4 hours. View in (a) the plane of velocity gradient and vorticity and (b) the plane of velocity and vorticity.

Fig. 27. Correlated perforations in three-phase lamellae of SIR-35. The sample was annealed at 120°C for 10 days after shearing at 230°C, 1 rad/s, and 100% for 4 hours. View in the plane of velocity gradient and vorticity.

Fig. 28. Monitoring order-order and order-disorder transitions of RSI-20 (a) by rheological measurement and (b) by monitoring the birefringence for a pre-aligned sample.

Fig. 29. (a) A hexagonal cylindrical morphology observed from a sample rapidly cooled after shearing for 100 minutes at 180°C, 50 rad/s, and 45% strain amplitude. (b) A well-aligned hexagonal cylindrical morphology of RSI-20 converts to a bicontinuous cubic Ia3d morphology by heating over the order-order transition temperature. The sample was sheared at 180°C, 50 rad/s, and 45% strain amplitude for 100 minutes, then heated to 235°C at 1°C/min before quenching to room temperature for TEM.

Fig. 30. Coexistence of hexagonal cylinders and bicontinuous cubic Ia3d structure during phase transition of RSI-20.

Fig. 31. (a) Dynamic moduli decrease while (b) birefringence increases during shear-induced orientation of cylindrical RSI-20.

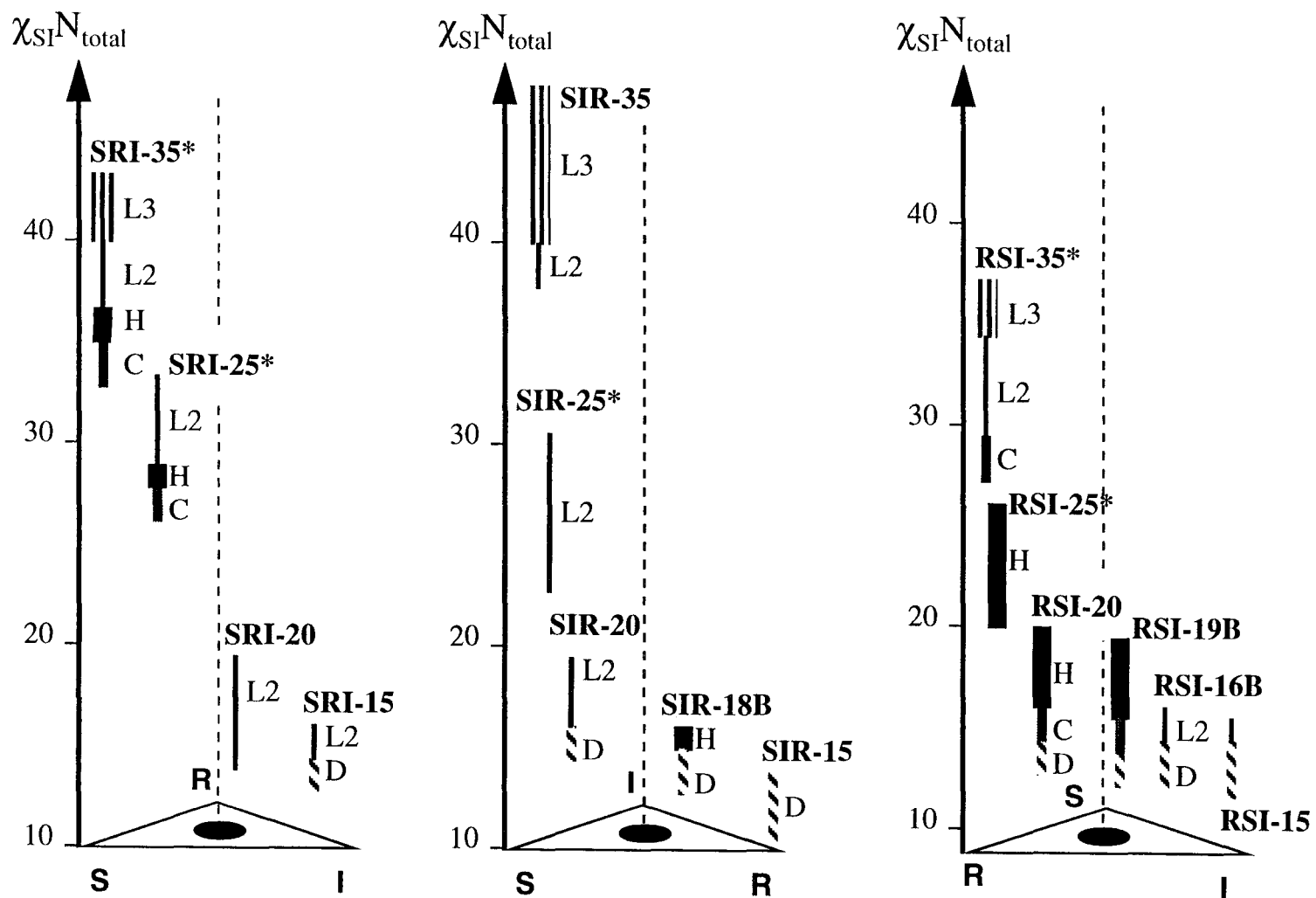
Fig. 32. The alignment kinetics of RSI-20 cylinders: (a) the effect of strain amplitude, and (b) the effect of temperature.

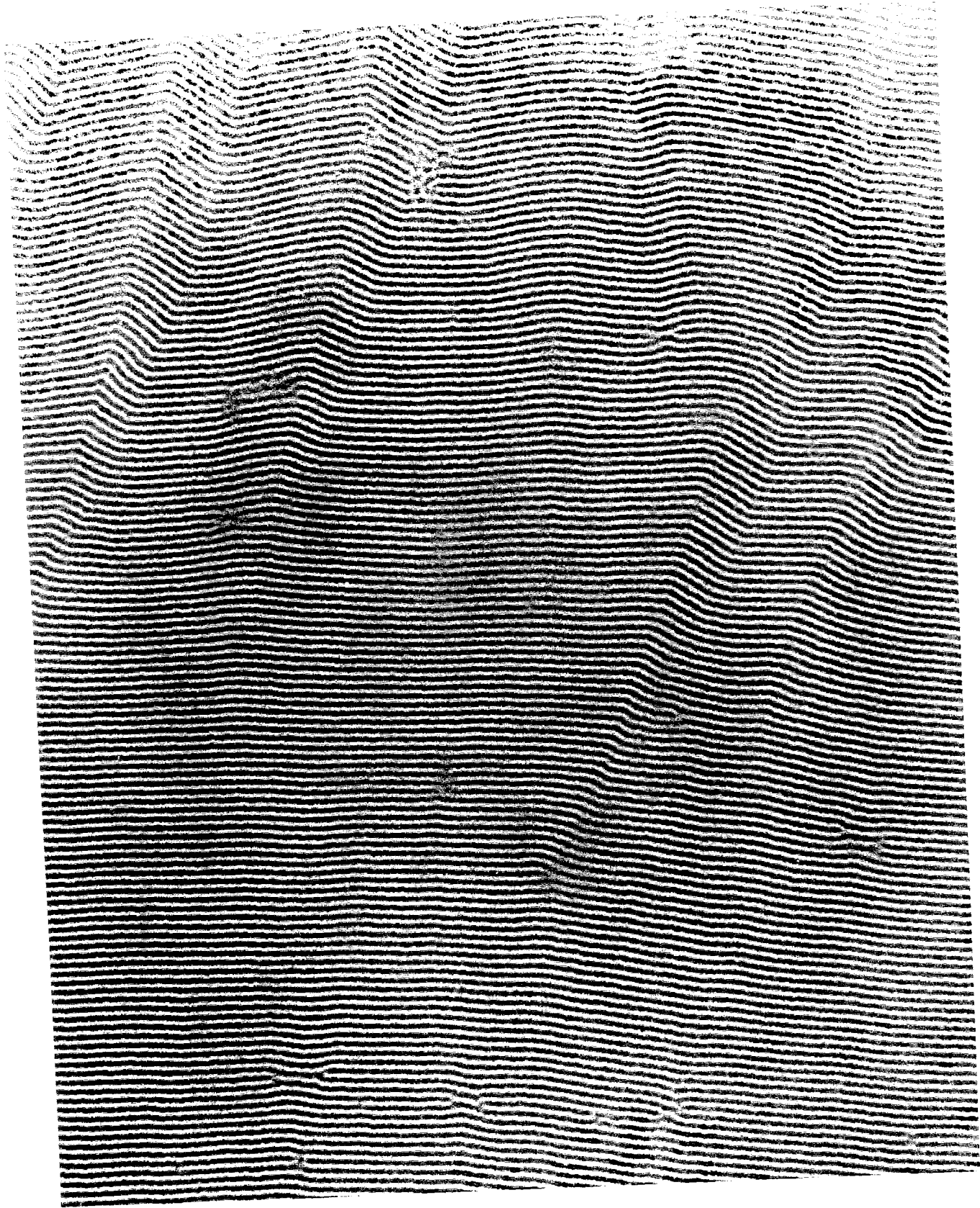
Fig. 33. Dynamic moduli of cylindrical RSI-20 before and after shearing for 100 minutes at 180°C, 50 rad/s, and 45% strain amplitude.

Fig. 34. Texture of partially disordered SIR-18B during shear-induced disordering at 120°C, $\gamma_0 = 100\%$, and 100 rad/s.

Fig. 35. Effect of tilting on the quality of TEM images illustrated in a solvent-cast SIR-35 sample. The three-nanophase structure disappears and reappear as the sample was tilted at different angles during imaging. The tilting angles are (a) 10°; (b) 0°; (c) -10°; and (d) -20°.

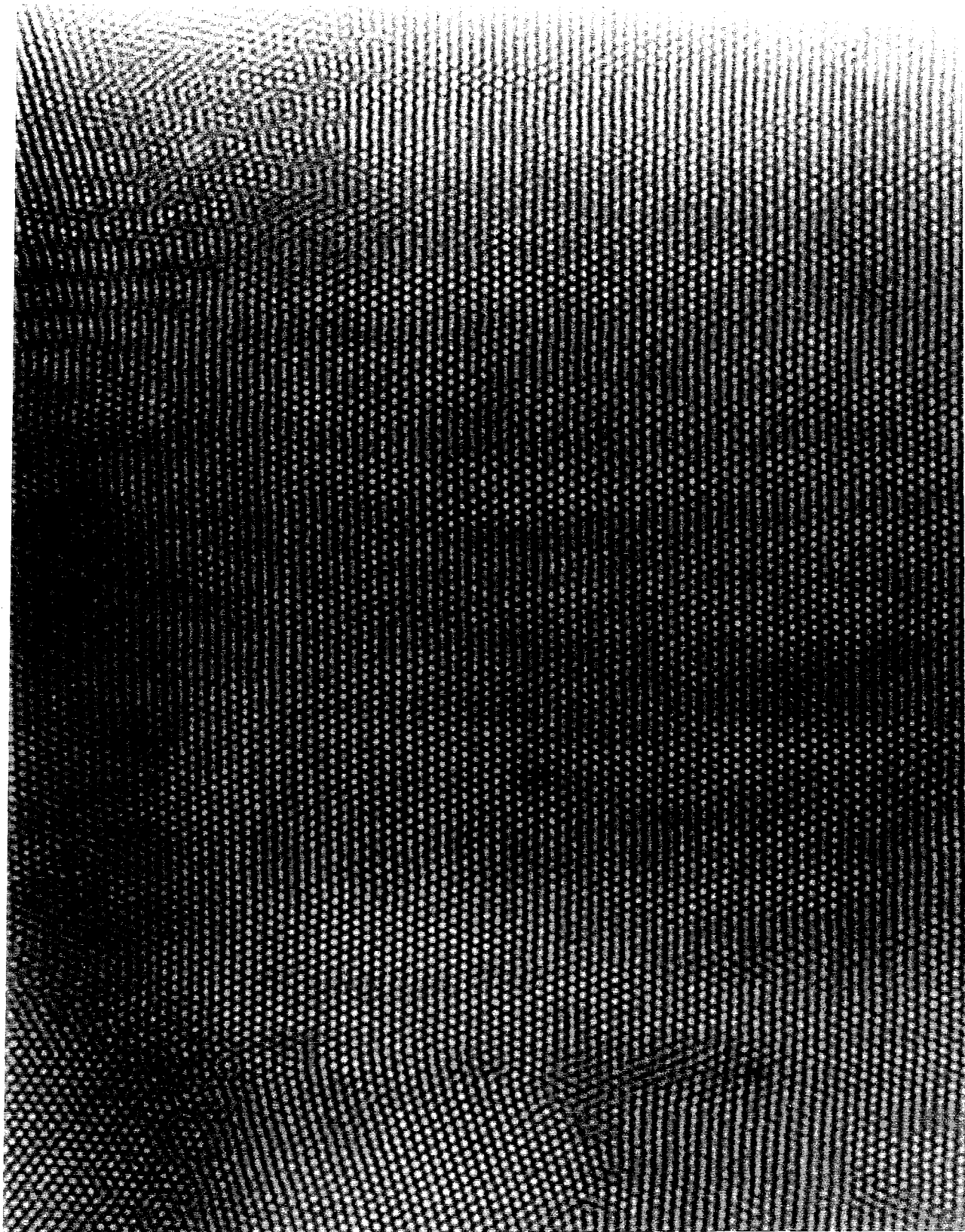
Fig. 1





200nm
|-----|

Fig.2a



200nm
|-----|

Fig.2b

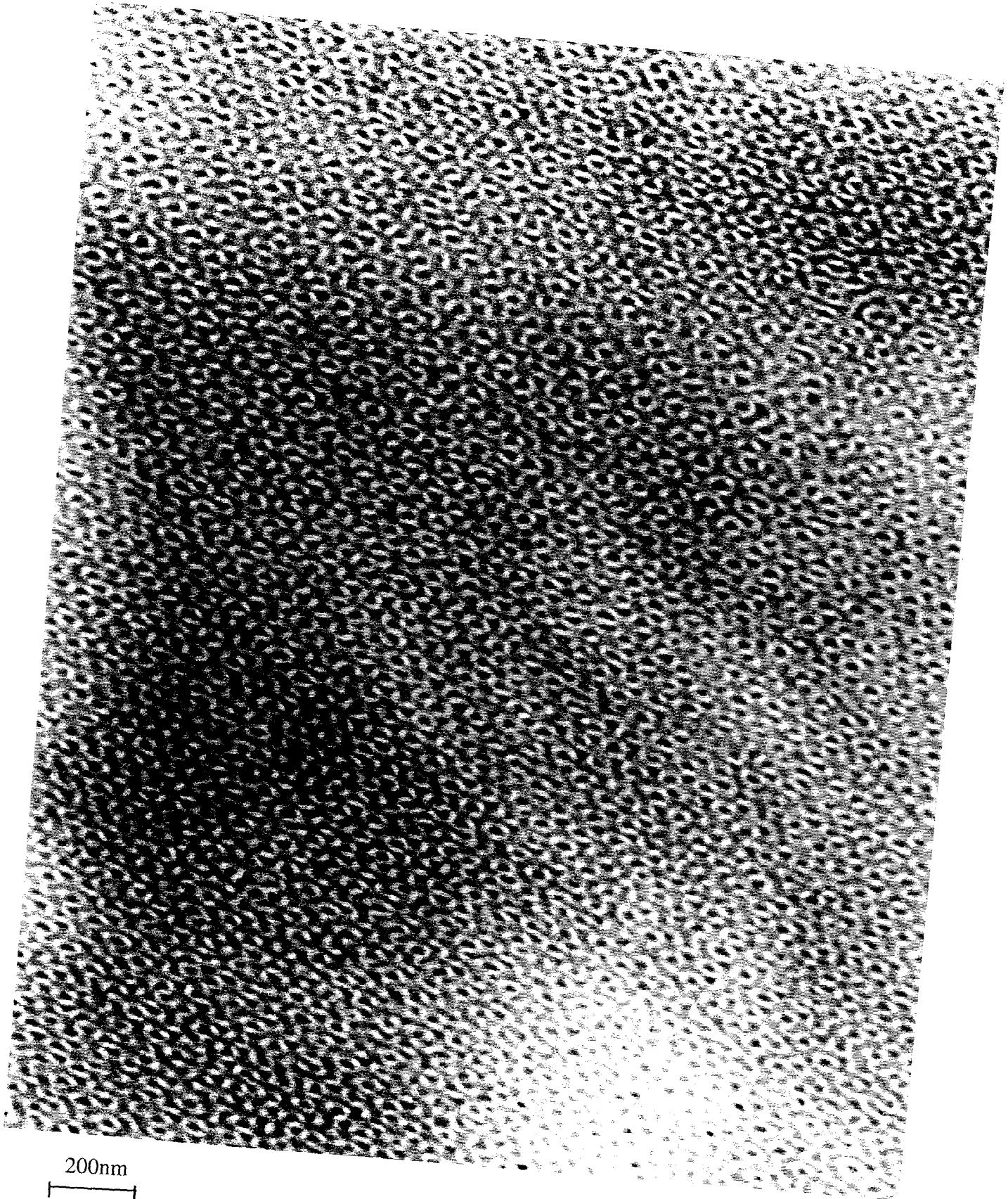


Fig.2c



200nm
|-----|

Fig.2d

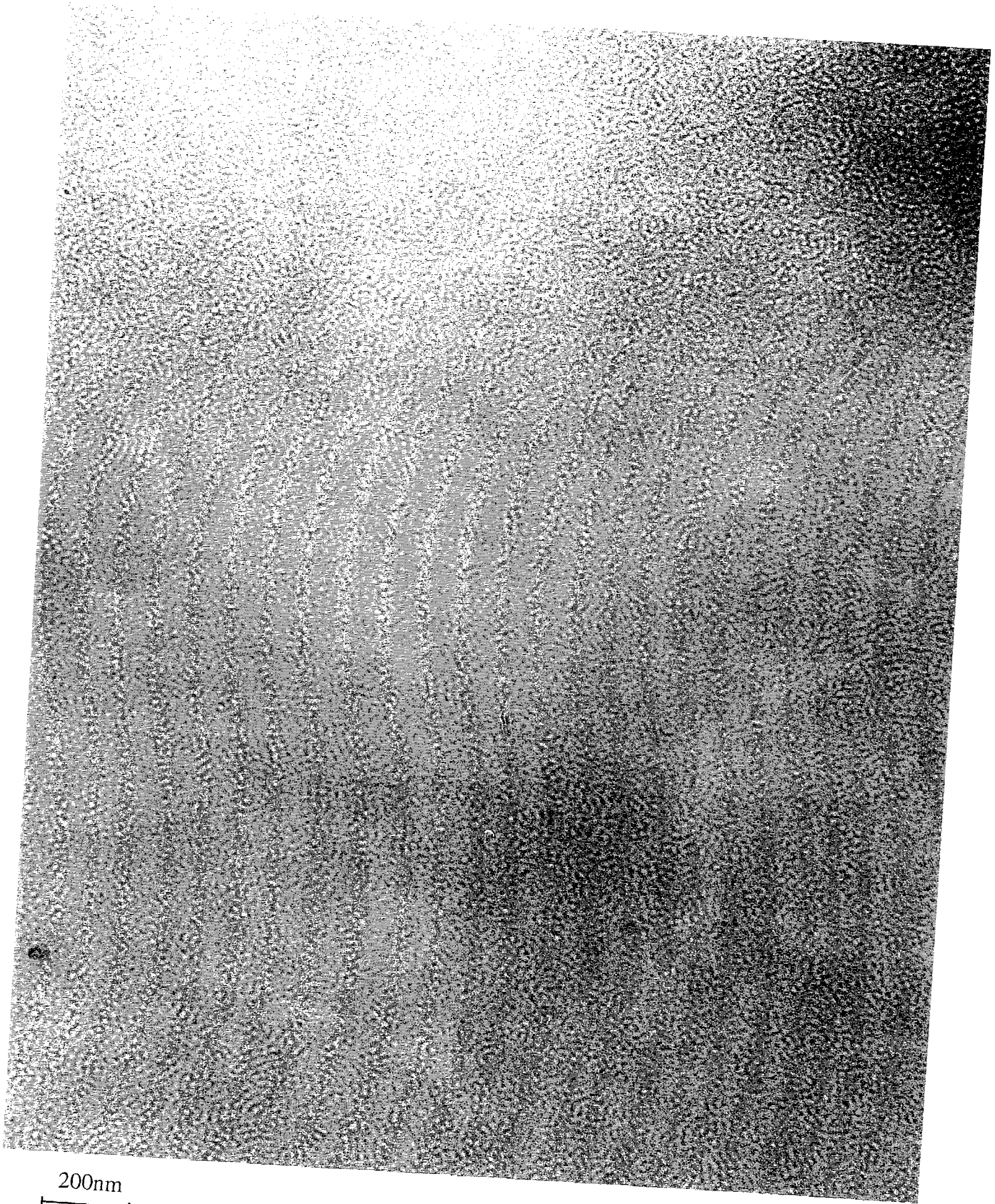
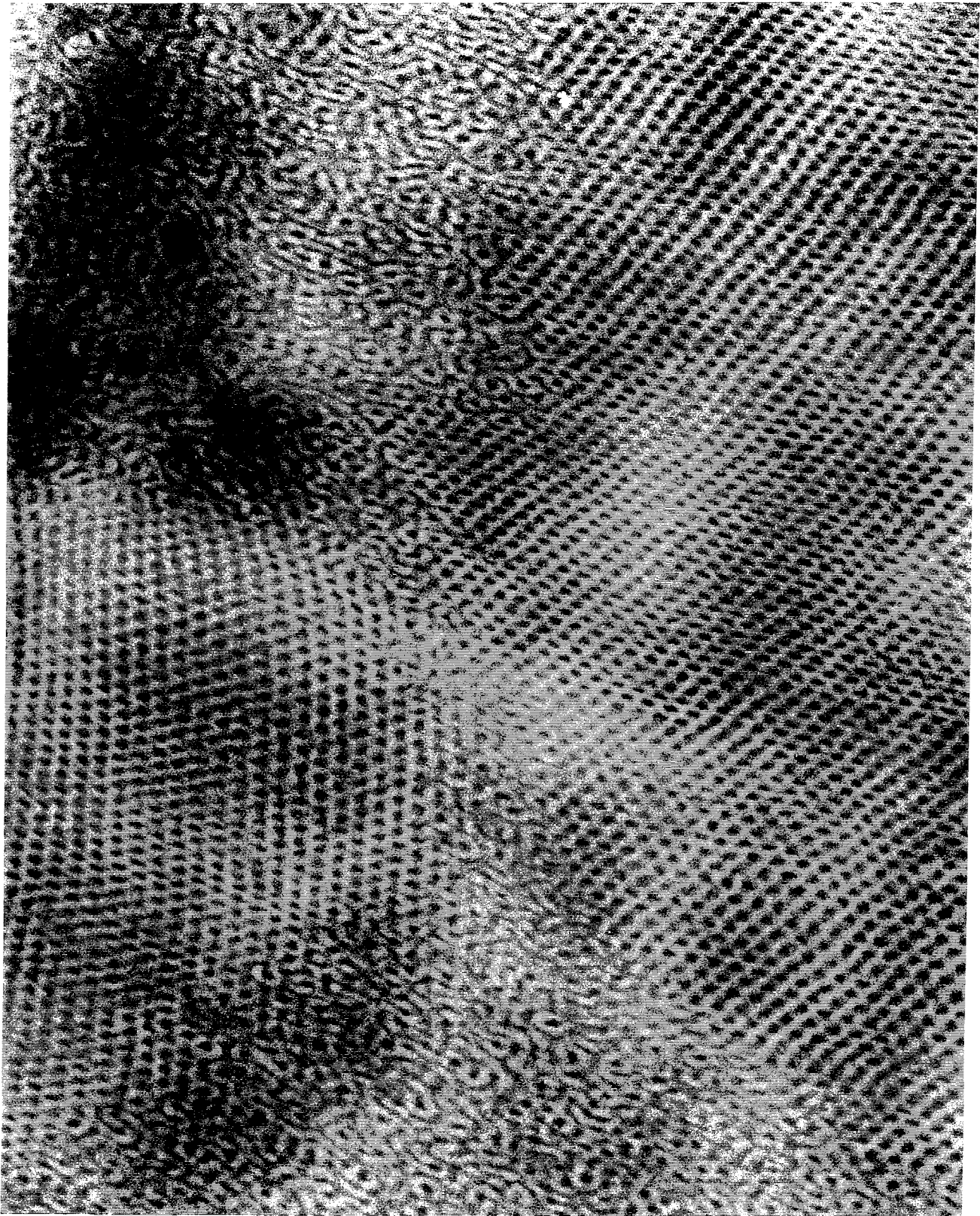
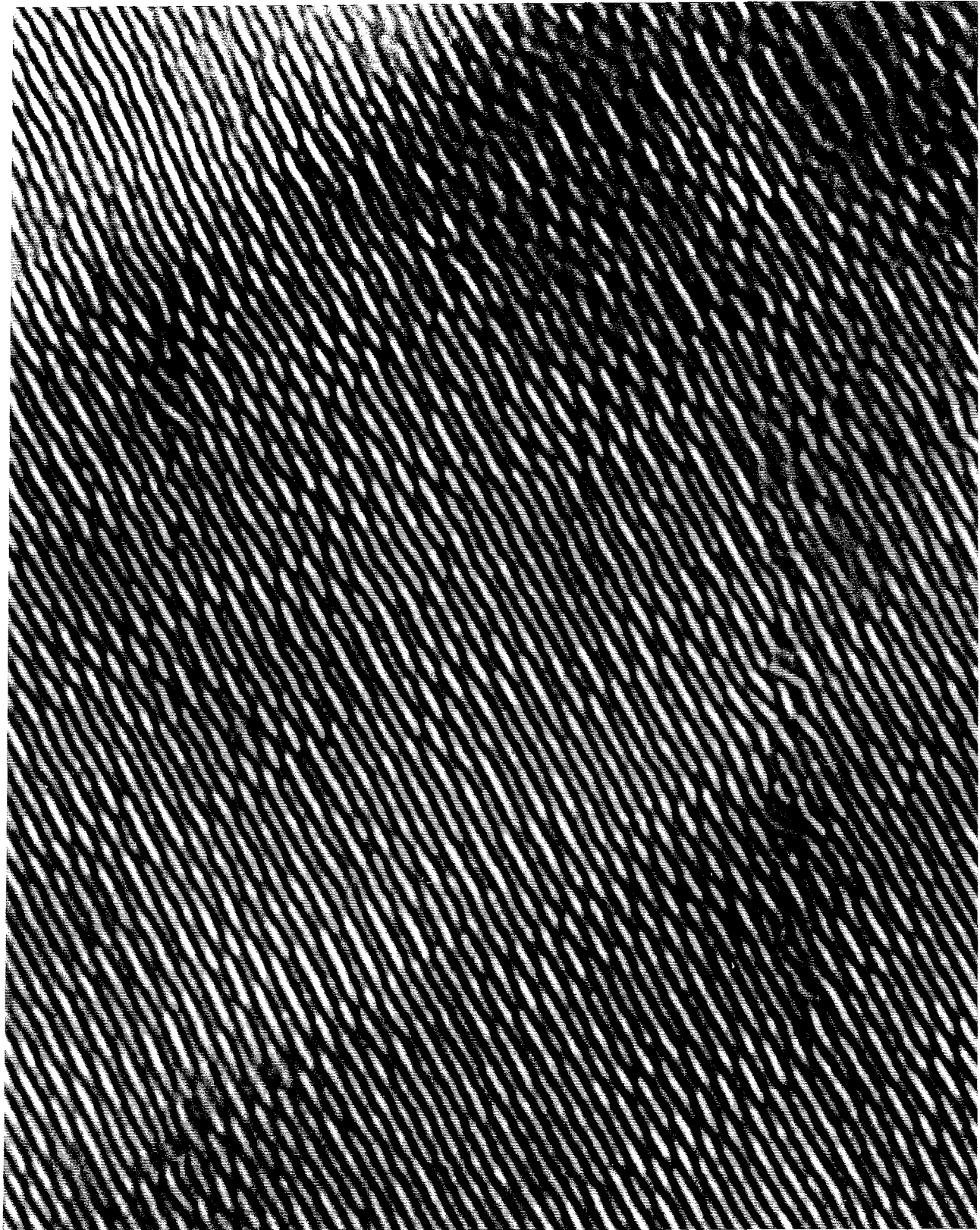


Fig.2e



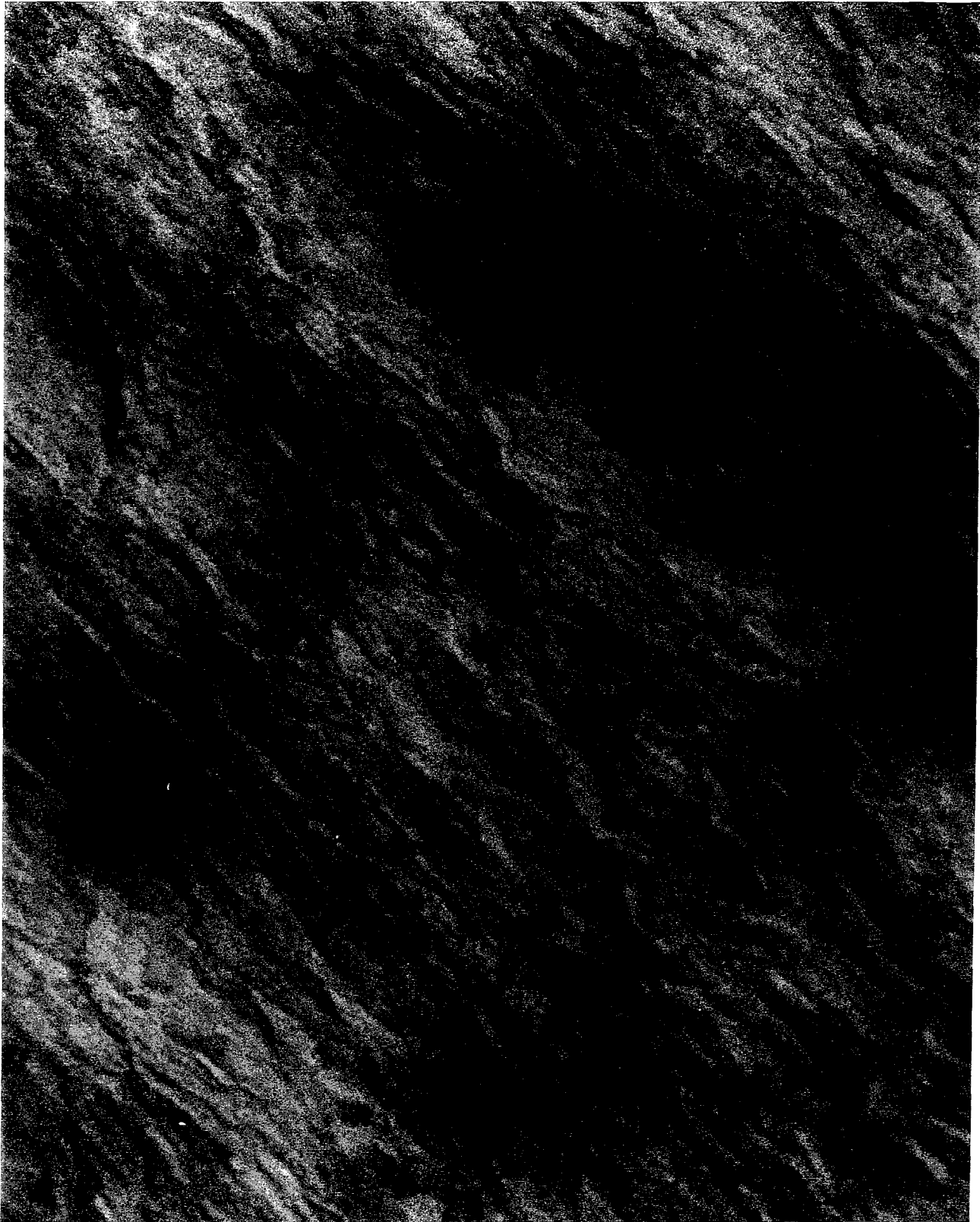
200nm
┌──────────┐

Fig.3



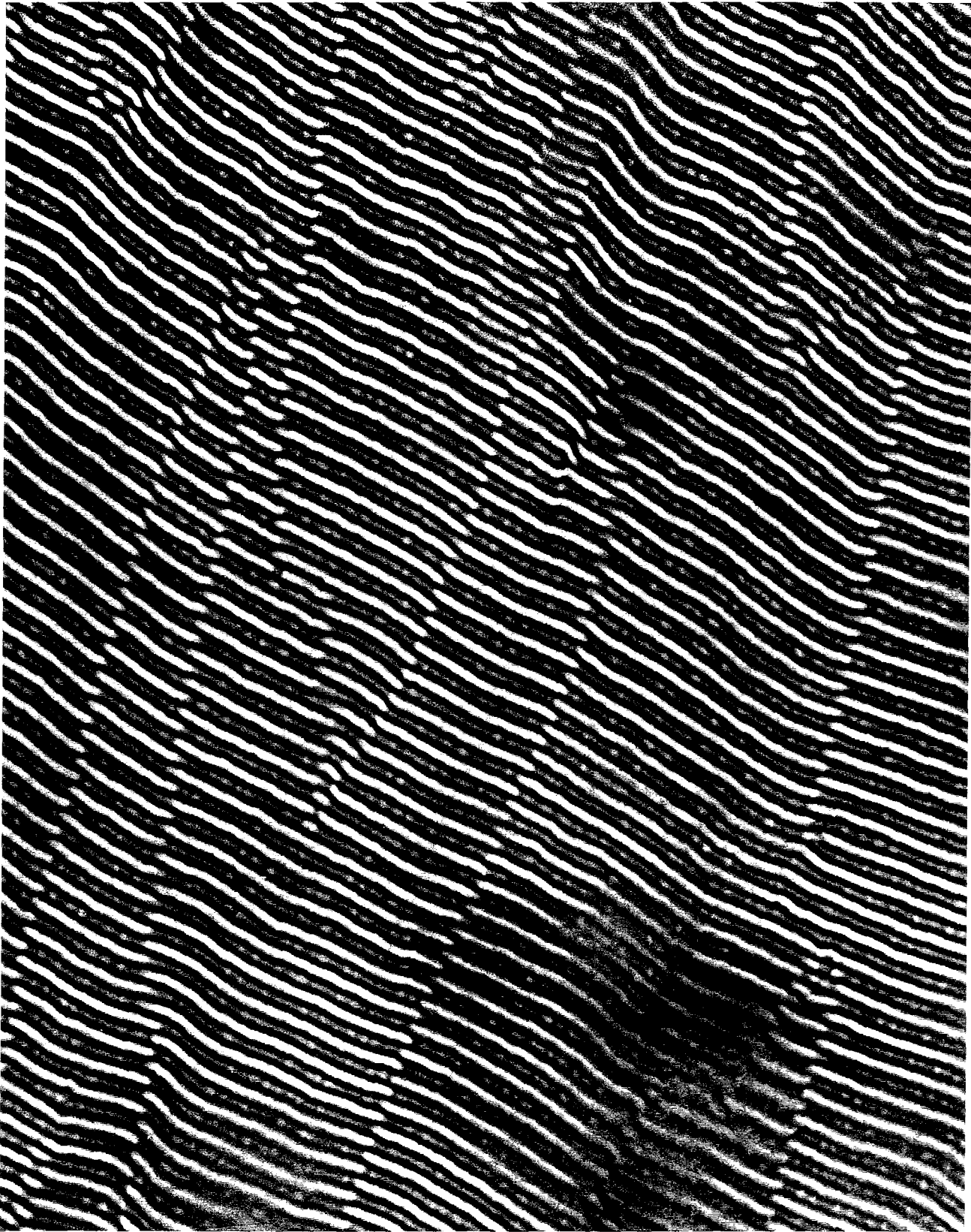
200nm
|-----|

Fig.4a



200nm

Fig.4b



200nm

Fig.5a



200nm
|-----|

Fig.5b

Fig. 6a

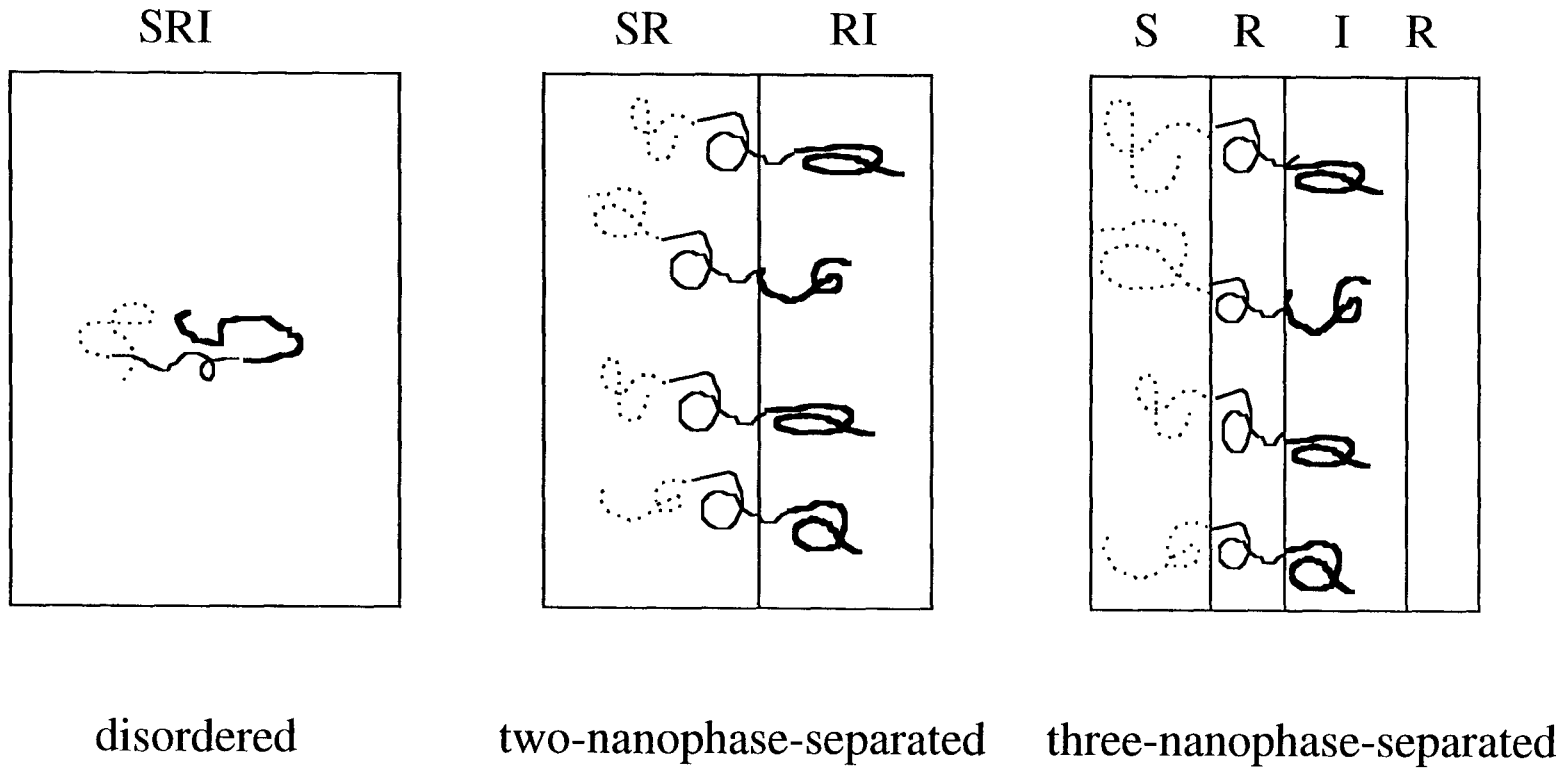


Fig. 6b

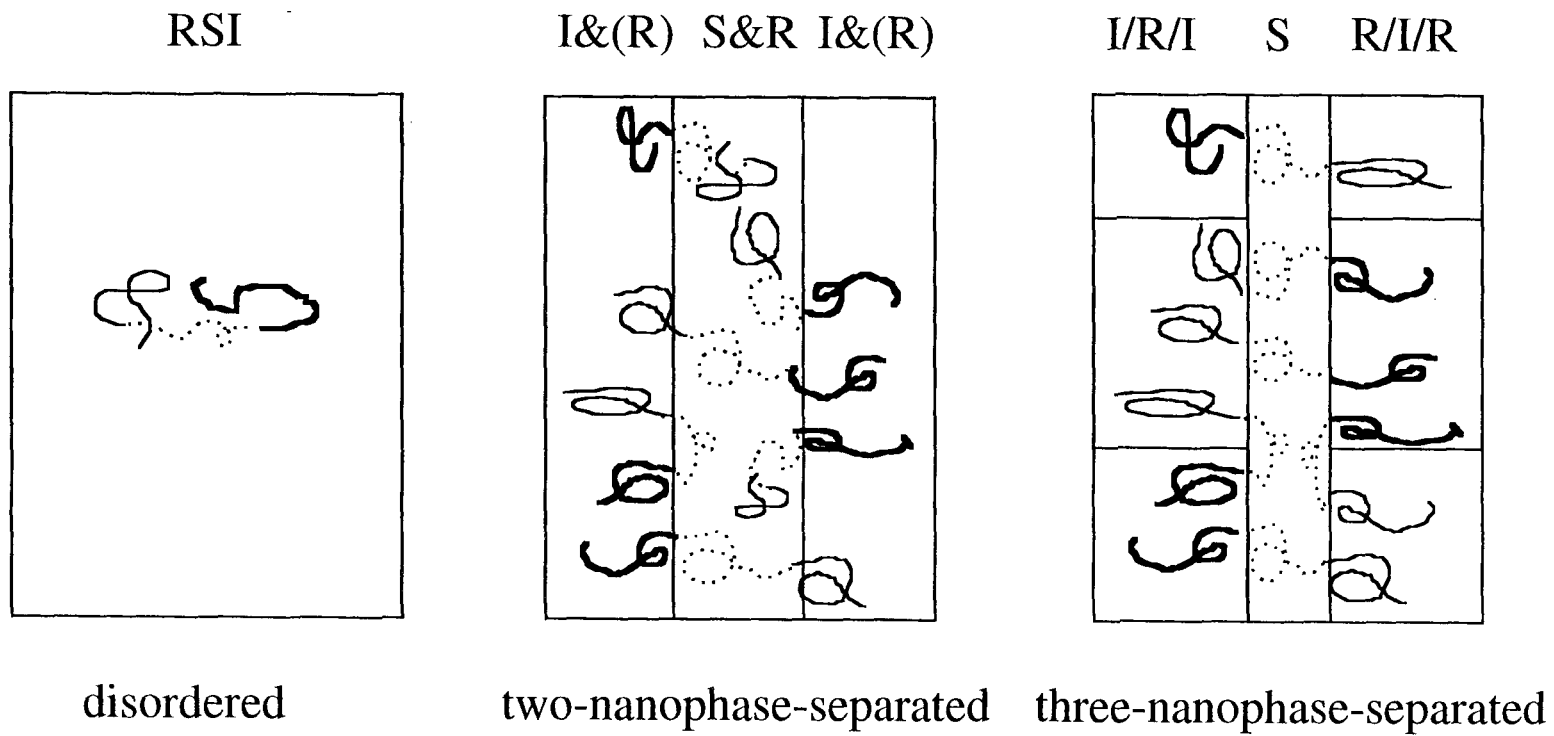
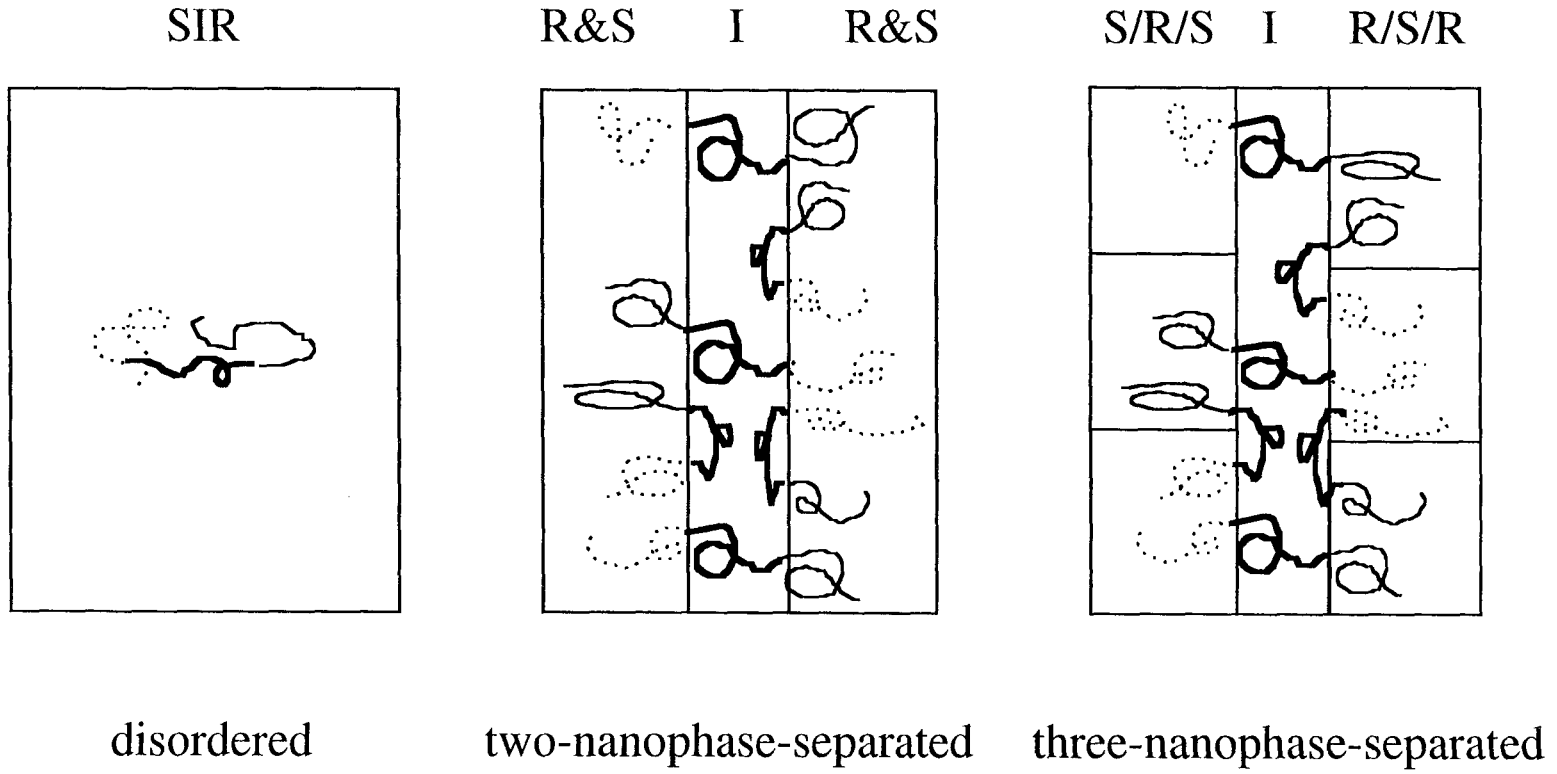


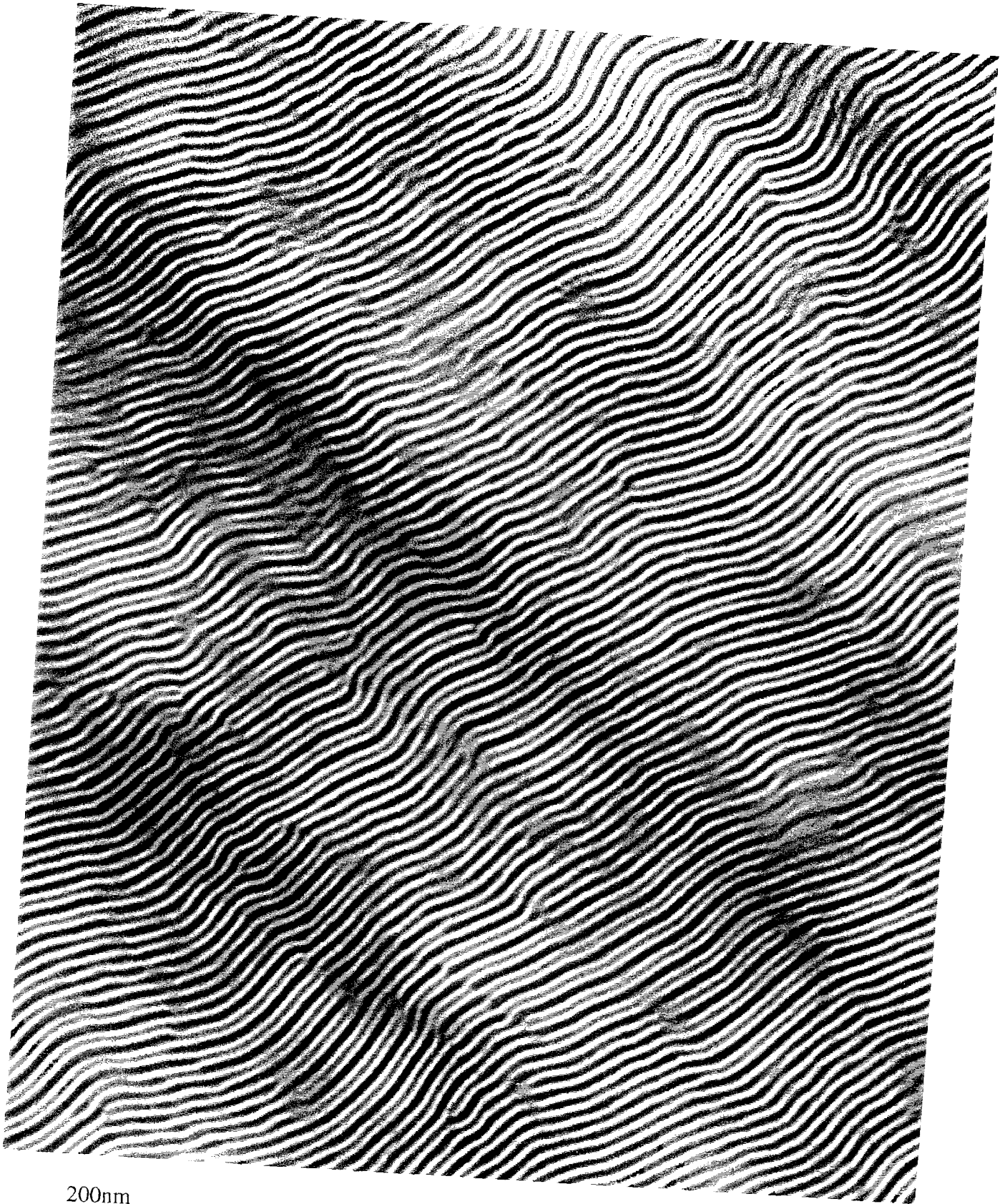
Fig. 6c





200nm
|-----|

Fig.7a



200nm

Fig.7b

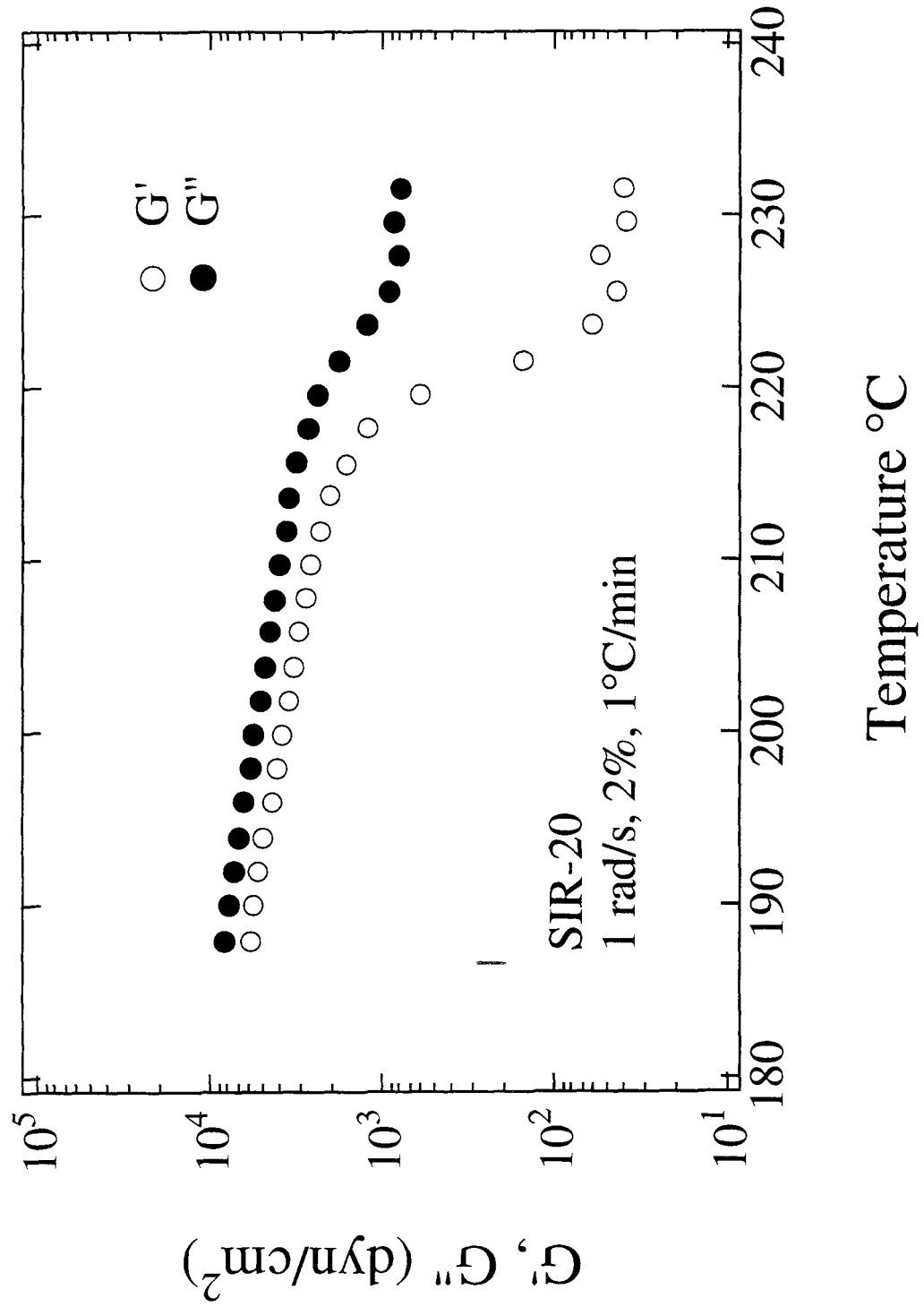


Fig. 8a

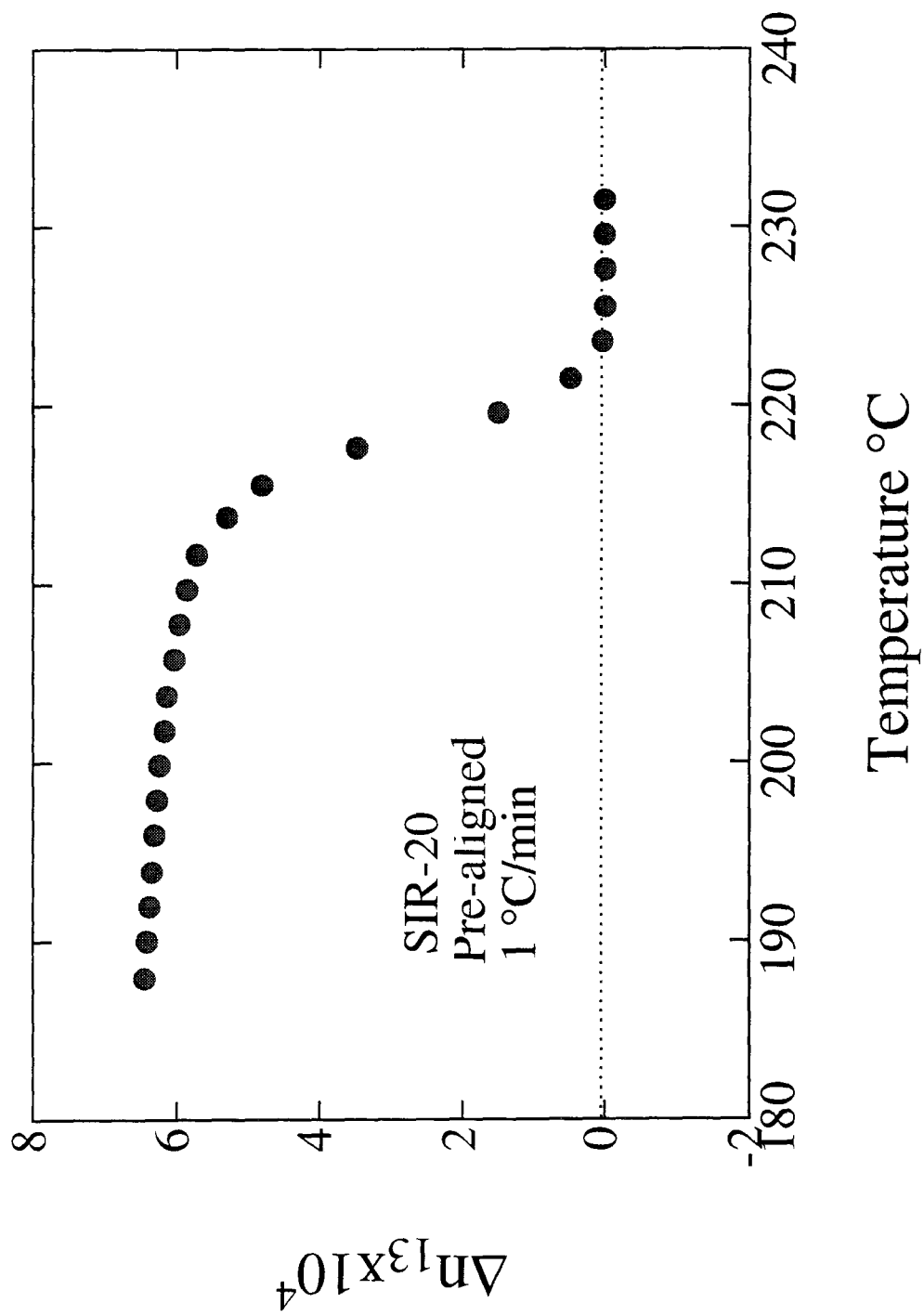
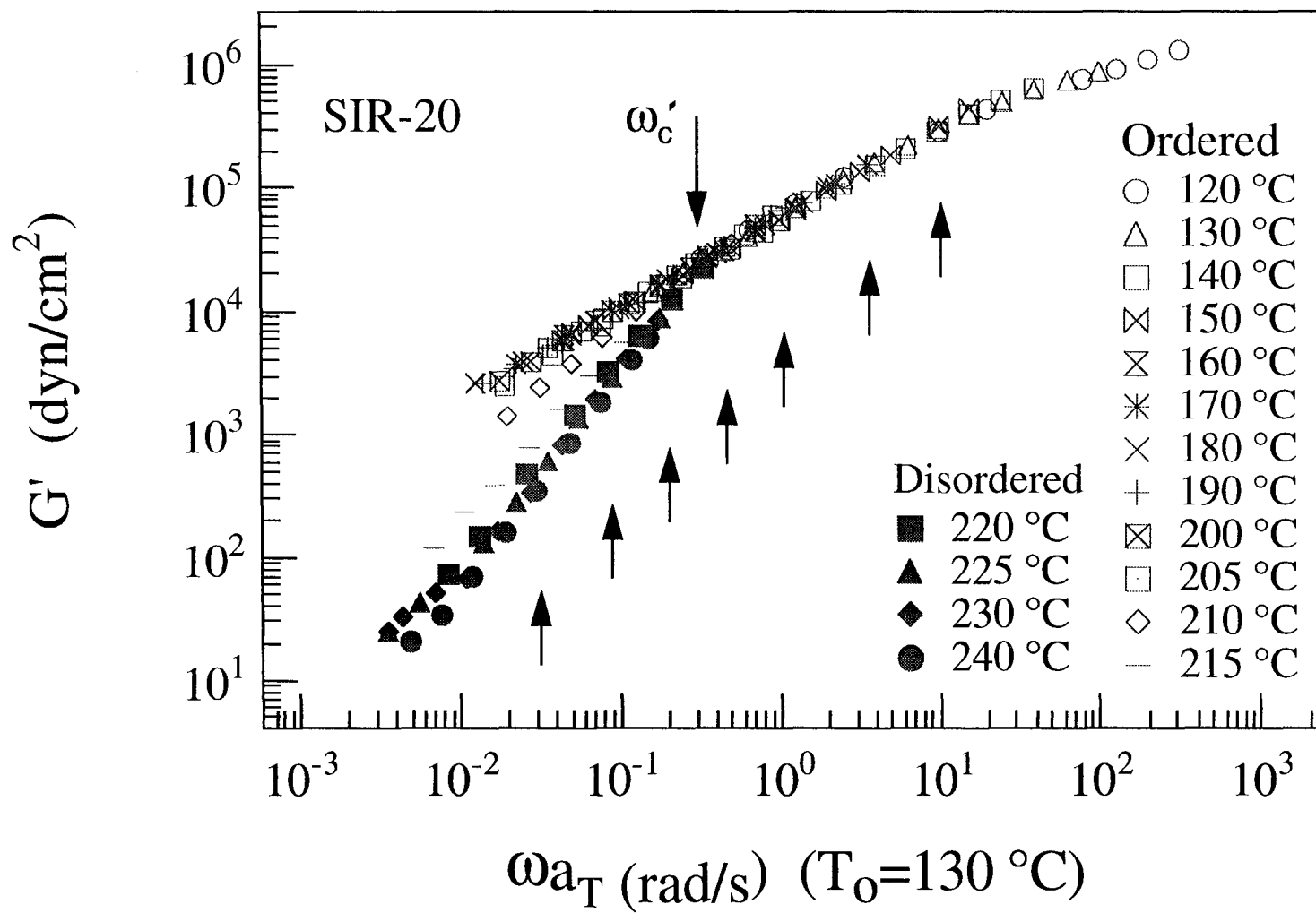


Fig. 8b

Fig.9



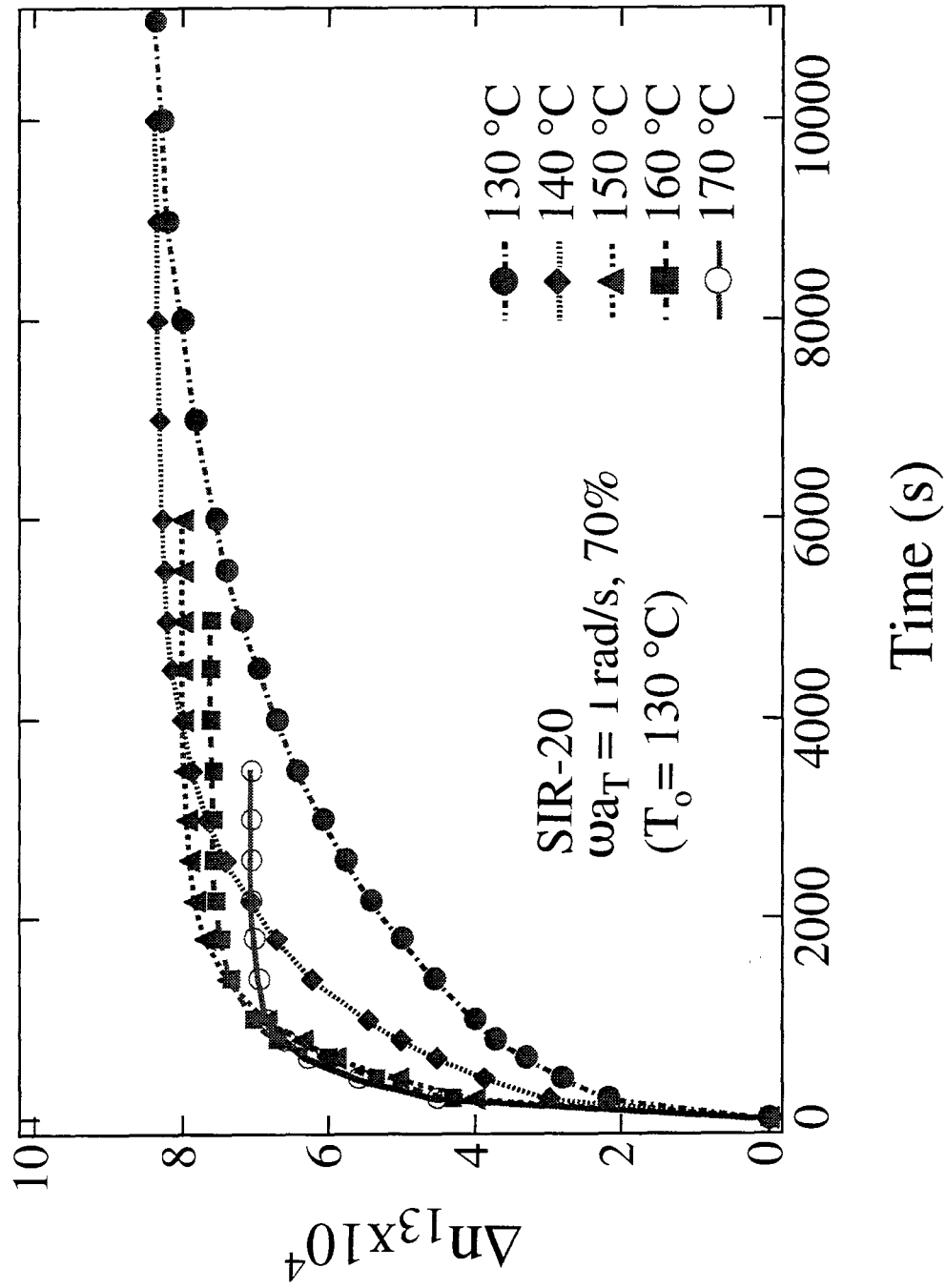


Fig. 10

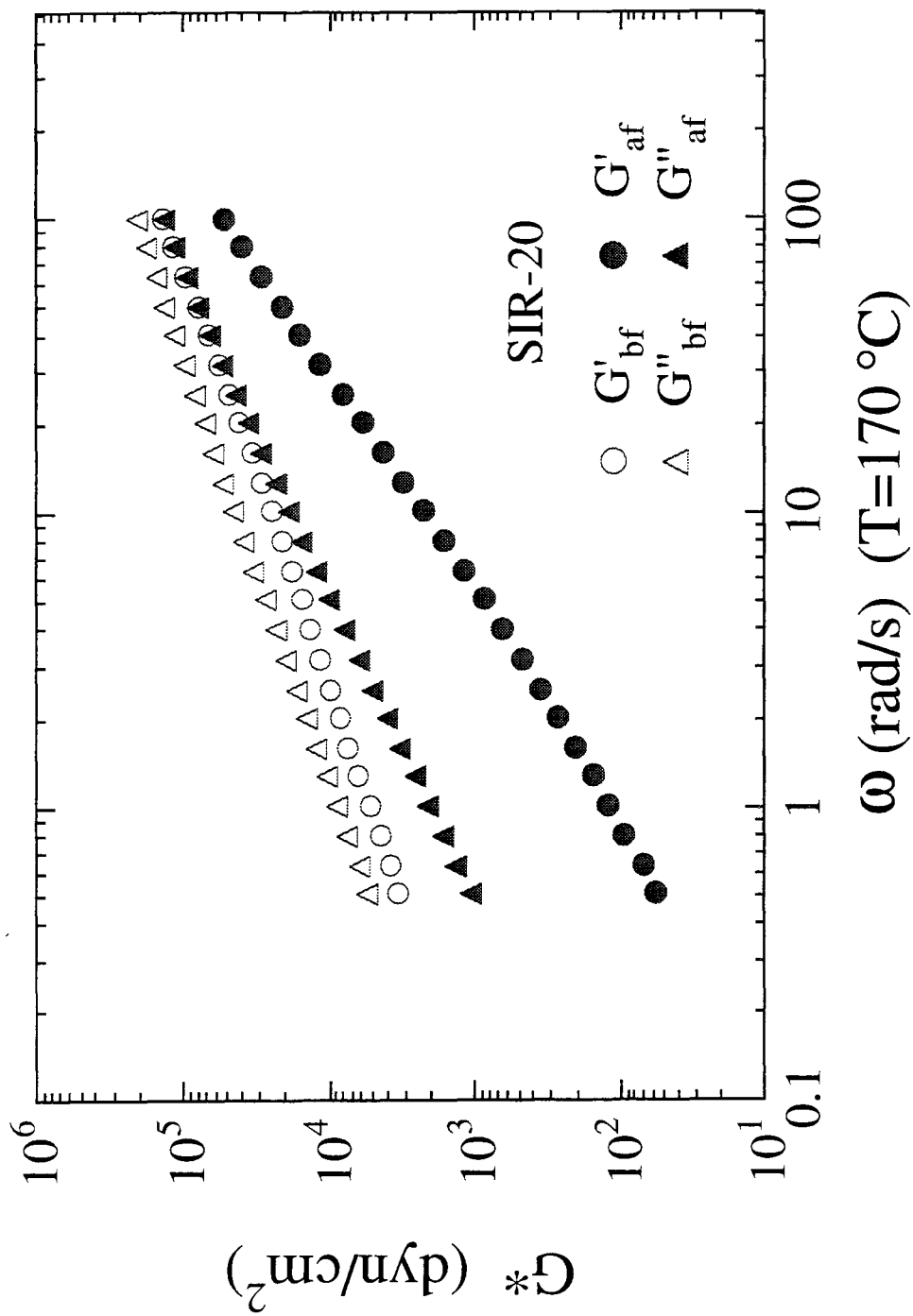


Fig. 11

200nm
|-----|

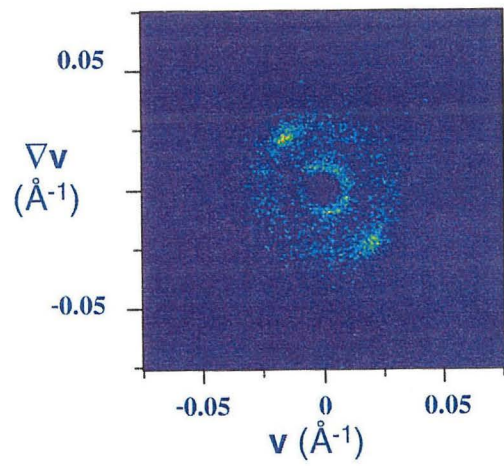
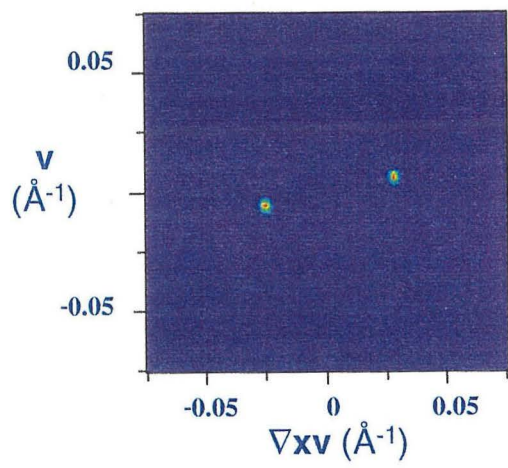
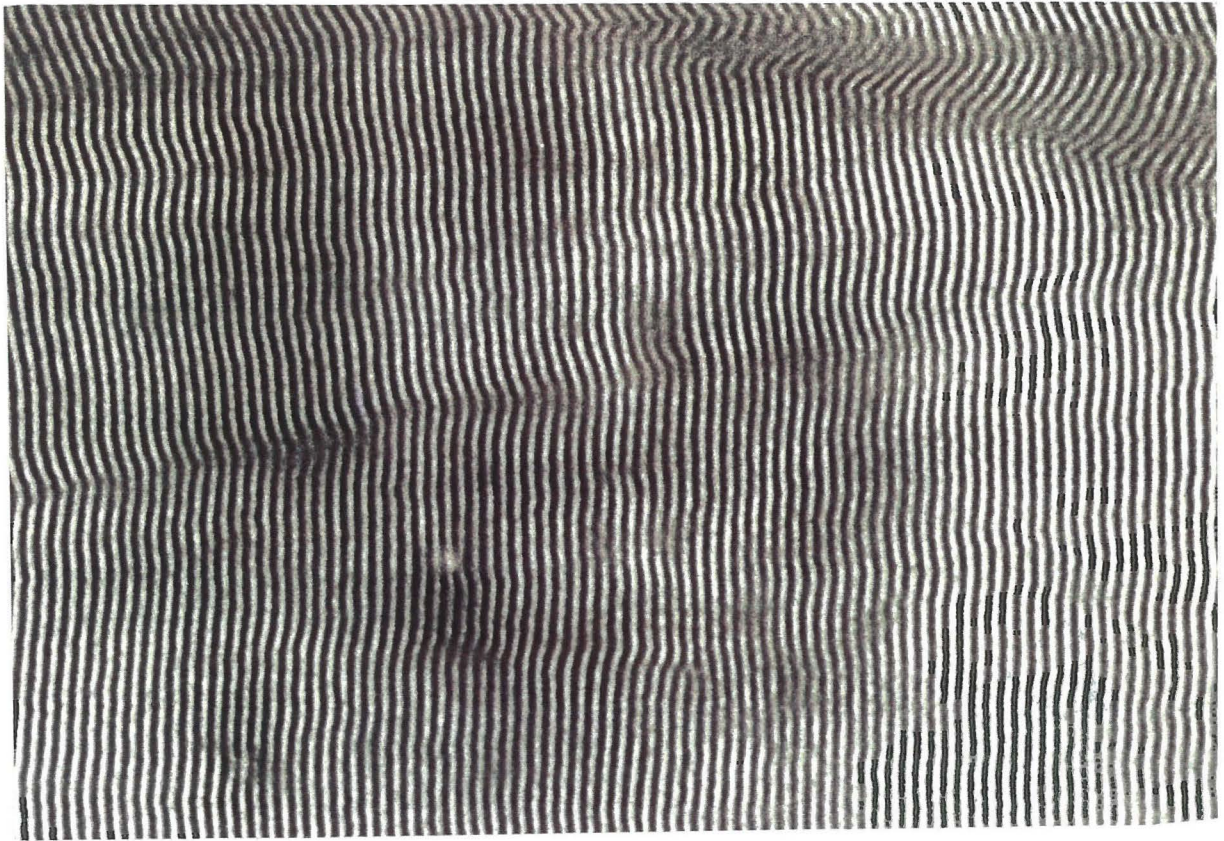


Fig.12

Fig. 13a

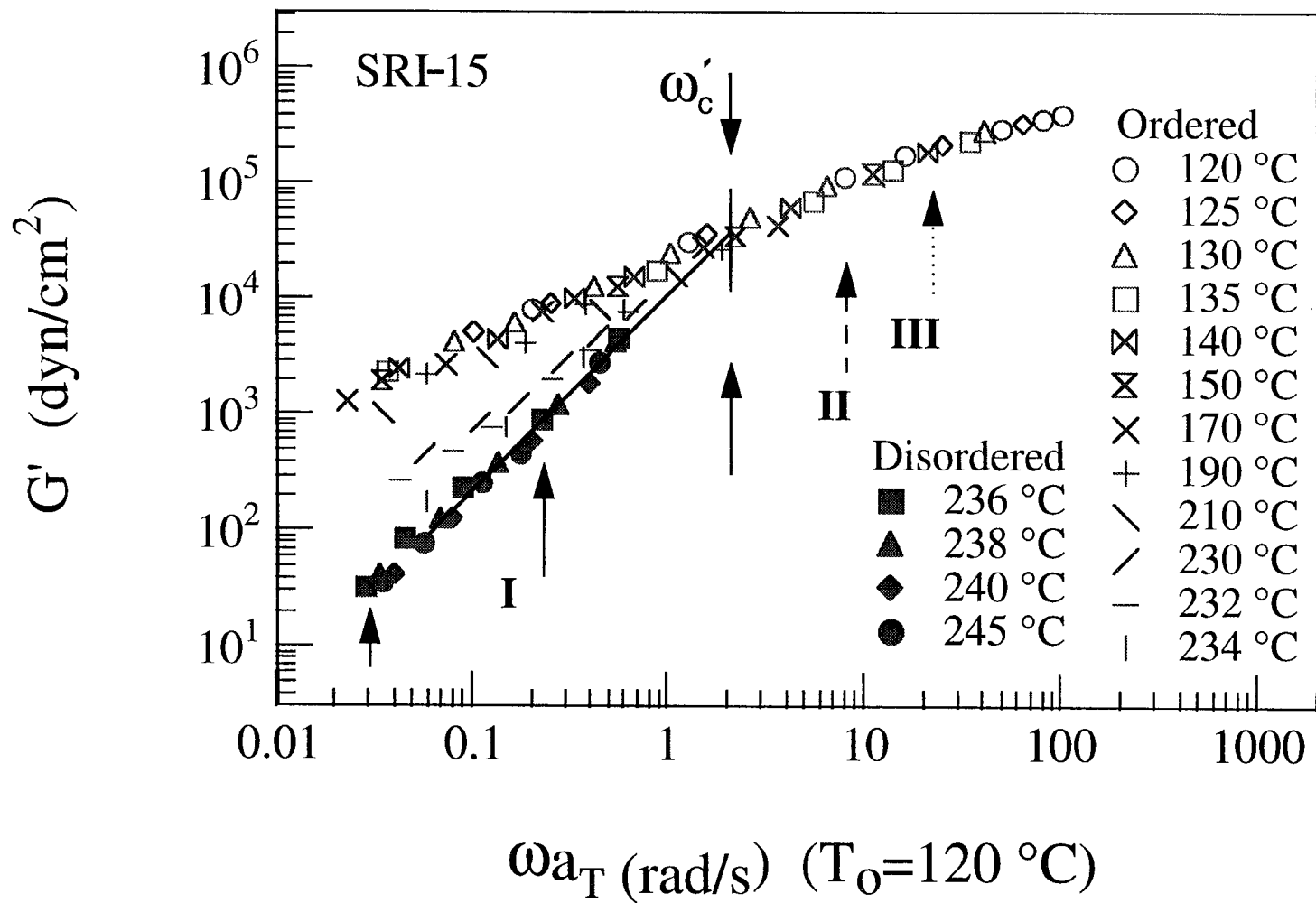


Fig. 13b

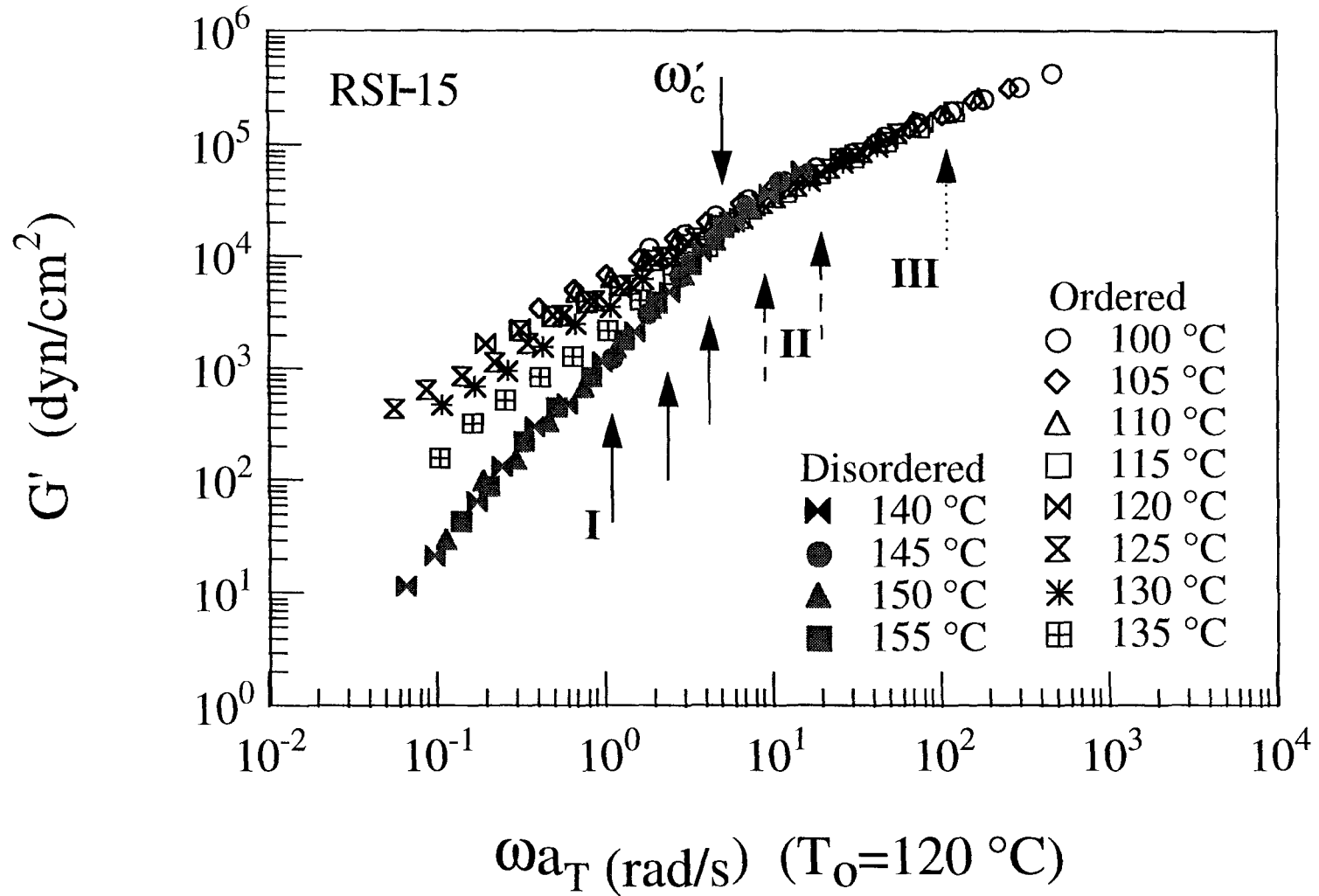
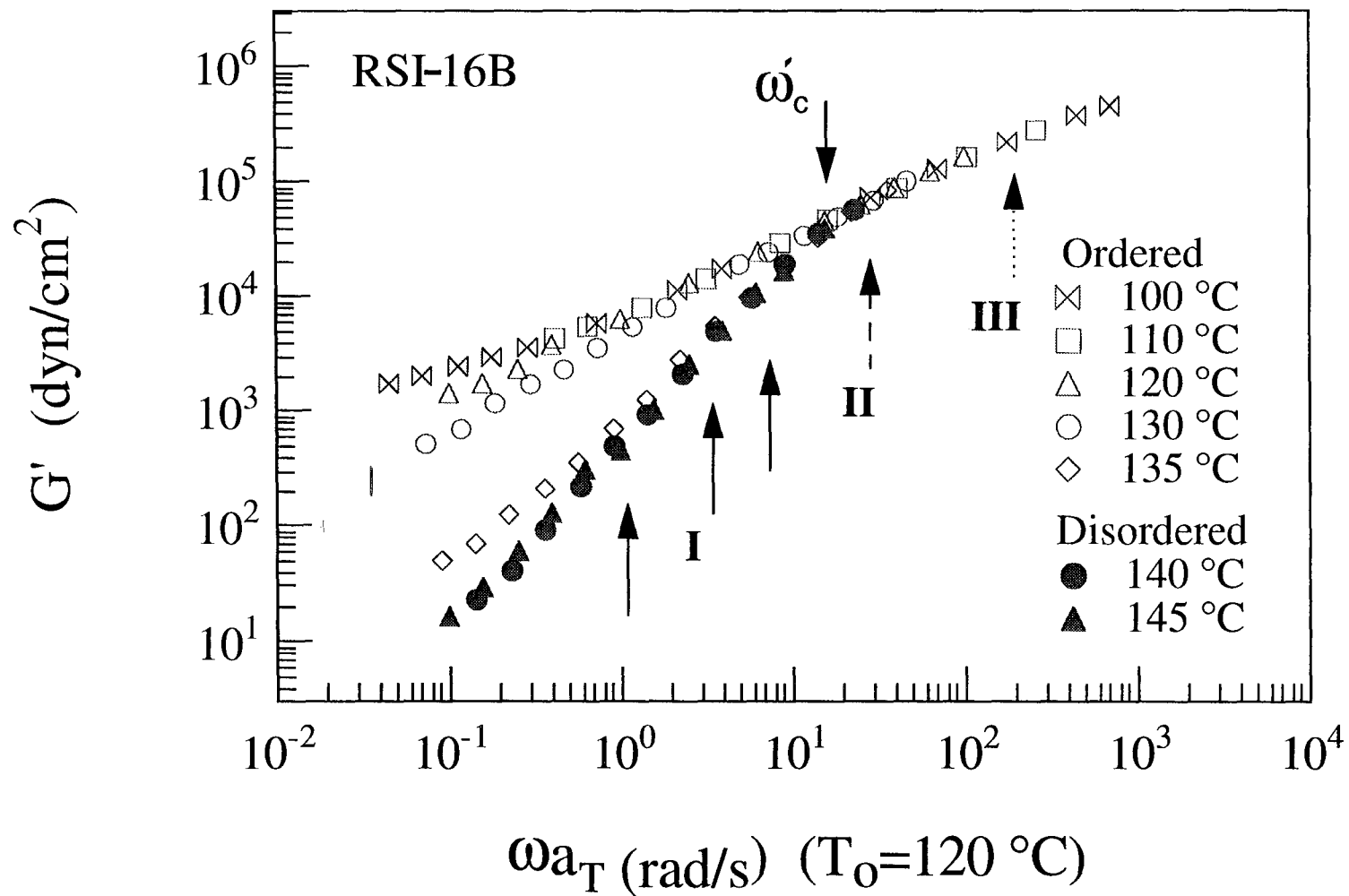


Fig. 13c



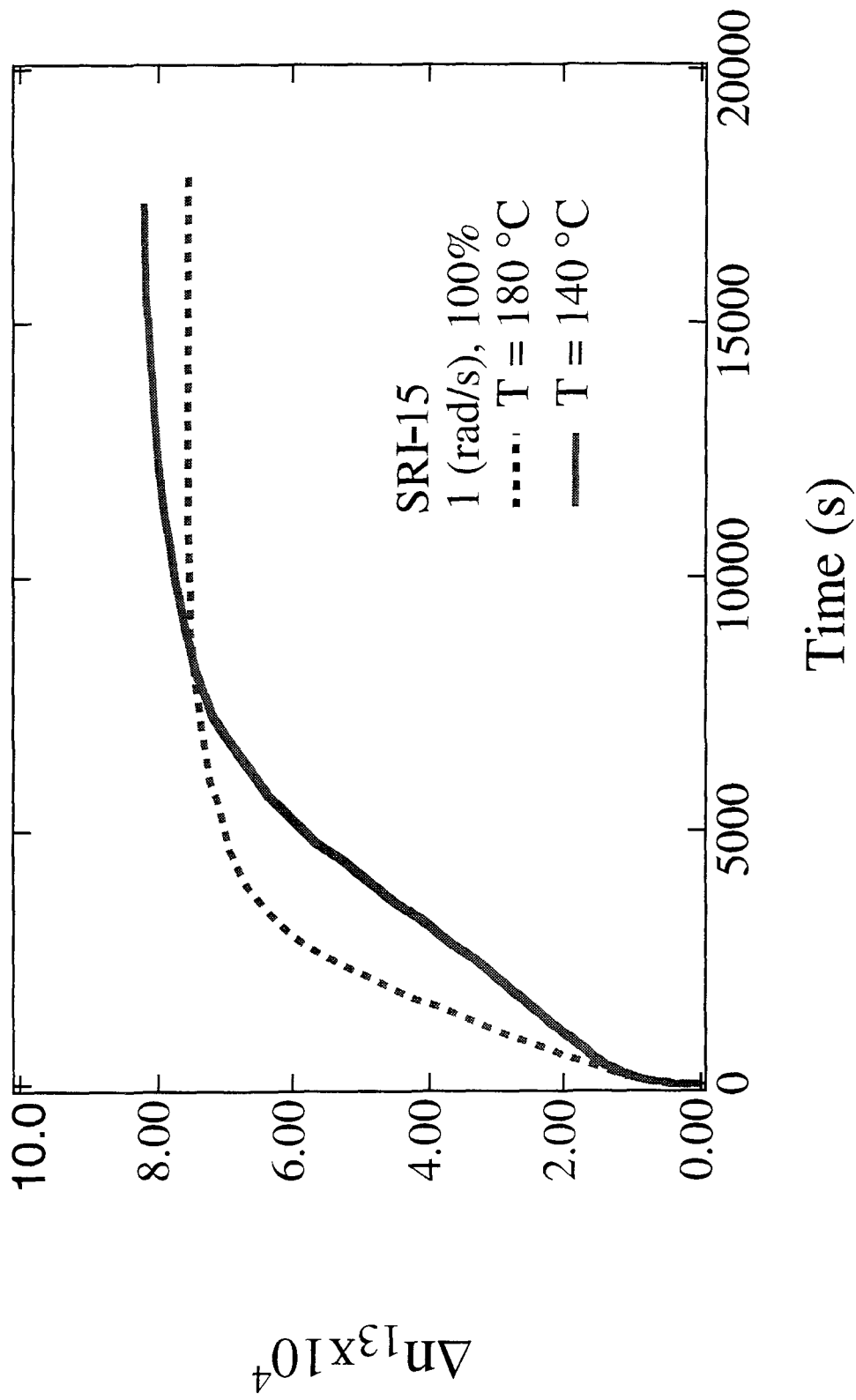


Fig. 14a

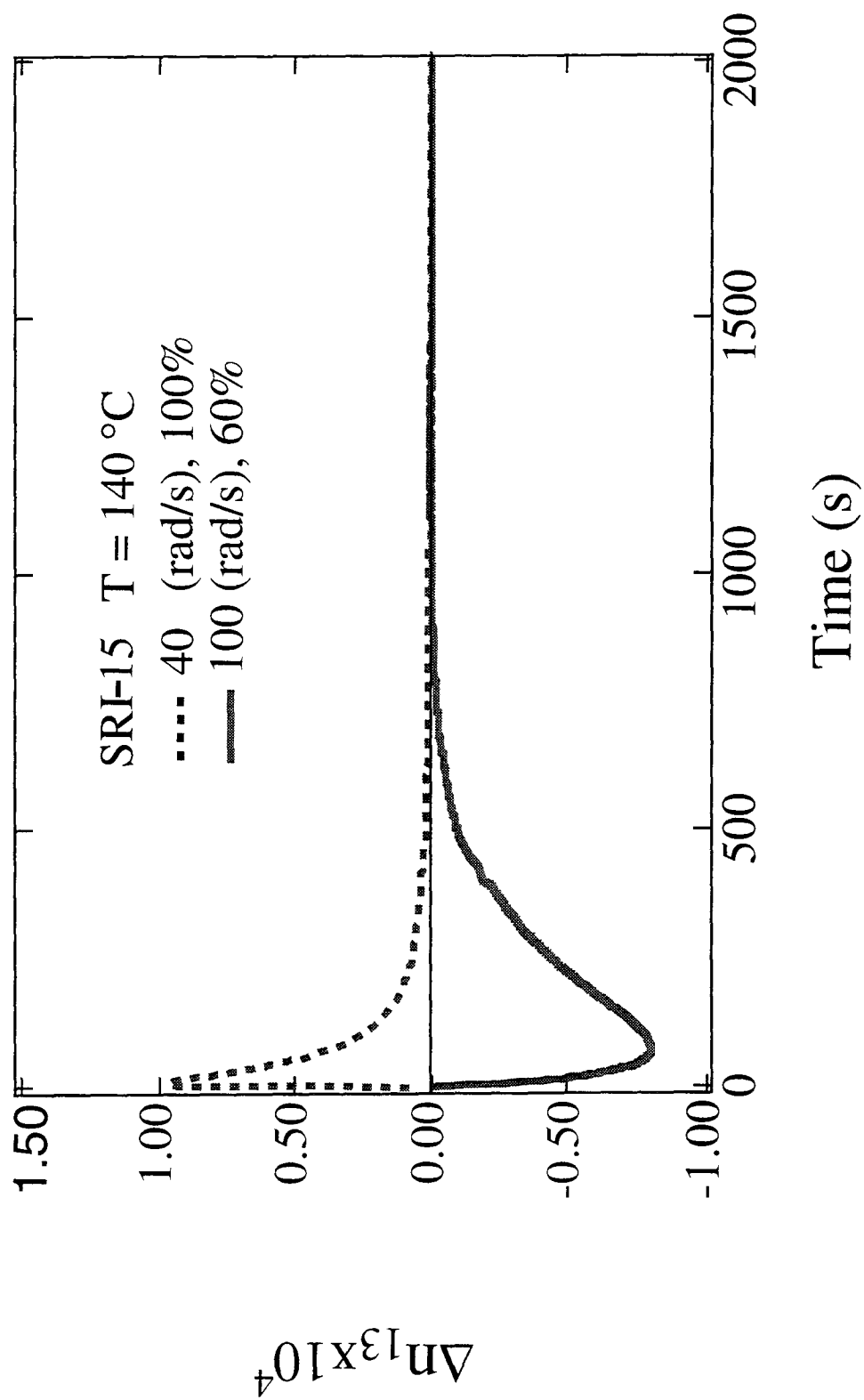


Fig. 14b

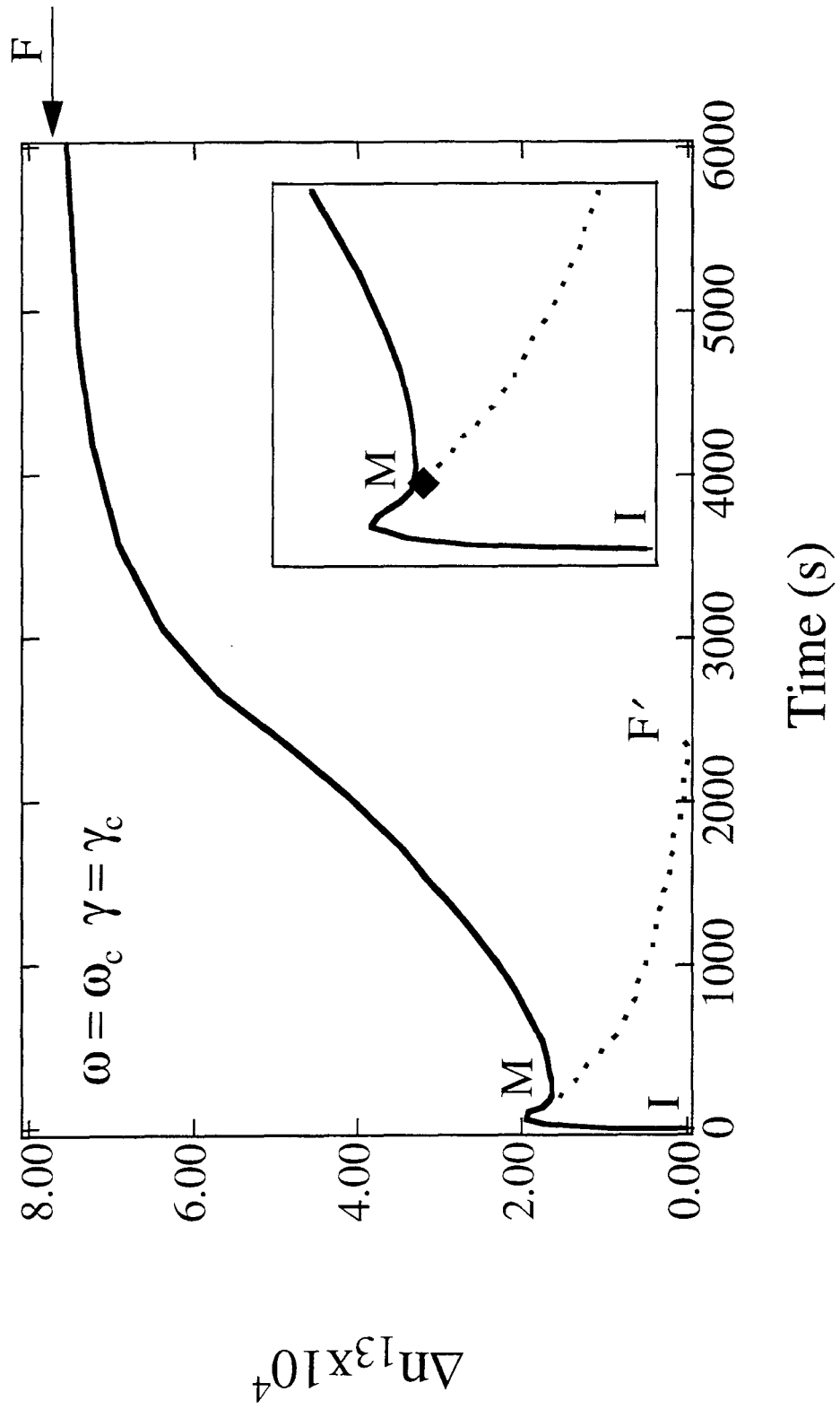


Fig. 14c

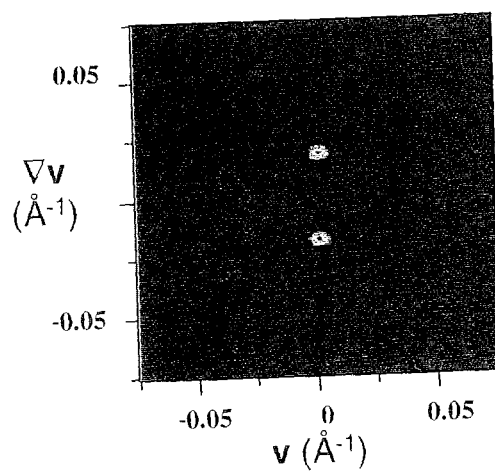
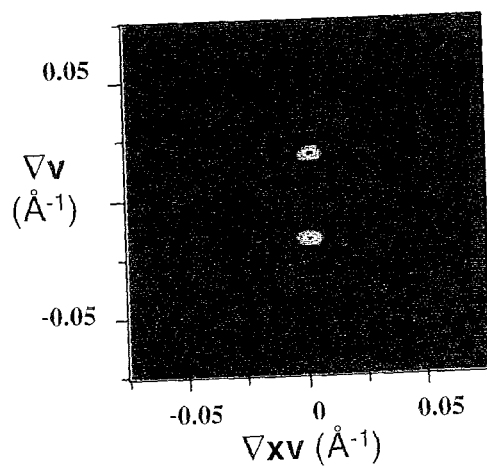
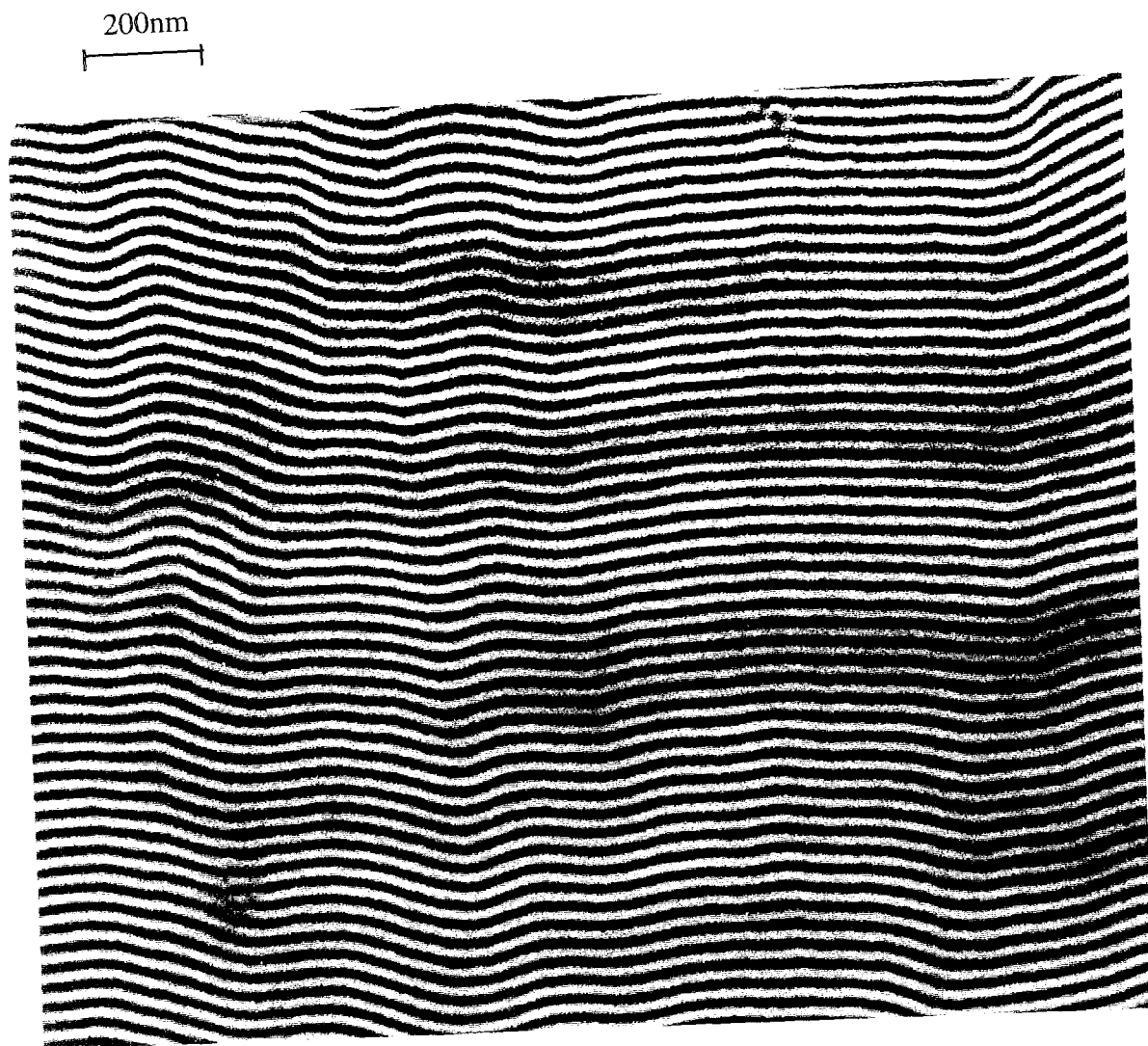


Fig.15

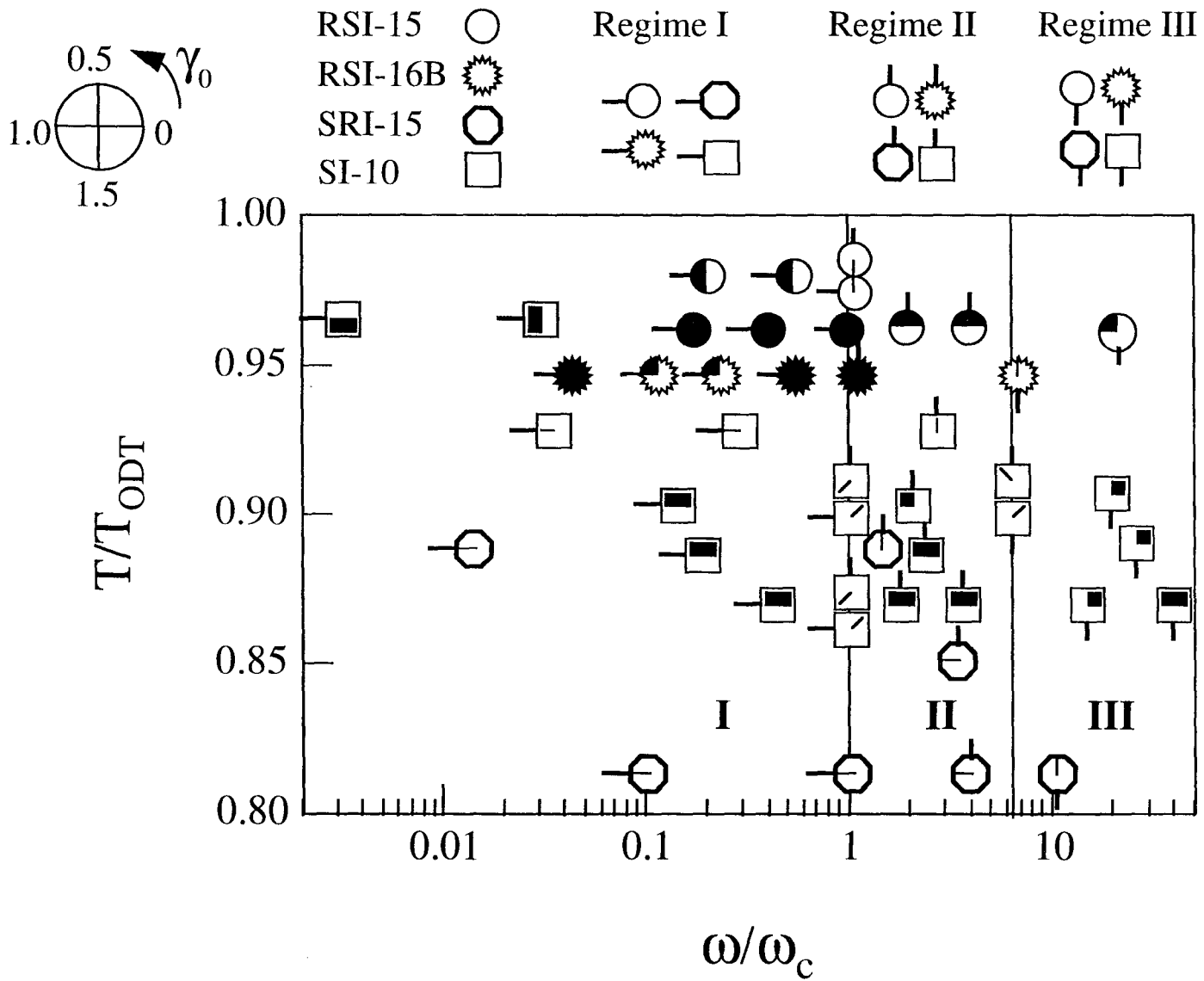


Fig. 16

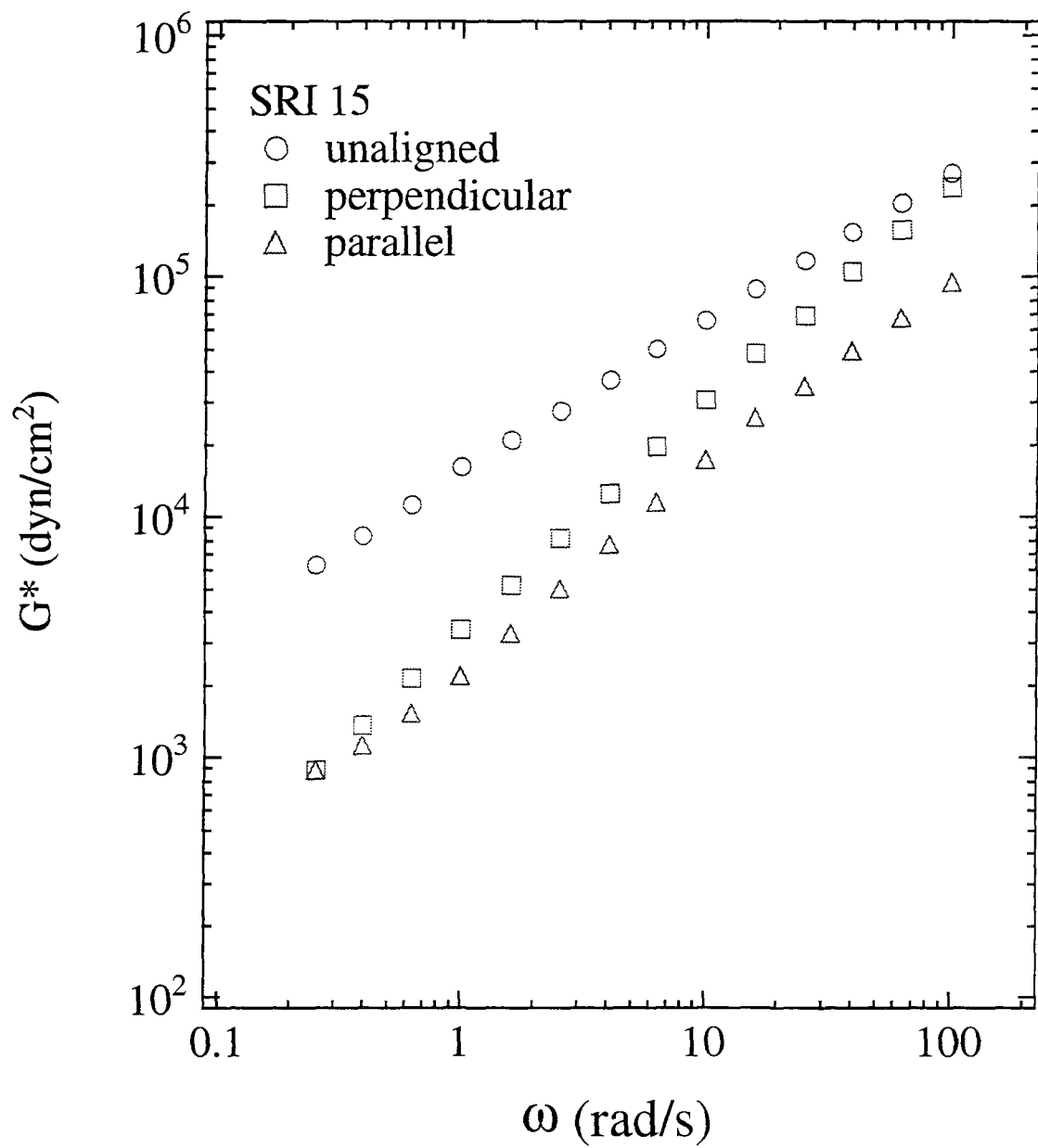


Fig. 17a

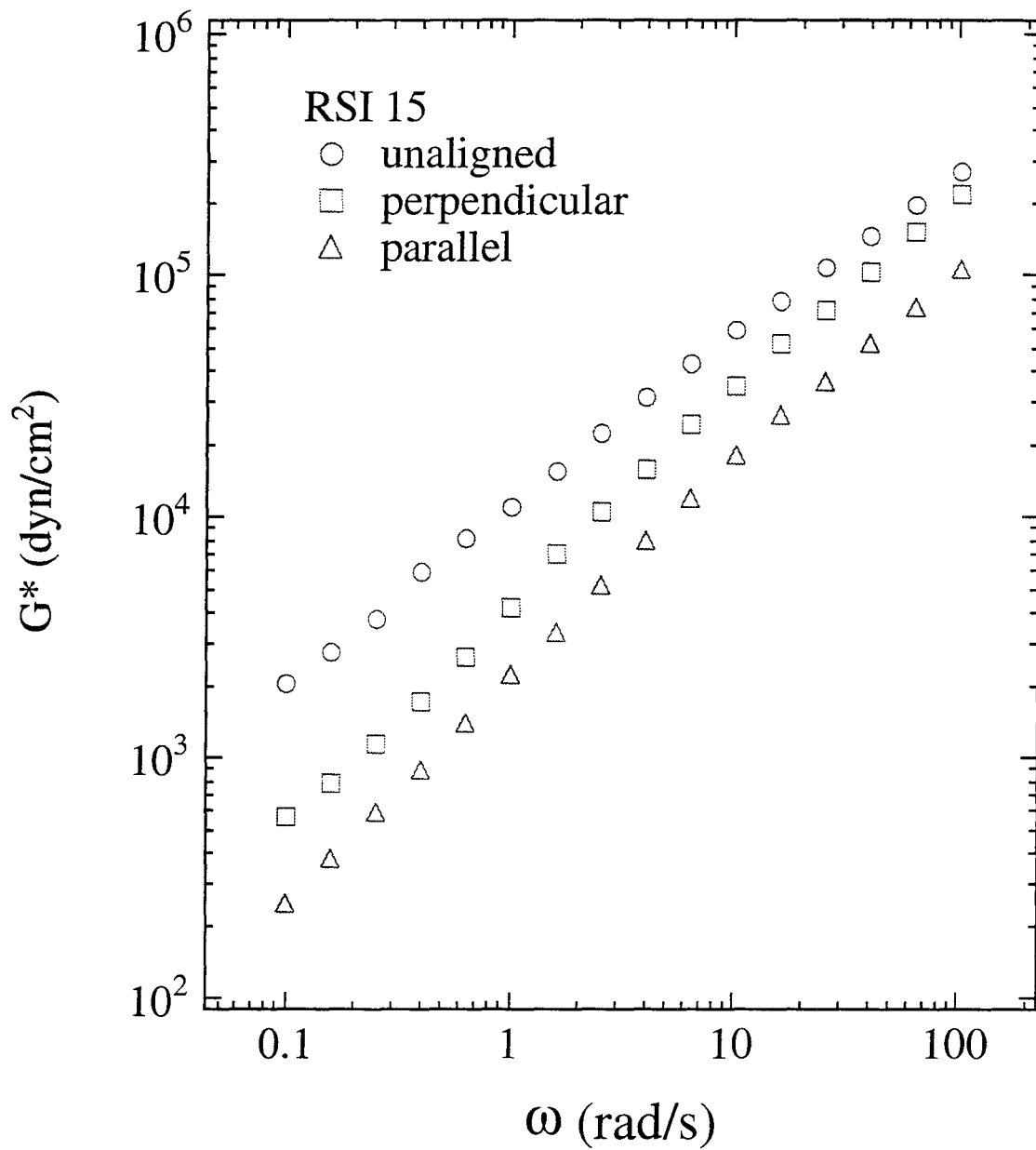


Fig. 17b

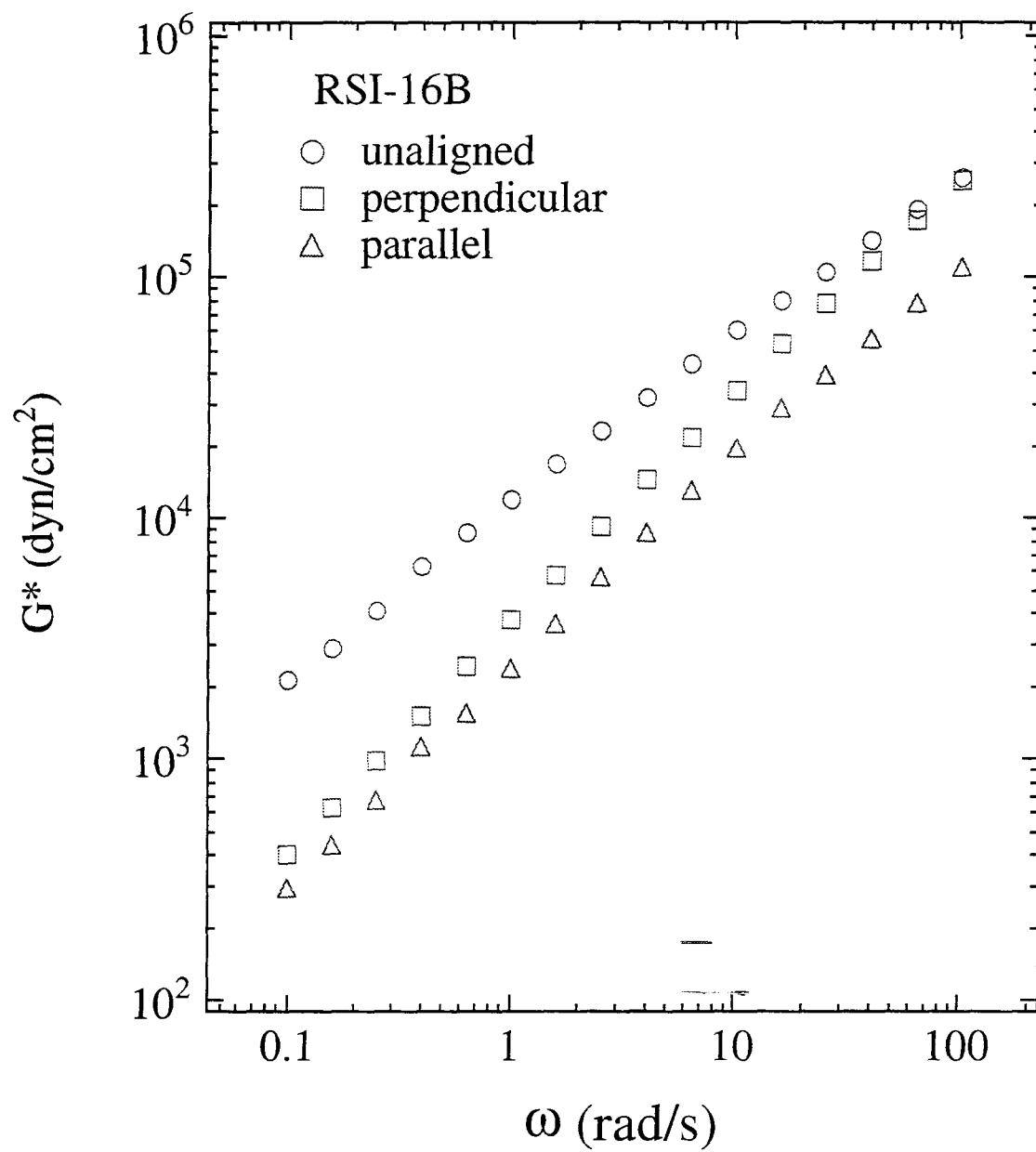
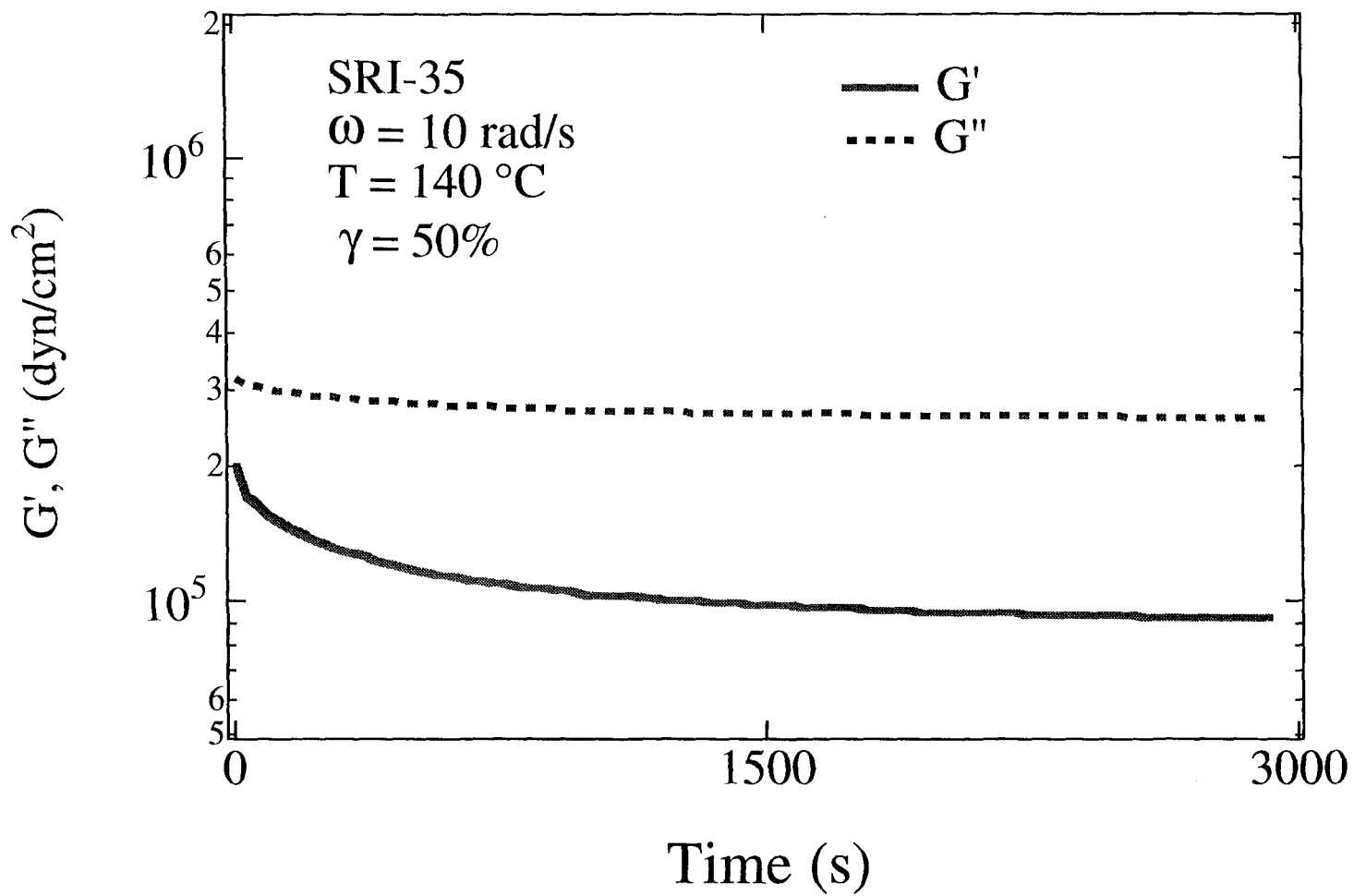


Fig. 17c

Fig. 18a



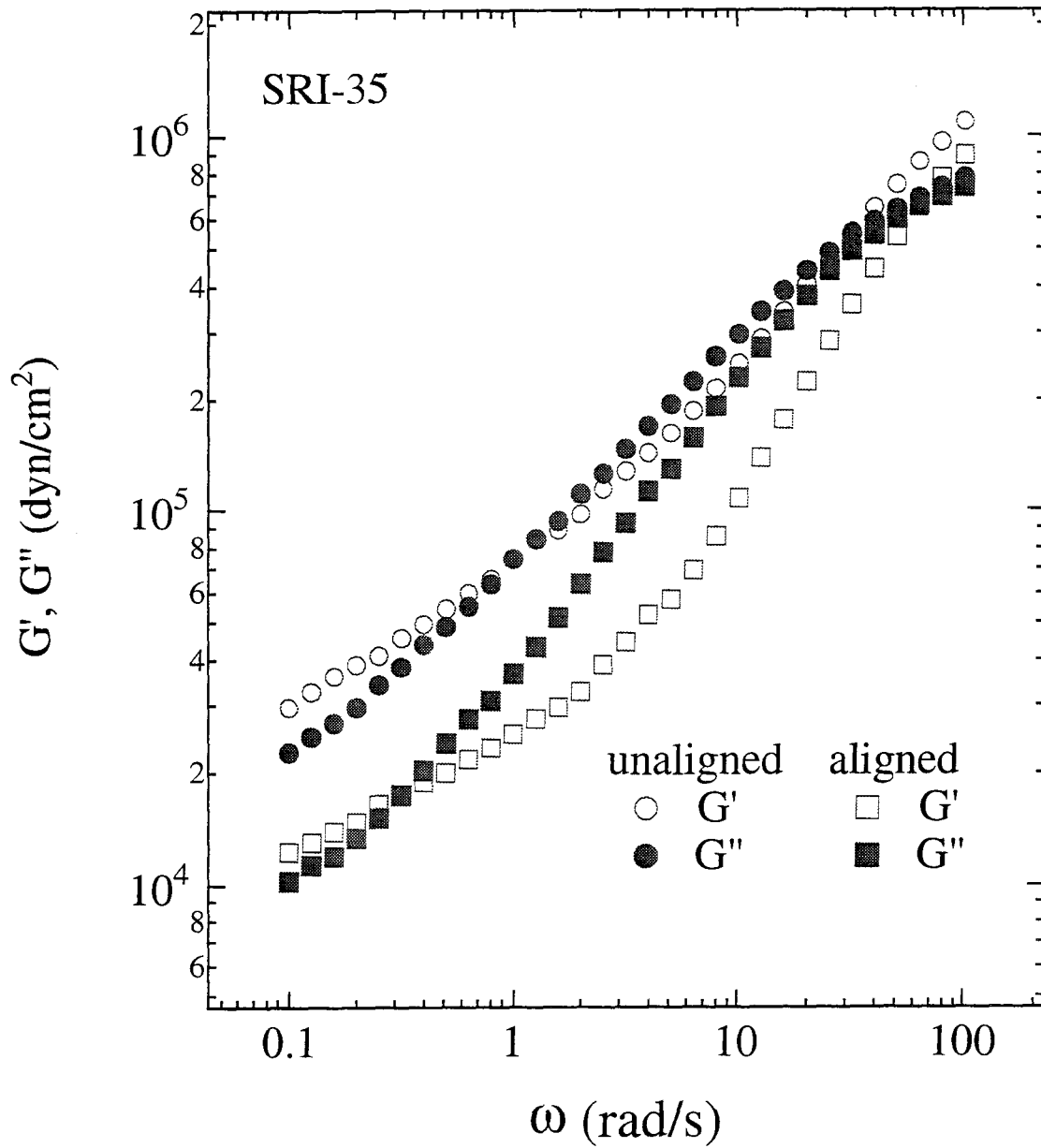
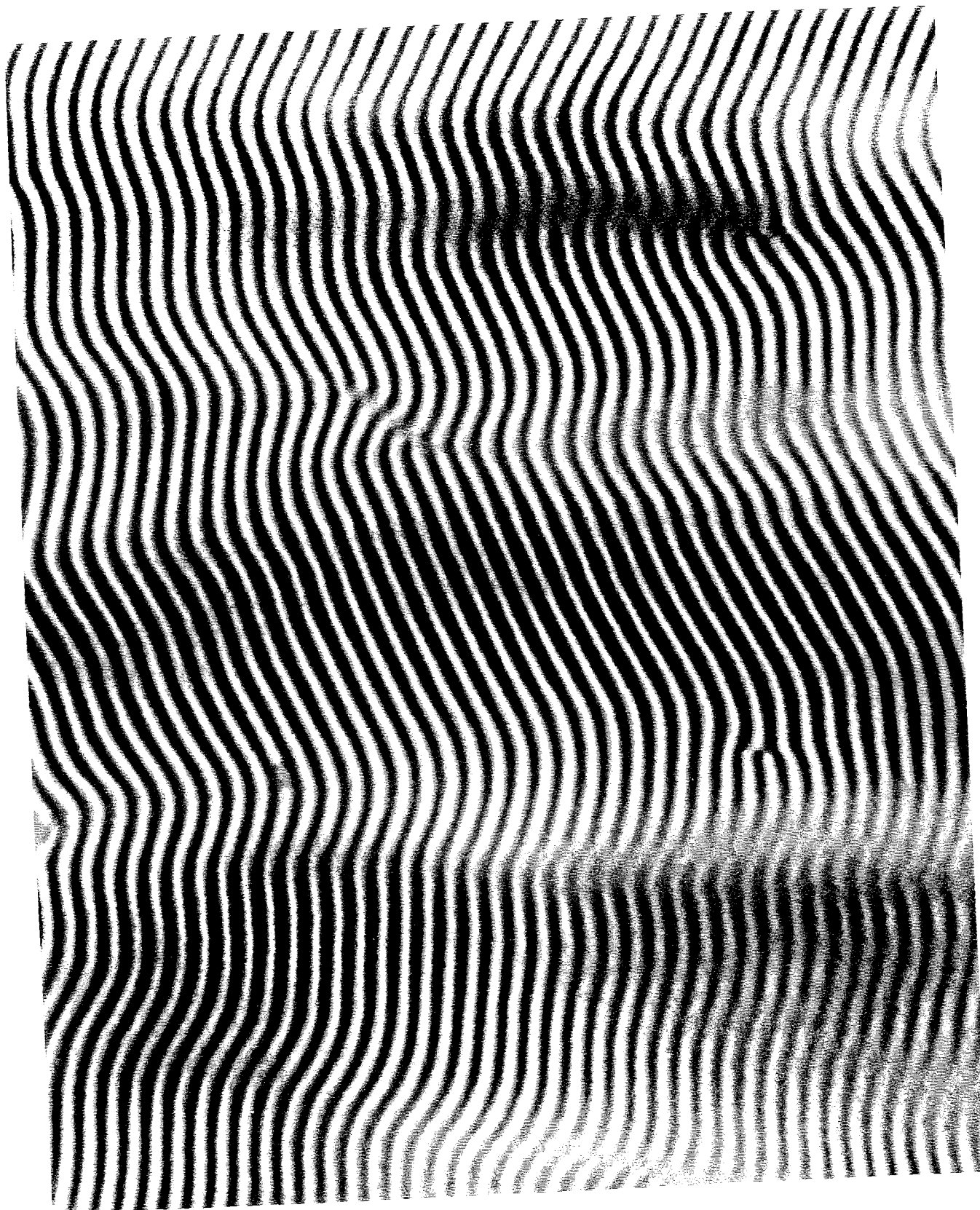


Fig. 18b



200nm
|-----|

Fig.19

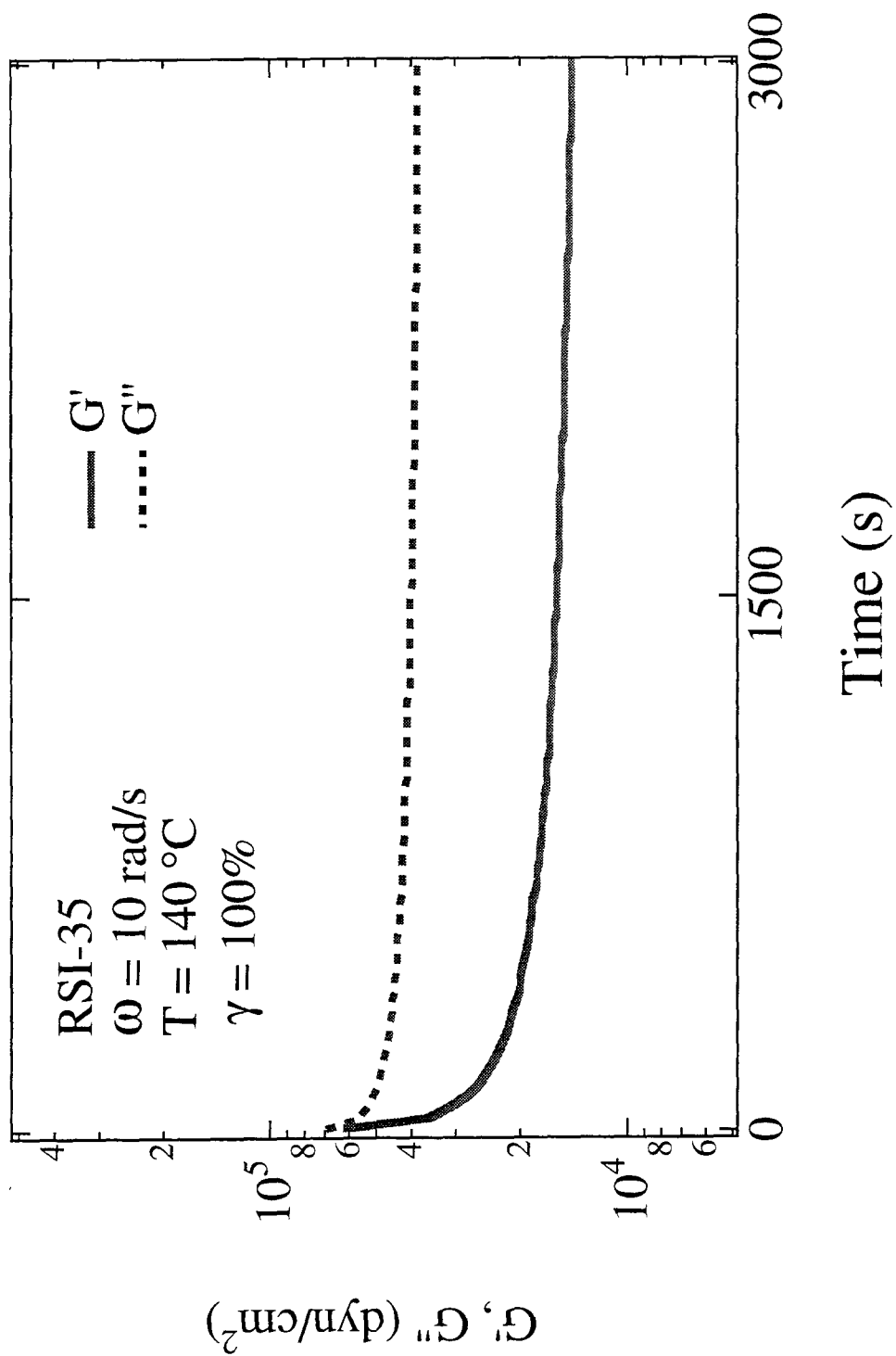


Fig. 20a

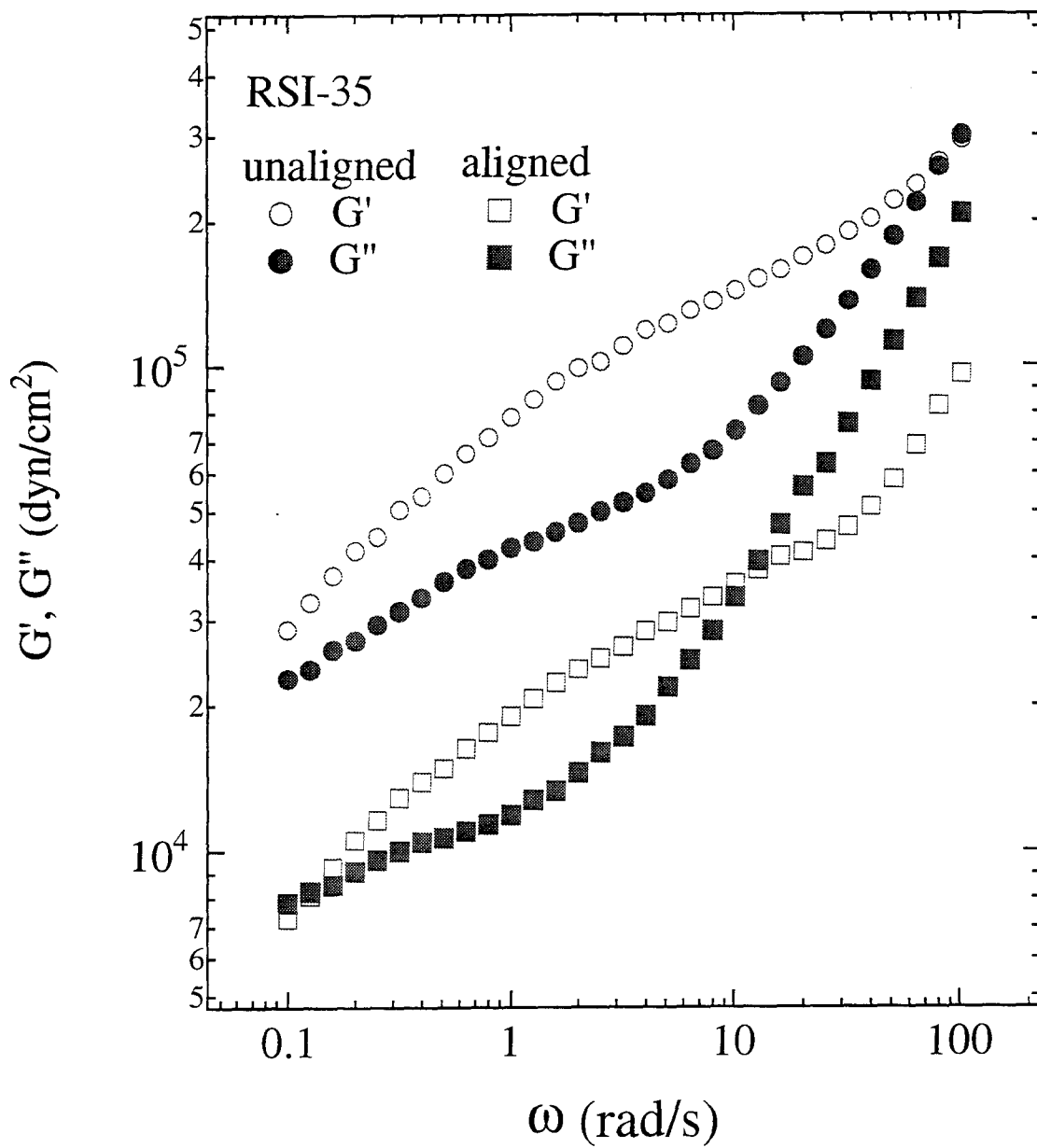
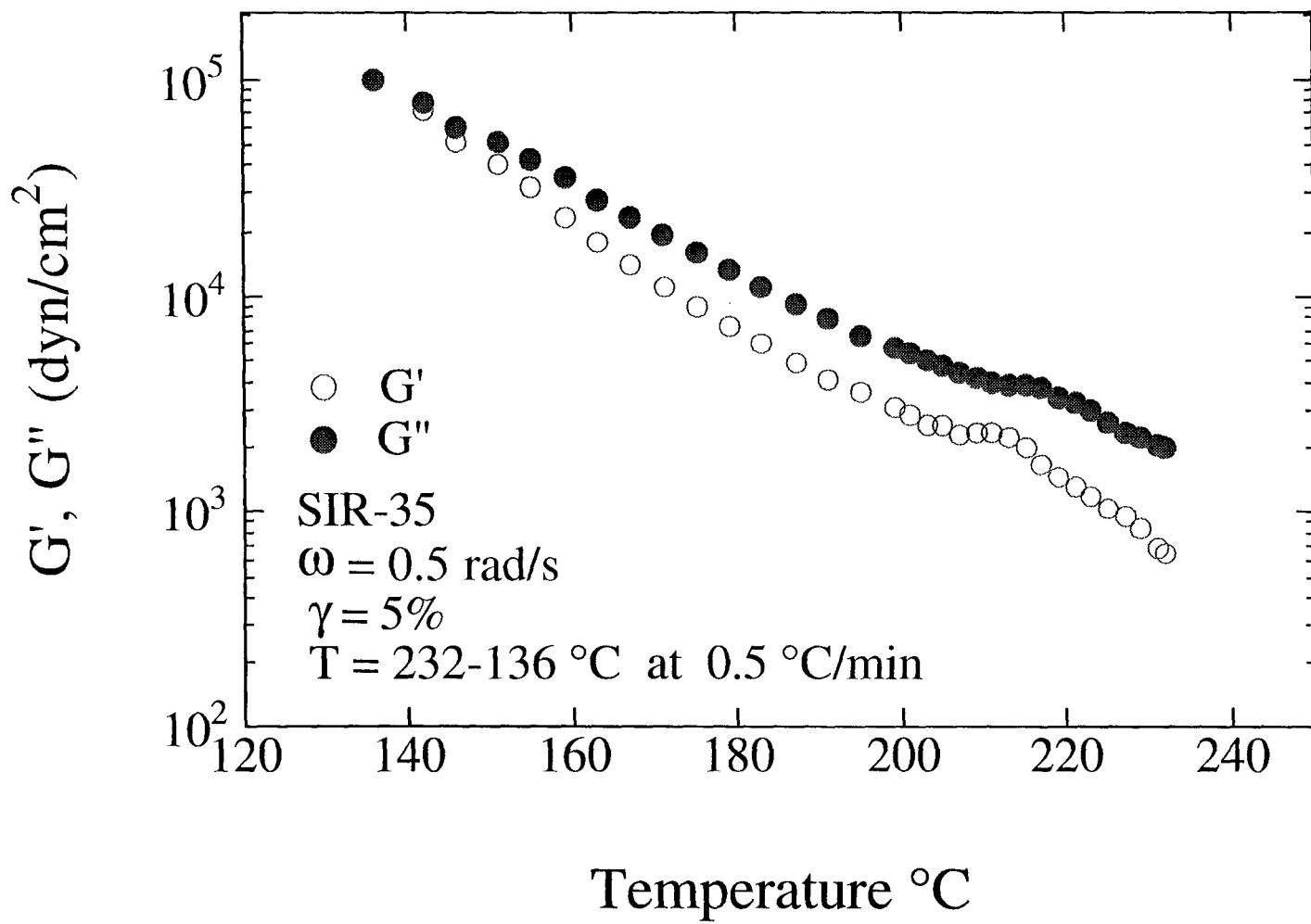


Fig. 20b

Fig. 21



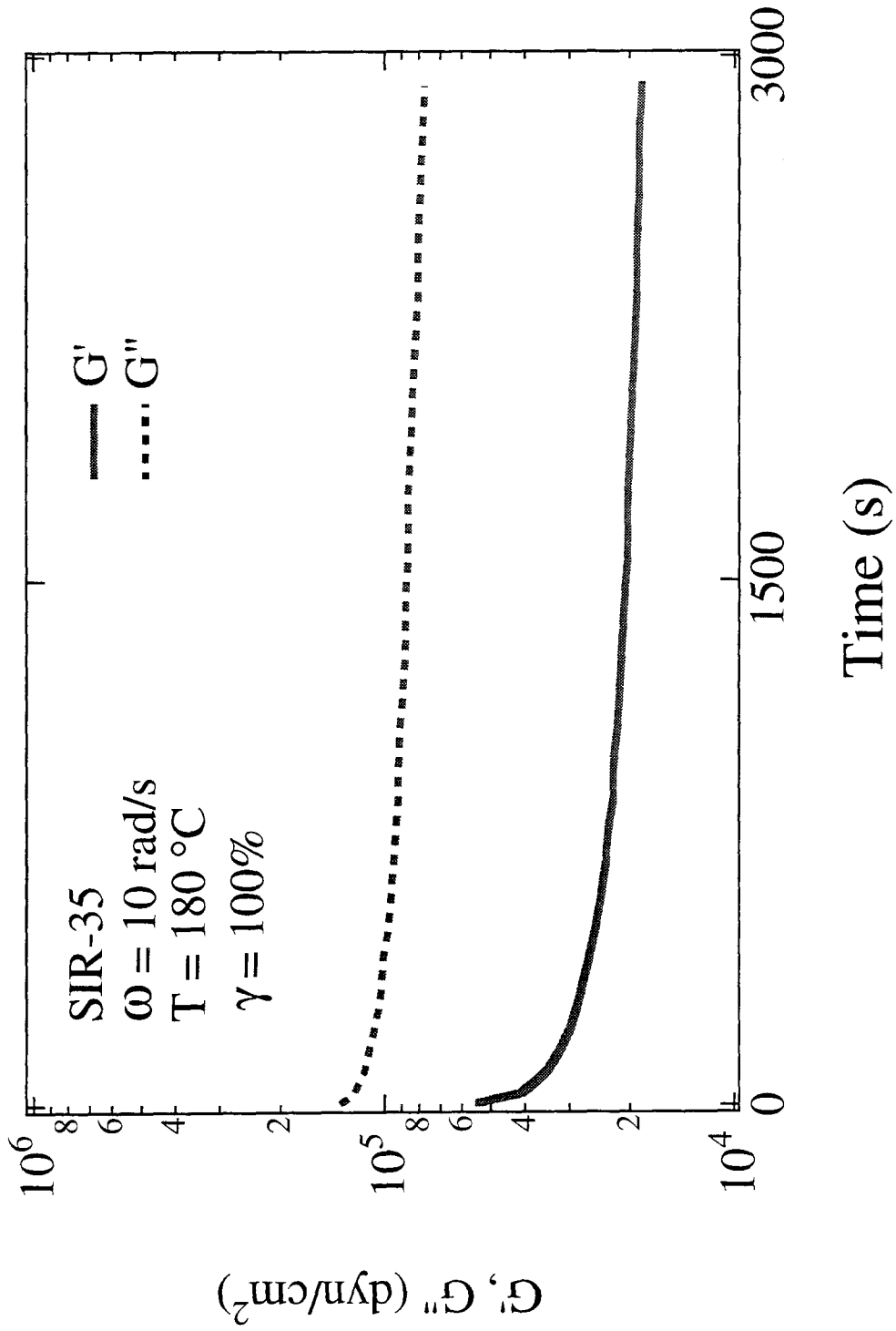


Fig. 22a

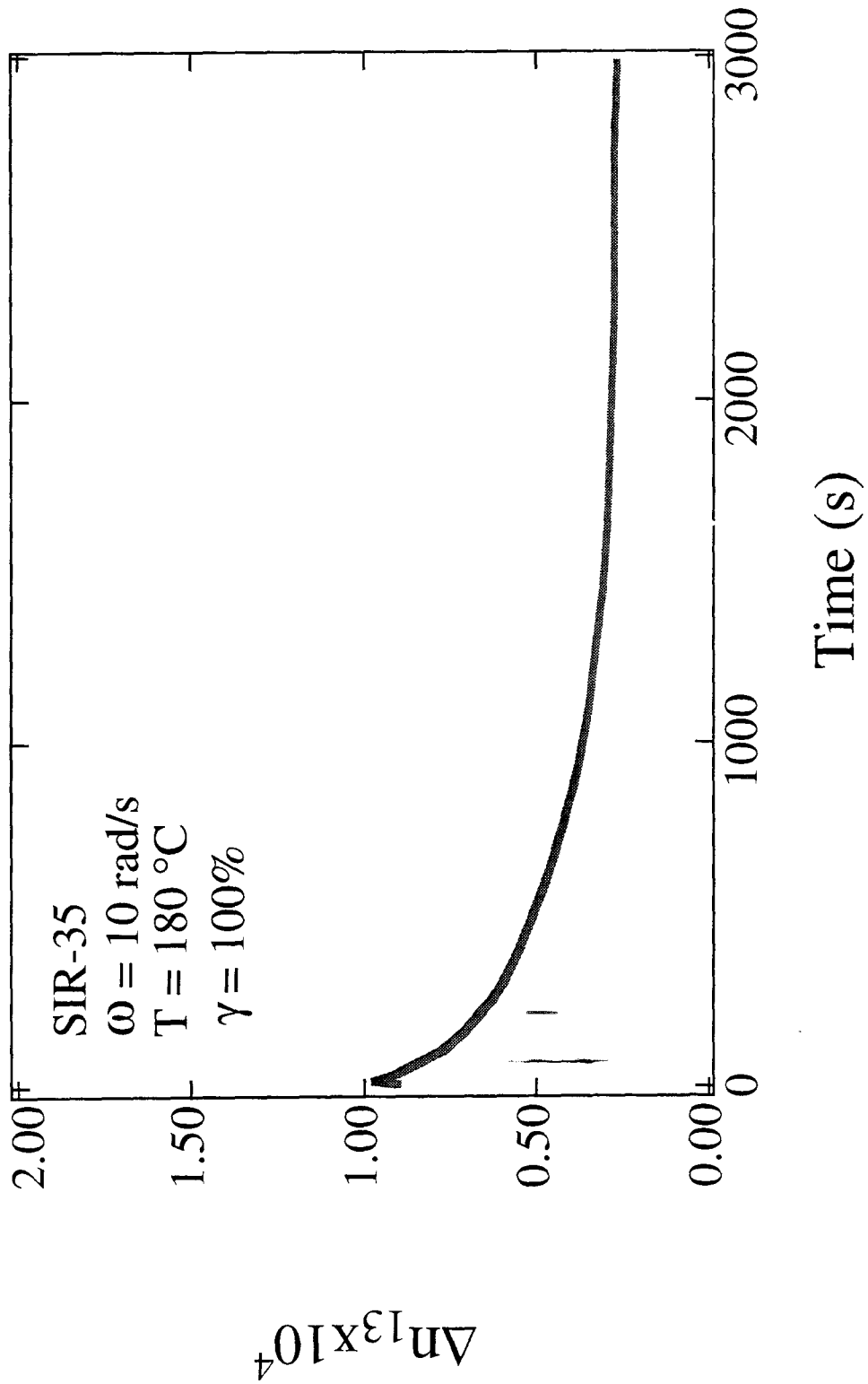


Fig. 22b

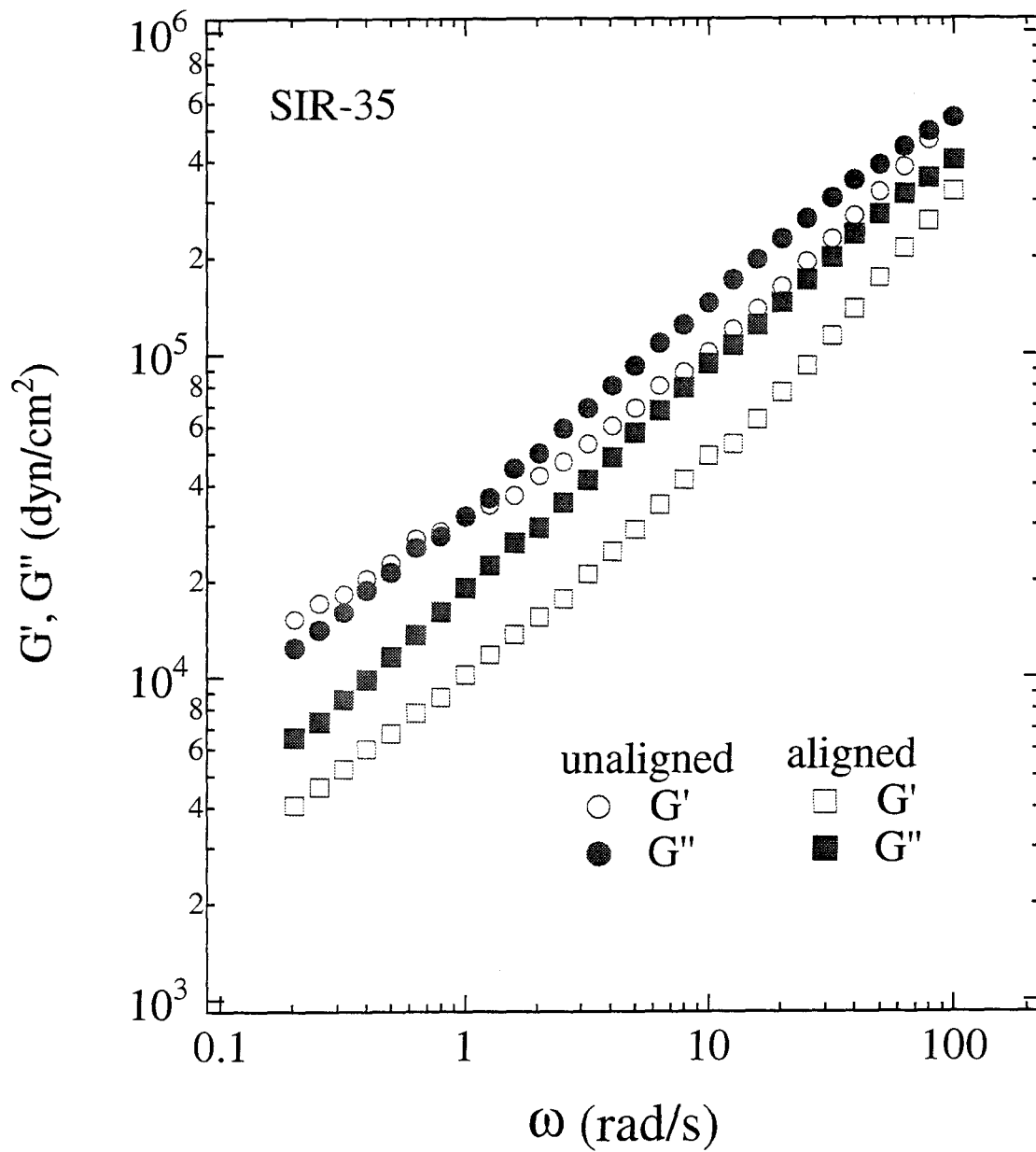
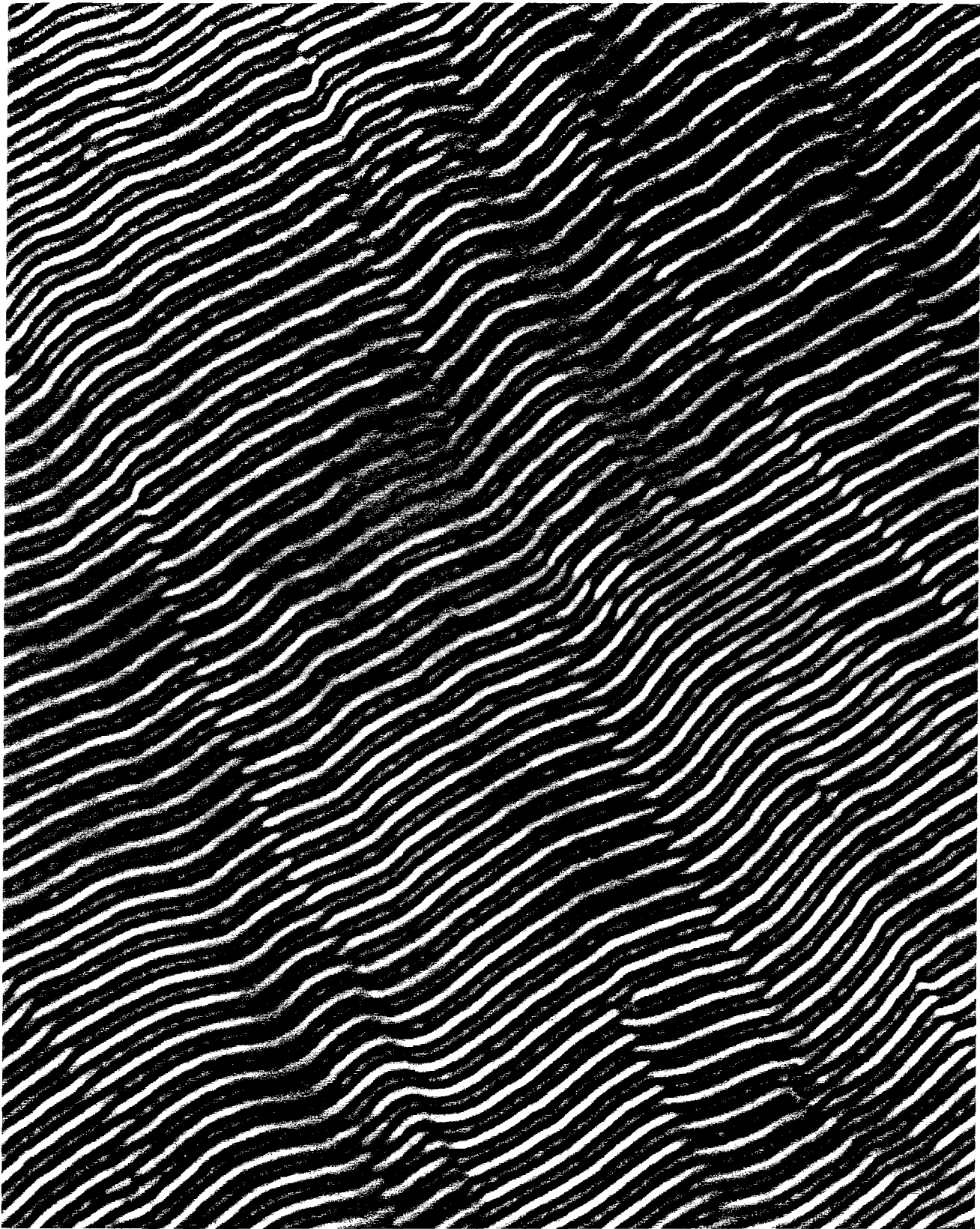


Fig. 23



200nm
|-----|

Fig.24

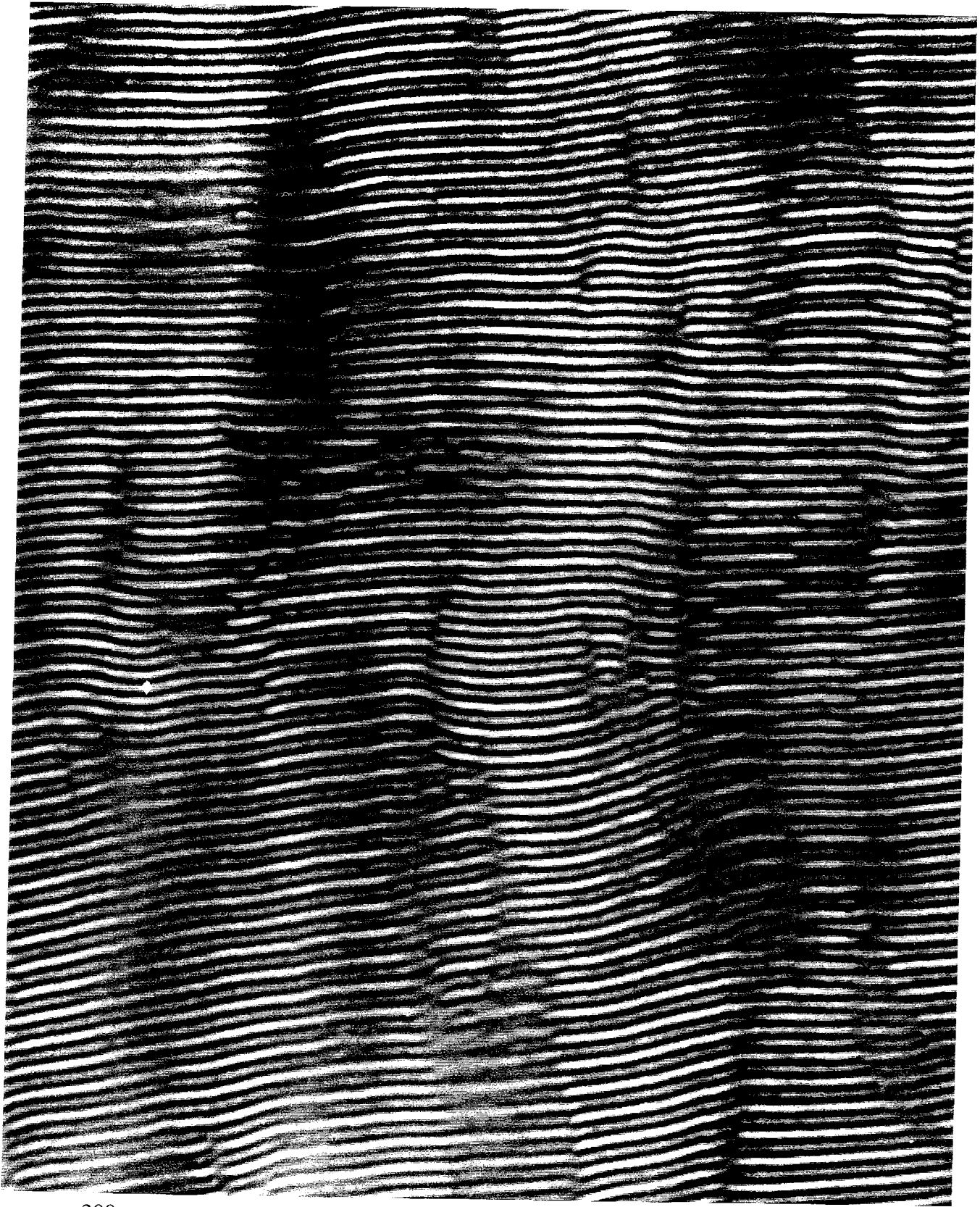
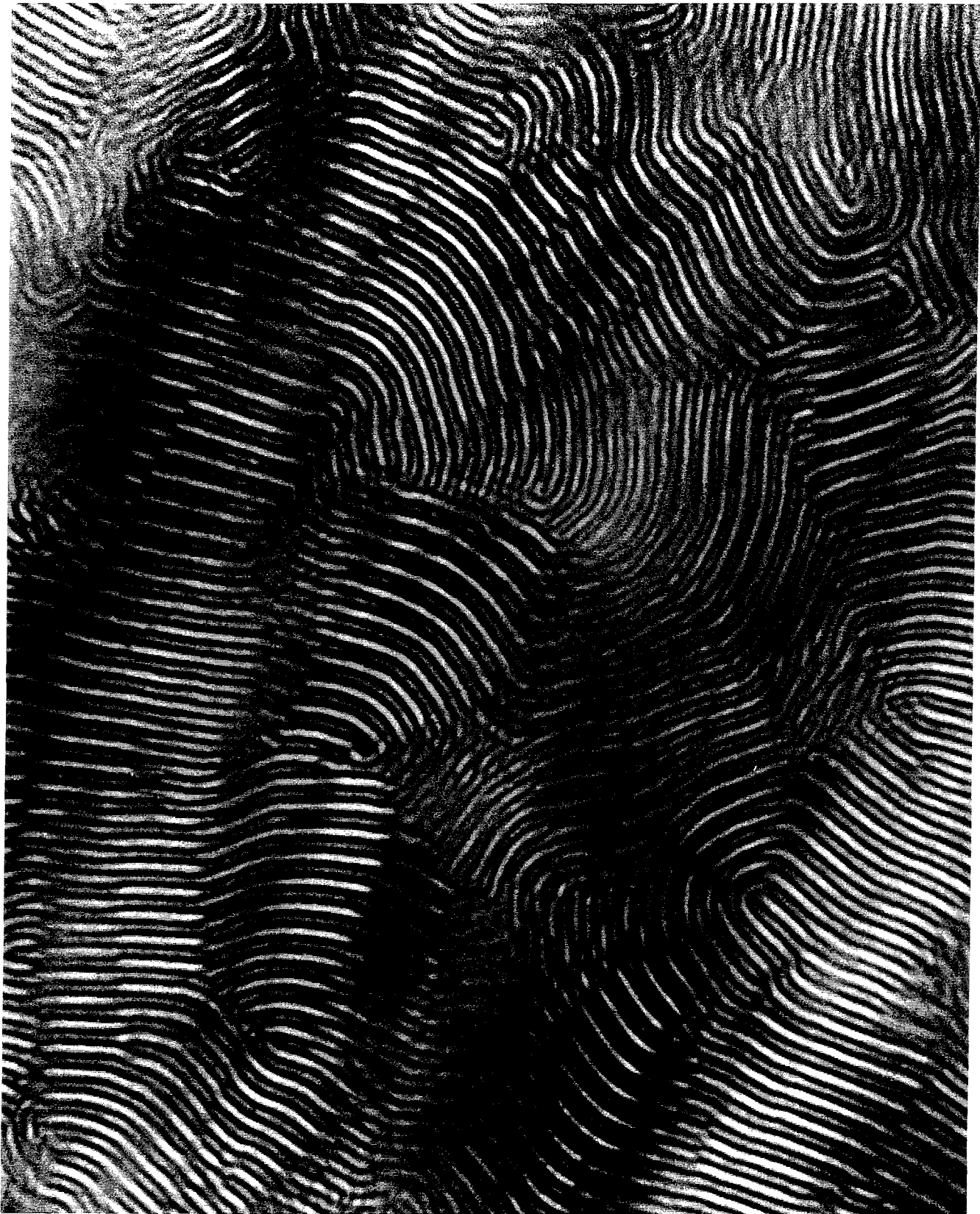
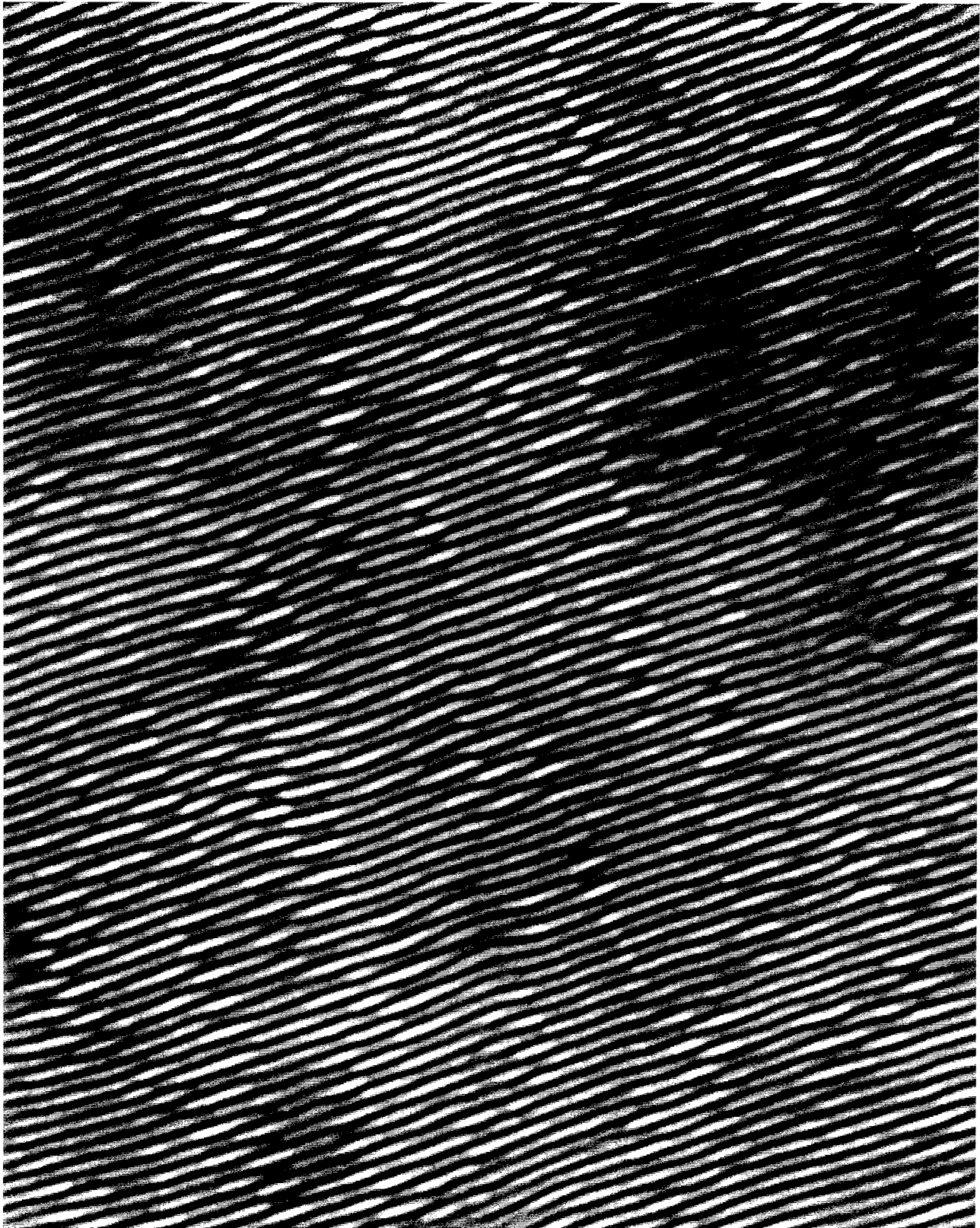


Fig.25a



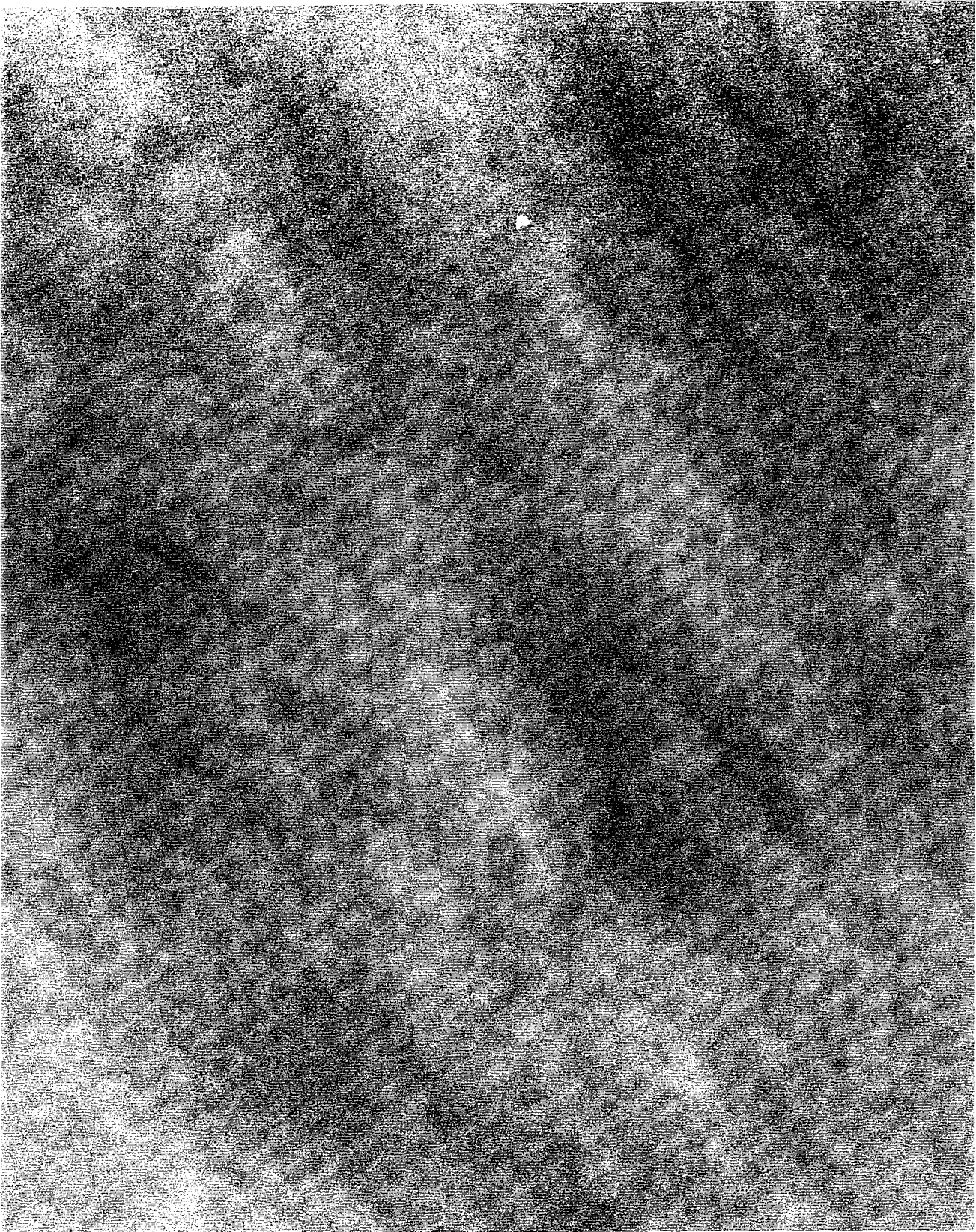
200nm
|-----|

Fig.25b



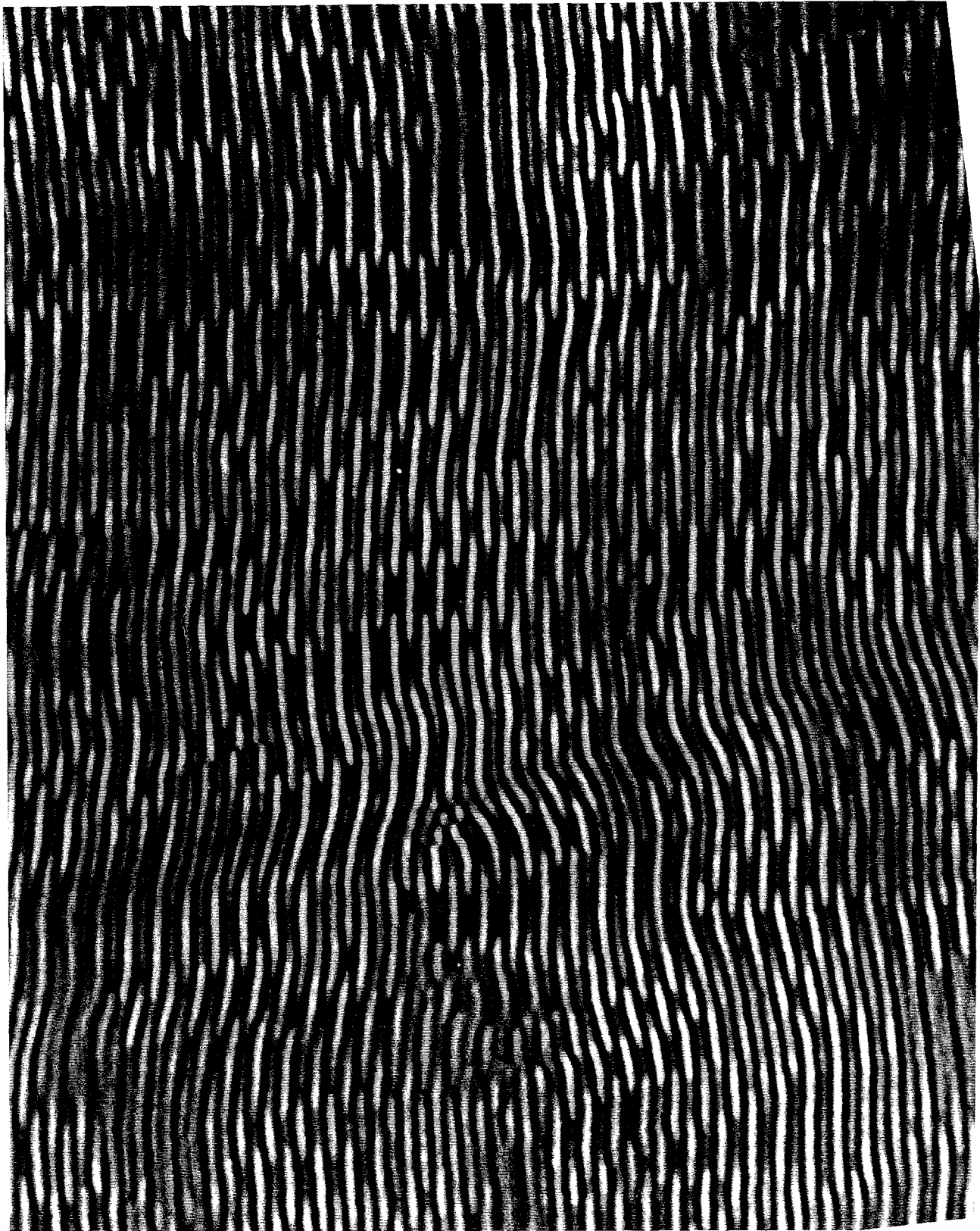
200nm
|-----|

Fig.26a



200nm

Fig.26b



200nm

Fig.27

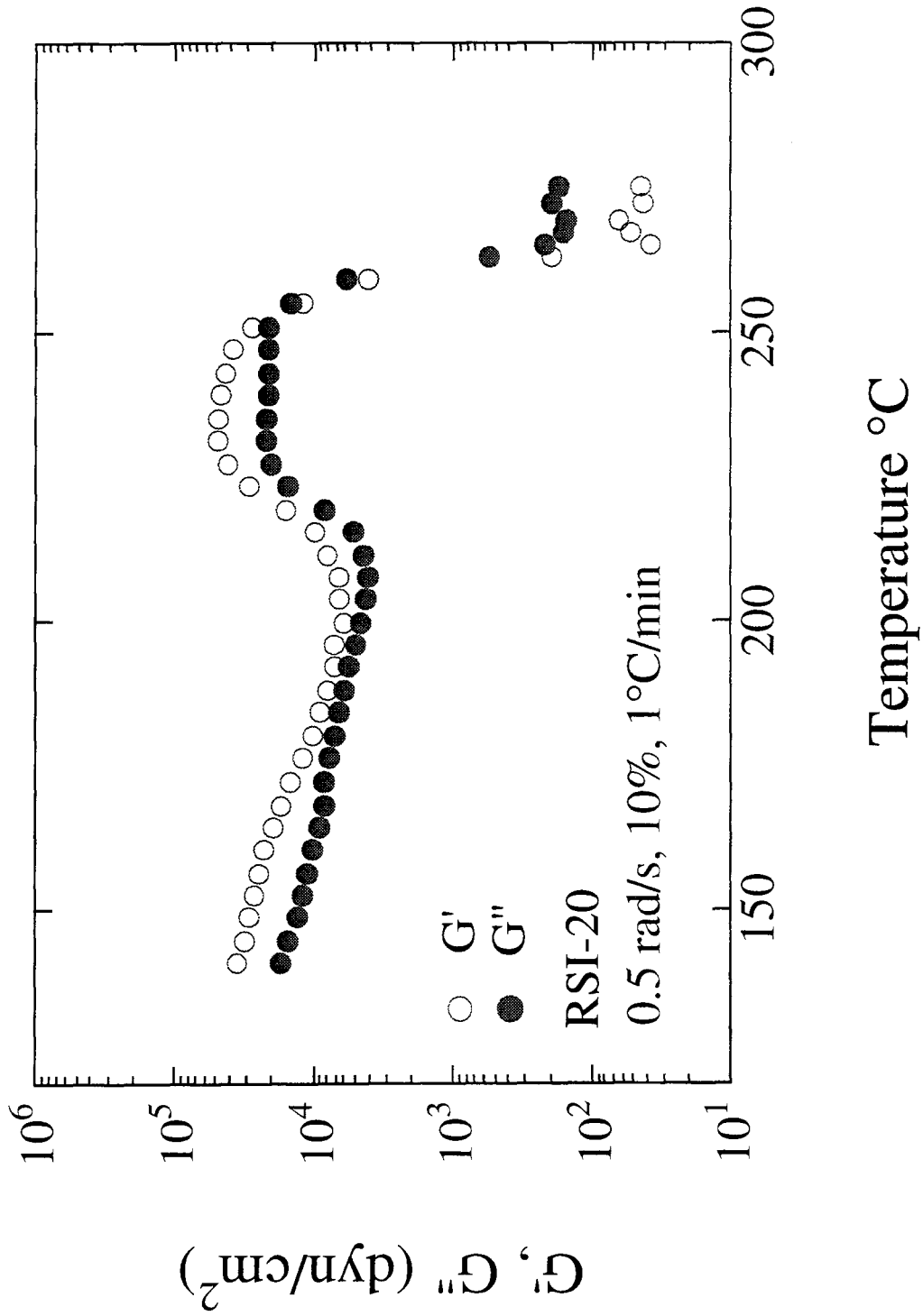


Fig.28a

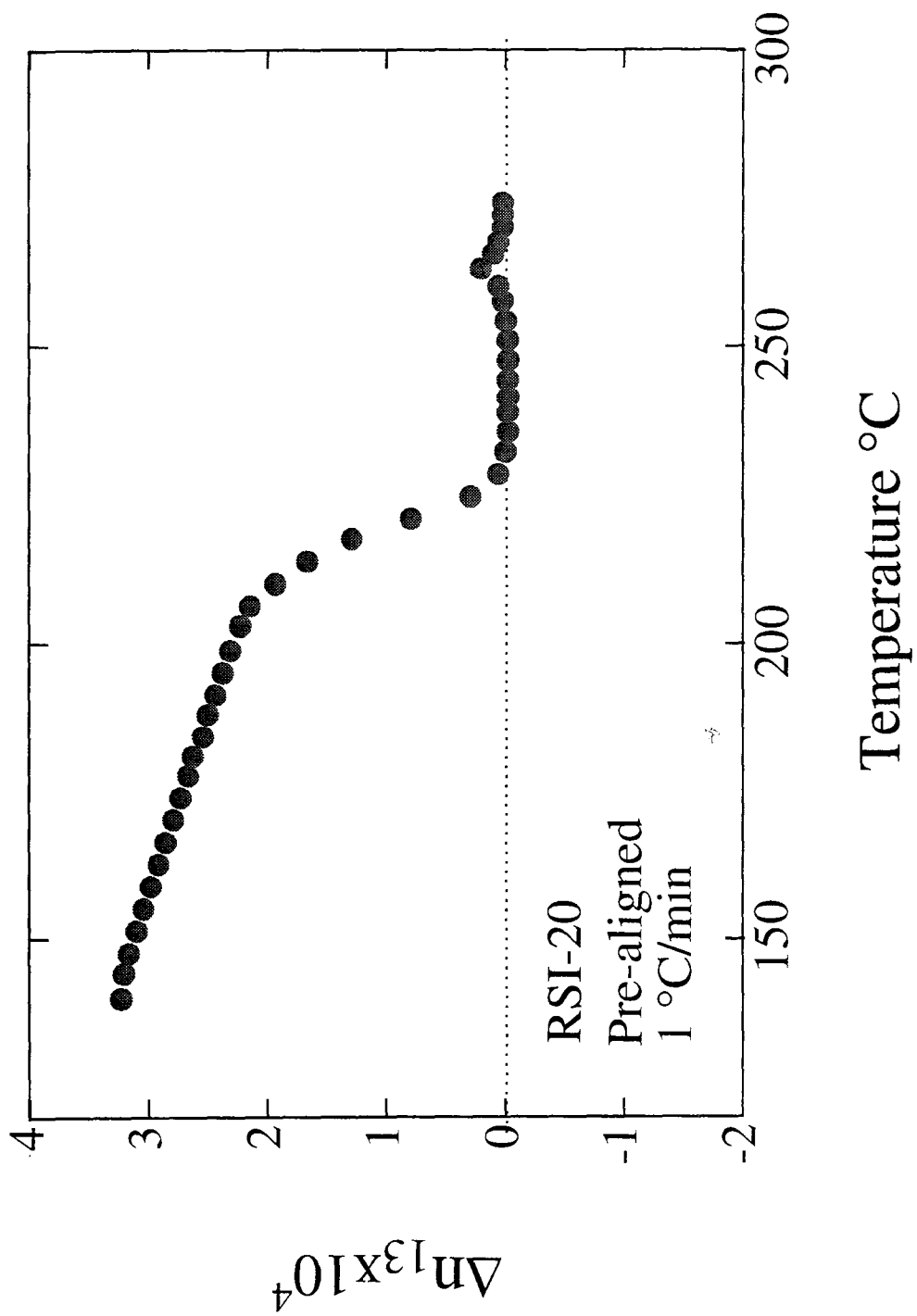


Fig.28b

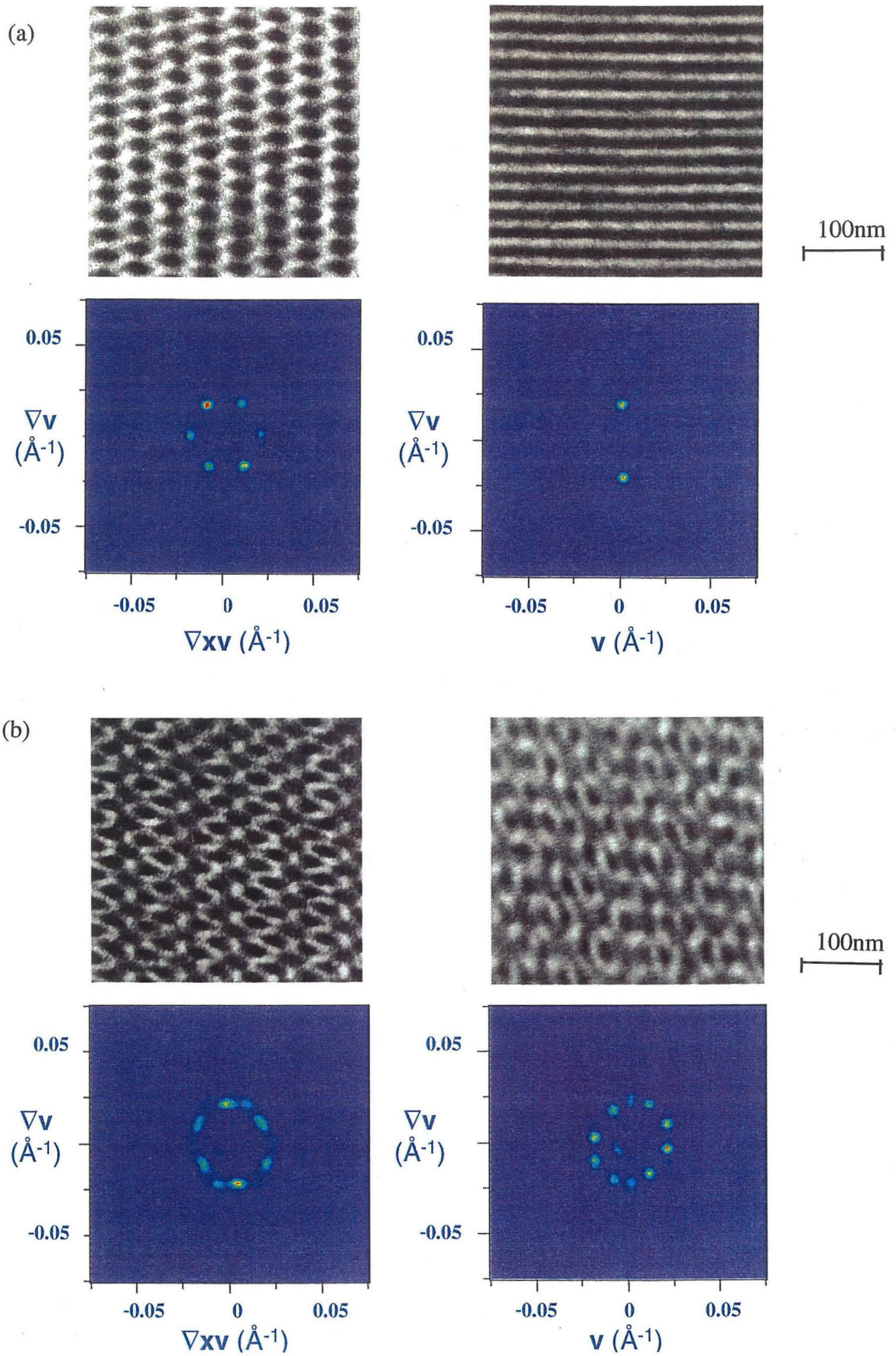
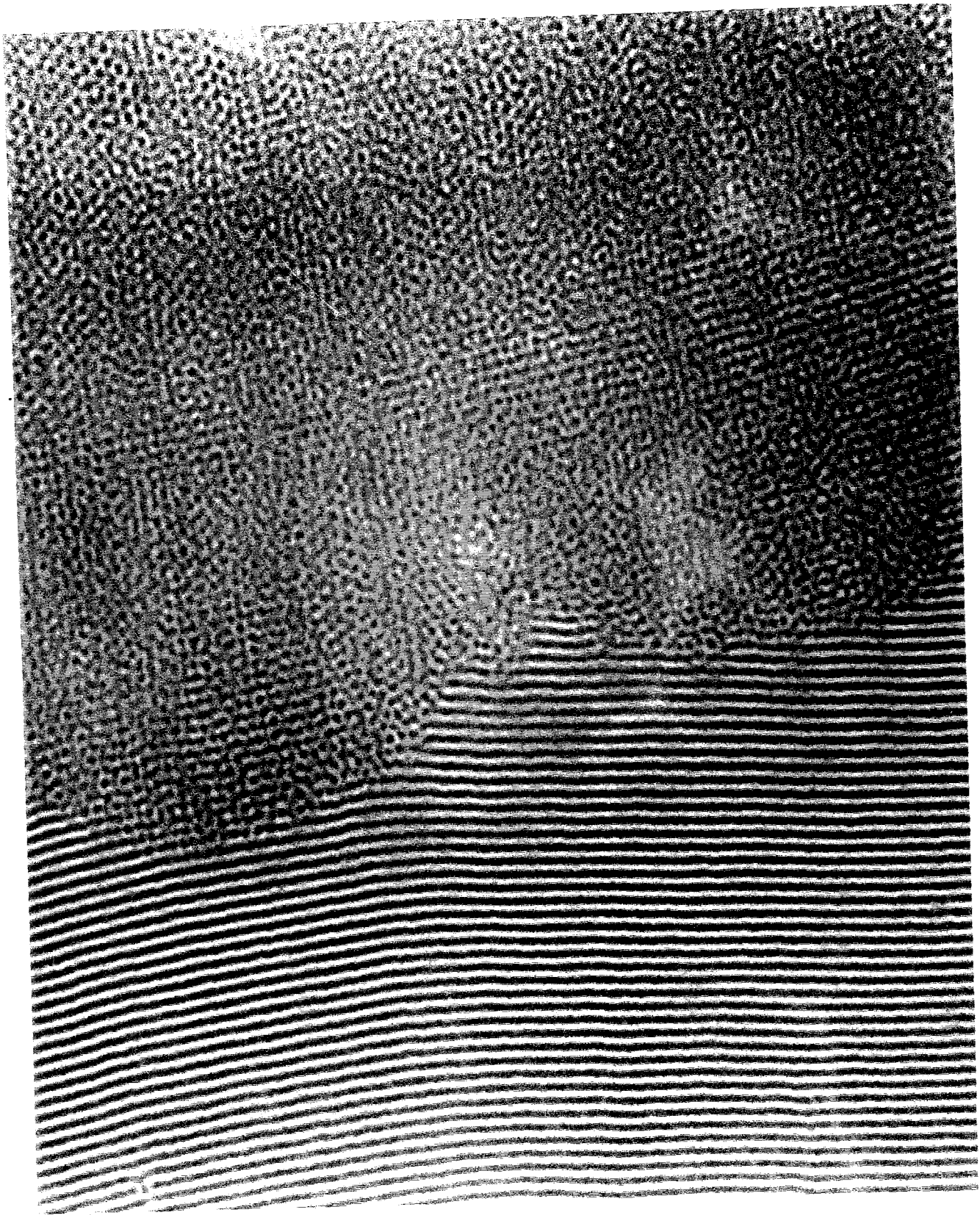


Fig.29



200nm
|-----|

Fig.30

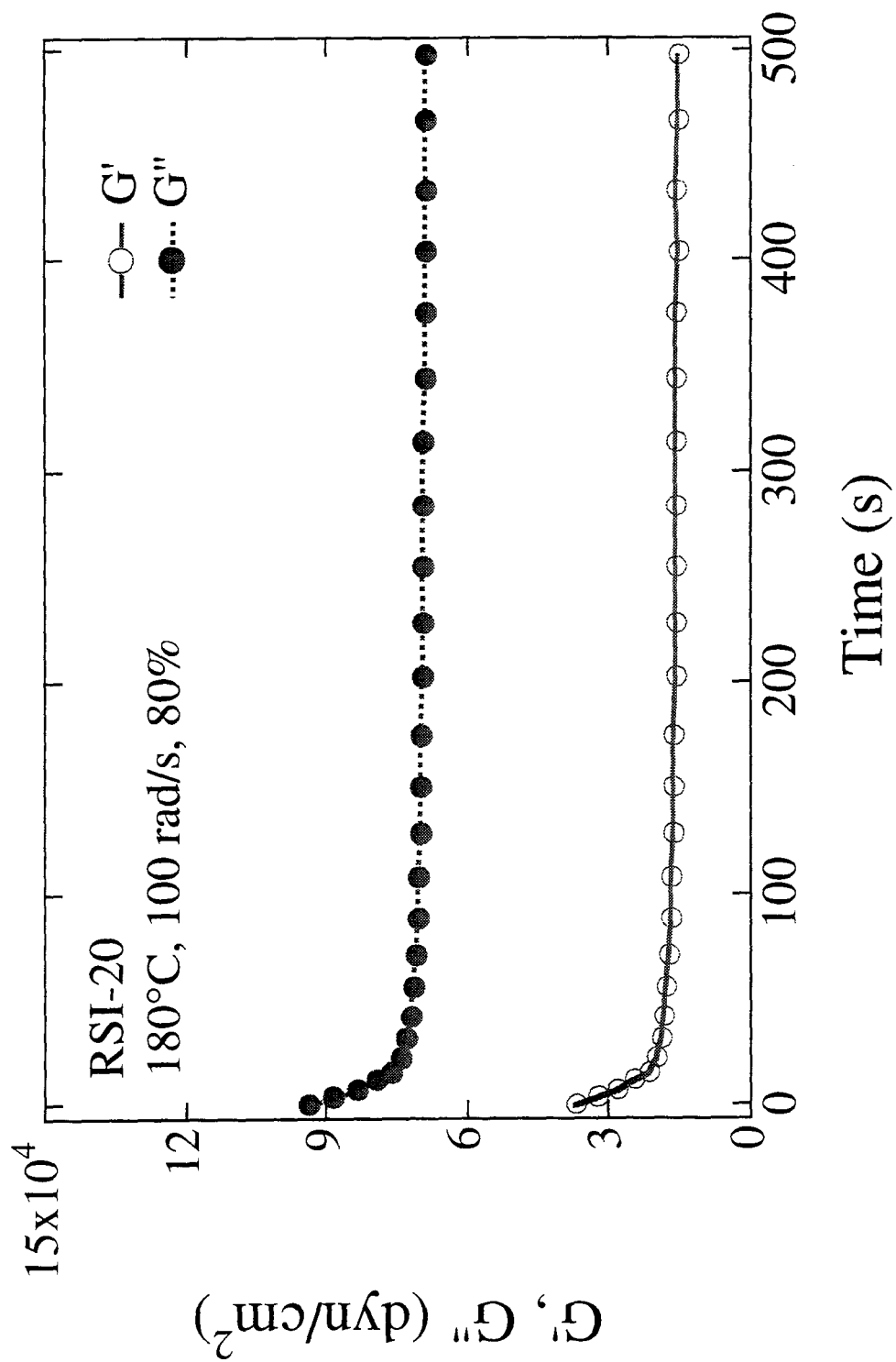


Fig. 31a

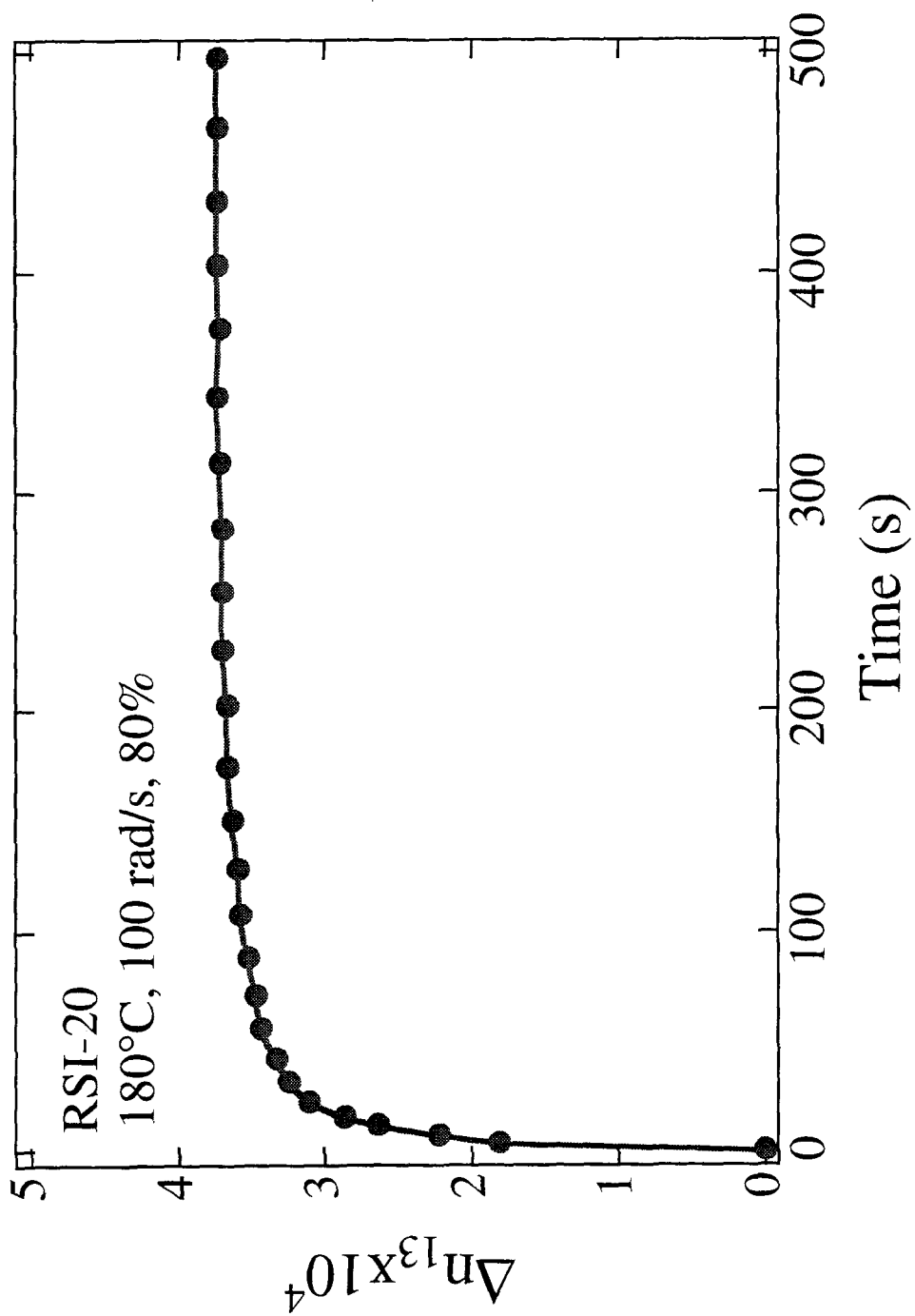


Fig. 31b

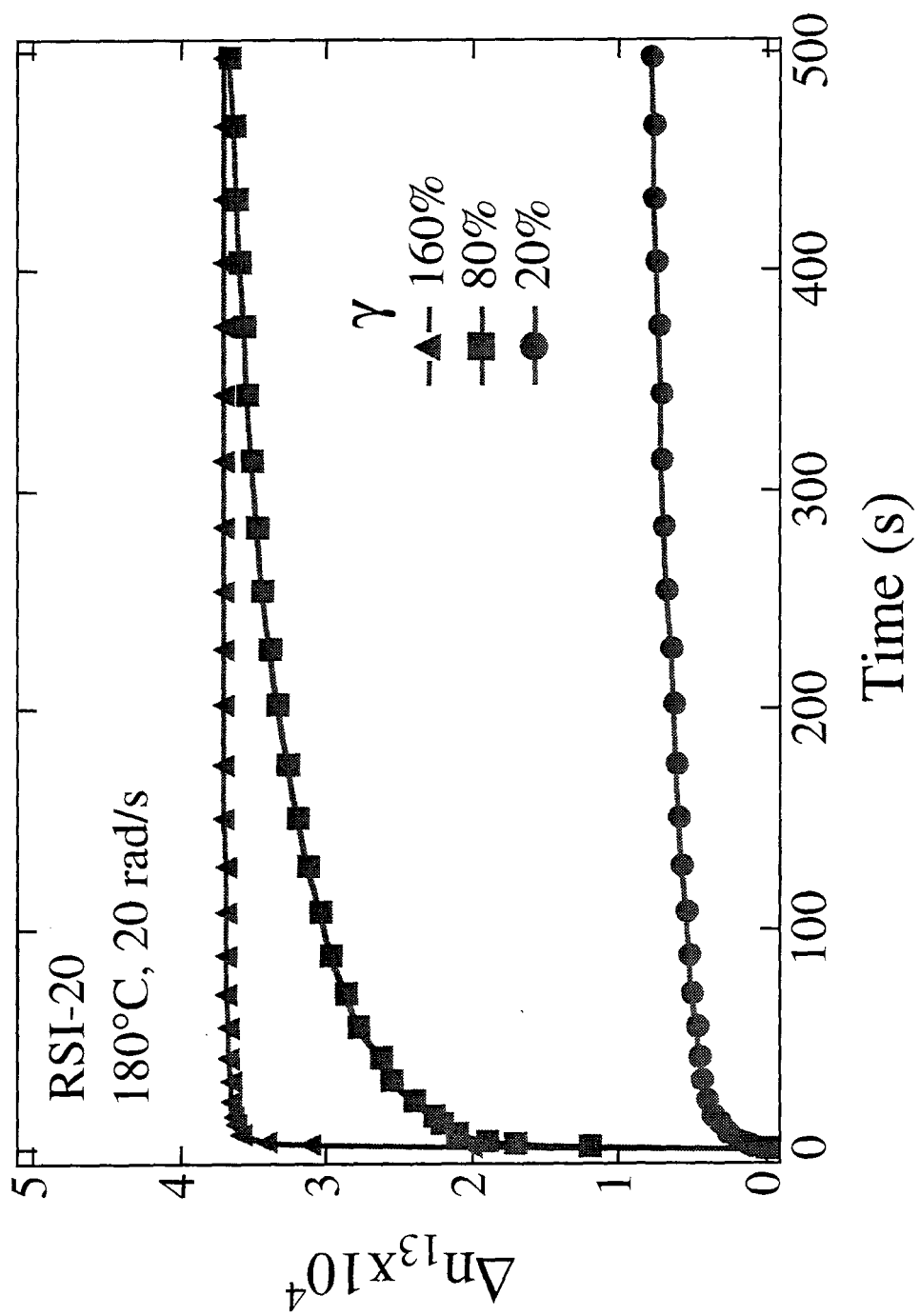


Fig. 32a

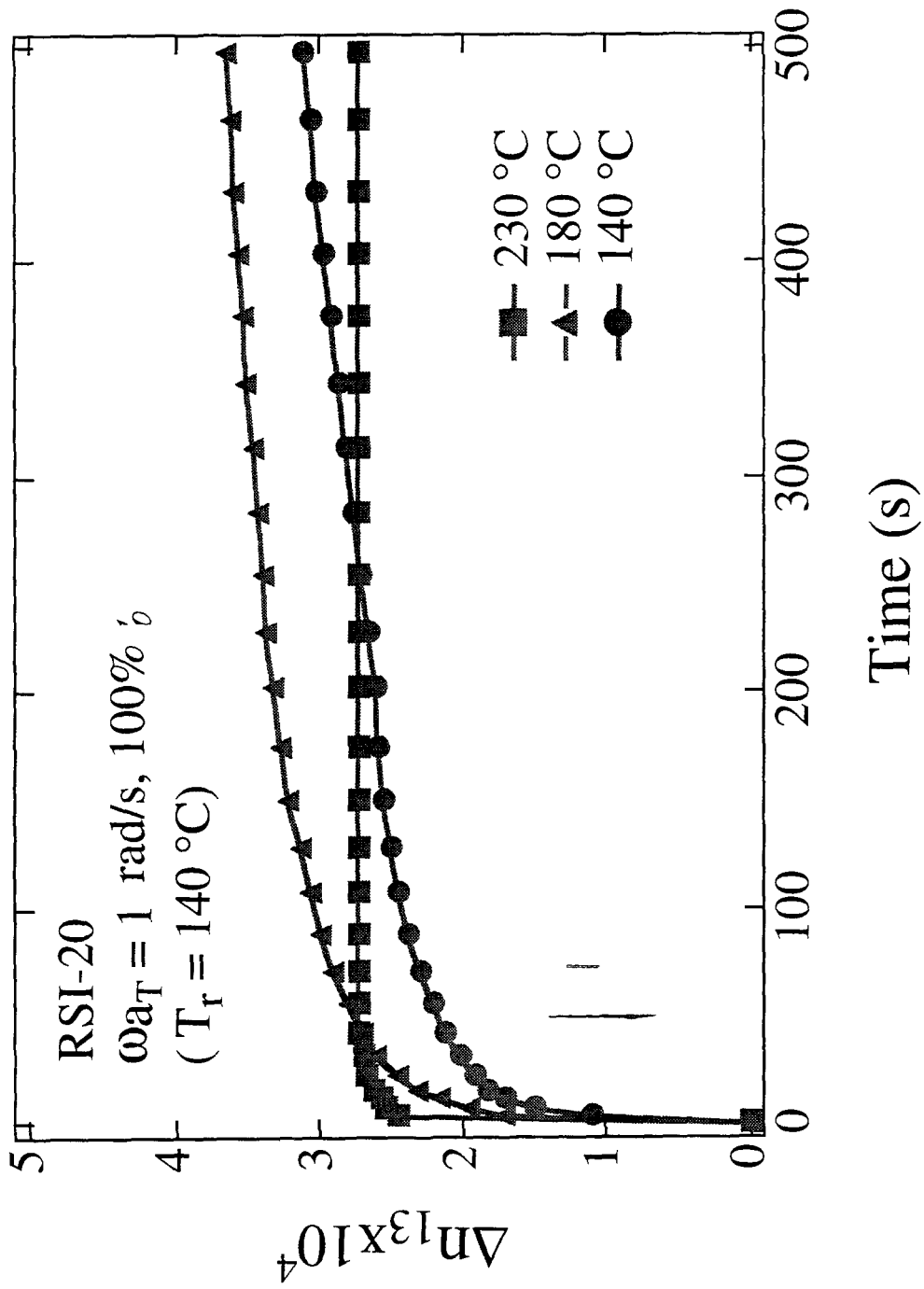


Fig.32b

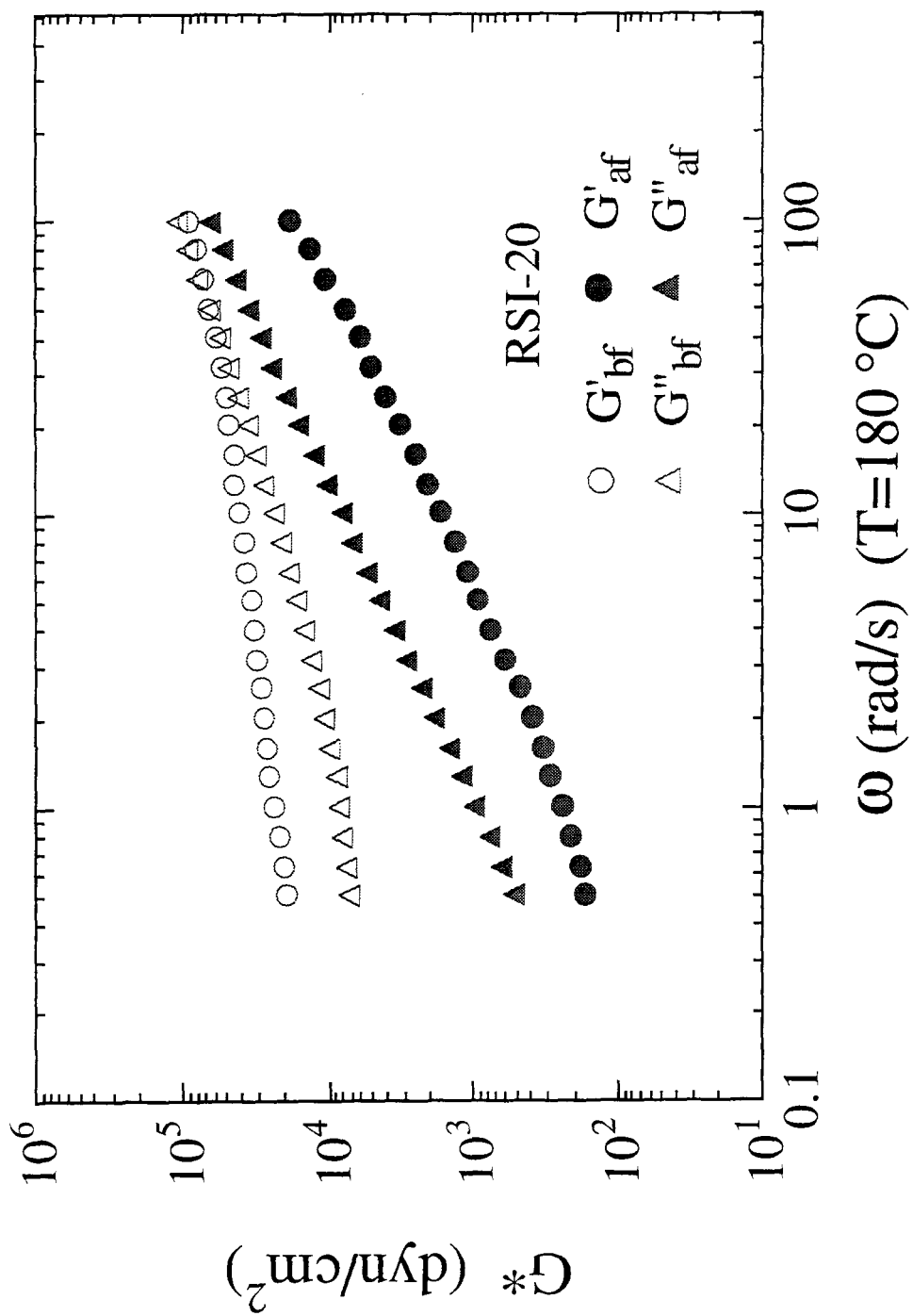


Fig. 33

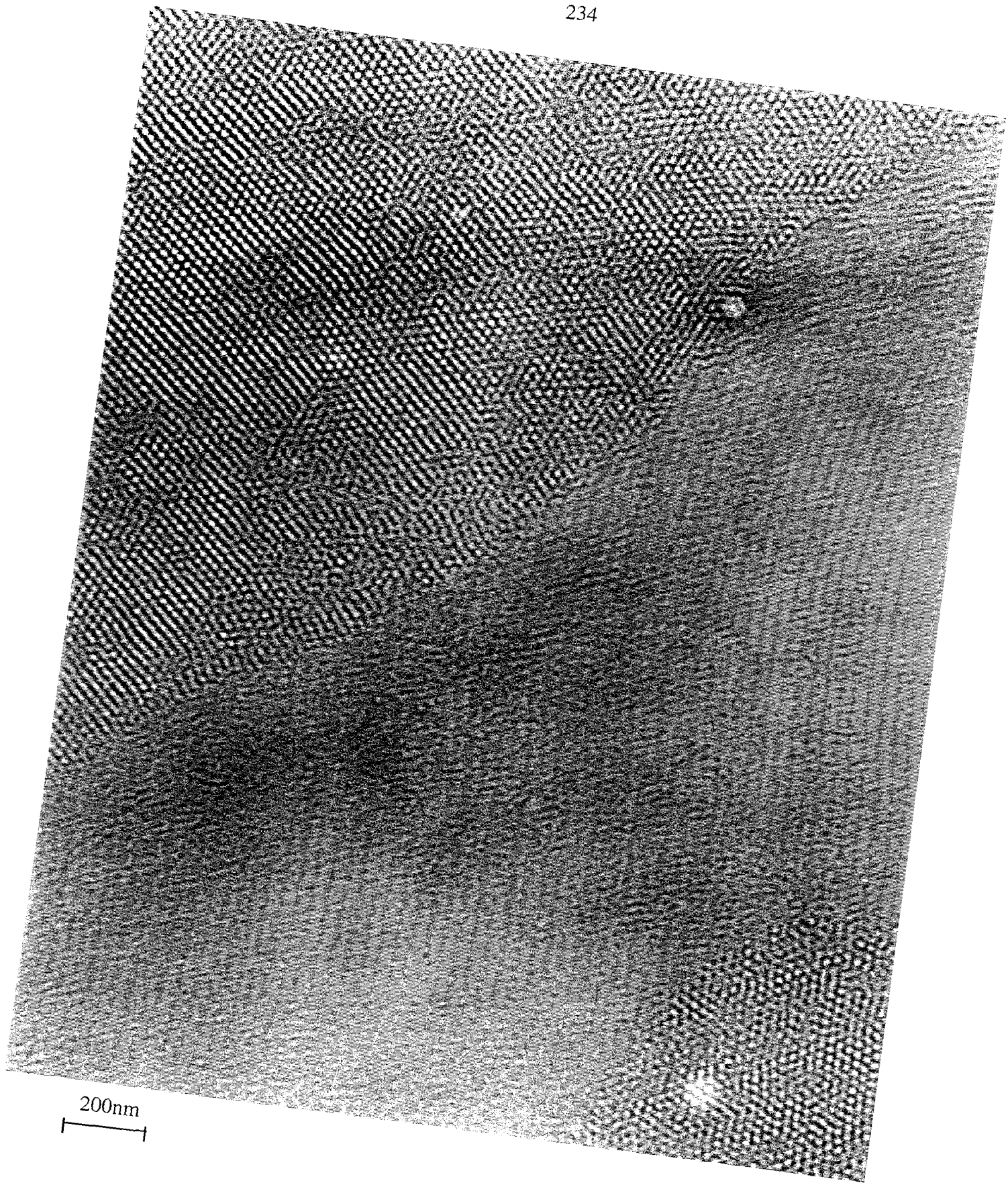


Fig.34



200nm
|-----|

Fig.35a



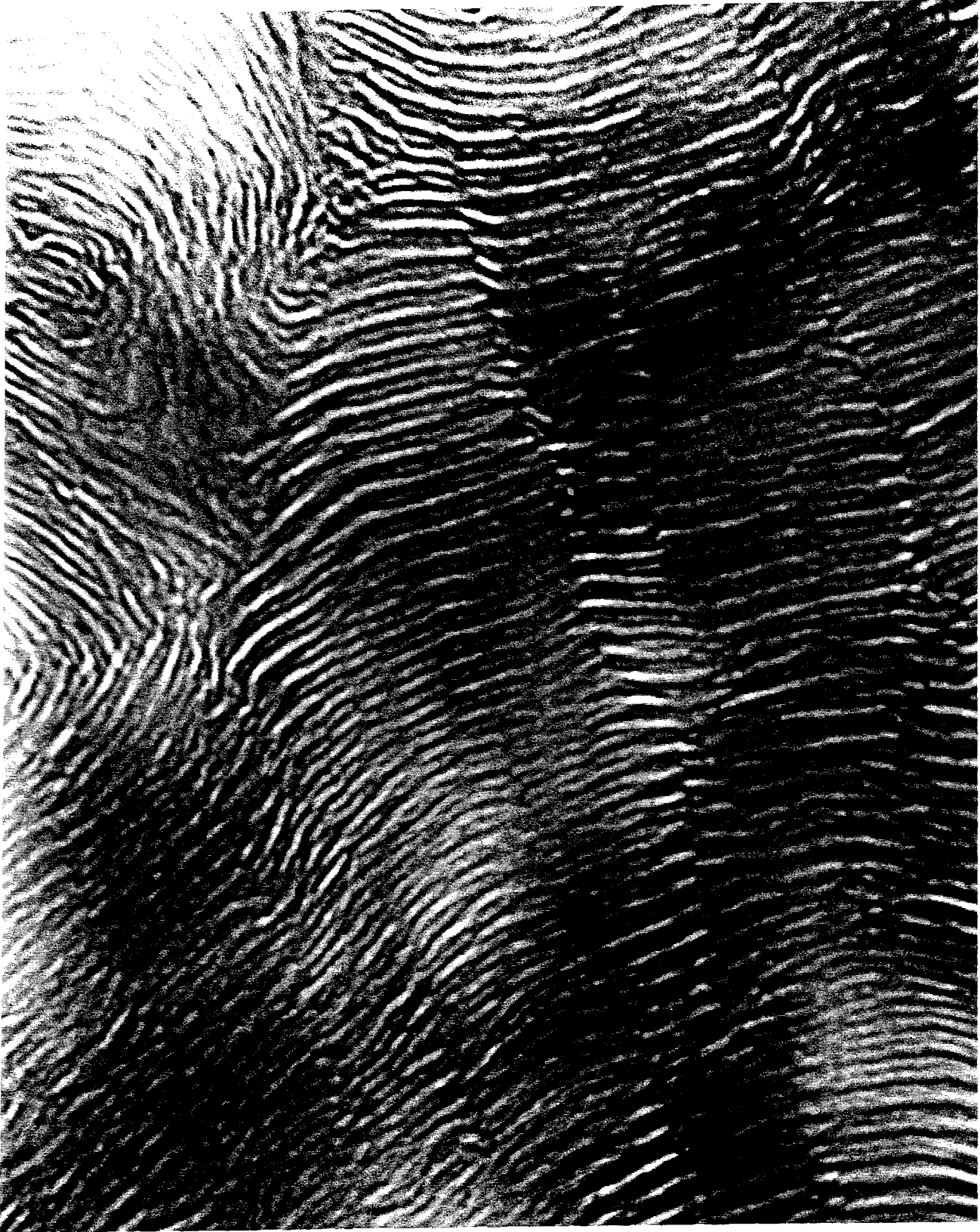
200nm
┌──────────┐

Fig.35b



200nm

Fig.35c



200nm
|-----|

Fig.35d

Chapter 4 Polymerizability of Cyclic Olefins and Ring-Closing Metathesis

Abstract

A combined computational and theoretical method is developed to predict the equilibrium ring-chain distribution of the products of ring-opening metathesis polymerization (ROMP). In ring-chain equilibria, the free energy change of reaction includes an entropic cost associated with forming cyclic rather than linear products, and an enthalpic cost if ring strain is significant (i.e. for small rings). The entropy change is determined using statistical mechanics (based on the Jacobson-Stockmayer theory). The enthalpy change is computed with a Monte Carlo configurational search using molecular mechanics (MM3). Using the resulting equilibrium constants, the calculated distribution of cyclic and linear products is in good agreement with experiment. To characterize the polymerizability of cycloolefins, we compute the critical concentration, defined as the total monomer lost to cyclic products. We also applied this method in ring-closing metathesis of eight-membered rings, which can be useful starting materials for drug synthesis.

1 INTRODUCTION

In the ring-opening metathesis polymerization (ROMP) of cycloolefins, the products generally consist of cyclic oligomers and linear polymers, since the catalyst is active enough to produce “back-biting” reactions [1, 2, 3, 4, 5, 6]. In the ROMP of cyclooctene, Höcker *et al.* [6] showed that there are no polymers formed until the monomer concentration exceeds 0.21 mol/l, which is much higher than the equilibrium monomer concentration $[M]_e$ of 0.002 mol/l [7]. Since $[M]_e$ provided such a poor indicator of polymerizability in this case, he proposed the concept of a critical concentration $[M]_c$, defined as the total amount of monomer per unit volume that forms cyclic products at ring-chain equilibrium. If the initial monomer concentration is less than $[M]_c$, only cyclics and linear oligomers are formed. After exceeding $[M]_c$, the equilibrium cyclics concentration is almost constant, and linear polymers begin to appear. Thus, $[M]_c$ characterizes the polymerizability of a given monomer. The critical concentrations of some cycloolefins have been determined experimentally [6, 7, 8, 9, 10, 11], but theoretical predictions of $[M]_c$ are lacking.

Jacobson and Stockmayer [12] developed a theory of ring-chain equilibria in 1950, based on consideration of the set of reaction equilibria:



where P_j and P_{i+j} are linear polymer chains of degree of polymerization j and $i+j$, respectively, and C_i is a cyclic oligomer of degree of polymerization i . The “J-S theory” includes four assumptions: (1) all rings are strainless and there is no heat of cyclization, (2) the end-to-end distances of linear chains obey Gaussian statistics, (3) the probability of ring formation is governed

by the fraction of all configurations for which the ends coincide, and (4) the reactivity of each terminal functional group is independent of chain length. It follows from the first assumption that only the entropic term contributes to the equilibrium constant. There are two contributions to the entropy change: a positive one due to the dissociation of one molecule into two, and a negative one due to the decreased number of configurations on going from a linear chain to a linear and a cyclic product. The reduction in configurational entropy increases with ring size i , but is independent of j . Thus, the equilibrium constant for Reaction (1) depends only on i and is given by

$$K_i = \left(\frac{3}{2\pi \langle r_i^2 \rangle_o} \right)^{\frac{3}{2}} \frac{1}{N_A \sigma_{R_i}} \quad (2)$$

where $\langle r_i^2 \rangle_o$ is the mean-squared end-to-end distance of a random flight chain of i units, N_A is Avogadro's number, and σ_{R_i} is the symmetry number that eliminates overcounting of indistinguishable configurations (for cyclics $\sigma_{R_i} = 2i$) [12]. Since $\langle r_i^2 \rangle_o \propto i$ for a random flight chain, K_i falls off with increasing ring size as $i^{-\frac{5}{2}}$.

While this scaling is in accord with experimental observations, the J-S theory requires an accurate value of $\langle r_i^2 \rangle_o$ in order to predict K_i . This need has been addressed by using the rotational isomeric state model (RIS) to calculate the end-to-end distances of chain molecules [11, 13]. The results of the "JS-RIS model" for K_i agree very well with the experimental data for macrocyclics (more than 30-40 backbone atoms). However, the predicted values of K_i for smaller cyclics are still too high (Fig. 3).

Two approaches have been taken to remedy the failure of the model for small cyclics: (1) avoiding the Gaussian chain approximation [5, 14], and (2) accounting for geometrical constraints imposed by the bond angle at the joining atom (FSM model) [14]. In relation to the impact of the Gaussian

chain approximation, Suter *et al.* found that a more detailed accounting of the distribution of end-to-end distances provides little improvement in predicting K_i even for small i [5, 11, 14]. On the other hand, accounting for directional correlation strongly reduces the number of configurations of small cyclics, causing K_i to decrease strongly for small i . While this qualitatively shifts the equilibrium away from small rings, as observed in experiment, they reported no results for rings smaller than approximately 25 backbone atoms.

Both of these approaches attempt to better describe mainly the entropic cost of forming small rings. In the context of the JS-RIS model, enthalpic effects enter only through the relative energy levels of the conformers in the RIS model. However there are a few facts that suggest that the discrepancy between the JS-RIS model and experiment has a strong enthalpic origin. First, experiments show that $[M]_e$ depends significantly on temperature (e.g. for cyclopentene, it increases 120% from 273 K to 303 K [9], whereas the JS-RIS model would predict an increase of only about 6%).

Secondly, the observed effect of ring size for small rings strongly affects the value of $[M]_e$ for various cyclic monomers. This effect is readily seen by considering the relative magnitudes of the equilibrium constants for reactions involving the monomer $K_1^{(\nu)}$, where ν denotes the number of backbone atoms in the cycloolefin monomer. For cyclobutene, cyclohexene and cyclooctene, experimental results show that $\frac{K_1^{(4)}}{K_1^{(6)}} \approx 0$, and $\frac{K_1^{(6)}}{K_1^{(8)}} \approx 5000$. However, if the basic reasoning of the FSM model is applied to these cases, it leads to $\frac{K_1^{(4)}}{K_1^{(6)}} \approx 4.5$ (much too large) and $\frac{K_1^{(6)}}{K_1^{(8)}} \approx 2.2$ (much too small)[15]. The inability to polymerize cyclohexene is attributed to lack of ring strain; conversely, it is the relatively higher ring strain in the four and eight member rings that drives the equilibria away from these small cyclics—an enthalpic effect.

Thus, we believe that the reason previous researchers fell short in predicting K_i for small rings is that they neglected ring strain. In fact, if a ring has less than 20 to 30 backbone atoms, there generally exists a strain energy, that can significantly affect ring-chain equilibrium constants. Therefore, the entropic contribution to the change in free energy in Reaction (1) must be augmented by determining the enthalpic contribution. Molecular mechanics, although empirical, provides a computational tool to determine the enthalpic contribution [16, 17]. Since molecular mechanics with the MM3 force field has been shown to accurately compute heats of formation for hydrocarbons [17, 18, 19], we employ this method to calculate the ring strain for small cyclic olefins. Then we calculate equilibrium constants of each ring-chain equilibrium reaction. Together with the knowledge of the molecular weight distribution of the linear chains, we are able to calculate the distribution of all species (cyclic and linear), from which we evaluate $[M]_c$.

2 THEORY AND METHODS

In order to analyze the contributions to the changes of enthalpy and entropy during these reactions, Reaction (1) can be viewed as two hypothetical reactions



There is no change in bond energy during Reaction (1), i.e. the same number of bonds are formed in Reaction (4) as are destroyed in Reaction (3). Therefore, the enthalpy change for Reaction (3) is recovered in Reaction (4) except for the strain energy of the cyclic product, which depends only on its

size, i . The entropy term, however, has contributions from both Reactions (3) and (4).

2.1 Calculation of the Entropic Term

Following the Jacobson-Stockmayer theory, we evaluate the entropy change of Reaction (1), considered as the hypothetical Reactions (3) and (4). The entropy change in Reaction (3) is positive due to the increase in center of mass freedom. It is evaluated by considering the chain units on each side of the bond to be broken: before the bond breaks, these segments are restricted to lie within a small distance of each other, but after the bond breaks, they may be at any distance from one another, limited only by the sample volume. The entropy change of Reaction (4) is negative, since the number of configurations available to the cyclic C_i is a small subset of those available to the linear chain P_i . The ratio of the number of configurations for C_i relative to P_i is simply the probability of P_i closing on itself. The net change in entropy per mole associated with Reactions (3) and (4) is

$$\Delta S_i = R \ln \left[\frac{1}{2iN_A} \left(\frac{3}{2\pi \langle r_i^2 \rangle} \right)^{\frac{3}{2}} \right], \quad (5)$$

where $\langle r_i^2 \rangle$ can be treated by RIS theory or equivalently by introducing the characteristic ratio of an i -mer, which is defined as $c(i) = \frac{\langle r_i^2 \rangle}{in_o l^2}$, where n_o is the number of bonds in a repeat unit and l is the bond length [13].

2.2 Calculation of the Enthalpic Term

In ring-chain equilibria the enthalpic change is due only to the strain energy, since the bond energy is unchanged in Reaction (1) and intermolecular interactions are barely changed. To evaluate the ring strain, the difference

between the heats of formation of corresponding cyclic and linear chains, there are three possible approaches: *ab initio*, semiempirical, and molecular mechanics calculations. The essence of the present problem is to compute the strain energy of a series of cyclic compounds (monomer, dimer, etc.). Ring strain becomes negligible only for molecules that contain 100 atoms or more. *Ab initio* calculations are prohibitive for such large molecules. Semiempirical approaches are generally better suited to calculate structure rather than accurate energetics of molecules. Molecular mechanics, on the other hand, can provide reasonably accurate differences in heats of formation with computations that can readily be performed on available workstations, even for the large molecules of interest here.

Within the context of molecular mechanics, numerous choices of force fields are available that successfully predict the configurations of molecules (e.g. AMBER, OPLS, MM3). Here, we choose the MM3 force field, since it has been shown to provide accurate heats of formation and ring strain for hydrocarbons [17, 18, 19]. Within molecular mechanics, the heat of formation is calculated as the sum of the energies of the covalent bonds, perturbed by distortion of bond lengths, bond angles and torsional angles about bonds. In the molecular mechanics literature, the first is termed the "bond-energy" (BE), and all of the rest are grouped together and termed "steric energy" (SE), which can be computed from the specific force field. For molecules having many possible configurations, SE is usually evaluated as that of the minimum energy configuration; this can be improved upon by performing a Boltzmann-weighted average over all configurations.

For sufficiently small molecules (fewer than 12 backbone atoms), all of the conformers (local minima) were realized for both linear and cyclic molecules. In these cases we evaluated SE using both a Boltzmann-weighted average

and the minimum energy conformation. In turn, the ring strain ($SE_{C_i} - SE_{P_i}$) was evaluated based on each approach. The two results for the strain energy were found to agree to within 1%. For larger molecules (more than 25 backbone atoms), it was not practical to enumerate all possible conformers of the molecule, and the Boltzmann-weighted average could not be determined. Therefore, for large molecules we adopted the usual practice of using SE determined for the lowest energy conformer found in a Monte Carlo search (greater than 10,000 realizations).

For a given degree of polymerization, linear molecules have many more accessible configurations than cyclics. Thus, the Monte Carlo search rapidly becomes extremely time-consuming with increasing linear chain length. Fortunately, one expects that the incremental energy associated with adding a repeat unit should eventually become a constant. Indeed, we find that SE_{P_i} increases linearly with degree of polymerization over the range of i for which the calculations were feasible, i.e. i up to 8 or 9 for cyclobutene (Fig. 1). The increment in SE_{P_i} per repeat unit is denoted SE_0 ; for example, $SE_0 = 20.3$ kJ/mol for linear chains of cyclobutene (Fig. 1). In calculations of the ring strain, the SE for a linear i -mer is evaluated as $i \cdot SE_0$.

For cyclic molecules that are sufficiently large, we find that the steric energy increases linearly with the degree of polymerization (Fig. 1). This indicates that the rings are large enough to be strain free, since ring strain decreases with ring size. Indeed, in the linear regime, the incremental SE per repeat unit is the same as observed for the linear chains. In contrast, for small rings, the steric energy SE_{C_i} decreases with increasing ring size i . This is attributed to the decrease in ring strain. To compute the ring strain, we first compute the difference between the steric energy of the cyclic i -mer and the linear i -mer. However, it is obvious that this difference becomes

constant for large i (Fig. 1). This offset should not be included in the ring strain. Previous researchers have attributed this offset to the difference in torsional degrees of freedom between cyclic and linear molecules [19]. The value of the offset in energy between SE_{C_i} and $i \cdot SE_0$ for large i (9.4 kJ/mol) is indeed equal to the value of the ΔTOR term proposed by Allinger *et al.* for hydrocarbons [19]. Thus, we calculate the strain energy as

$$\Delta H_i = (SE_{C_i} - i \cdot SE_0) + \Delta TOR \quad (6)$$

where SE_{C_i} is the steric energy of i -meric cyclics and $\Delta TOR = -9.4$ kJ/mol.

2.3 Ring-Chain Equilibrium Calculation

To calculate ring-chain equilibria, we need to know the K_i and the molecular weight distribution for linear chains. The equilibrium constants are calculated from the change in free energy of Reaction (1), with the entropy change given by Eq. (5) and the enthalpy change given by Eq. (6):

$$\ln K_i = -\frac{\Delta H_i}{RT} + \ln \left[\frac{1}{2iN_A} \left(\frac{3}{2\pi \langle r_i^2 \rangle} \right)^{\frac{3}{2}} \right] \quad (7)$$

The molecular weight distribution of the linear chains is the most-probable distribution under the equal reactivity assumption [20]

$$[P_i] = \frac{[I + X]_o}{1 + p} \left(\frac{p}{1 + p} \right)^i, \quad (8)$$

where p is the average degree of polymerization and $[I + X]_o$ is the concentration of initiator and chain transfer agent. For this distribution of linear chains, the equilibrium condition gives the distribution of cyclics:

$$[C_i] = K_i \left(\frac{p}{1 + p} \right)^i \quad (9)$$

The average degree of polymerization of the linear chains is

$$p = \frac{[M]_o - [M]_c}{[I + X]_o} \quad (10)$$

where the critical concentration is the sum of all monomers lost to cyclic products

$$[M]_c = \sum i[C_i] \quad (11)$$

Equations (7-11) completely determine $[P_i]$, $[C_i]$, and $[M]_c$. With this information, we determine the distribution of cyclic and linear products for a given initial monomer concentration $[M]_o$ and concentration of initiator and chain transfer agent $[I + X]_o$ (i.e., number of linear chains).

2.4 Computational Methods

We performed the computations on Silicon Graphics IRIS-4D1-4.0.5 and Sun workstations. The programs applied were *InsightII*, *Discover* and *Polymer* by Biosym Technologies, Inc., and *Macromodel* by Columbia University. Statistical weights of rotational isomers, bond lengths and bond angles for polyethylene and polybutadiene are taken from the literature [13, 21] and are used in calculating the characteristic ratio $c(i)$ for polycycloolefins. The mean-square end-to-end distance and characteristic ratio of chain molecules are determined by a Monte Carlo/RIS calculation. The MM3 force field is used for the Monte Carlo configurational search and steric energy calculations.

3 RESULTS AND DISCUSSION

3.1 Effect of Ring Strain on Equilibrium Constants

To evaluate the equilibrium constants K_i using Eq. (7), we must compute the ring strain ΔH_i using molecular mechanics and the characteristic ratio $c(i)$ using rotational isomeric state theory.

Ring strain energy is significant for small rings of up to about 20 backbone atoms (with the exception of cyclohexene). Based on experimental heats of combustion, there is almost no strain energy for cyclics with more than 30-40 backbone atoms [22]. Indeed, we find that as the number of backbone atoms exceeds 20 ($i=5$ for cyclobutene), the slope of SE versus i for both cyclics and linear chains are almost the same (dashed curves, Fig. 1). The ring strain ΔH_i , Eq. (6), decreases with increasing ring size; e.g., for cyclobutene, ΔH_i is nearly zero for $i \approx 6$, i.e. 24 back-bond atoms (solid curve, Fig. 1).

The characteristic ratio $c(i)$ of the linear molecules increases with the degree of polymerization, and reaches a constant c_∞ (Fig. 2). For the homologous series of cyclobutene, cyclohexene, cyclooctene, cyclodecene, and cyclododecene, the c_∞ values at 300 K are 5.8, 6.5, 7.0, 7.2, and 7.3, respectively, for the all-*trans* polymers. With decreasing unsaturation, c_∞ tends toward the value for polyethylene, which extrapolates to 7.8 at 300 K. For polyolefins the characteristic ratio for the *trans* conformation is larger than *cis*. For example, all-*cis* cyclobutene has $c_\infty = 4.9$ at 300 K, approximately 20% lower than the value for all-*trans* polycyclobutene. The values of c_∞ computed for all-*trans* and all-*cis* polycyclobutene are in good agreement with the literature values [21]. As temperature increases, $c(i)$ decreases (Fig. 2), since the difference in energy between *trans* and *gauche* conformers becomes less important.

Using the computation results for ΔH_i and $c(i)$, we evaluate K_i . The resulting values of K_i agree well with experimental data for cyclobutene, even for small i (Fig. 3). This success is in contrast to the J-S theory, which captures the scaling behavior of K_i for large i , or the JS-RIS model, which captures the values of K_i only for large i (Fig. 3). In the J-S theory, K_i is evaluated using Eq. 2 with $\langle r_i^2 \rangle = in_o l^2$; the JS-RIS model, uses Eq. 2 with $\langle r_i^2 \rangle = c_\infty in_o l^2$; in the present model, K_i is evaluated using Eq. 7 with $\langle r_i^2 \rangle = c(i)in_o l^2$ and ΔH_i evaluated as described in section 2.2.

3.2 Equilibrium Cyclics Distribution for Cycloolefins

We choose cyclobutene, cyclooctene and cyclododecene to test our model for the ring-chain equilibrium of cycloolefins, since experimental results are available for comparison. The total cyclic concentration increases with initial monomer concentration $[M]_o$ and ultimately reaches a constant that is defined as the critical concentration $[M]_c$ (Figs. 4, 5). The importance of correctly predicting ring-chain equilibrium constants of small rings becomes obvious when determining $[M]_c$, because small deviations of K_i (e.g. see JS-RIS model in Fig. 3) cause large errors in $[M]_c$ (Fig. 4). For example, our model leads to $[M]_c = 0.45$ mol/l for cyclobutene in good accord with experimental observations [11], whereas the JS-RIS model gives 1.8 mol/l, the J-S theory gives 13.8 mol/l (Fig. 4). For cyclooctene, we find $[M]_c = 0.21$ mol/l (Figs. 5, 6), in agreement with the experimental value of approximately 0.2 mol/l [11]. For cyclododecene, we obtain $[M]_c = 0.13$ mol/l.

When $[M]_o$ is lower than $[M]_c$, the majority of products are cyclics (Fig. 5), with a small amount of linear oligomers. For example, for cyclooctene with $[M]_o = 0.23$ mol/l and $[I + X]_o = 0.0023$ mol/l, if cyclics were not present, the degree of polymerization would be $p \approx 100$. Instead, the ROMP

products consist of 0.164 mol/l of cyclics (71% wt. of the products) and 0.066 mol/l of linear oligomers with $p \approx 30$. As $[M]_o$ increases, the fraction of cyclic products decreases dramatically (Fig. 5). When $[M]_o$ is large enough, the amount of cyclics remains almost constant at $[M]_c$, and all additional monomers contribute to form linear polymers. The effect of $[M]_o$ on the total cyclics concentration predicted by the present model is in good agreement with experiment (Fig. 6) [6].

Since the JS-RIS model neglects ring strain, it performs very poorly in predicting the concentration of small rings (Fig. 7) and consequently overpredicts $[M]_c$ (Fig. 6). The predictions of macrocyclic concentration by the JS-RIS model are nearly the same as our model for rings with more than 60 backbone atoms (e.g., $i \approx 8$ for cyclooctene). This is because the two models coincide when ring strain vanishes and when $c(i) \rightarrow c_\infty$. For cyclics with 30 to 60 backbone atoms, the error in the JS-RIS model is mild (Fig. 7). For example, in the case of cyclododecene, ring strain is significant only for monomers, and thus the JS-RIS model performs well except for the monomer concentration. Nevertheless, even this small deficiency results in a fairly large error ($> 100\%$) in predicting $[M]_c$.

The cyclics distribution calculated with the present model agrees quite well with experimental data for polymerization of 4, 6, 8, and 12 membered cyclic olefins (Figs. 7-8). Although the entropic cost to form a small ring is less than that to form a larger one [23], the enthalpic cost is usually much higher for smaller cyclics. The enthalpic penalty is so significant that there are almost no monomers left at ring-chain equilibrium for 4, 8, and 12 membered cyclic olefins (Figs. 7-8); for cyclobutene, even dimer is hardly present (Fig. 8a). In contrast, cyclohexene is free of strain, and actually there is a small enthalpic cost for cyclohexene to form linear molecules or larger cyclics.

The equilibrium constant K_1 is so large that $[M]_c$ is estimated as about 7 mol/l, almost the bulk concentration. Since $[M]_c$ is so high, it is not possible to polymerize cyclohexene, and the corresponding polymer spontaneously depolymerizes to monomers and a small amount of cyclic and linear oligomers. If the initial monomer concentration $[M]_o$ is about 7.0 mol/l, only minute amounts of cyclic and linear oligomers form (Fig. 9). This calculated result is in accord with observations that cyclohexene is unpolymerizable. In experiment, only a trace amount of cyclic oligomers were found even in bulk cyclohexene [3].

3.3 Effect of Reaction Conditions on Ring-Chain Equilibria

The effect of monomer concentration, concentrations of initiator and chain transfer agent, solvent quality and temperature on polymerizability and product distributions are of obvious practical interest. For a given monomer, the primary way to control the yield and average molecular weight of linear polymer is by varying the initial monomer concentration $[M]_o$ and the ratio of monomer to catalyst and chain transfer agents $[M]_o/[I + X]_o$. The effect of $[M]_o$ on total cyclics concentration has already been presented above (in section 3.2 and Figs. 4-6). Regarding its effect on the distribution of cyclics and linear chains, increasing $[M]_o$ beyond $[M]_c$, the distribution of cyclics hardly changes (Fig. 10a), while it increases the yield and length of linear polymer (Fig. 10b). Since many applications require polymers with a degree of polymerization larger than 200, synthesis conditions will typically lie in a regime where the cyclics distribution changes very little with $[M]_o$ (Fig. 10a and 11a). In this regime the linear chain distribution varies dramatically with increase in $[M]_o/[I + X]_o$ (Fig. 11b).

Other conditions of practical importance are temperature and solvent quality. For most cycloolefins (except for cyclohexene), K_i increases with temperature, and thus the equilibrium cyclic concentrations and $[M]_c$ increase. The increase in $[M]_c$ arises predominantly from the decreased significance of the enthalpic (ring strain) contribution, and secondarily from the decrease in the end-to-end distances (Eq. 7). Generally, the effect of temperature on the product distribution is quite mild compared to radical polymerization, for example, because ring strain is small compared to bond energy.

When considering the effect of the solvent, there is almost no enthalpic contribution, since differences in solvation energy between cyclics and linear chains are negligible. Solvent quality can have a significant effect on the entropic term if the polymer solution is dilute and the solvent is good, since the chain becomes expanded and the probability of its ends meeting falls dramatically (scaling approximately as i^{-2} for a linear i -mer) [24, 25]. In this case, the equilibrium concentration of cyclics and, consequently, $[M]_c$ decrease; and the slope of the lines in Fig. 3 becomes nearly -3 . This effect has been observed in the polymerization of cyclooctene in heptane and in benzene: fewer cyclics are formed in the better solvent (benzene) [26].

3.4 Definition of Critical Concentration

The value of $[M]_c$ defined so far depends on reaction conditions such as $\frac{[M]_0}{[I+X]_0}$, temperature, and solvent quality. For convenience in comparing different monomers, a number, rather than a function, is preferred to characterize the polymerizability of cycloolefins. Therefore, we define $[M]_{c,\infty}$ as the critical concentration at room temperature, in a θ -solvent or concentrated solution, and at infinite degree of polymerization of linear chains p (i.e. large

$\frac{[M]_o}{[I+X]_o}$). Thus, $[M]_{c,\infty}$ can serve as a characteristic parameter in determining polymerizability. We obtain $[M]_{c,\infty} = 0.23$ mol/l for cyclooctene, which is very close to the $[M]_c(p)$ when p is about 200 ($[M]_c(200) = 0.21$ mol/l). So in practice, if p is greater than 200, we can use $[M]_c \approx [M]_{c,\infty}$.

3.5 General Approach to Predicting Polymerizability

The model developed here is successful in predicting ring-chain equilibria in ring-opening metathesis polymerization of cycloolefins. Historically, there have been two theoretical treatments of polymerization thermodynamics. The traditional thermodynamic analysis of Dainton-Ivin *et al.* [7] is based on the free energy changes during the aggregation processes from monomers to polymers. This theory has been applied very successfully to many types of polymerizations, especially to radical chain polymerization. The concepts of ceiling temperature and equilibrium concentration $[M]_e$ are widely used to describe the polymerizability of monomers. However, Ivin's treatment is not adequate for polymerizations in which cyclic products are formed.

Systems involving both cyclic and linear products have been described separately by the Jacobson-Stockmayer theory and its descendents. These models are not able to predict the polymerizability of cyclic monomers, because 1) the J-S theory only succeeds in predicting the scaling of equilibrium constants for large rings, 2) the JS-RIS model does not describe the equilibria involving small rings, and 3) correcting the model to account for directional correlation did not provide reasonable results for small cyclics [11].

The model developed here, is the first to account for ring strain and succeeds in quantitatively predicting the critical concentration and equilibrium ring-chain distribution. We define $[M]_{c,\infty}$ as the determining parameter for polymerizability, and we find that this model fills the same role in ring-

opening polymerization as Dainton-Ivin's treatment in radical chain polymerization. Furthermore, when the polymerization mechanism prohibits the formation of cyclics, $[M]_{c,\infty}$ has only the first term, i.e., the equilibrium concentration of monomer $[M]_e$. Thus, we can also use this model to deal with polymerization systems where only cyclic monomer and polymers exist.

4 CONCLUSION

To accurately predict the equilibrium constants for both macrocyclics and small cyclics, we introduce the ring strain as an enthalpic term and use molecular mechanics to compute its value. Regarding entropic contributions, we use the JS-RIS model. By combining molecular mechanics and statistical mechanics, we have developed a new method that quantitatively predicts the polymerizability of cycloolefins and the distributions of cyclic and linear chain products. The critical concentration $[M]_{c,\infty}$ is the determining parameter to predict the polymerizability of a given monomer at a specified temperature. If the initial monomer concentration exceeds the critical concentration, almost all of the additional monomer contributes to linear products, increasing the yield and average degree of polymerization. For given polymerization conditions, such as initial monomer concentration, the ratio of monomer to chain transfer agent and catalyst, temperature, and solvent, the complete product distribution can be computed.

Based on the success of this method in the case of ROMP of cycloolefins, we expect it to work for other types of cyclic monomers, such as heterocyclics, and for other kind of polymerizations. In reaction conditions that allow the system to approach equilibrium, the model provides guidance in the development of synthetic strategy. For example, when making cyclic species

is the goal, low monomer concentrations (close to the critical concentration) are desired to achieve the highest yield of cyclic products [27, 28]. In addition, this new model can be applied to analyze polymer degradation by metathesis reactions [29].

References

- [1] Grubbs, R. H.; Tumas, W. *Science* **1989**, 243, 907.
- [2] Novak, B. M.; Risse, W.; Grubbs, R. H. *Adv. Polym. Sci.* **1992**, 102, 47.
- [3] Ivin, K. J. *Olefin Metathesis*; Academic Press: London, **1983**.
- [4] Dragutan, V.; Balaban, A.T.; Dimonie, M. *Olefin Metathesis and Ring-Opening Polymerization of Cyclo-Olefins*; John Wiley & Sons: Chichester, U. K., **1985**.
- [5] Semlyen, J. A. *Cyclic Polymers*; Elsevier Applied Science Ltd: **1986**.
- [6] (a) Reif, L.; Höcker, H. *Macromolecules* **1984**, 17, 952. (b) Höcker, H. *J. Mol. Catal.* **1980**, 8, 202.
- [7] Ivin, K. J. *Die Makromol. Chem. Macromol. Symposia* **1991**, 42/43, 1.
- [8] Scott, K. W. *Adv. Chem. Ser.* **1969**, 91, 399.
- [9] Ofstead, E. A.; Calderon, N. *Die Makromol. Chem.* **1972**, 154, 21.
- [10] Thorn-Csanyi, E.; Hammer, J.; Pflug, K. P.; Zilles, J. U. *Abstracts, MacroAkron'94, 35th IUPAC International Symposium on Macromolecules*; Akron, Ohio, USA. **1994**, 241.
- [11] Suter, U. W.; Höcker, H. *Makromol. Chem.* **1988**, 189, 1603.
- [12] Jacobson, H.; Stockmayer, W. H. *J. Chem. Phys.* **1950**, 18, 12, 1600.
- [13] Flory, P. J. *Statistical Mechanics of Chain Molecules*; Hanser Publishers: **1988**.

[14] Flory, P. J.; Suter, U. W.; Mutter, M. *J. Am. Chem. Soc.* **1976**, *98*, 5733.

[15] Following J-S theory, the entropy change of reaction (1) is the sum of that for reactions (3) and (4):

$$\Delta S_3 = k \ln\left(\frac{V}{2v_s}\right) \quad (12)$$

$$\Delta S_4 = k \ln\left(\frac{\mathcal{P}(i, \nu)}{i}\right) \quad (13)$$

where V is the volume of the system, v_s is the volume swept out by a bond, i is the number of repeat units in the cyclic product, and $\mathcal{P}(i, \nu)$ is the probability that a linear i -mer has a configuration compatible with cyclization: the ratio of the number of configurations of the ring to that of the corresponding linear molecule. Let $K_i^{(\nu)}$ denote the equilibrium constant for the case of ν bonds per repeat unit: $K_i^{(\nu)} = \left(\frac{V}{2v_s}\right)\left(\frac{\mathcal{P}}{i}\right)$. For the equilibria involving cycloolefin monomers ($i=1$) cyclobutene, cyclohexene and cyclooctene ($\nu = 4, 6$ and 8), the relative magnitude of the equilibrium constants are: $\frac{K_1^{(a)}}{K_1^{(b)}} = \frac{\mathcal{P}(1,a)}{\mathcal{P}(1,b)}$, independent of V and v_s . For cyclobutene there is only one conformation of the ring, but 3^3 rotational isomers of the linear analogue, leading to $\mathcal{P}(1, 4) \approx 0.037$. For cyclohexene, there are two conformations of the ring, and 3^5 rotational isomers of the linear analogue: $\mathcal{P}(1, 6) \approx \underline{0.0082}$. For cyclooctene, there are 8 conformations of the ring, and 3^7 rotational isomers of the linear analogue: $\mathcal{P}(1, 8) \approx 0.0037$. Based on these value, $\frac{K_1^{(4)}}{K_1^{(6)}} \approx 4.5$ and $\frac{K_1^{(6)}}{K_1^{(8)}} \approx 2.2$. Thus, accounting for directional correlations, which lead to the very small number of configurations for small rings, cannot explain the experimental results that $K_1^{(6)}$ is vastly higher than $K_1^{(4)}$ and $K_1^{(8)}$.

- [16] (a) Lipkowitz, K. B.; Boyd, D. B. *Reviews in Computational Chemistry vol 5*; VCH: , **1994**. (b) Hirst, D. M. *A Computational Approach to Chemistry*; Blackwell: London, **1990**.
- [17] Burkert, U.; Allinger, N. L. *Molecular Mechanics*; American Chemical Society: Washington D.C., **1982**.
- [18] (a) Allinger, N. L.; Li, F.; Yan, L. *J. Comptl. Chem.* **1990**, 11, 848. (b) Allinger, N. L.; Li, F.; Yan, L. *J. Comptl. Chem.* **1990**, 11, 868.
- [19] (a). Allinger, N. L.; Zhu, Z.; Chen, K. *J. Am. Chem. Soc.* **1992**, 114, 6120. (b). Allinger, N. L.; Yuh, Y. H.; Li, Jenn-Huei *J. Am. Chem. Soc.* **1989**, 111, 8551.
- [20] Flory, P. *Principles of Polymer Chemistry*; Cornell University: **1953**.
- [21] (a) Mark, J. E. *J. Am. Chem. Soc.* **1966**, 88, 4354. (b) Mark, J. E. *J. Am. Chem. Soc.* **1967**, 89, 6829.
- [22] (a) Penczek, S.; Kubisa, P.; Matyjaszewski, K. *Adv. Polym. Sci.* **1985**, 68/69, 16. (b) Cherednichenko, V. M. *Vysokomol. soyed* **1978**, 5, 1086.
- [23] This statement is based on J-S theory with Gaussian chains, although it is unlikely that short chains still obey Gaussian statistics. For a general reference, see Semlyen, J. A. *Cyclic Polymers*; Elsevier Applied Science Ltd: **1986**.
- [24] de Gennes, P-G. *Scaling Concepts in Polymer Physics*; Cornell University: **1971**.
- [25] des Cloizeaux, J. *Physical Review A* **1974**, 10, 1665.

- [26] Höcker, H. *Makromol. Chem.* **1976**, 177, 1707.
- [27] Fu, G. C.; Nguyen, S. T.; Grubbs, R. H. *J. Am. Chem. Soc.* **1993**, 115, 9856.
- [28] Miller, S. J.; Kim, S-H; Chen, Z-R; Grubbs, R. H. *J. Am. Chem. Soc.*
in press
- [29] Hummel, K.; Zekoll, H.; Chemelli, R. *Makromol. Chem.* **1987**, 188, 1075.

Figure Captions

Figure 1: Steric energy of cyclic and linear i -mers and ring strain of cyclic i -mers formed from ROMP of cyclobutene. The precise choice of end groups has no effect on the overall change in free energy of Reaction (1); the results shown here are for a linear i -mer constructed by adding one hydrogen each on the two ends of an opened cyclic monomer, and subsequent linear chains constructed by inserting one repeat unit.

Figure 2: Characteristic ratio $c(i)$ as a function of temperature for linear i -mers of all-*trans* cyclobutene

Figure 3: Ring-chain equilibrium constants K_i for the reactions that form cyclic i -mers of cyclobutene: comparison of three different models at 300 K in a θ solvent.

Figure 4: Effect of initial monomer concentration on total cyclics concentration at equilibrium: comparison of three different models for cyclobutene at 300 K in a θ solvent, with $\frac{[M]_o}{[I+X]_o} = 200$. Total cyclics concentration is in terms of the amount of monomer incorporated in cyclics $\Sigma i[C_i]$.

Figure 5: Fraction of cyclics (dashed curve, right axis) and total cyclics concentration (solid curve, left axis) as a function of initial monomer concentration: calculated by the present model for cyclooctene at 300 K in a θ solvent, with $\frac{[M]_o}{[I+X]_o} = 200$. As $[M]_o$ increases, the amount of monomer that forms cyclics reaches a constant at $[M]_c = 0.21$ mol/l.

Figure 6: Total cyclics concentration as a function of initial monomer concentration: comparison of the JS-RIS model, the present model and experimental results for cyclooctene at 300 K in a θ solvent, with $\frac{[M]_o}{[I+X]_o} = 200$.

Figure 7: Cyclics distribution, i.e. concentration of cyclic i -mer as a function of size: comparison of three models and experimental results for cy-

clooctene at 300 K in a θ solvent with $\frac{[M]_o}{[I+X]_o} = 200$. For the J-S theory, when $i=1, 2, 3$ etc, cyclics concentrations are off scale. Coentration of monomer ($i = 1$), $i[C_i] = 3.1$ mol/l.

Figure 8: Calculated and observed cyclics distribution at 300K in a θ solvent, for (a) cyclobutene and (b) cyclododecene at 300 K in a θ solvent, with $[M]_o = 1.0$ mol/l and $\frac{[M]_o}{[I+X]_o} = 200$.

Figure 9: Ring-chain equilibrium of cyclohexene predicted by the present model at 300 K, $[M]_o = 7.0$ mol/l, with $\frac{[M]_o}{[I+X]_o} = 200$. Over 90% wt. of species persists as monomer (peak in the main graph), with the trace amounts of linear and cyclic products (insert, expanded scale).

Figure 10: Effect of initial monomer concentration on ring-chain equilibrium of cyclooctene calculated by the present model at 300 K in a θ solvent, with $\frac{[M]_o}{[I+X]_o} = 200$: distribution of (a) cyclic and (b) linear products. Notice that the distribution of cyclics becomes independent of $[M]_o$ once it is sufficiently large compared to $[M]_c$.

Figure 11: Effect of the ratio of $\frac{[M]_o}{[I+X]_o}$ on ring-chain equilibrium of cyclooctene calculated by the present model at 300 K in a θ solvent with $[M]_o = 1.0$ mol/l: distribution of (a) cyclic and (b) linear products.

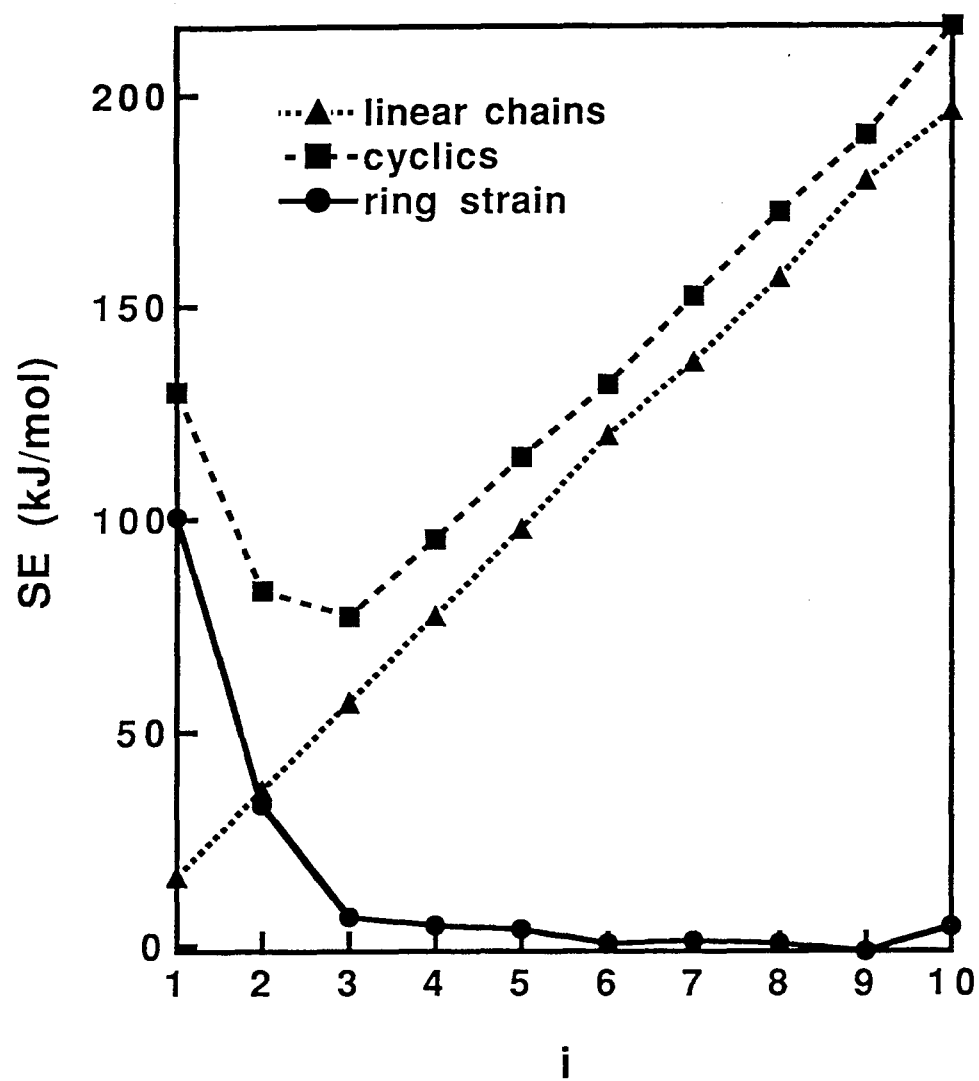


Fig.1

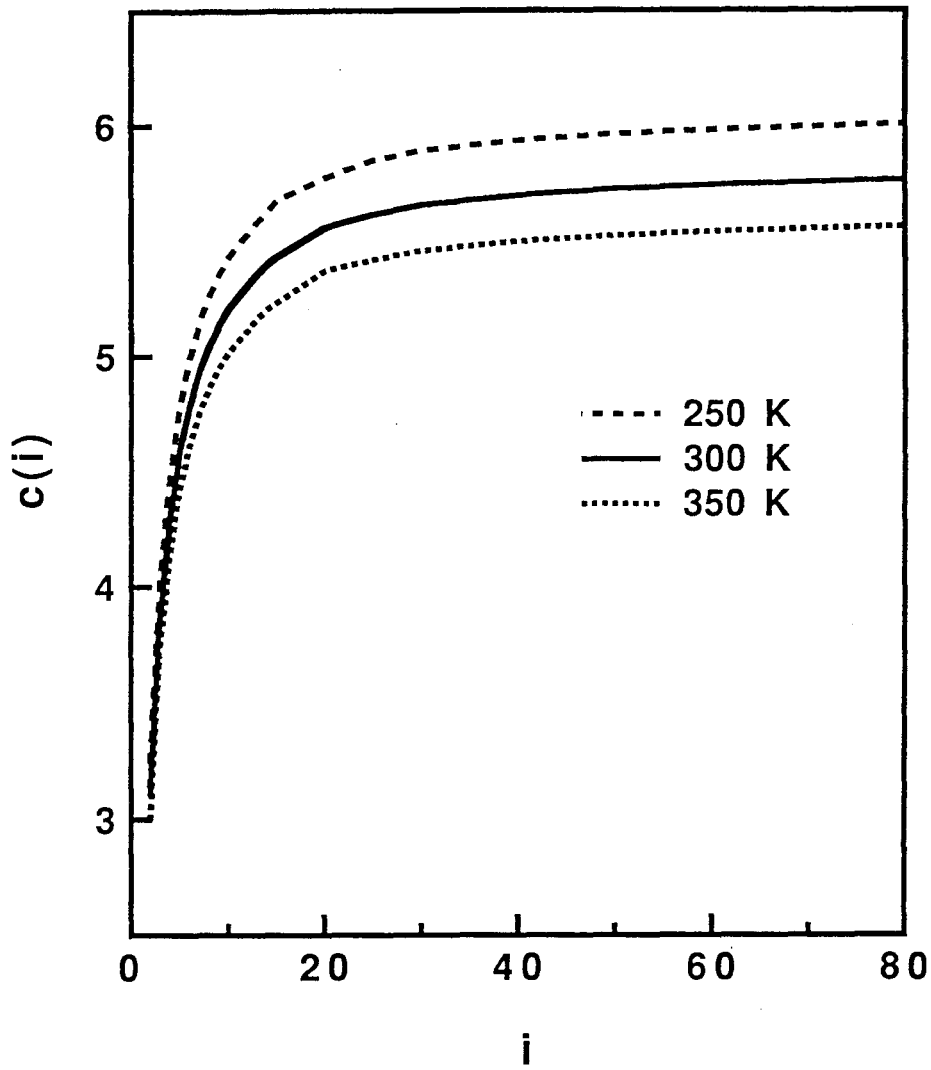


Fig.2

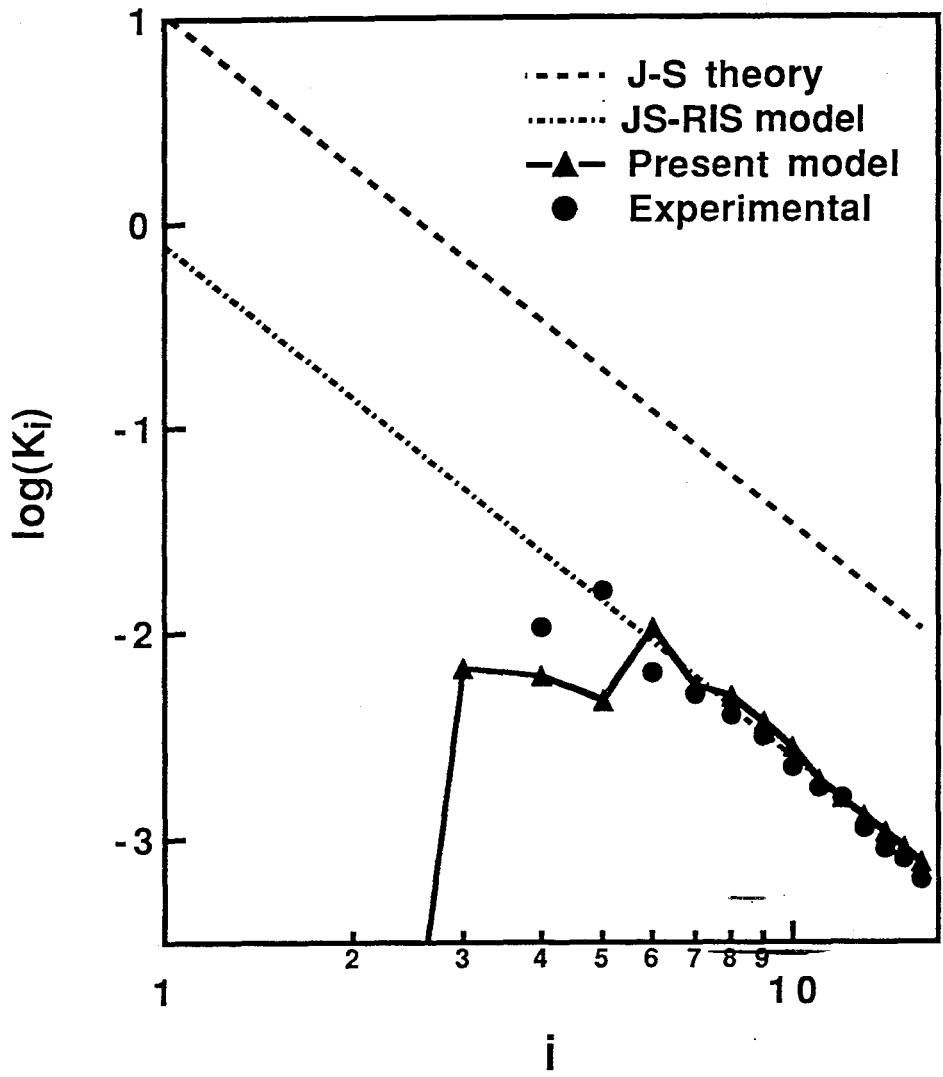


Fig.3

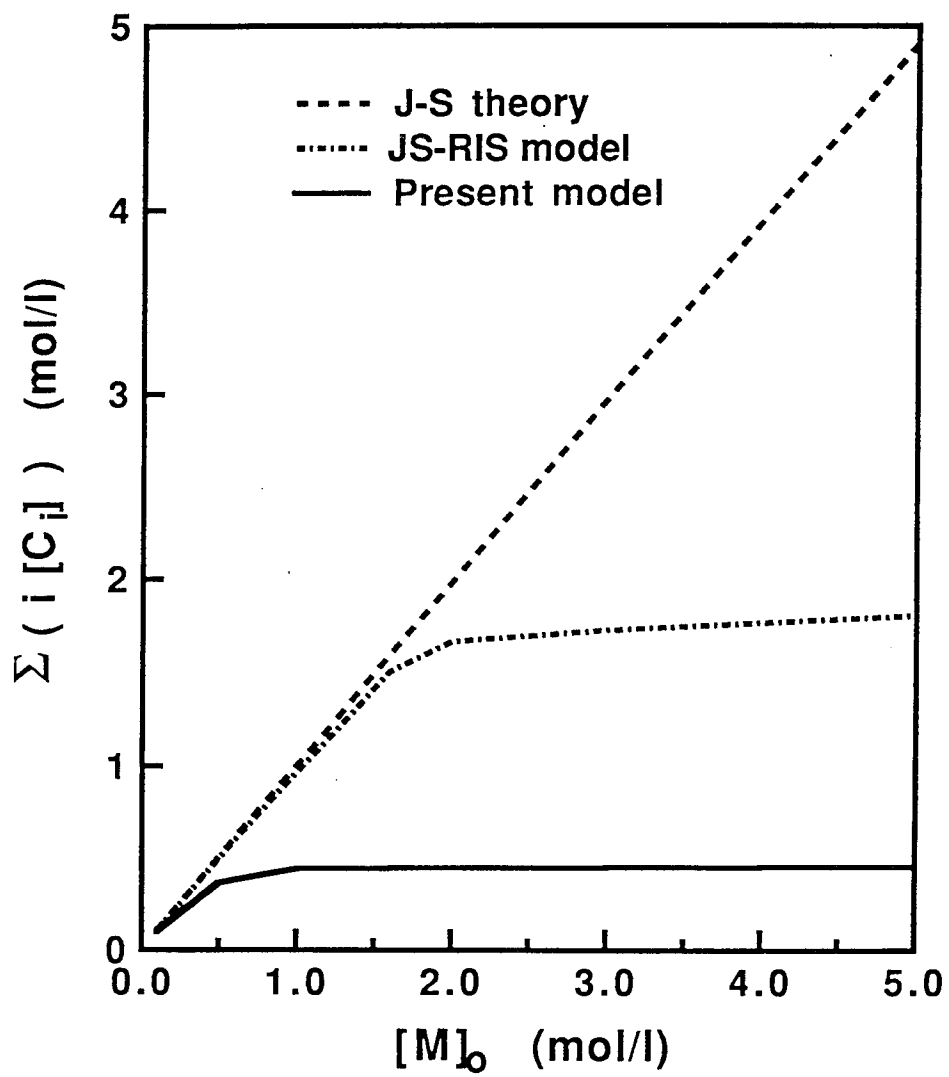


Fig.4

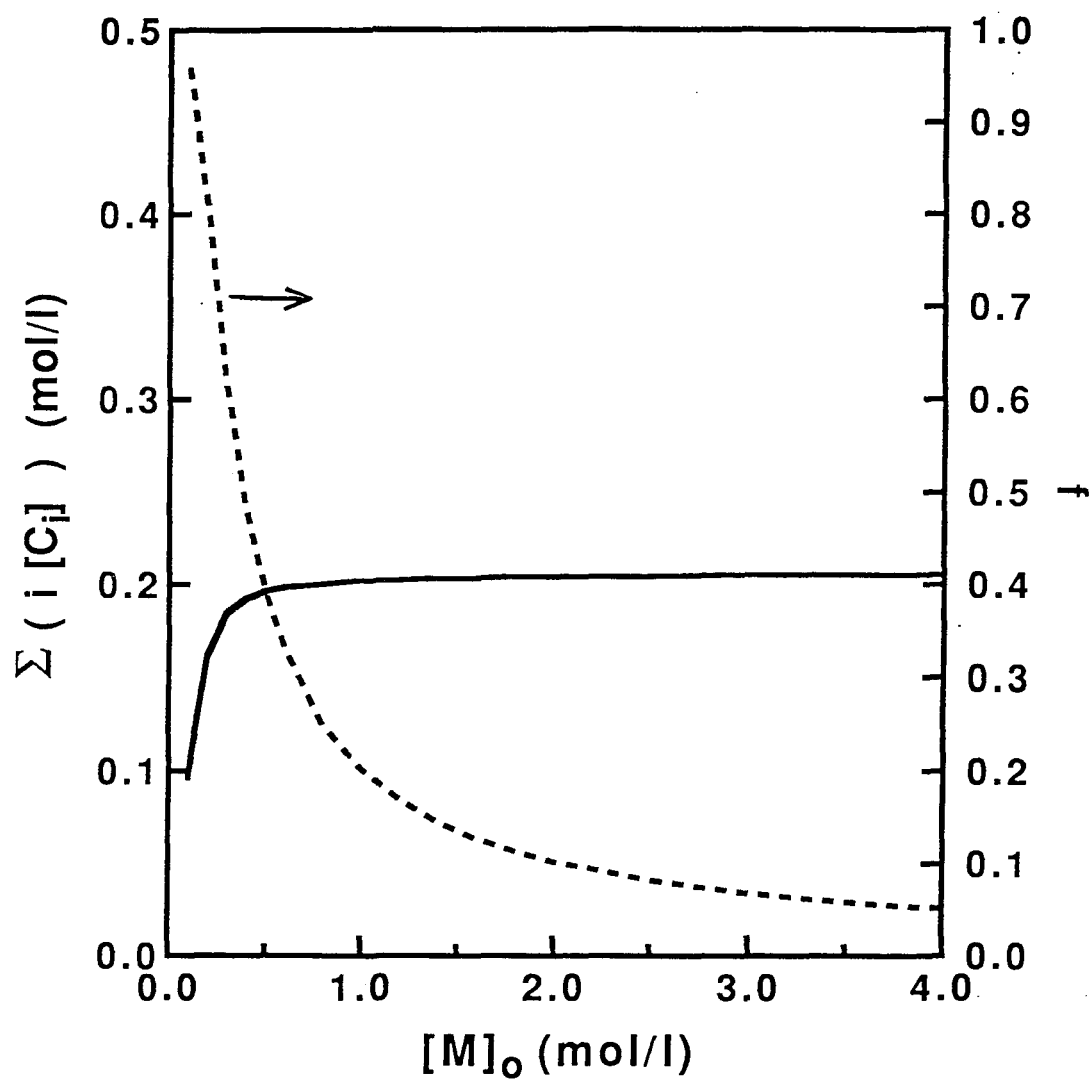


Fig.5

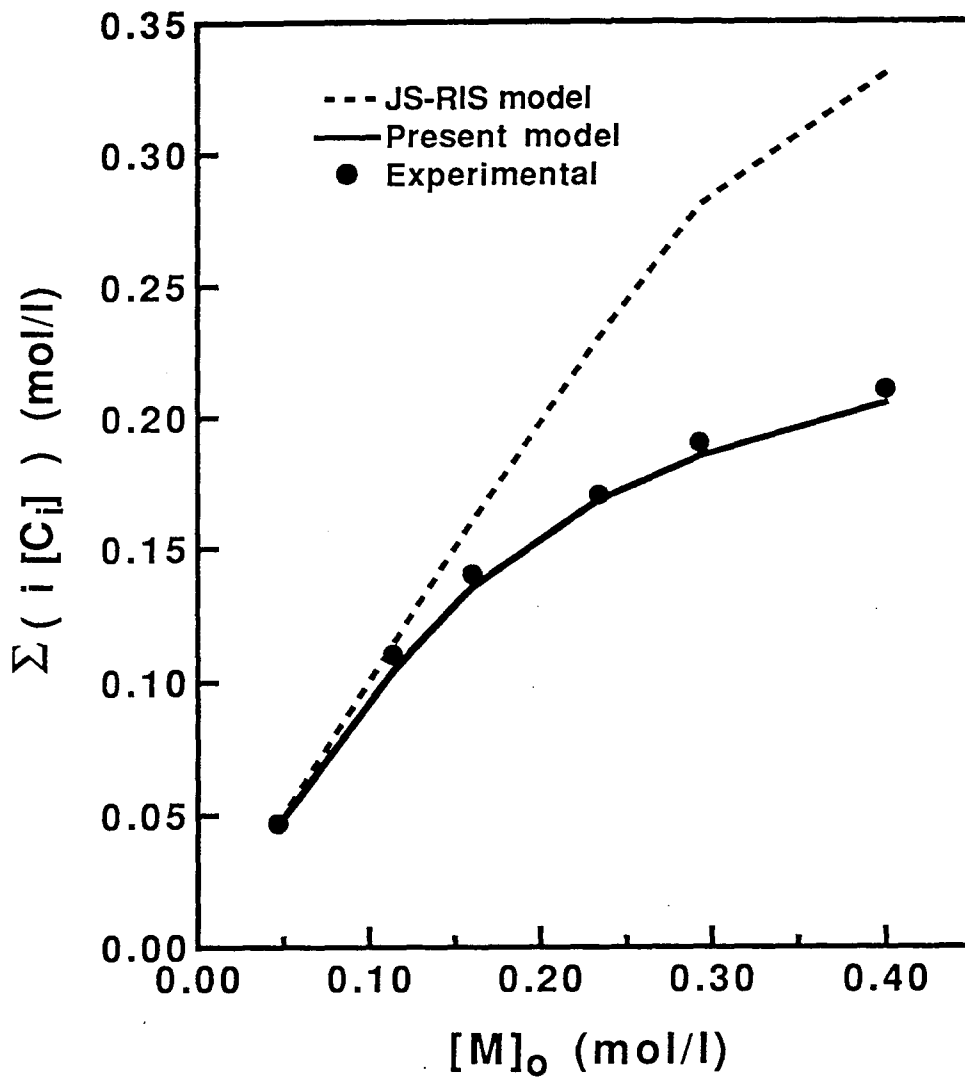


Fig.6

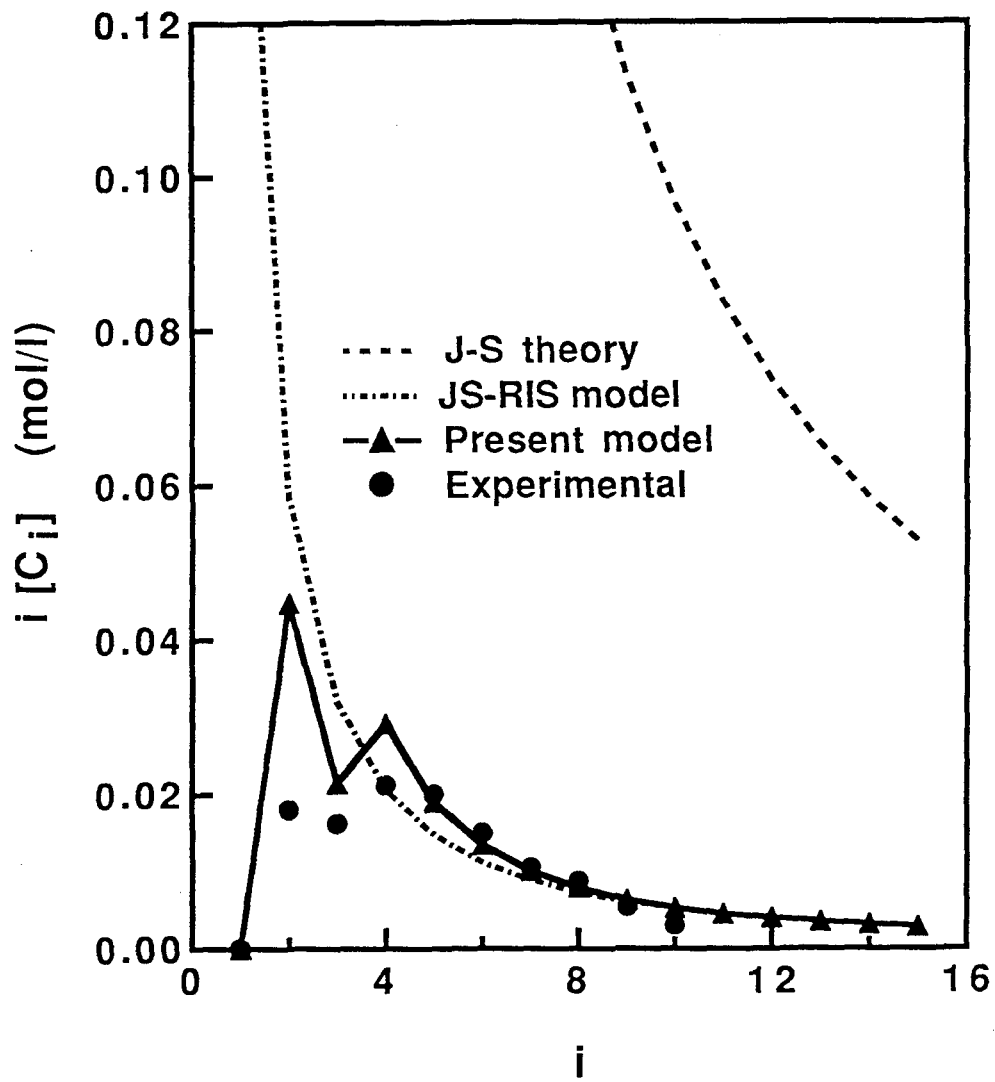


Fig.7

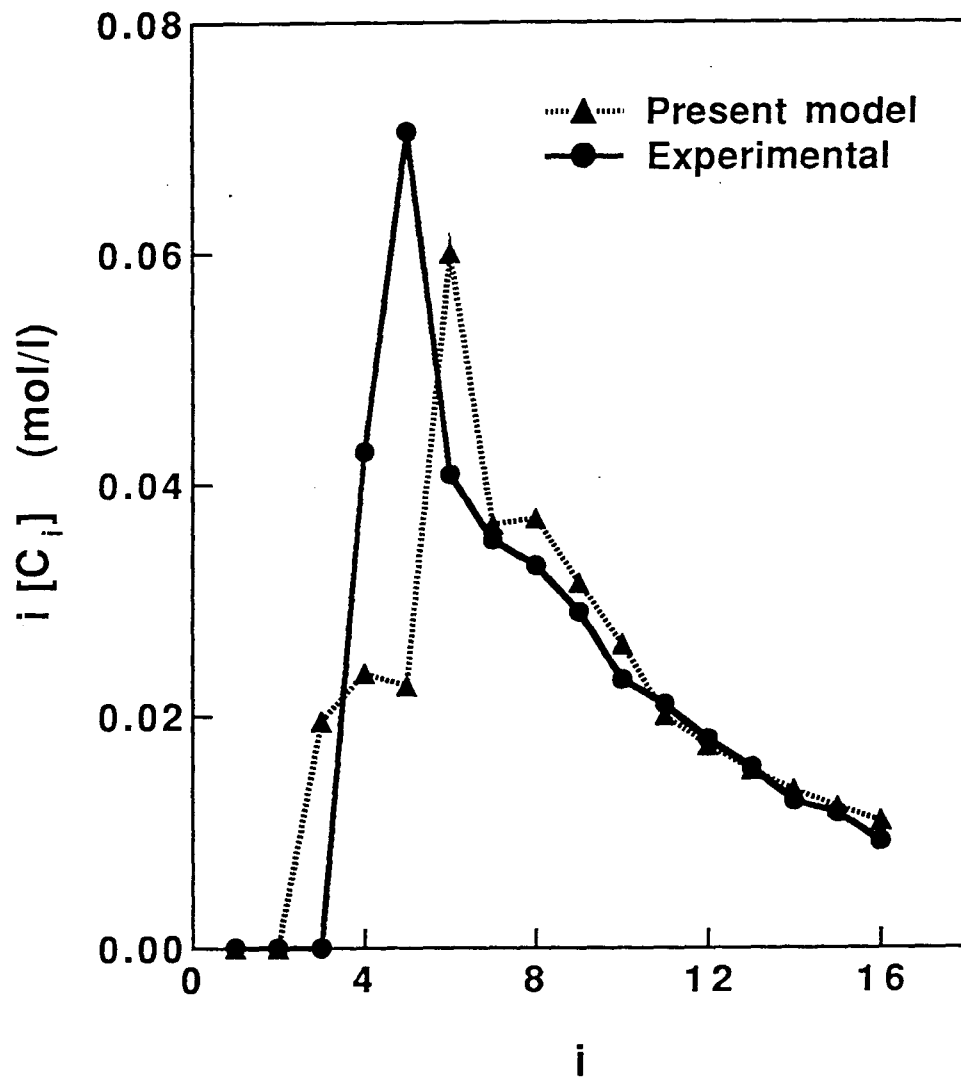


Fig.8a

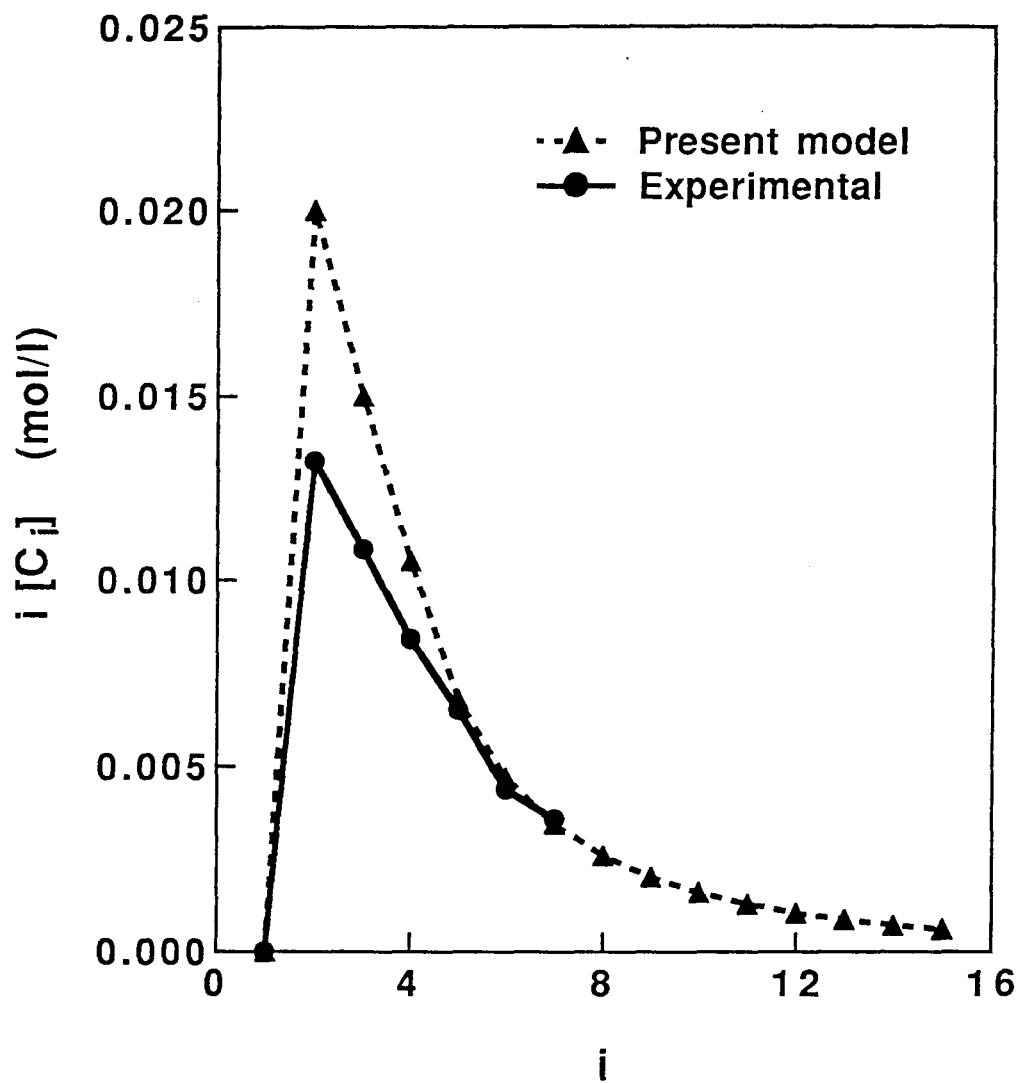


Fig.8b

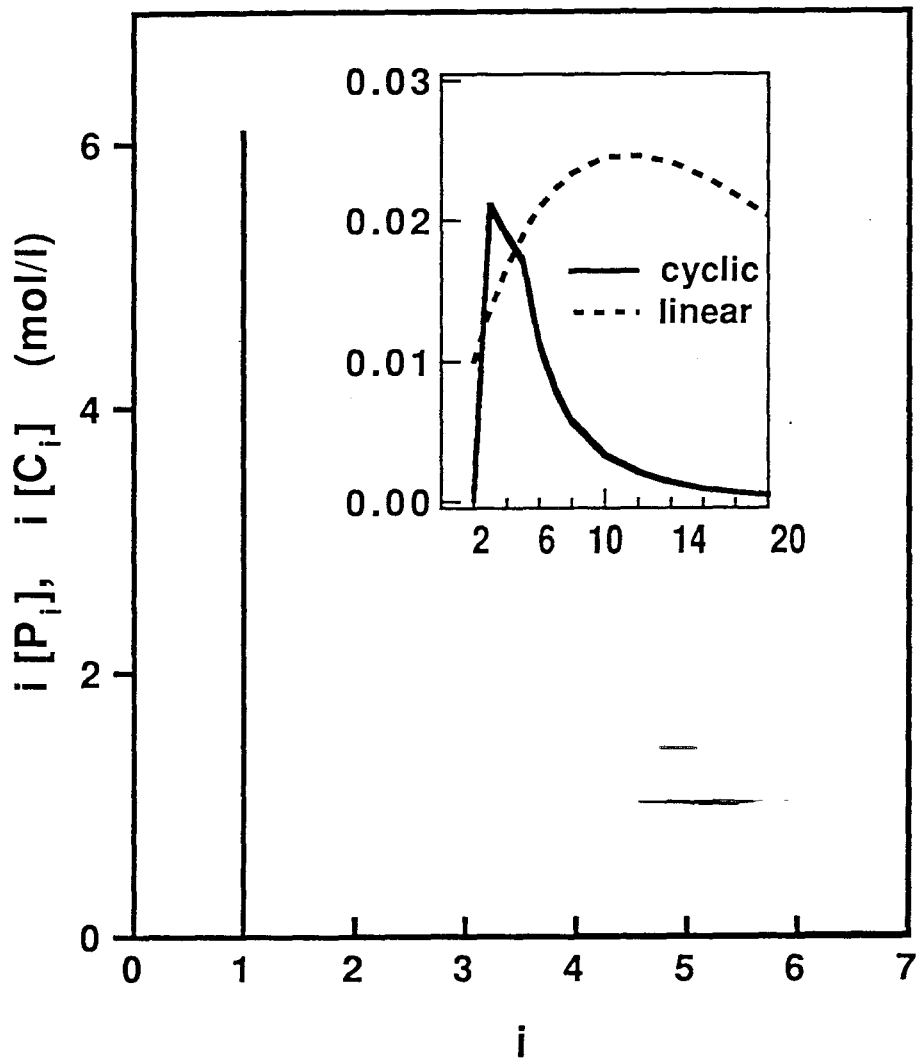


Fig.9

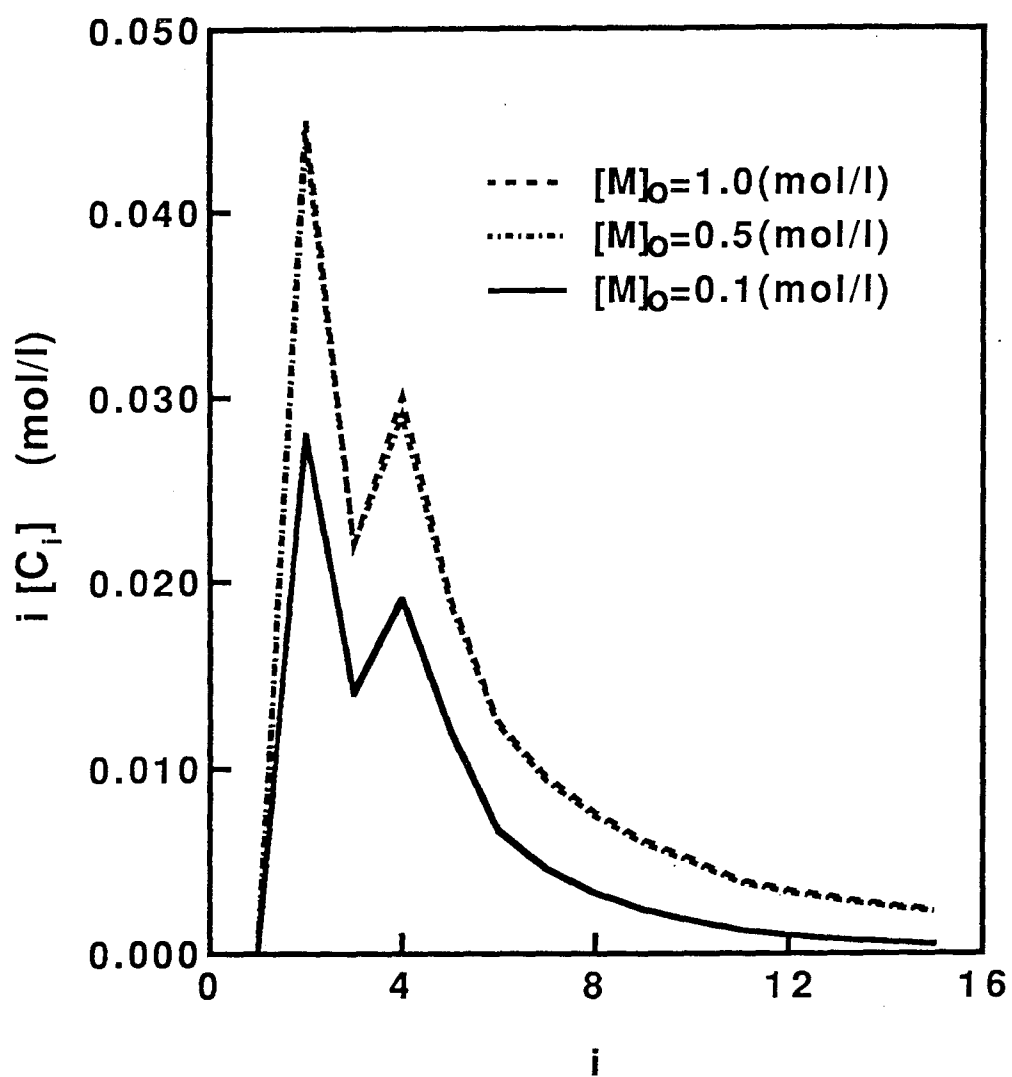


Fig.10a

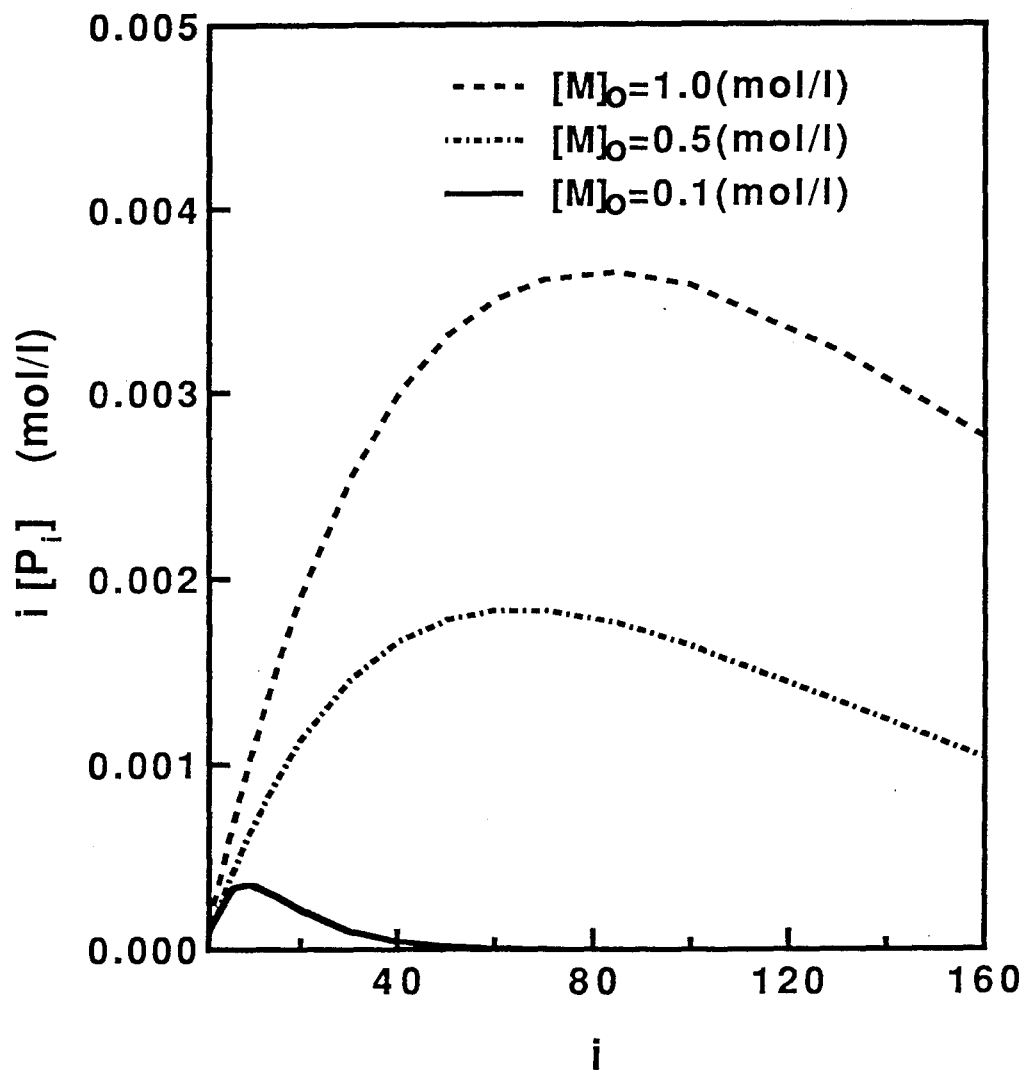


Fig.10b

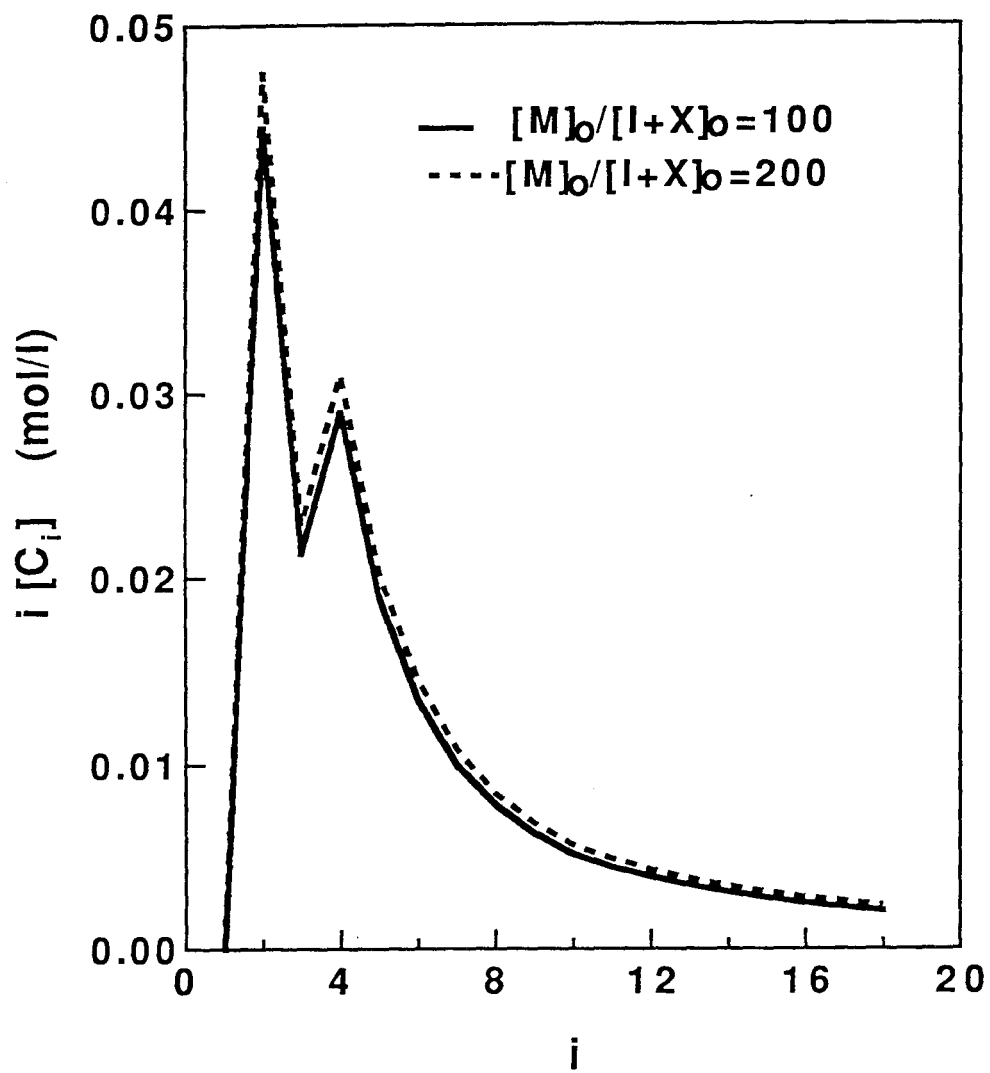


Fig.11a

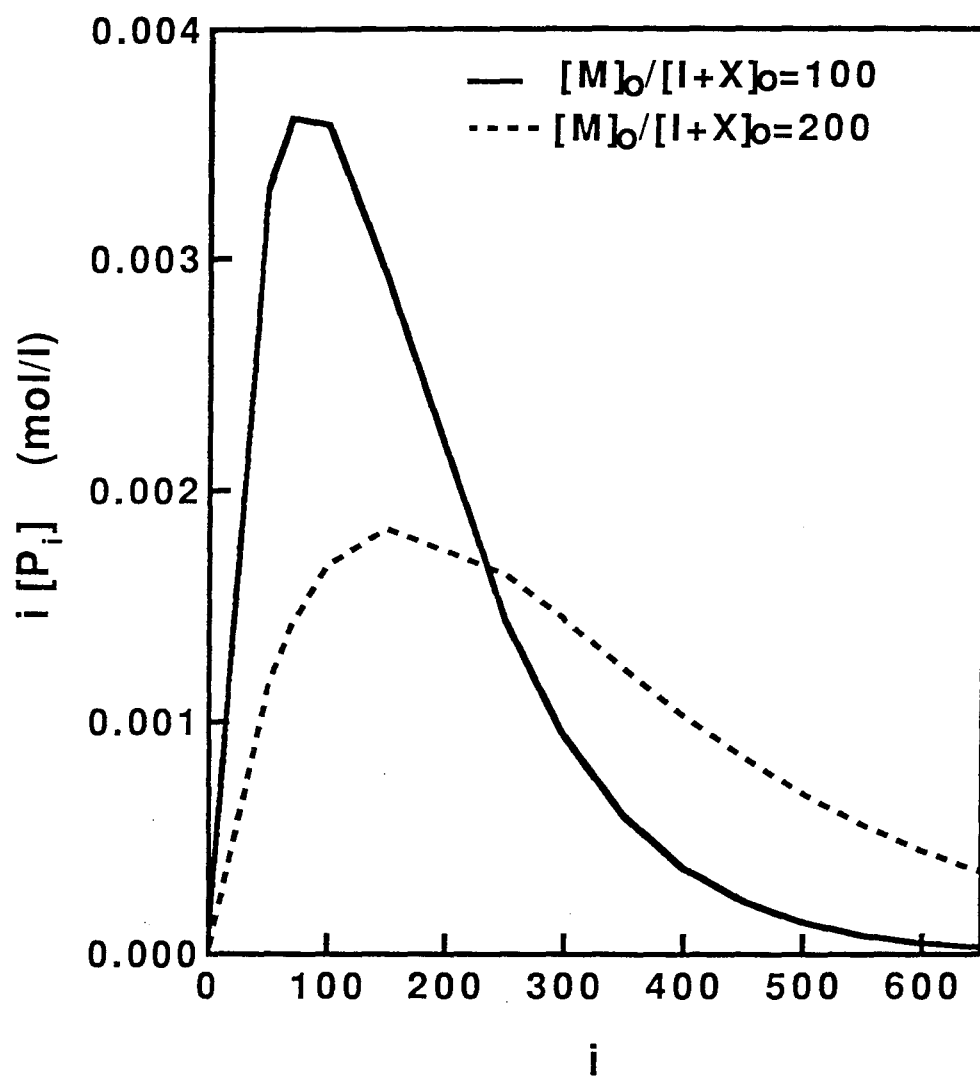


Fig.11b

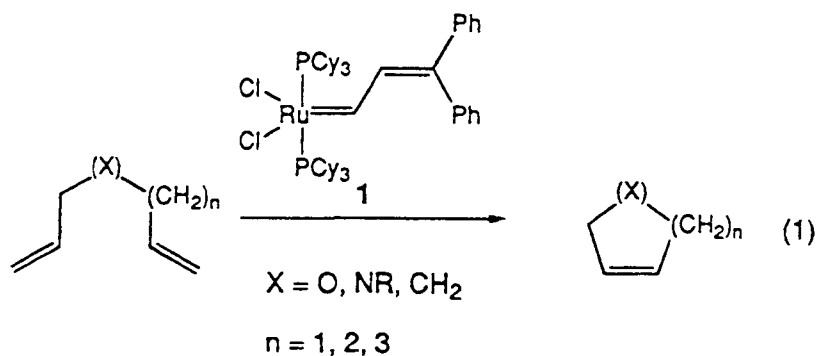
Catalytic Ring-Closing Metathesis of Dienes: Application to the Synthesis of Eight-Membered Rings

Scott J. Miller, Soong-Hoon Kim, Zhong-Ren Chen, and
Robert H. Grubbs*

*Contribution No. 9045, The Arnold and Mabel Beckman
Laboratory for Chemical Synthesis
Division of Chemistry and Chemical Engineering
California Institute of Technology
Pasadena, California 91125*

Received October 12, 1994

Previous reports from these laboratories have demonstrated that the ruthenium complex **1** efficiently catalyzes ring-closing metathesis (RCM) reactions to form five-, six-, and seven-membered carbocycles and heterocycles (eq 1).^{1,2} The synthesis of eight-membered rings, common structural elements in numerous natural products,³ has proven to be a challenging extension of this methodology. Presumably, the kinetics of ring closure, the strain inherent in many eight-membered rings, and the competing metathesis-based polymerization of reactants and/or products are among the factors contributing to this problem. The subject of this communication is the application of catalyst **1** to the RCM of several eight-membered-ring targets.



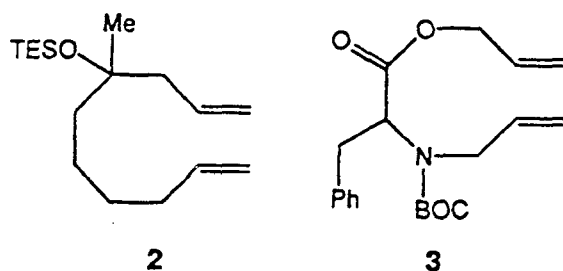
Our initial studies focused on the RCM reactions of acyclic precursors which, upon treatment with catalyst **1**, would afford eight-membered rings. Whereas acyclic diene precursors could successfully undergo RCM to form small (five- to seven-membered) rings, no eight-membered-ring products were observed when acyclic precursors **2** and **3** were subjected to standard RCM conditions. In contrast to the smaller ring analogs, acyclic dienes afforded only dimeric products resulting from intermolecular metathesis reactions, even when the reactions were performed at high dilution or under syringe pump conditions.

However, we have found that the introduction of a conformational constraint greatly enhances the ability of analogous dienes to undergo RCM to afford eight-membered rings (Table 1).⁴ For example, the catechol derivative **4** undergoes rapid RCM to form the eight-membered ring **5** in 75% yield within 3 h at 55 °C (entry 1). Similarly, the *trans*-substituted cyclo-

(1) Previous reports on RCM from this laboratory: (a) Fu, G. C.; Grubbs, R. H. *J. Am. Chem. Soc.* **1992**, *114*, 5426. (b) Fu, G. C.; Grubbs, R. H. *J. Am. Chem. Soc.* **1992**, *114*, 7324. (c) Fu, G. C.; Grubbs, R. H. *J. Am. Chem. Soc.* **1993**, *115*, 3800. (d) Fu, G. C.; Nguyen, S. T.; Grubbs, R. H. *J. Am. Chem. Soc.* **1993**, *115*, 9856. (e) Fujimura, O.; Fu, G. C.; Grubbs, R. H. *J. Org. Chem.* **1994**, *59*, 4029. (f) Kim, S. H.; Bowden, N.; Grubbs, R. H. *J. Am. Chem. Soc.* **1994**, *116*, 10801. For recent applications of RCM to natural product synthesis: (g) Martin, S. F.; Liao, Y.; Rein, T. *Tetrahedron Lett.* **1994**, *35*, 691. (h) Borer, B. C.; Deerenberg, S.; Bieraugel, H.; Pandit, U. K. *Tetrahedron Lett.* **1994**, *35*, 3191. For a review on applications of olefin metathesis in organic synthesis: Grubbs, R. H.; Pine, S. H. In *Comprehensive Organic Synthesis*; Trost, B. M., Ed.; Pergamon: New York, 1991; Vol. 5, Chapter 9.3.

(2) For the preparation and characterization of catalyst **1**: (a) Nguyen, S. T.; Johnson, L. K.; Grubbs, R. H.; Ziller, J. W. *J. Am. Chem. Soc.* **1992**, *114*, 3974. (b) Nguyen, S. T.; Grubbs, R. H.; Ziller, J. W. *J. Am. Chem. Soc.* **1993**, *115*, 9858.

(3) Petasis, N. A.; Patane, M. A. *Tetrahedron* **1992**, *48*, 5757.

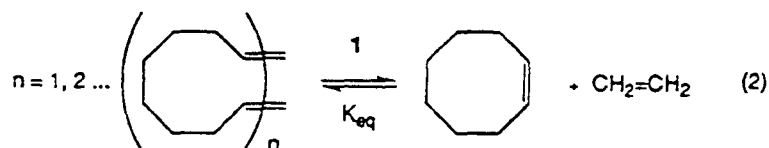


hexanes **6** and **10** (entries 2 and 4) are good substrates for RCM and afford the bicyclic [6.4.0] systems **7** and **11** in 75% and 60% yields, respectively. Presumably, the incorporation of the olefins which undergo metathesis into systems where they are constrained to be in proximity to one another predisposes the substrates **4**, **6**, and **10** to RCM on entropic grounds.

In contrast, the *cis*-substituted cyclohexane derivatives **8** and **12** were found to be poor substrates for RCM. When these compounds were submitted to the conditions which were found to work well for the *trans*-substituted analogs **6** and **10**, low yields of ring-closed products **9** (33%) and **13** (20%) were obtained. In each case, significant amounts of side products resulting from intermolecular metathesis, in addition to recovered starting material, were obtained.

Because RCM involves an equilibrium between ring-closed and open-chain products (eq 2),⁵ it seemed reasonable that the relative ratio of cyclic product to acyclic materials might correlate to the relative free energy changes for given processes (eq 3). Therefore, we sought to calculate the difference in the free energy changes for two reactions which were identical, except in the stereochemical arrangement at the ring junction. Our approach is illustrated by the transformation of **10** to **11** versus **12** to **13** (entries 4 and 5, Table I). Since the entropy change for each reaction is very similar, the relative difference in the free energy change for the two reactions is manifested primarily in the difference in the enthalpy changes, which in this case is primarily composed of the relative steric energies (SE). Molecular mechanics (MM3) calculations⁶ were carried out on compounds **10**–**13**, and the free energy change of entry

5 was found to be 1.8 kJ/mol (0.44 kcal/mol) greater than that for entry 4 (eqs 3–5). The ratio of ring-closed products to open-chain products presumably reflects the greater ring strain encountered in the formation of bicycle 13 relative to 11 upon going from reactant to product.



$$\Delta G(\text{entry 5}) - \Delta G(\text{entry 4}) = [\Delta H(\text{entry 5}) - \Delta H(\text{entry 4})] - [T\Delta S(\text{entry 5}) - T\Delta S(\text{entry 4})] \quad (3)$$

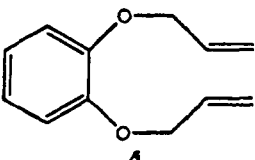
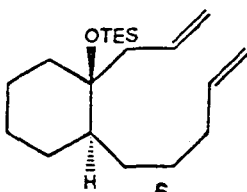
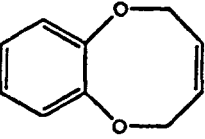
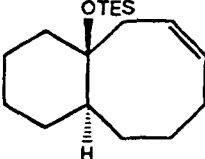
$$\Delta H(\text{entry 5}) - \Delta H(\text{entry 4}) = [\text{SE}(13) - \text{SE}(12)] - [\text{SE}(11) - \text{SE}(10)] \quad (4)$$

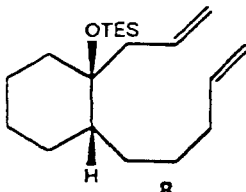
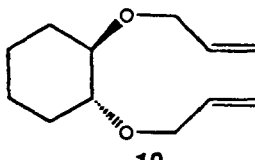
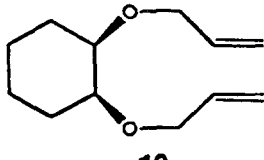
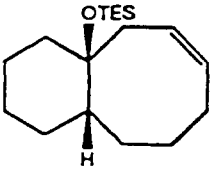
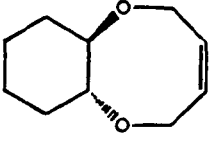
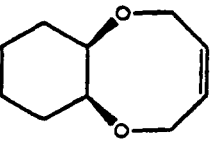
(4) Compounds were identified on the basis of their ^1H NMR, ^{13}C NMR, IR, and mass spectral characteristics (see supplementary material). Representative experimental procedure: Ruthenium catalyst 1 (FW 925.1, 0.08 equiv, 21 mg) in C_6H_6 (10 mL) was added through a cannula to a solution of 4 (FW 190, 1.0 equiv, 0.28 mmol, 55 mg, Table 1, entry 1) in C_6H_6 (10 mL, 0.015 M). The resulting light brown solution was placed in a 55 °C oil bath. After 3 h, the starting material was converted to compound 5 (TLC $R_f = 0.25$, 25% CH_2Cl_2 /hexanes). The solution was concentrated under reduced pressure and purified by flash chromatography (25% CH_2Cl_2 /hexanes) to afford the product 5 as a colorless, volatile oil (35 mg, 75% yield).

(5) For a discussion of the thermodynamics of ring-opening polymerizations with implications for RCM, see: Ivin, K. J. *Makromol. Chem., Macromol. Symp.* 1991, 42/43, 1.

(6) The MacroModel program was generously provided by Professor W. C. Still, Columbia University. For each structure 1000–5000 conformations were generated by MonteCarlo conformational searching. Subsequent minimizations of each conformation were carried out using the MM3 force field in the batch minimization mode.

Table 1. Catalytic RCM Synthesis of Eight-Membered Rings

Entry	1	2
Substrate		
Product		
Conditions (Yield)	8 mol% 1 , 3 h, 55 °C, 75%, C ₆ H ₆ (0.015 M)	5 mol% 1 , 4 h, 25 °C, 75%, C ₆ H ₆ (0.010 M)

3	4	5
		
		
5 mol% 1 , 20 h, 25 °C, 33%, C ₆ H ₆ (0.010 M)	8 mol% 1 , 2 h, 55 °C, 60%, C ₆ H ₆ (0.015 M)	8 mol% 1 , 2 h, 55 °C, 20%, C ₆ H ₆ (0.015 M)

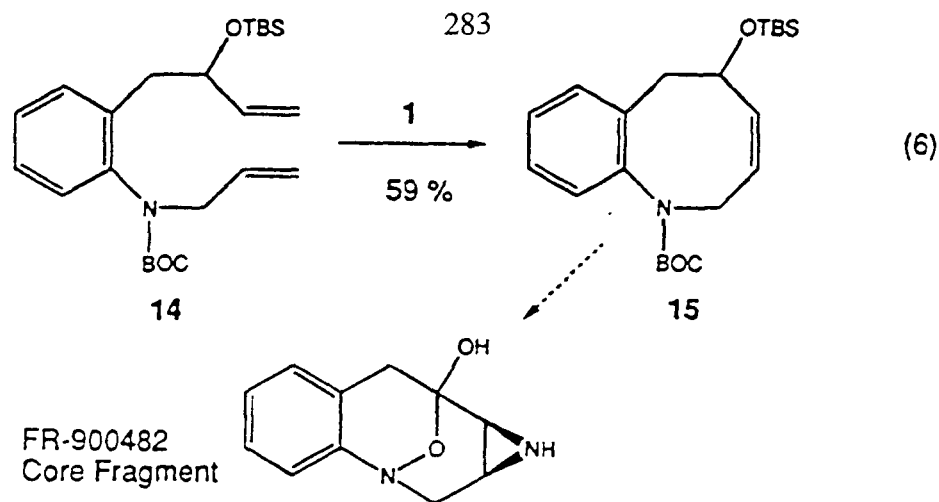
$$\Delta G(\text{entry 5}) - \Delta G(\text{entry 4}) = (119.6 - 109.0) - (112.9 - 104.1) = 1.8 \text{ kJ/mol (5)}$$

Despite the small magnitude of this difference, the implication for the relative equilibrium constants is in fact significant. The exact values of K_{eq} cannot be calculated, but a difference 0.4 kcal/mol could translate to a difference between one K_{eq} which is on the order of 1.4 ($\Delta G \sim -0.2$ kcal/mol, favorable for RCM) and one which is 0.71 ($\Delta G \sim 0.2$ kcal/mol, favorable for ring opening).^{7,8} Interestingly, this analysis is quite consistent with our experimental results, where the *trans*-fused bicycle **11** is isolated in 60% yield, while the *cis*-fused counterpart **13** is isolated in only 20% yield.

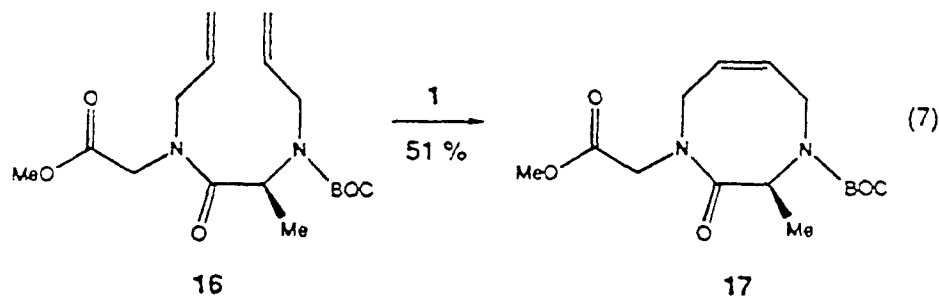
It is significant to note that this analysis is not rigorously accurate because the system does not actually reach equilibrium (the catalyst becomes sequestered by small amounts of oligomeric materials and decomposes over time), nor are the entropy changes rigorously equivalent.⁹ However, it is of interest in the sense that the differences in the calculated strain energies may be used to predict the relative facility of given RCM reactions within a stereoisomeric pair.

Finally, we wished to demonstrate the application of RCM to some targets of biomedical importance. For example, Kishi¹⁰ and Fukuyama¹¹ have demonstrated that suitably functionalized structures related to **15** can be converted to the anticancer agents mitomycin and FR-900482 (eq 6). To test the application of RCM to this structure class, compound **14** was prepared in four steps (see supplementary material for details) and subjected to RCM. When **14** was treated with catalyst **1** (10 mol %, 0.0025 M, 60 °C, 24 h), compound **15** was obtained in 59% yield.¹²

In addition, we are pursuing RCM as a means of synthesizing conformationally constrained peptides. An example of this strategy is illustrated in eq 7 where in the bis(*N*-allyl) dipeptide **16** has been prepared and subjected to RCM (eq 7). When **16** was treated with complex **1** (10 mol %, 0.005 M, 60 °C, 24 h), the cyclic dipeptide **14** was isolated in 51% yield. The cyclization is of particular interest when considered in comparison to the *N,O*-bis(allyl) amino ester **3**, which fails to undergo RCM under the conditions investigated. In the case of **16**, the equilibrium among the possible rotamers facilitates



the production of a rotamer which is conformationally disposed toward RCM.



In summary, this paper has presented our results concerning the application of complex 1 to the RCM reaction to prepare eight-membered rings. Unlike the application of 1 to the RCM of smaller rings, the present study reveals that eight-membered rings are more demanding in terms of both the amount of catalyst employed and the reaction conditions necessary to obtain good results (concentration, reaction time, temperature). However, we have found that a number of eight-membered-ring substrate classes are amenable to synthesis in reasonable yield by RCM. Defining the parameters which influence the cyclization reaction and extending this reaction to systems of bioorganic importance are among our current objectives.

(7) For a more rigorous and general treatment of ring-chain equilibria in ring-opening metathesis, see: Chen, Z.-R.; Claverie, J. P.; Grubbs, R. H.; Kornfield, J. A. Submitted to *Macromolecules*.

(8) Analogous calculations were performed on compounds 6-9, and a similar result was obtained.

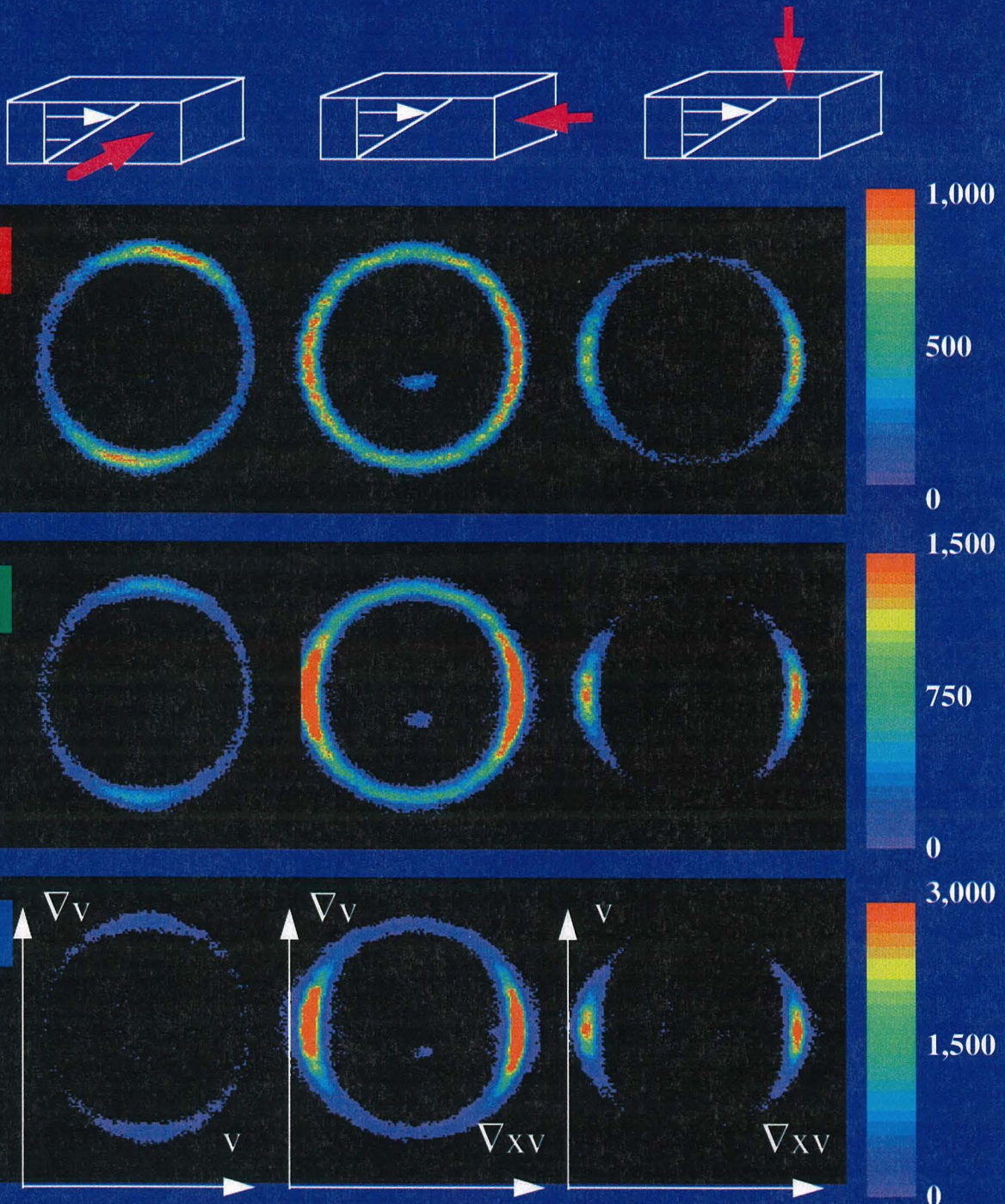
(9) Attempts to purge ethylene from the system have not resulted in significant enhancements of yields or rates.

(10) Kishi, Y. *J. Nat. Prod.* **1979**, *42*, 549 and references therein.

(11) Fukuyama, T.; Xu, L.; Goto, S. *J. Am. Chem. Soc.* **1992**, *114*, 383.

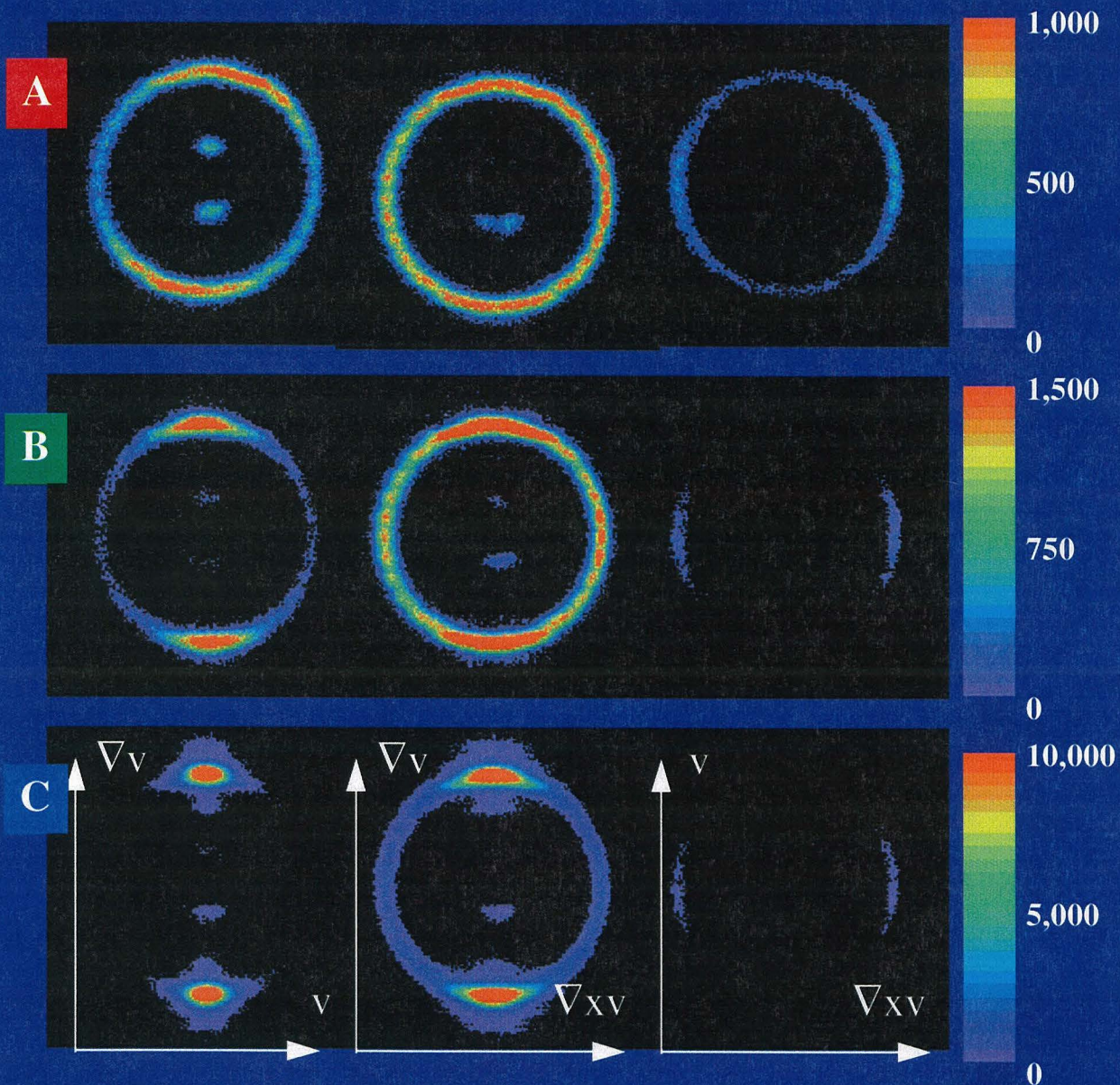
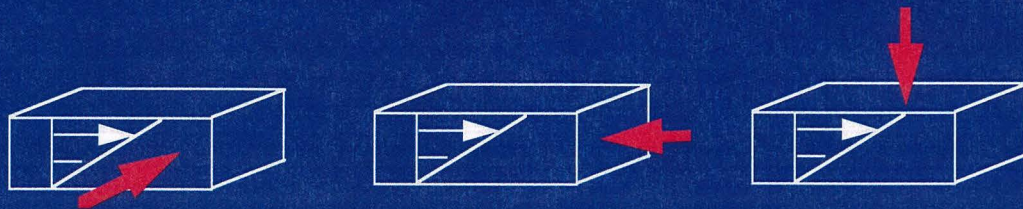
(12) Professor Stephen Martin of the University of Texas has informed us that he is applying a similar approach to the total synthesis of FR-900482.

Points Along the Way to Perpendicular (Regime I)



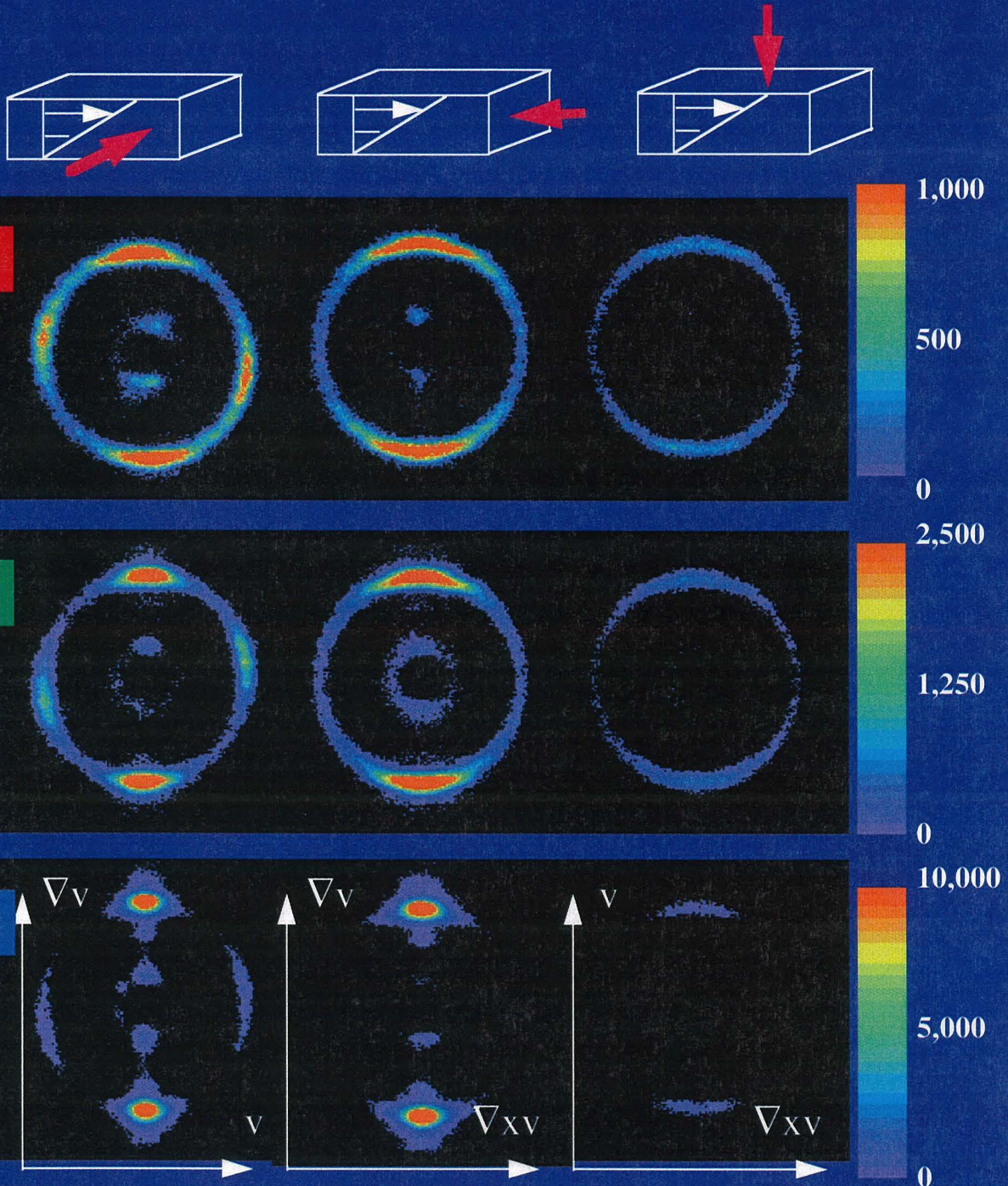
Z. R. Chen et al., *Science*, 277, 1248 (1997)

Points Along the Way to Parallel (Regime II)

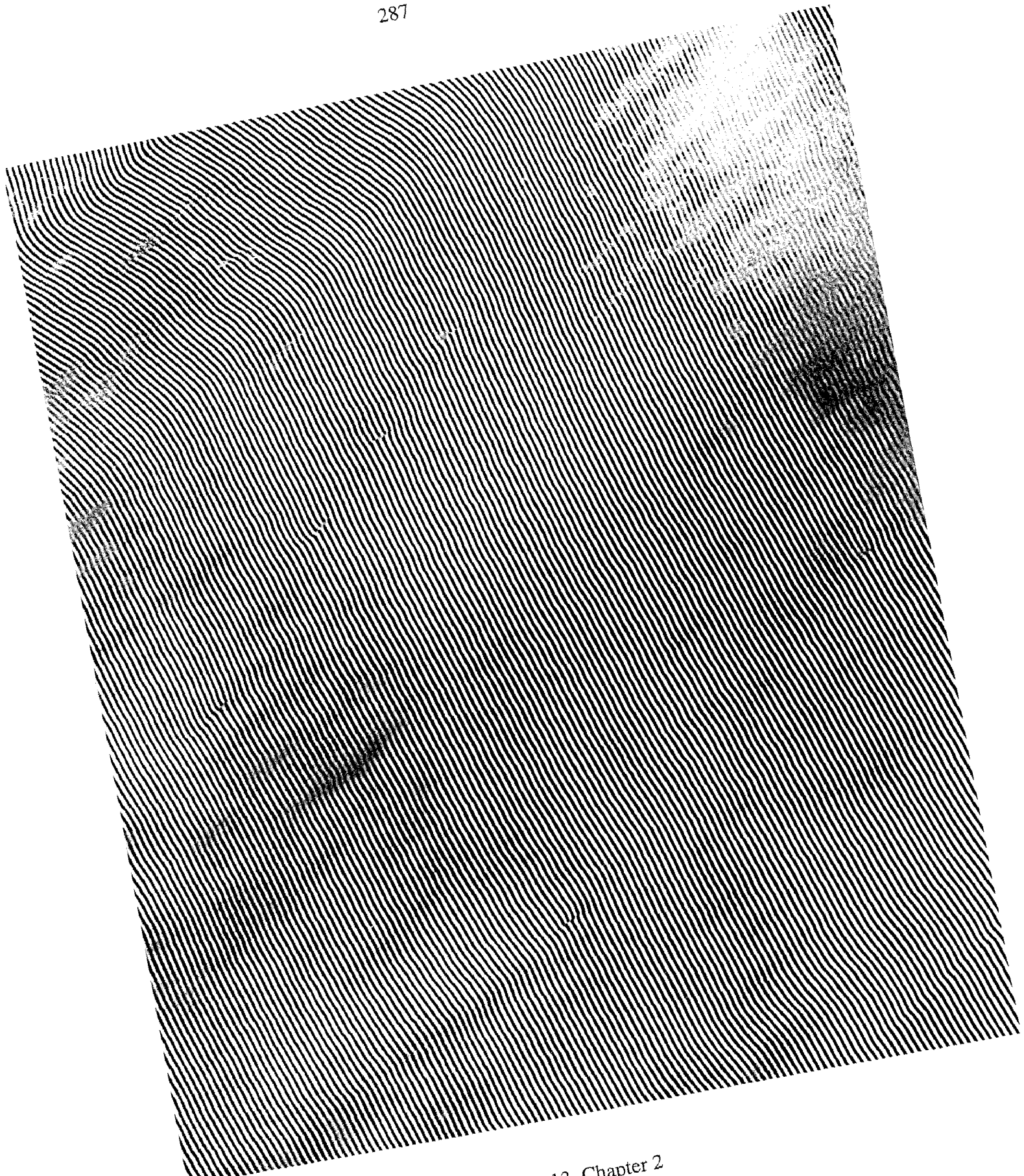


Z. R. Chen et al., *Science*, 277, 1248 (1997)

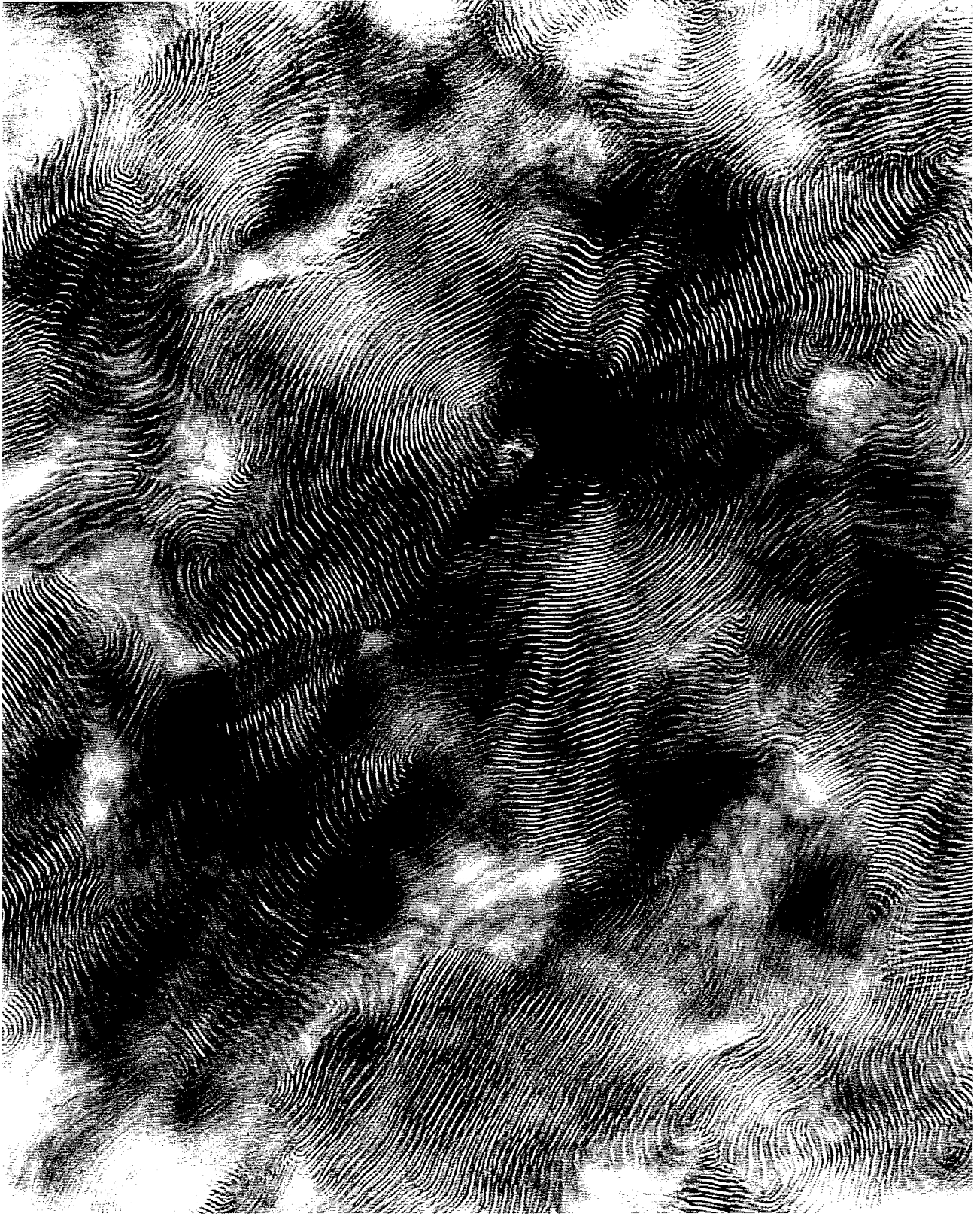
Points Along the Way to Parallel (Regime III)



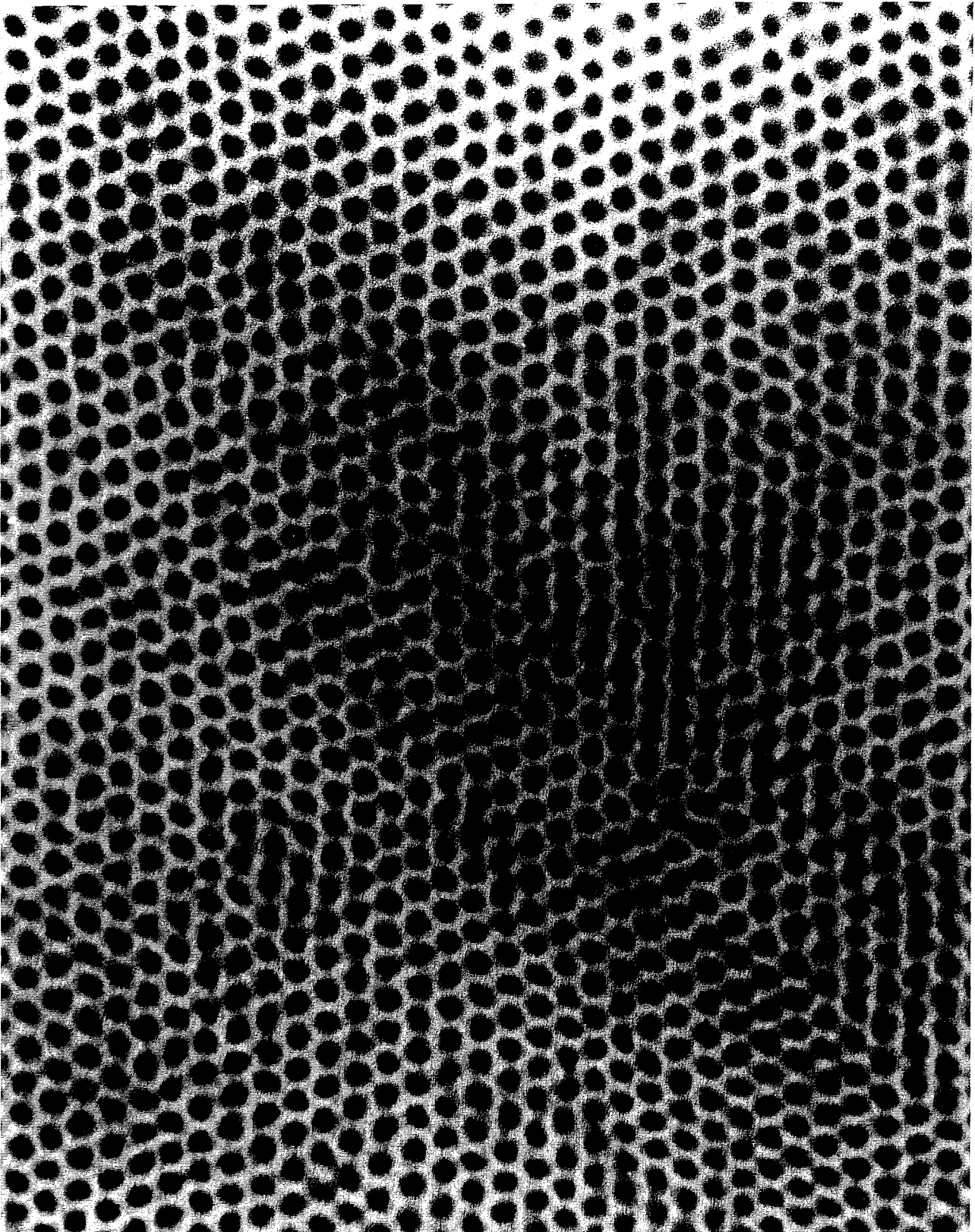
Z. R. Chen et al., *Science*, 277, 1248 (1997)



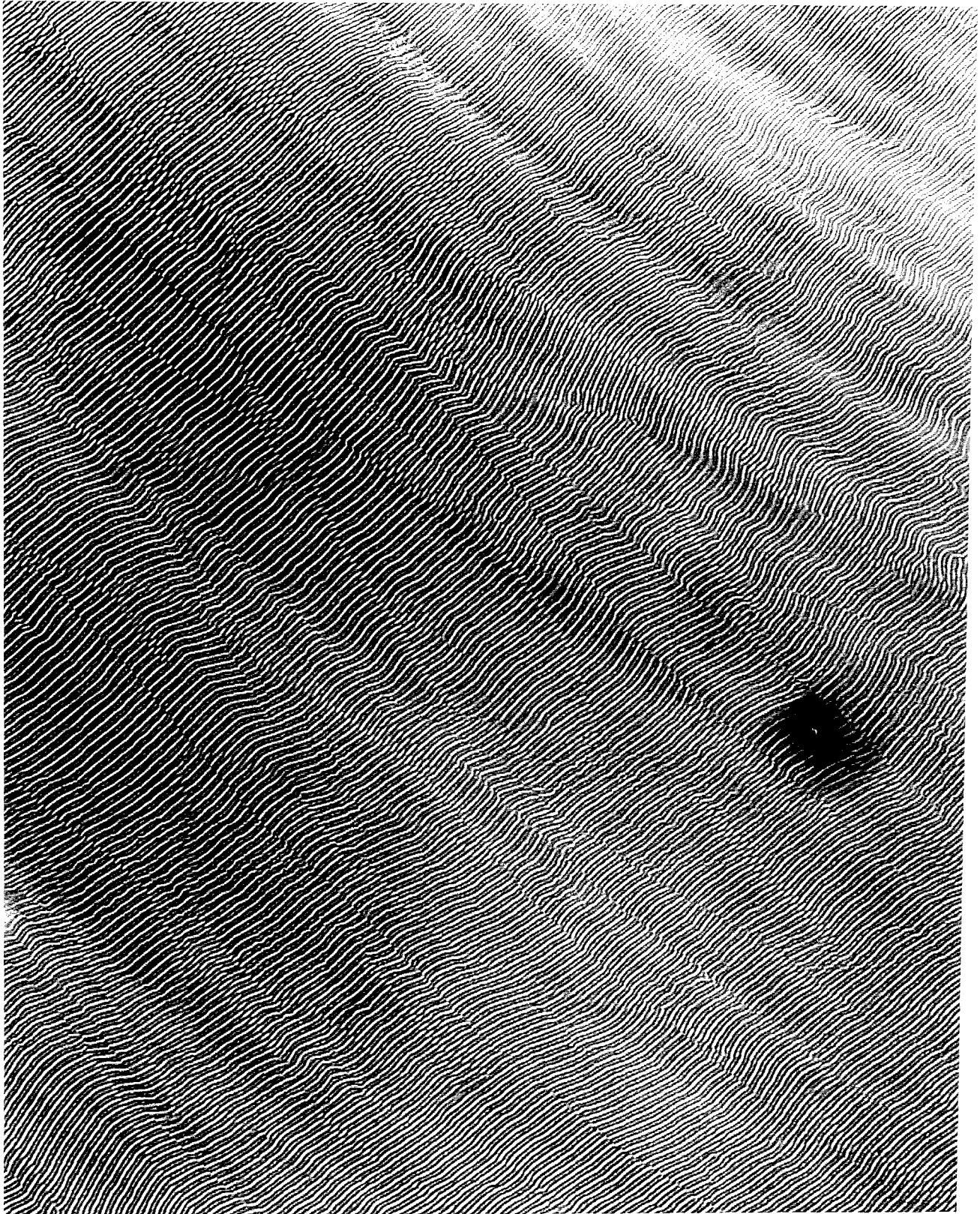
Reproduced from Fig.13, Chapter 2



Reproduced from Fig.2d, Chapter 3



Reproduced from Fig. 29a, Chapter 3



Morphology of SIR-35, after Shearing while Cooling Experiment (Section 4C, Chapter 3)